INTERFACE FRACTURE IN HIGH STRENGTH CONCRETE

by

Kwang-Myong Lee

B.S., Civil Engineering, Seoul National University, Seoul, Korea (1983)
M.S., Civil Engineering, Seoul National University, Seoul, Korea (1985)

Submitted to the Department of Civil and Environmental Engineering
in Partial Fulfillment of the Requirements for the Degree of

DOCTOR OF PHILOSOPHY

at the

MASSACHUSETTS INSTITUTE OF TECHNOLOGY

February 1993

Signature of Author _____
Department of Civil and Environmental Engineering
December 14, 1992

Certified by _____
Oral Buyukozturk
Professor, Department of Civil and Environmental Engineering
Thesis Supervisor

Accepted by _____
Ole S. Madsen
Chairman, Departmental Committee on Graduate Students

INTERFACE FRACTURE IN HIGH STRENGTH CONCRETE

by

Kwang-Myong Lee

Submitted to the Department of Civil and Environmental Engineering
on December 14, 1992, in partial fulfillment of the
requirements for the degree of
Doctor of Philosophy

Abstract

Deformation and failure behavior of concrete composites is influenced by the characteristics of interfaces, such as mortar-aggregate interfaces and cement paste-fiber interfaces. Recently, the interest in the study of the role of mortar-aggregate interfaces on the material behavior has increased particularly due to the need for the development of high performance cementitious materials. Presently, there is a need for the development of a fracture mechanics based approach for the characterization of interface fracture properties. In this study, novel fracture models are proposed to quantify the fracture properties of mortar-aggregate interfaces. Sandwich specimens are developed and used to measure the fracture toughness of the mortar-aggregate interfaces in concrete. The tests indicate that the interface fracture toughness is markedly increased with the increase in the effects of shear loading relative to that of tensile loading due to shear interlocking effects. It is observed that the fracture toughness of high strength mortar-aggregate interfaces is much higher than those of normal-strength mortar-aggregate interfaces due to the silica fume effects with the use of superplasticizers and the reduced water amount on the interfaces.

The crack path criterion for elastically homogeneous materials is not valid when the crack advances at an interface because, in this case, the consideration of the relative magnitudes of the fracture toughness between the interface and the aggregate or the mortar are involved. For the prediction of crack growth at the interfaces, a criterion based on energy release rate concepts is considered and an experimental/numerical study is presented on the two-phase composite beam models of concrete to investigate the crack penetration vs. crack deflection scenarios in the interfacial regions of concrete. The interface fracture toughness values measured from the sandwich models is well correlated with the results from the physical testing and the finite element simulation of the composite models. From these studies fracture mechanics parameters influencing deformation and cracking of high strength concrete are defined. On the basis of established fracture mechanics parameters, general guidelines are proposed for the mix design to produce high performance concrete materials.

Thesis Supervisor: Dr. Oral Buyukozturk

Title: Professor of Civil and Environmental Engineering

Dedicated to

My father and mother

Acknowledgement

I would like to give my sincerest thanks to my thesis supervisor, Professor Oral Buyukozturk, for his guidance, support, and encouragement. Working with him has been truly a great pleasure. I feel very lucky to have experienced his way of thinking and this experience will continue to benefit me significantly in the future.

Special thanks go to Professor Christopher K. Y. Leung for his valuable suggestions on the research. I would like to deeply thank Professor John W. Hutchinson of Harvard University for his contribution to my understanding of the Interface Fracture Mechanics. Also, I would like to thank Professor Thanasis C. Triantafillou for his interest and advice.

I am indebted to my previous supervisors, Professor Young Ki Shin, Professor Seung Pil Chang, and Professor Byung Hwan Oh at the Seoul National University in Korea, for introducing me to structural engineering and for their encouragements.

This research was supported by the NSF Grant Number MSM-9016814 and partially by W. R. Grace & Co., Cambridge, MA. I would like to thank to Dr. Ken P. Chong, the cognizant official in NSF program, for his interest and support and Dr. N. Berke of W. R. Grace & Co for his helpful discussions.

I am also grateful to fellow students in High Performance Materials and Structures Program. I furthermore appreciate the many friendship and valuable discussions: Dr. Jong Gye Shin, Dr. Seong Wook Cho, Hyung Il Lee, Hyun June Yim, Dr. Hyun Seok Yang, Dong Ho Choi, Seong Jin Song, and other friends. My appreciation is extended to Arthur and Steven Rudolph for helping me during my experimental work.

My academic achievements would have been impossible without the spiritual support of my family, and I especially want to give my deepest thanks to my mother. Special love goes to my wife, Hyunah, and my son, Joohyong. I have greatly enjoyed the life in MIT with them.

Contents

List of Figures

List of Tables

Notation

The following major symbols are used in this thesis:

a = crack length;
E_i = Young's modulus of material i;
ν_i = Poisson's ratio of material i;
$\bar{E}_i$ = $E_i/(1-\nu_i^2)$;
G = energy release rate;
G_d = energy release rate of deflected crack;
G_p^{max} = maximum energy release rate of penetrated crack;
G_{max}^t = maximum energy release rate of kinked crack;
h = thickness of sandwich layer;
$K = K_1 + iK_2$ = interface stress intensity factor;
$K^\infty = K_I + iK_{II}$ = stress intensity factor;
L = structure size;
$\hat{L}$ = fixed length for reporting data;

α, β = Dundurs' mismatch paramters;
Γ_1 = mode I fracture toughness of material 1;
Γ_i = fracture toughness of interface;
γ = crack hitting angle in beam composite model;
δ_1, δ_2 = crack surface displacements distance r behind crack tip;
ϵ = oscillation index;
θ_i = inclination angle of Brazilian disk specimen;
σ_{22}, σ_{12} = normal stress and shear stress, respectively;
ϕ = $tan^{-1}(K_{II}/K_I)$;
ψ = phase angle of $KL^{i\epsilon}$;
$\hat{\psi}$ = phase angle of $K\hat{L}^{i\epsilon}$;
ψ^* = phase angle of $Kh^{i\epsilon}$; and
$\omega(\alpha, \beta)$ = phase shift in sandwich specimen.

Chapter 1

Introduction

Concrete is one of the most important materials used by men. Since its invention in 1824, concrete, along with steel, has become the foundation of modern civilization. Its use has enabled the development of advanced transportation, water and sewage treatment systems, contemporary architecture, and urbanism. The easy with which concrete is manufactured in the field in any shape and its high compressive strength are some of the reasons why concrete is the most common construction material in the world. At present, a significant fraction of the world structures consists of concrete.

In the past decades, three developments have permitted modern concrete to improve its potential as a construction material, namely: the introduction of air-entraining admixtures to improve freeze-thaw resistance; the use of high-range water reducers (or superplasticizers) to enable easier placing and improvements in physical properties; and condensed silica fume additionally to enhance overall durability and strength. With the advent of superplasticizers in the 1970's the use of silica fumes has been increased; the superplasticizers reduce the silica fume's high water demand. Together with superior designs and processing techniques, these advances make it possible to produce stronger and more durable structures.

In the coming decades, concrete will be increasingly called upon to serve as a construction material for hostile environments such as seafloor tunnels, offshore piers and platforms, and confinement structures for solid and liquid wastes containing toxic chemicals and ra-

dioactive materials. Also, due to the high cost of repair, most of these structures will be required to have a service life of hundreds of years, instead of 40 to 50 years normally expected from ordinary concrete. In order to meet this challenge high-performance concrete (HPC) mixtures are being developed. High performance is generally assumed to be synonymous with high strength, although this is not true in every case. In this thesis, high performance concrete will imply concrete with high strength and improved ductility properties.

1.1 Background

1.1.1 Development of High Strength Concrete

Recently, the use of high strength concrete (HSC) up to compressive strengths of 138 MPa (20,000 psi) is increasing considerably because of its greater strength and stiffness, reduced creep and drying shrinkage, and improved durability. This increased use of high strength concrete has necessitated many engineering studies to enhance the mechanical properties of the concrete and to achieve better control in producing the concrete. The present investigation may be considered as one of the needed studies in these aspects.

While high strength concrete was defined as concrete with compressive strength higher than 41 MPa (6,000 psi) in the workshop held in Chicago in 1979, in the more recent symposiums concrete with compressive strength in excess of 69 MPa (10,000 psi) are considered to be high strength concrete. Clearly, a definition for high strength concrete change with research developments. In general, there are two methods of producing high strength concrete: (1) lowering the water/cement ratio with a better selection of individual materials, (2) using chemical or mineral admixtures such as superplasticizers, fly ash, and silica fume. The use of silica fume in combination with superplasticizers has been considerably increased in producing high strength concrete during the past decade due to its significant

water reducing effects and high pozzolanic reaction.

Silica fume (SF) is a by-product which emerges during the production of silicon and ferrosilicon alloys. This is a kind of pozzolanic mineral admixture and has been widely used to improve many qualities of concrete, such as increasing strength and reducing permeability and bleeding. With these desired influences on concrete properties, SF has been used in various engineering applications such as shore approach projects, bridge overlays, parking garages, fiber reinforced members, and precast structural members like lightweight concrete rooftile, and road construction.

Traditionally, the mix design of high strength concrete has followed a 'trial and error' approach. While there is some qualitative understanding as to how concrete properties are influenced by the characteristics of mortar matrix, aggregate, and the interface between them, there is no quantitative guidelines for mix design of high strength concrete similar to the ACI Committee 211 Recommended Practice for 'Selecting Proportions for Concrete Mixtures'. As a result, the materials and mix proportions are selected empirically by extensive laboratory testing. This implies that when high strength concrete needs to be made from locally available materials, the problem is complicated by a variety of newly developed chemical and mineral admixtures that may have to be incorporated simultaneously into the concrete mixture [Mehta and Aitcin, 1990a]. Furthermore, the selection of materials for coarse aggregate is also important.

Although high strength concrete overcomes many disadvantages of normal strength concrete, high strength concrete may possess some undesirable characteristics. Two major problems are the lack of ductility and the low tensile strength. The ductility of high strength concrete (HSC) is even lower than that of normal strength concrete and a brittle and explosive failure could occur in high strength concrete structures. Thus, the future ACI code should place stringent provisions to account of the lack of ductility of HSC. A low tensile strength relative to the high compressive strength is the other important problem in

HSC, indicating that special attention should be paid when HSC is used in flexural members. Thus, the use of HSC might be limited. Recently, many attempts have been made to improve HSC by varying the mix proportion, and/or adding ingredients such as fibers.

1.1.2 Stress-strain Behavior of Concrete

Cement-based composites can be generally categorized into three classes by their stress-strain response to a uniaxial compression (Fig. 1.1). Class I materials are deemed "tough" and exhibit nonlinear behavior at an ultimate load, followed by a long tail. Fiber reinforced concrete is included in this class. Class II materials exhibit linear behavior in the beginning of the ascending branch and subsquently, inelastic behavior up to a load maximum, followed by a relatively short tail. Such behavior is usually observed in normal strength concrete having compressive strength less than 41 MPa (6,000 psi). In this material, bond cracking play a significant role in the inelastic deformation behavior and the final failure occurs through the formation of continuous cracks in mortar matrix, bridging the bond cracks. Class III materials have a steeper, more linear ascending part of the stress-strain curve than Class II materials and fail catastrophically. High strength concrete (stronger than 41 MPa (6,000 psi)) is an example of class III materials and its increased linearity in the ascending part can be attributed to an increase in the bond strength which delays crack formation until higher stresses and strains are reached. The distinction between Class II and Class III is primarily governed by the interfacial properties and the resulting effects on mortar cracking as well as properties of constituents. Therefore, the development of high strength concrete with improved toughness and durability requires a fundamental understanding of the behavior of the interfaces introduced in this material.

1.2 Research Approach

1.2.1 Importance of Interface in Concrete

Concrete is a heterogeneous material, and its behavior is complicated by the interaction of the constituents. Thus, the mechanical properties of cement-based materials are determined by: (1) the chemical composition, the microstructure, and the pore geometry of the cementitious materials; (2) the properties of the aggregate; and (3) the nature of the cement-aggregate bond. Particularly, the various interfaces between different phases in concrete system (e.g. between cement paste and aggregate, concrete and steel), and the associated interfacial properties significantly influence the properties of concrete. Therefore, to understand the mechanical behavior of the concrete the nature of the deformation and failure of matrix-aggregate interfaces needs to be considered. Interfaces which represent discontinuities are intrinsic to the concrete, and, conventionally, we regard the interfacial regions as the "weak links" in the concrete structure.

The terms "interfacial zone" and "interface" can be defined as follows. The layer which incorporates all of the naturally and artificially formed anomalities in the vicinity of the aggregate surface is referred to as the interfacial zone, transition zone, or interphase. The term interfacial zone is chosen here and will be used throughout this study. The interface is a two-dimensional boundary between two distinct materials. It has no thickness, and, therefore, no constitutive property of its own. The properties that can be assigned to an interface are the bond strength and the fracture toughness.

The microstructure of the interfacial zone may be affected by the rate of mixing, admixtures, and additions such as silica fume during the production of high strength concrete. The addition of silica fume alone does not appear to change the strength of cement pastes for a constant water/cement ratio. However, silica fume increases the strength of concrete due to an improvement in bond strength and alterations in the microstructure of the inter-

facial zone [Bentur et al., 1988; Mindess, 1988]. It has been shown that fine particles of silica fume are helpful in improving the interfacial zone characteristics through processes of pore refinement and grain refinement. Then, the properties of interface are influenced by the nature of the interfacial zone.

At present, the following questions arise in the high strength concrete field [Mindess, 1988]: (1) what is the role of interfacial zone or interface on the strength and ductility of concrete? and (2) can the ductility of concrete be improved, as well as the strength by altering the interfacial zone or the interface? In particular, the important question in the development of high strength concrete is the brittleness of the material and the role of the properties of mortar-aggregate interfaces. Although a strong bond at the interface between the mortar and the aggregate may enhance the overall strength and stiffness of the concrete system, the increase in the interfacial bond would cause a brittle deformation and failure. To solve this problem two principal aspects of interfaces in concrete should be studied as follows:

- the microstructural features of the interfacial zones, including their effects on concrete properties; and
- the interfacial properties, namely, the bond strength and the fracture toughness, including their influences on the concrete behavior.

A better understanding of interfacial microstructure, bond strength, interfacial fracture toughness, and how they affect crack growth is extremely important for efficient high strength concrete development. In particular, interface fracture toughness plays a key role in improving the mechanical properties such as the stiffness and durability of high strength concrete. However, the characterization and modeling of the interfacial behavior through fracture mechanics concepts is very limited. Quantitative studies of interfacial fracture resistance

can offer great potential for the understanding of the overall concrete behavior, leading to the development of advanced materials.

1.2.2 Two-phase Composite Model for Concrete

For any rigorous study of the effects of internal events on the overall mechanical behavior of concrete, idealizations must be made and relatively simple models which capture the essential elements of the behavior must be constructed. Buyukozturk et al. [1971, 1972] modeled concrete as a two-phase composite consisting of mortar and aggregate inclusions and investigated the cracking problems through laboratory testing of physical models and numerical analysis using the finite element method. Figure 1.2 shows a concrete composite as a two-phase material in which the stiffnesses and strengths of the mortar and aggregate materials, and the characteristics of the interface between them greatly influence the composite behavior. Various scenarios of crack initiation and crack propagation in the matrix versus at the interface, or crack penetration into the aggregate need to be studied to engineer the concrete for optimal behavior.

Recently, Yamaguchi and Chen [1991] predicted the propagation of microcracks in two-phase concrete models by finite element analysis. They used the smeared cracking model for mortar, and interface finite elements for bond coupled with the generalized plasticity concepts. In these studies a Mohr-Coulomb type failure criterion was employed for cracking at the interfaces. The approach developed by these previous studies led to some very useful information with respect to the understanding how bond cracking affects the global concrete behavior. However, the results obtained in this way are limited due to the phenomenological nature in which the interface bond property was assumed and the bond cracking criterion was established. Hence, there is a need to develop methodologies for defining and quantifying explicitly the mortar-aggregate interface characteristics such that fundamental knowledge essential in engineering high performance concrete materials can

be derived. In this thesis, a novel methodology involving both testing of physical laboratory models and employment of interface fracture mechanics concept is developed to study the interface fracture in high strength concrete. Throughout this research two-phase composite specimens will be used as experimental models. Figure 1.3 shows the present research approach for the development of high strength concrete.

1.3 Objectives

The objectives of this research are

1. To study and characterize the fracture behavior of mortar-aggregate interface in high strength concrete with silica fume through novel interface fracture models,

2. To experimentally and numerically investigate the cracking scenarios in interfacial regions of two-phase composite models with an aggregate inclusion, and

3. To establish the material design parameters governing the cracking behavior of high strength concrete.

The research represents a fundamental study of the fracture behavior of mortar-aggregate interface in high strength concrete. Tests and analyses on two-phase composite models for the high strength concrete provide data on the interfacial fracture properties and their effects on the cracking behavior. The interfacial cracking is believed to be a major mechanism governing the overall deformation and failure of concrete. A model called the "sandwich test specimen" is developed and used to determine the fracture toughness of mortar-aggregate interface. The experimental parameters are the aggregate type, the mortar type, and the loading condition. Numerical analyses based on fracture mechanics concepts are performed to simulate the cracking scenarios in high strength concrete. Finally, preliminary

guidelines for the development of high strength concrete are discussed, based on the fracture mechanics parameters influencing the cracking behavior of the concrete. This research provides valuable insight into the deformation behavior and the failure in high strength concrete structures, thus increasing the safety in engineering design application of high strength concrete.

1.4 Thesis Organization

The organization of this thesis is as follows:

Chapter 1 has provided the general background and the motivation for this work. The objectives of the research and the organization are presented.

Chapter 2 reviews pertinent literature on high strength concrete, including the production techniques, the selection of materials, and the material properties of high strength concrete.

Chapter 3 describes the characteristics of the interfaces in concrete. Bond cracking and interfacial microstructures of both high strength concrete and normal strength concrete are compared. The effects of silica fume on these aspects are examined. Interfacial properties influencing the material behavior of high strength concrete are also discussed.

Chapter 4 reviews the interface fracture mechanics applicable to mortar-aggregate interfaces in concrete as a theoretical basis for testing models.

Chapter 5 describes an interface fracture testing model, the sandwich test specimen, developed for measuring the interfacial fracture toughness between the mortar and the aggregate. The specimen consists of a thin aggregate layer embedded in a mortar matrix.

Chapter 6 describes the experimental work performed on the sandwich specimens. Interfacial fracture toughness are assessed for selected mortar/aggregate combinations.

Chapter 7 describes the numerical analysis scheme to evaluate two interfacial fracture parameters, the energy release rate and the loading phase angle. The numerical results of

two applications with interfacial cracks are presented.

Chapter 8 describes the experimental work on two-phase beam composite models. The test results are compared with numerical results.

Chapter 9 discusses the factors governing the properties of high strength concrete. Novel physical models are proposed and tested to investigate the role of interfaces in high strength concrete and for the same purpose real concrete specimens are tested. Results from both tests are discussed. Based on material design parameters and general considerations for material selection and proportioning, a fracture mechanics based mix design procedure for high strength concrete is proposed.

Chapter 10 summarizes the results of this work and lists the conclusions and recommendations for future research work.

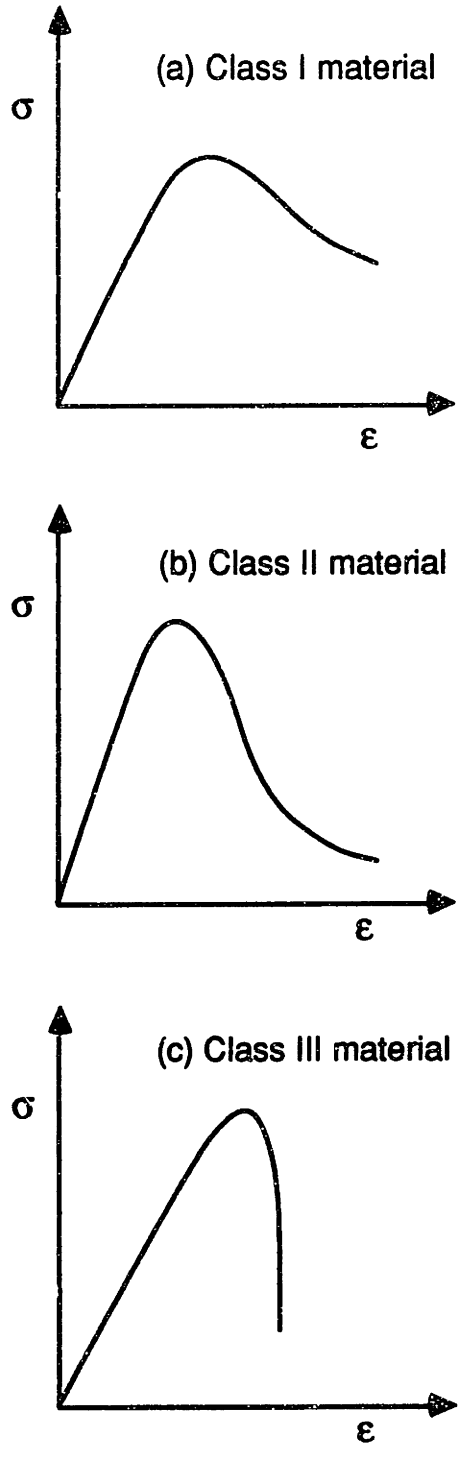

Figure 1.1 Stress-strain curves for cement-based composites

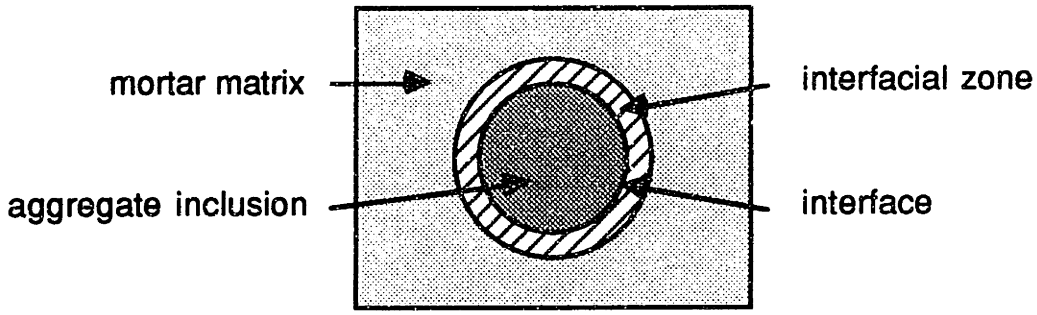

(a) Interface and interfacial zone

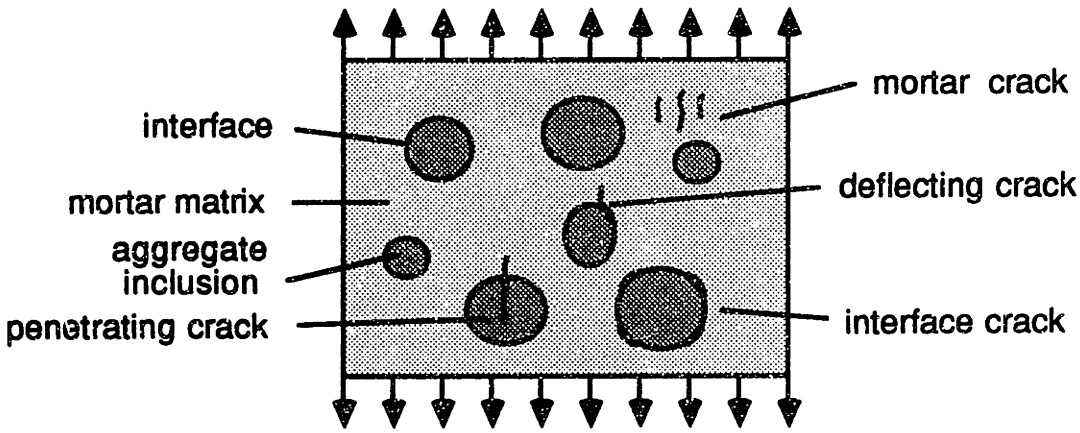

(b) Various cracking mode

Figure 1.2 Two-phase concrete composite

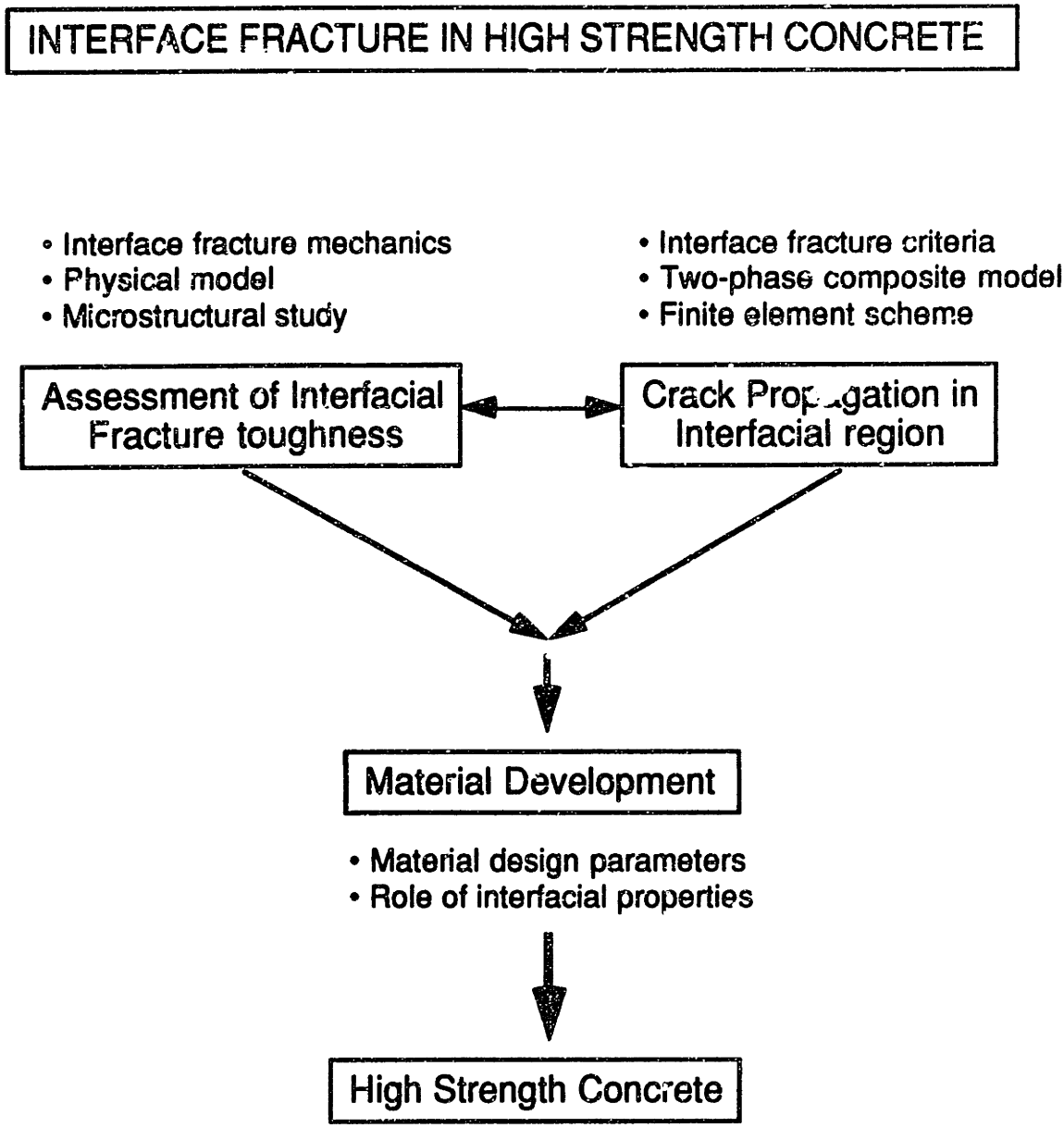

Figure 1.3 Research approach

Chapter 2

Review of High Strength Concrete

Recently, the use of high strength concrete is increased for a variety of engineering applications due to its ability to satisfy the demands of developers and government agencies for improved structural efficiency and reduced construction costs. This chapter will concentrate on production, material properties, and application of high strength concrete. In particular, the use of silica fume in making high strength concrete will be emphasized.

2.1 Introduction

2.1.1 Definition of High Strength Concrete

For almost a century, concrete strength has ranged from 21 MPa to 35 MPa (3,000 to 5,000 psi). Today concrete strength of up to 207 MPa (30,000 psi) has been reported in laboratory experiments, while concrete with compressive strength of 41 MPa (6,000 psi) to 83 MPa (12,000 psi) has been produced and used in structural applications. High strength concrete has been successfully used in the 75-story Texas Commerce Plaza Tower Building [Colaco, 1985]. More recently, concrete with compressive strength over 110 MPa (16,000 psi) has been used in high-rise buildings and prestressed concrete members. In Seattle, concrete with compressive strength of 131 MPa (19,000 psi) has been used in the 50-story Pacific First Center Building [Randall and Foot, 1989].

In general, high strength concrete is defined as "concrete with a compressive strength of greater than that which is commonly used" [Peterman and Carrasquillo, 1986]. This definition is widely accepted since maximum strength varies considerably with region and time. Several definitions of high strength concrete have been given by various investigators. High strength was defined as a compressive strength of about either 41 MPa (6,000 psi) when normal weight aggregate is used, or above 28 MPa (4,000 psi) when lightweight aggregate is used [ACI Committee 363, 1984; Shah, 1979]. At present, high strength concrete means a compressive strength in excess of 69 MPa (10,000 psi).

2.1.2 Advantages of High strength Concrete

High strength concrete provides many advantages over normal strength concrete in structural applications as follows.

- High strength concrete yields a high stiffness which limits maximum deflection under ultimate loads.
- High strength concrete reduces the axial shortening of columns because of its high modulus of elasticity and its effect on vertical differential movements.
- High strength concrete is more resistant to severe environments, such as carbon dioxide, chlorides, or even water in case of freezing and thawing cycles.
- High strength concrete reduces the construction cost due to significant reductions in columns and in total structural dead weight.
- High strength concrete allows the designer to use new types of structural elements or systems.

Despite its advantages, high strength concrete has some drawbacks such as a lack of ductility and low tensile strength. These disadvantages may cause cracking and durability

problems as well as structural problems. The use of high strength concrete is also restricted by production difficulties and strict quality control requirements, along with a general lack of information about its material and structural properties.

2.1.3 Use of High Strength Concrete

Traditionally, high strength concrete has been used mostly for axially loaded members. Now, more attention is given to the use of high strength concrete in flexure. Lacroix and Jaugey [1985] have investigated the use of high strength concrete in axially loaded and flexural members in the following cases:

- For medium and large span bridges - greater flexibility,
- For high rise buildings - reduction of the height of beams and the cross section of the columns,
- For prestressed concrete structures - slender cross sections and longer spans,
- For offshore construction - weight reduction of platform columns, and
- For precast beams - weight reduction and shorter production cycles

High strength concrete is especially attractive for use in arches and shell structures where the structural system acts primarily in compression. In particular, in long span prestressed beams the weight ratio and economics of high strength concrete compares favorably with steel. Another promising application of high strength concrete is for trussed girders in which the tensile members are prestressed [ACI Committee 363, 1984].

2.2 Production of High Strength Concrete

2.2.1 High Strength Concrete Production Techniques

In general, there are two methods of producing high strength concrete: (1) lowering the water/cement ratio with a better selection of component materials; and (2) using chemical or mineral admixtures such as high range water reducer (HRWR, or superplasticizers), fly ash, and silica fume. The most important point in increasing the strength of concrete is by proper adjustments of the mix proportions such as water/cement ratio and cement/sand ratio [Peterman and Carrasquillo, 1986]. Mineral admixtures such as silica fume (SF), a kind of pozzolanic mineral admixture, and fly ash in combination with HRWR can be used to produce high strength concrete [Jahren, 1983; Mehta, 1983; Mehta, 1989], and their use has been increased considerably during the past decade.

Several specialized techniques have also been developed for the production of high strength cements and concretes. These include slurry infiltrated fiber cement, autoclaved cements and concretes, polymer impregnated cements and concretes, and low porosity pressure compacted cements.

2.2.2 Selection of Materials

Selection of the proper types of constituent materials, including coarse aggregate, fine aggregate (sand), cement, and admixtures is very important for the production of high strength concrete. Furthermore, since high strength concrete is much more sensitive to variations in batch quantities and properties of component materials than ordinary concrete, stringent material requirements and careful quality control are needed.

It seems that at very low water/cement ratios, the type and the amount of mineral admixtures have strong effects on strength and other characteristics of concrete. Aggregate type also has a great influence on concrete properties, as well as the cement/aggregate ratio. The

use of an aggregate with a very low elastic modulus may result in concrete with high creep and drying shrinkage. Material requirements for high strength concrete are summarized as follows [ACI Committee 363, 1984; Mehta and Aitcin, 1990b].

(a) Cement

Any standard ASTM type portland cements can be used to produce high strength concrete. Unless high initial strength is needed, such as in prestressed concrete, there is no need to use Type III cement. However, it is noted that different brands of portland cement have different strength development characteristics.

(b) Aggregates

The properties of fine aggregates are not as important as those of coarse aggregates. The important parameters in the selection of fine aggregates are particle shape and angularity, gradation, and fineness. Silicious sand with a fineness modulus of about 2.5 to 3.0 provides the best workability and compressive strength.

For the production of high strength concrete, coarse aggregates are one of the most important materials. Aggregate should have high compressive strength and rough exterior surface to improve mechanical bonding with the mortar matrix. The ideal aggregates are clean, cubical, angular, and 100 percent crushed with a minimum amount of flat and elongated particles. The size of coarse aggregates is also important. In general, the smaller the aggregate the stronger the concrete. With most aggregates, 10 to 15 mm maximum size may be considered optimum for high strength concrete production.

(c) Chemical Admixtures

Chemical admixtures, including air-entraining admixtures, retarders, and high range water reducers (HRWR), are added to concrete to improve consistency, controlling the time of

set, and provide protection against deterioration by freezing and thawing cycles. In high strength concrete, the reduction of water content in concrete mixture, while maintaining the desired workability, is important. To improve the poor mixability and workability of the concrete, HRWR agents, popularly known as superplasticizers, can be used. The superplasticizers are high molecular weight anionic surfactants derived from sulfonated fomaldehyde of naphthalene or melamine. When used in quantities ranging from 1 to 2% solid by weight of cementitious materials, they produce a powerful temporary dispersing effect on the cement paste. To circumvent this problem, a portion of the superplasticizer dosage may be saved for later addition when the concrete mixture has arrived at the site.

(d) Mineral Admixtures

Mineral admixtures are fine powders generally composed of silicate glasses or noncrystalline silica. The incorporation of mineral admixtures in concrete improves cohesiveness and stability; and reduces bleeding, segregation, rate of slump loss in fresh concrete, and the high concentration of large pores and large crystals of calcium hydroxide.

Fly ash is a pozzolanic material produced from coal combustion. Fly ash consists of fine and smooth spherical particles with a surface area of about 500 m^2/kg and an amorphous silica content of 45 to 50 percent. It reacts with free lime in the cement to form calcium silicate hydrate (C-S-H) much in the same manner as silica fume. However, due to its low surface area and low silica content, it does not work as efficiently as silica fume. The most important benefit of fly ash is an increase in workability and finishability. Fly ash particles are spherical and roughly the same size as cement grains, which are angular. Thus, the replacement of cement with fly ash reduces internal shear forces during concrete flow and allows a smoother and more workable mix.

Silica fume (SF) is a kind of pozzolanic mineral admixture and is a product which emerges during the production of silicon and ferrosilicon alloys. SF can be used to increase

strength and reduce permeability and bleeding [Jahren, 1986; Malhotra, 1984; Radjy et al., 1986]. In practice, SF has been used in various engineering applications ranging from offshore structures to road construction. More description of silica fume will be given in Section 2.3.

2.2.3 Mix Proportioning of High Strength Concrete

Mix proportioning is the process of determining the right combination of component materials that will produce a concrete mixture with desired characteristics at the lowest possible cost [Mehta and Aitcin, 1990b]. Even with ordinary concrete the process is not easy because it involves various conflicting requirements. The ACI Committee 211 recommendations are applicable for proportioning concrete mixtures with 13 to 40 MPa compressive strength and even up to 60 MPa compressive strength by extrapolation. However, ACI tables are not applicable for very high strength concrete (above 60 MPa), high-slump (above 175 mm), superplaticized concrete mixtures with less than 0.3 water/cement ratio. Concretes of this type contain substantial amount of unhydrated cement particles and a compact microstructure with strong interfacial zone. Their strength characteristics are highly sensitive not only to the aggregate type but also to very small changes in water content of the concrete mixture. In conclusion, since the aggregate type and the types and amounts of admixtures can have a great influence on the strength characteristics of high-strength concrete mixtures, a novel approach is needed for determining the mix proportions.

Extensive laboratory testing must be carried out before a satisfactory proportion of materials is arrived at. Mix proportioning of high strength concrete reported in a variety of field and laboratory work is presented in Table 2.1 [Mehta and Aitcin, 1990b]. It is noted that Concrete Mixtures 1 and 2, which were produced during the seventies, contained normal water-reducing admixtures. All other concrete mixtures in Table 2.1 were made during the eighties and contained superplasticizers. It is seen that the strength of concrete with super-

plasticizers is very sensitive to even small changes in the water content. Mixtures produced in recent years all included mineral admixtures such as fly ash and silica fume. With regard to the fine and coarse aggregate, the data in Table 2.1 show that the total aggregate content and the fine/coarse aggregate proportions did not vary significantly with concrete strength, in spite of differences in the physical characteristics of aggregates. On average, approximately 650 kg/m^3 fine aggregate and 1,100 kg/m^3 coarse aggregate were used with mixtures listed in Table 2.1. In this research, the mix proportions for the first trial batch of mortar mixture were determined based on the general considerations described in this section.

2.3 Silica Fume in High Strength Concrete

2.3.1 Use of Silica fume

Although the first laboratory experiment with silica fume at the Norwegian Institute of Technology was performed in 1950, its first use in structural concrete was reported in 1971 [Sellevold and Nilsen, 1987]. Silica fume is a new pozzolanic material that has received a great amount of attention recently. The applications and investigations of silica fume have been mainly conducted in Iceland and the Scandinavian countries which are subjected to severe environments. The combined use of silica fume and superplasticizers can produce high strength concrete with significant reduction in water demand. Although the initial interest in silica fume was for high strength concrete, silica fume is successfully used as a cement replacement material and an admixture to improve corrosion resistance and freeze-thaw resistance.

2.3.2 Material Properties of Silica Fume

Silica fume (SF) is a by-product resulting from the reduction of high-purity quartz with coal in electric arc furnaces in the production of silicon and ferrosilicon alloys. SF is collected

from the waste gases released in this process. SF is composed of extremely fine spherical particles with a specific surface of the order of 20,000 m^2/kg. For comparison, cement has a surface area of 300-400 m^2/kg and fly ash has 400-700 m^2/kg, as measured by nitrogen absorption techniques. The amorphous silicon dioxide (SiO_2) content varies with the source and is usually between 90 - 95 percent. The chemical composition of silica fume is listed in Table 2.2.

Silica fume varies from light to dark gray in color with a diameter of 0.01 - 1.0 μm. The average diameter of silica fume particles is approximately 100 times smaller than the average cement particle. The specific gravity of a typical silica fume is about 2.2 as compared to 3.1 for normal portland cement; however, in some cases it can be as high as 2.5. The bulk density of silica fume is of the order of 250 to 300 kg/m^3 as compared with about 1,200 kg/m^3 for normal portland cement [ACI Committee 226, 1987].

2.3.3 Characteristics of Silica Fume Concrete

Silica fume can reduce bleeding and permeability, and increase compressive strength and durability of concrete. Bleeding is reduced because of silica fume's affinity for water, resulting in little free water for bleeding. In general, this is an advantage, but it might increase the risk of cracking by plastic shrinkage. Furthermore, fresh concrete incorporating silica fume appears more cohesive and less prone to segregation.

The main contribution of silica fume is to improve the concrete strength. Strength development is about the same as ordinary concrete for about three days. Afterward, silica fume concrete shows an increase in compressive strength over ordinary concrete. The strength enhancement of concrete induced by silica fume is chiefly due to the decrease of water/cement ratio and the increase of aggregate-matrix bond. The relationship between the compressive strength and silica fume content has varied in several studies [ACI Committee 226, 1987]. The strength development pattern of flexural and splitting tensile strengths of silica fume

concrete is similar to that for compressive strength.

Silica fume concrete is much less permeable than ordinary concrete. Although total porosity is nearly the same, the average size of the pores is reduced significantly. This is related to the ingranular densification produced by use of silica fume. Therefore, the number of coarse pores of the cement paste with silica fume decreases. Air-entrained concrete incorporating up to 20 percent silica fume performs satisfactorily in freezing and thawing tests.

2.3.4 Application of Silica Fume Concrete

In general, a part of the cement may be replaced by much smaller quantities of silica fume without loss of strength. For example, one kilogram (kg) of silica fume can replace 3 to 4 kg of cement. Cement replacement is usually attractive from economic reasons, or technical reasons such as heat reduction [Radji et al., 1986]. Silica fume with high range water reducers has been used to produce very high strength [higher than 69 MP (10,000 psi)]. The effects of silica fume on concrete strength is highly dependent on factors such as curing temperature, workability, curing time, dosage rate levels, and HRWR used [Jahren, 1986]. Silica fume binds up the alkali of cement and reduces the detrimental alkali-silica reaction for the improvement of concrete strength [Gjorv, 1983]. The use of silica fume can improve the early-age strength of concrete made using fly ash and blast-furnace slag. At elevated curing temperatures above 40°C the early strength application of silica fume can be very cost effective [Radji et al., 1986].

Silica fume can be used to increase abrasion resistance. A larger fraction than 10 percent of silica fume of cement weight is necessary to increase the abrasion resistance [Carlsson et al., 1986]. This application is important in the repair of hydraulic structures subjected to abrasion-erosion damage. Because of its low permeability, silica fume concrete offers high resistance to aggressive chemical solutions such as chloride, sodium or magnesium, and

sulfates, and even dilute acids [Mehta, 1989]. This property has led to its use in concrete bridge decks and concrete parking structure to control the ingress of de-icing salts into concrete, and thus to reduce the chloride associated corrosion of the reinforcing steel.

2.4 Properties of High Strength Concrete

2.4.1 Stress-Strain Behavior in Uniaxial Compression

Uniaxial compressive stress-strain curves for concrete with compressive strength up to 83 MPa (12,000 psi) are shown in Fig. 2.1. The shape of the ascending part of the stress-strain curve is more linear and steeper for high strength concrete than those for conventional concrete [ACI Committee 363, 1984; Carrasquillo et al., 1981a; Chen et al., 1985; Nilson, 1985; Wittmann, 1979]. Generally, an increased strain corresponding to the peak stress level is obtained with brittle failure [Chen et al., 1985; Gerstle, 1979; Shah, 1979]. The slope of the descending part becomes steeper for high strength concrete and are very dependent on the strain rate and the testing method. For this reason the post-peak portion of the stress-strain curve in Fig. 2.1 is shown as a dashed line representing typical behavior rather than a solid line representing expected behavior. High strength concrete exhibits less internal microcracking than lower strength concrete for a given imposed axial strain [Carrasquillo et al., 1981a]. As a result, the relative increase in lateral strains is less for high strength concrete. Under biaxial compression, increased strength and stiffness properties were observed due to confined internal microcracks [Chen et al., 1985].

2.4.2 Modulus of Elasticity and Poisson's Ratio

In general, modulus of elasticity of high strength concrete is higher than that for normal strength concrete [Shih et al., 1989]. The modulus of elasticity is influenced by many factors, including the type and volume of coarse aggregate, moisture content, measurement methods, and porosity and composition of the interfacial zone. The stiffness of concrete is

mainly dependent on the strength of both the mortar and the aggregate, while the strength of concrete is mainly influenced by the strength of mortar [Carrasquillo et al., 1981b]. Furthermore, a higher aggregate-matrix bond strength would increase the modulus of elasticity of high strength concrete.

Some empirical relationships for a relationship between the modulus of elasticity and the compressive strength of normal weight concrete have been proposed. American Concrete Institute (ACI)-318 provides an equation for the modulus of elasticity of concrete

$$E_c = 33 w_c^{1.5} \sqrt{f'_c} \tag{2.1}$$

where, E_c is static modulus of elasticity of concrete in psi, w_c is air-dry weight of the concrete at time of test in pcf, and f'_c is compressive strength of the concrete at time of test in psi. The equation for the static modulus of elasticity suggested by Carrasquillo et al. [1981b] was recommended by the ACI Committee 363 [1984] for concrete having compressive strengths between 21 MPa (3,000 psi) and 83 MPa (12,000 psi):

$$E_c = 3,320\sqrt{f'_c} + 6,900 \quad MPa, \qquad E_c = 40,000\sqrt{f'_c} + 1.0 * 10^6 \quad psi \tag{2.2}$$

Recently, Shih et al. [1989] suggested an empirical equation for the modulus of elasticity of concrete having compressive strengths between 21 MPa (3,000 psi) and 83 MPa (12,000 psi), based on the experimental data through least square regression analysis:

$$E_c = 4,660\sqrt{f'_c} - 1,370 \quad MPa, \qquad E_c = 55,000\sqrt{f'_c} - 120,000 \quad psi \tag{2.3}$$

Figure 2.2 shows the experimental results obtained by several investigators and proposed equations for calculating the modulus of elasticity of concrete. ACI Committee 363

[1984] pointed out that the ACI 318 expression given in Eqn. (2.1) overestimates the modulus of elasticity for concrete with compressive strengths over 41 MPa (6,000 psi) and the experimental data reported by several investigators showed higher values of modulus of elasticity than those predicted by Eqn. (2.2). For the prediction of the modulus of elasticity of high strength concrete with silica fume Eqn. (2.3) is recommended because silica fume in a slurry form was used, while fly ash has been used in Eqn. (2.2).

Poisson's ratio of high strength concrete in the elastic range seems comparable to that of ordinary concrete. In the inelastic range, the relative increase in lateral strains is less for high strength concrete than for normal strength concrete; i.e. high strength concrete exhibits less volume dialation than normal strength concrete [Ahmad and Shah, 1985]. This implies less internal microcracking for high strength concrete.

2.4.3 Tensile Splitting Strength and Modulus of Rupture

Tensile strength of high strength concrete may be as low as five percent of compressive strength, while direct tensile strength of ordinary concrete is usually about ten percent of the compressive strength. Several empirical formulae have been proposed to predict the tensile splitting strength and the modulus of rupture of high strength concrete as a function of compressive strength. Carrasquillo et al. [1981b] proposed the following equation for tensile splitting strength of concretes having compressive strength between 21 MPa (3,000 psi) and 83 MPa (12,000 psi):

$$f'_{sp} = 0.59\sqrt{f'_c}\ \ MPa, \quad f'_{sp} = 7.4\sqrt{f'_c}\ \ psi \tag{2.4}$$

For comparison, an equation for normal strength concrete is $f'_{sp} = 6\sqrt{f'_c}\ \ psi$. Ahmad and Shah [1985] proposed a mean curve for tensile splitting strength based on available data

$$f'_{sp} = 0.46(f'_c)^{0.55} \ MPa, \quad f'_{sp} = 4.34(f'_c)^{0.55} \ psi \tag{2.5}$$

For determining the modulus of rupture of concrete (f'_r), ACI code provides the equation:

$$f'_r = 0.62\sqrt{f'_c} \ MPa, \quad f'_r = 7.5\sqrt{f'_c} \ psi \tag{2.6}$$

Carrasquillo et al. [1981b] modified Eqn. (2.6) to include the effect of high strength concrete having compressive strength up to 83 MPa (12,000 psi) as follows:

$$f'_r = 0.94\sqrt{f'_c} \ MPa, \quad f'_r = 11.7\sqrt{f'_c} \ psi \tag{2.7}$$

Ahmad and Shah [1985] concluded that the equation proposed by Raphael [1984] is valid for concrete with compressive strength up to 83 MPa (12,000 psi):

$$f'_r = 0.44(f'_c)^{2/3} \ MPa, \quad f'_r = 2.3(f'_c)^{2/3} \ psi \tag{2.8}$$

It is noted that factors used for predicting both the tensile splitting strength and the modulus of rupture of high strength concrete are larger than those for normal strength concrete.

2.4.4 Ductility and Fracture Toughness

It is generally accepted that as concrete becomes stronger, it also becomes more brittle. However, a quantitative method of expressing brittleness of concrete does not exist. In concrete, the ductility is often related to the area under the post-peak portion of the compressive stress-strain curve or the flexural load-displacement curve. For very high strength

concrete, this post peak area all but vanishes (Class III material in Fig 1.1). This inverse relationship between strength and ductility may be a problem for some structural applications. Ductility or toughness can also be measured using a fracture mechanics approach through such parameters as K_{IC} or G_{IC}, and then it is observed that K_{IC} increases with the increase of compressive strength [Shah, 1988]. This trend is contrary to the generally accepted observation that high strength concrete is more brittle, that is, less tough.

The material behavior can be defined by the stress-crack tip opening displacement along the crack face (or tension softening curve). The shape of the tension softening curve can significantly influence structural behavior and ductility of concrete. This curve contains information in the tensile strength, f_t, the fracture energy, G_F, calculated as the area under the curve. In particular, from the considerations of this curve, a characteristics length can be defined as

$$l_{ch} = \frac{EG_F}{f_t^2} \tag{2.9}$$

where, E is the elastic modulus. This parameter has no physical interpretation but determines the size of the process zone during fracture. The smaller l_{ch}, the more brittle the concrete. Of several possible fracture parameters, the most appropriate fracture toughness parameter for concrete needs to be defined. The effect of the brittle behavior on structural performance is just starting to be explored.

Ductility in normal strength concrete is mostly due to the fact that bond cracks do not form at the same time as the mortar cracks. This time lag between the formation of bond cracks, and the formation and propagation of mortar cracks is responsible for ductility in normal strength concrete [Oumera, 1991]. Because the mortar-aggregate interface in high strength concrete is much stronger than the one in normal strength concrete, bond cracks form at a higher load level, and thus, the reduced time lag between the formation of bond

and mortar cracks decreases the ductility. In normal strength concrete cracks go around the aggregates, indicating weak bonding, and thus, the fracture energy of concrete increases. In high strength concrete, on the other hand, cracks usually pass through the aggregates, resulting in low fracture energy. The crack penetration into aggregates is caused by the strong interface in high strength concrete. Thus, the decrease in ductility of high strength concrete is closely related to the characteristics of the interfaces. Therefore, a good knowledge of the physical and chemical properties of the interfacial zone and the mechanical properties of the interface is necessary in order to improve the ductility in high strength concrete.

The lack of ductility of high strength concrete might limit the use of high strength concrete for fear of a brittle and explosive failure. However, the structural implications of the high strength concrete may not be very serious. A properly designed reinforced concrete section can have substantial ductility. Ductility may also be enhanced by confinement or fiber reinforcement [Swamy et al., 1978]. The optimization of both strength and ductility in concrete is an important subject that requires more quantitative and qualitative information.

2.4.5 Shrinkage and Creep

Many researchers have found that the ultimate drying shrinkage of high strength concrete is slightly less or equivalent to that of ordinary concrete although the initial rate of shrinkage in high strength seems to be higher than in ordinary concrete. The addition of silica fume seems to have little or no effect on the drying shrinkage of high strength concrete. In high strength concrete most drying shrinkage develops early because this is attributed to the rapid rate and high heat of hydration in high strength concrete [Swamy, 1986].

The maximum specific creep for high strength concrete has been reported to be less than that of lower strength concrete loaded at the same age [Ngab et al., 1981]. However, high strength concretes are subjected to higher stresses, and thus the total creep will be about the same for any strength concrete. As is found with lower-strength concrete, creep decreases

as the age at loading increases, and there is a linear relationship with the applied stress. Swamy [1986] showed that although ultimate creep in high strength concrete was reduced when compared with ordinary concrete, the early rate of creep was much higher in high strength concrete.

2.4.6 Freeze-Thaw Resistance

Freeze-thaw resistance of high strength concrete has been subject to contradictory experimental results. Freeze-thaw resistance test is influenced by many factors, including air content, curing conditions, water/cement ratio, testing method, and compressive strength of concrete. Wolsiefer [1984] found that air entrained high strength concrete with silica fume (w/c = 0.22, $f_c' = 76$ MPa) had a high durability factor as well as good de-icer scaling resistance. Yamato et al. [1987] reported that high strength concrete with silica fume performed poorly in comparison to non-silica fume concretes except at very low w/c ratios. In general, at w/c ratio of 0.25, high strength concrete containing silica fume performed satisfactorily to repeated cycles of freezing-thawing. Concrete with low w/c ratio may contain so little free water that it becomes effectively freeze-thaw resistant. Thus, it may be that only medium strength concrete has poor freeze-thaw resistance due to low porosity, while high strength concrete is protected by its extremely low free water content despite a low porosity.

2.5 Research Needs for High Strength Concrete

Despite the amount of research that has been performed on high strength concrete, there are still research needs in many areas to insure the economical and proper application of the material [ACI Committee 363, 1987]. These research needs will be summarized as follows:

- Mechanical properties of high strength concrete

  Evaluations should include the use of different chemical and mineral admixtures to

produce the high strength concretes and the effects of these admixtures on mechanical properties and durability over a long period of time. The role of mineral admixtures, such as silica fume, for a high strength concrete should be carefully examined.

- Effects of aggregate characteristics

  Research work is needed to investigate the effects of various aggregate mineral properties and particle shapes on mechanical properties and durability for both normal-weight aggregates and lightweight aggregates used in high strength concrete.

- Ductility of high strength concrete

  Low ductility of high strength concrete would result in a brittle and explosive failure in high strength concrete structures, for example, under seismic conditions. Research is needed to find a way to improve the ductility of high strength concrete.

- Proportioning and evaluating high strength concrete

  The requirements specified for proportioning and evaluating concrete strength provided by ACI are based on statistical data from testing normal strength concrete. Research is needed to collect and evaluate more strength data for high strength concrete at strengths higher than 41 MPa (6,000 psi) and furthermore, to develop an efficient method for the selection of materials and the mix proportioning for high strength concrete.

The scope of the present work is based on these research needs in high strength concrete.

In particular, more attention should be paid to the study of ductile behavior of high strength concrete members. Low ductility of high strength concrete can be observed from the stress-strain behavior. High strength concrete has a steeper, more linear ascending branch of the stress-strain curve and a steeper descending branch than normal strength concrete, resulting from an increase in the bond strength which delays crack formation until

high stresses are reached. Therefore, the development of high strength concrete with improved ductility requires a study of interfacial zone and interfacial cracking. In Chapter 3, bond cracking and interfacial microstructure will be described for increasing the fundamental understanding of the interfacial characteristics.

Table 2.1 Mix proportions for selected high-strength concrete mixtures

(from Mehta and Aitcin [1990b])

Component Materials in 1-m^3 concrete batch, kg/m^3									
No.	Description of concrete	Avg. compressive strength, 28-day, MPa	Cementitious material PC	FA	SF	Total water	Fine aggregate	Coarse aggregate	Super-plastisizer, L/m^3	Water to cementitious ratio by weight
1	Water Tower Place, Chicago	65	500	60	-	178	608	1068	-	0.32
2	Commerce Tower, Houston	65	390	100	-	161	575	1141	-	0.33
3	International First Plaza, Dallas	80	360	150	-	148	603	1157	3	0.29
4	Experimental column, Montreal	90	500	-	30	135	700	1100	15	0.25
5	Laboratory Mix	70	485	-	-	130	762	1143	3.4	0.27
6	Laboratory Mix	82	449	-	39	130	758	1149	11.0	0.27
7	Laboratory Mix	91	427	-	59	132	754	1139	14.9	0.27
8	Laboratory Mix	93	450	-	50	140	687	1108	17	0.28
9	Laboratory Mix	97	500	-	42	138	675	1130	10	0.25
10	Laboratory Mix	100	486	-	54	135	661	1112	20	0.25
11	Laboratory Mix	103	580	-	70	140	620	1025	12	0.22
12	Laboratory Mix	107	517	-	58	126	641	1126	25	0.22

Table 2.2 Chemical composition of silica fume from silicon furnaces in Norway and North America (from ACI Committee [1987])

Constituent, percent	Elkem Spigerverket A/S, Norway	SKW Canada, Inc.	SKW Alloys, Calvert City, KY, and Niagara Falls, NY, USA
SiO_2	90.0 - 96.0	89.0 - 95.0	90.0 - 93.0
Al_2O_3	0.5 - 3.0	0.1 - 0.7	0.5 - 0.6
Fe_2O_3	0.2 - 0.8	0.1 - 3.1	3.4 - 4.5
MgO	0.5 - 1.5	0.3 - 1.0	0.3 - 0.5
CaO	0.1 - 0.5	0.1 - 1.0	0.5 - 0.8
Na_2O	0.2 - 0.7	0.1 - 0.2	0.1 - 0.3
K_2O	0.4 - 1.0	0.5 - 1.4	1.0 - 1.2
C	0.5 - 1.4	2.1 - 4.2	1.3 - 3.6
S	0.1 - 0.4	0.1 - 0.2	0.1 - 0.2
LOI=(C+S)	0.7 - 2.5	2.3 - 4.4	1.4 - 3.8
SO_2	-	0.1 - 0.6	0.4 - 1.3
Free moisture, H_2O	0.0	0.0 - 0.6	0.0 - 4.8

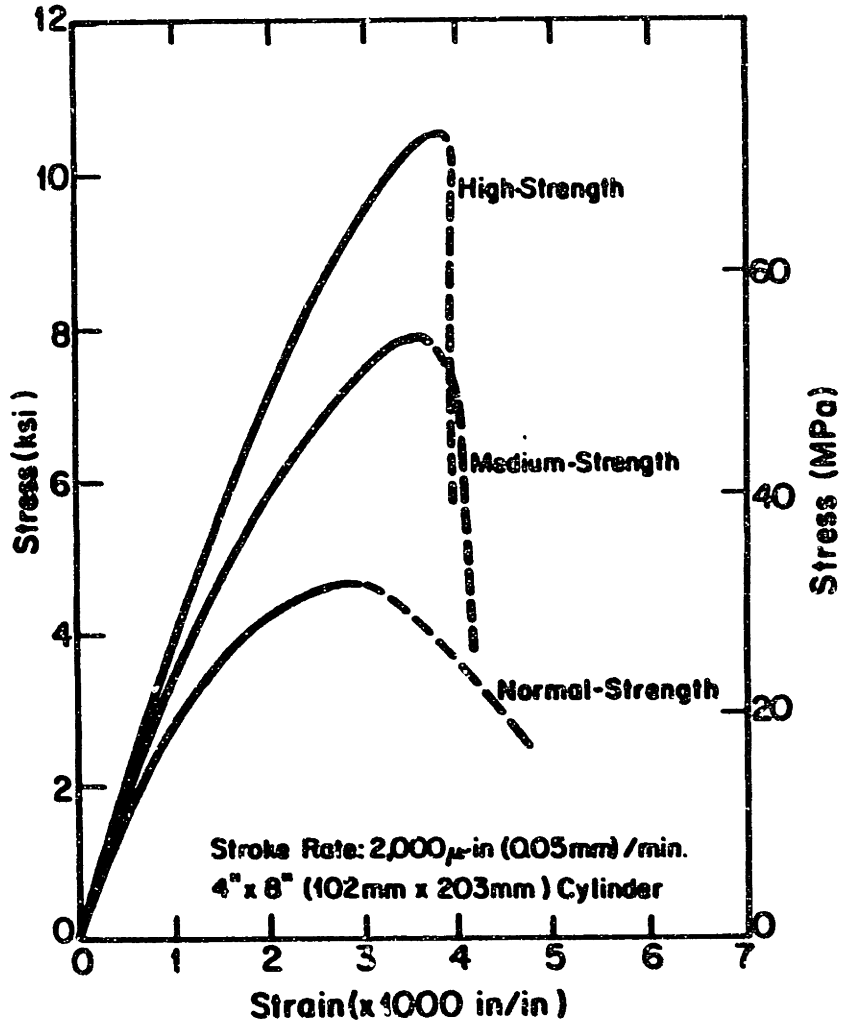

Figure 2.1 Uniaxial compressive stress-strain curves for concrete

(from Carrasquillo et al. [1981a])

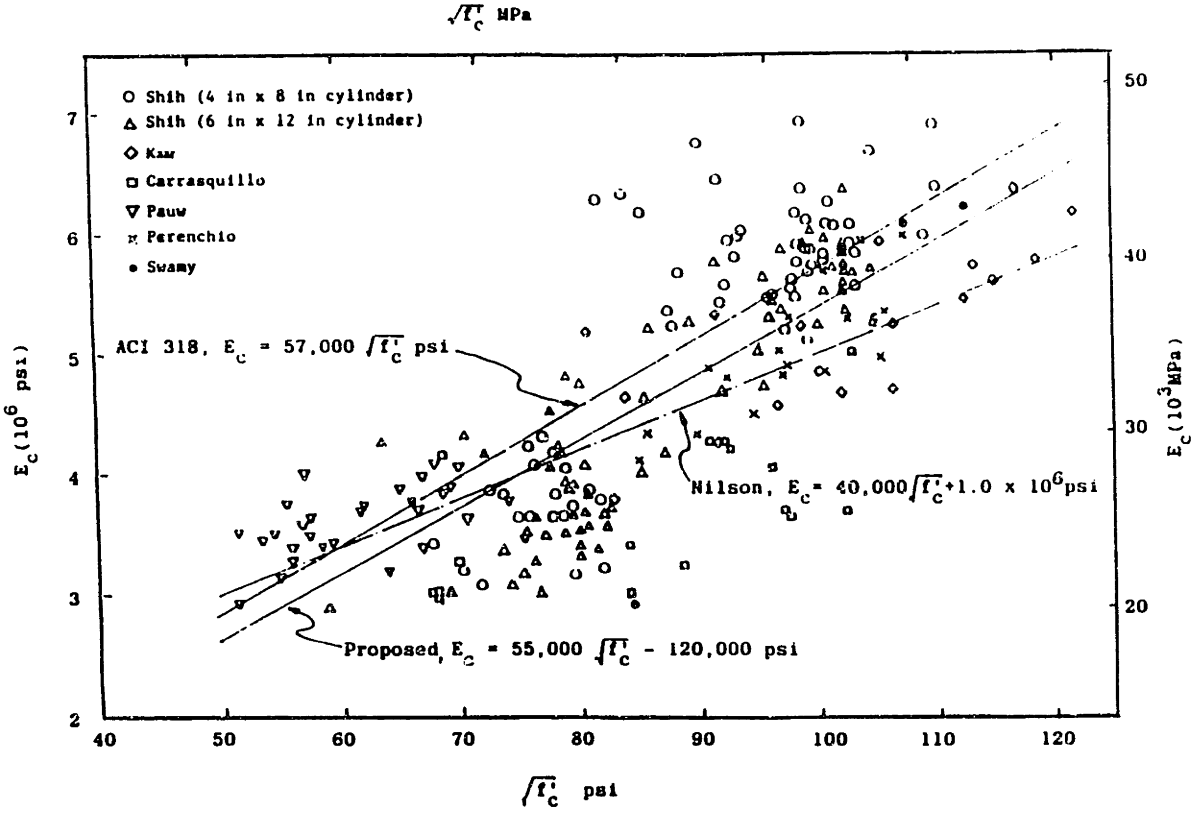

Figure 2.2 Expermental results for Young's modulus of concrete

(from Shih et al. [1989])

Chapter 3

Bond Cracking and Microstructure of Interfacial Zone

3.1 Introduction

Concrete is considered to be a composite material consisting of mortar matrix and aggregate inclusions. Interfaces between the matrix and the aggregate are intrinsic to concrete, and its structural performance is generally influenced by these interfaces as well as the internal elements. Therefore, development of advanced concrete materials with improved toughness and durability requires a fundamental understanding of the characteristics of the interfaces introduced in the concrete. In normal strength concrete interfacial zones seem to be primary sites of weakness, where microcracks originate when concrete is subjected to any internal or external stresses. In severe environments, a weak interfacial zone will have a serious influence on durability of concrete. For concrete to perform satisfactorily it is essential that the interfacial zone be as dense as possible, giving a good bonding between the aggregate and the matrix.

Recently, more attention has been given to the effects of the cement paste-aggregate interfaces on the concrete properties with the development of high strength concrete. It has been suggested that the improved strength properties of high strength concrete can be attributed to the increase in interfacial bond strength due to alteration in the microstruc-

ture of the mortar-aggregate interfaces through the use of silica fume and superplasticizers [Bentur et al., 1988; Mindess, 1988; Mehta and Monteiro, 1988]. A recent work reported by Rosenburg and Gaidis [1989] also emphasized the effect of silica fume in strengthening of concrete through enhancement of the paste-aggregate bond behavior. Addition of silica fume alone does not appear to change the strength of cement pastes for a constant water/cement ratio. However, silica fume increases the strength of concrete by improving bond strength and altering the microstructure of the interfacial zones. A better understanding of interfacial microstructure and how it affects crack growth is extremely important for efficient high strength development.

Despite the importance of the interfaces in concrete, little experimental and prototype experience and information on the interface in high strength concrete is available. The modeling of the interfaces through fracture mechanics is also very limited. In this chapter, the general characteristics of the interfaces and the interfacial zones will be reviewed, including bond cracking and interfacial microstructure of both normal strength concrete and high strength concrete. In particular, an emphasis will be on the effects of silica fume on the interfacial zone. Finally, interactions between matrix and aggregate and assessment of interfacial properties will be described.

3.2 Normal Strength Concrete

3.2.1 Bond cracking and Microcracking Development

In normal strength concrete the non-linearity of the stress-strain curve is closely related to the formation of microcracks, and later of macrocracks that propagate through the mortar. Over the past twenty years, a vast amount of research has been conducted to study the microcrack development, the nonlinear deformation behavior, and the failure mechanisms of normal concrete. It has been generally established that the development of bond cracks at

the interfaces between mortar and aggregates plays a significant role in the inelastic deformation behavior and that final failure occurs through the formation of continuous cracks in mortar, bridging the bond cracks [Buyukozturk et al., 1971, 1972; Hsu et al., 1963; Shah and Winter, 1966; Struble et al., 1980]. The two-dimensional two-phase composite model composed of circular aggregate discs embedded in a mortar matrix is shown in Fig. 3.1. The progressive propagation of microcracks under increasing compressive strength was investigated by Liu et al. [1972] by testing this model. Concrete loaded in compression exhibits cracking parallel to loading direction implying that cracks open in tension. Liu et al. [1972] summarized the formation and propagation of microcrack in concrete as follows:

- Shrinkage cracks and cracks caused by bleeding around aggregates (bond cracks) clearly do exist (Fig. 3.1(a)). In nearly every case these initial cracks spread to cause major cracks at failure.

- Bond cracks occur first around the larger aggregates (Fig. 3.1(a)). At loads lower than 65 percent of ultimate, no appreciable change occurred at the interface, and with increasing loads the bond crack increased in width and length along the interface (Fig. 3.1(b)).

- At about 85 percent of the ultimate load mortar cracks were initiated as shown in Fig. 3.1(c). The mortar cracks tend to bridge bond cracks of larger aggregates in preference to those on small aggregates.

- At ultimate load, these cracks form parallel to the applied load. Such cracks eventually cause the splitting modes of failure (Fig. 3.1(d)).

3.2.2 Interfacial Microstructure

The mechanical behavior of normal strength concrete is influenced by the microstructure of the interfacial zones between cement pastes and aggregates. In normal strength concrete

the interfacial zones are generally characterized by a highly heterogeneous microstructure, containing numerous areas of large pores and preferentially oriented and large crystals of calcium hydroxide. These characteristics of the interfacial zones seem to be primary sites of weakness, at which microcracks originate. The interfacial zones consist of a duplex film and a transition zone or "aureole de transition" shown in Fig. 3.2. These two phases of the interfacial zone have been examined by using X-rays, scanning electron microscope (SEM), backscattered electron imaging method (BEI), or other available techniques.

Duplex Film

Duplex film occurs immediately adjacent to the aggregate surface. The film is composed of a layer of calcium hydroxide (CH), of approximately $0.5\mu m$ thickness in contact with the aggregate surface, and a second layer of calcium silicate hydrate (CSH) in the form of short fibers that extend into the cement paste. The total thickness of the duplex film has been estimated to approximately 1 μm [Struble, 1988]. In other studies, researchers have not succeeded detecting the existence of the duplex film. Using the scanning electron microscope Odler and Zurz [1988] detected the existence of a hydrated material layer about 1 μm thick which they believed is identical to the duplex film found by other researchers. However, they were not able to detect any special subdivision. Using the backscattered electron imaging method (BEI), Scrivener and Gartner [1988] could detect a film around the aggregate, but they were not able to see a double layer even with high magnification.

Transition Zone

The transition zone, or "aureole de transition" is a layer region approximately 50 μm wide and contains a large number of hollow-shell hydration grains: calcium hydroxide (CH) and ettringite. Using X-rays diffraction techniques, Mehta and Monteiro [1988] concluded that the concentration of CH and ettringite was the highest at the interface and decreased grad-

ually toward the bulk paste. At early ages the inefficient packing of the cement particles around the aggregate surface leads to the formation of large pores near the aggregate surface which are filled with water. As the hydration process continues, these pores are not effectively filled, resulting in a transition zone much more porous than the bulk matrix [Goldman and Bentur, 1989]. The higher porosity at the transition zone has been reported by many researchers [Mehta and Monteiro, 1988; Scrivener and Gartner, 1988]. Calcium hydroxide and needle like crystals of ettringite, formed during hydration and oriented in an inefficient manner, fill very poorly the transition zone leaving very large voids in the vicinity of the mortar-aggregate interface. Consequently, the porosity is much higher at the interface. Porosity and distance from the interface are plotted in Fig. 3.3. This figure implies that the porosity at the interface is very high and drops to a relatively constant level after about 30 μm. The high porosity, the presence of preferentially oriented crystals characterized by poor binding ability, and low density lead to the weak mechanical strength of the transition zone.

3.3 High Strength Concrete

3.3.1 Microcracking and Crack Growth

Conflicting observations and suggestions have been made about the deformation behavior and failure mechanisms [Carrasquillo et al., 1981a; Chen et al., 1985; Gerstle, 1979; Nilson, 1985; Shah, 1979; Wittmann, 1979; Zia, 1979]. In high strength concrete, bond cracks at the aggregate-mortar interfaces were observed even before the application of the external loads [Gerstle, 1979]. It was suggested, however, that the amount of bond cracks at pre-loading stage is less than that of normal strength concrete [Carrasquillo et al., 1981a].

In high strength concrete, the growth of microcracks at the interface between mortar and aggregate occurs at a higher stress ratio (with respect to the compressive strength). It was

reported that high strength concrete can be loaded to higher stress-strain ratio before the bridging of microcracks starts to form continuous crack patterns leading to failure [Nilson, 1985]. It can be concluded that a larger linear portion of the stress-strain curve for high strength concrete would correspond to a higher stress level at which bond cracks start to grow, implying better qualities of mortar-aggregate interfaces. It is reasonable that high strength concrete has higher bonding strength than normal strength concrete.

Little information is now available on the nature of progressive failure of the high strength concrete. In some cases cracks through aggregate were observed [Carrasquillo et al., 1981a; Gerstle, 1979; Zaitsev, 1983; Zia, 1979], indicating a less pronounced effect of crack arrest by the aggregates, while in other cases progression of bond cracks around the aggregates were reported [Bentur and Mindess, 1986; Chen et al., 1985]. These different trends indicate the importance of relative strength and stiffness properties of the mortar, aggregate, and the interface between them in the cracking behavior of high strength concrete. Furthermore, it should be also noted that the type, shape, surface of aggregates used and the loading rate may have a considerable effect on the crack growth.

3.3.2 Interfacial Microstructure

High strength concrete differs in many aspects from normal strength concrete in their interfacial microstructure. The addition of mineral admixtures such as silica fume (SF) in combination with high range water reducer agents (HRWR, i.e., superplasticizers) is effective for producing high strength concrete, leading to the significant water reduction [Bentur et al., 1988]. This effect and the high pozzolanic reaction result in the reduction of total porosity and the finer pore size distribution which leads to high strength. An additional effect of silica fume with high specific surface area is to densify the paste matrix microstructure in the vicinity of the aggregate surface, improving the bond strength.

Mehta and Monteiro [1988] found that the use of mineral admixtures produced a re-

markable reduction in the transition zone thickness, resulting in an overall homogeneous interfacial zone and improved bond strength. With the use of silica fume, the thickness of the transition zone was reduced from 50 μm to about 8 μm. Scrivener and Gartner [1988] observed also that calcium hydroxide (CH) was significantly reduced in cement paste with silica fume, indicating that the pozzolanic reaction has occurred. Sakar et al. [1988] noted that the porous layer in interfacial zone normally is absent and the aggregate is in direct contact with the dense calcium silicate hydrate (CSH) which is characterized by positive binding ability. The increased compactness and the reduction in the thickness of the transition zone improve the transfer of stresses from the paste to the aggregate.

A simplified schematic diagram showing the formation of the transition zone in concrete with and without silica fume is shown in Fig. 3.4 [Goldman and Bentur, 1989]: (a) fresh concrete without silica fume, showing the water filled space around the aggregate surface, due to bleeding and inefficient cement grain packing at the boundary; (b) transition zone of the mature system in (a) showing filling of the transition zone with $Ca(OH)_2$ and CSH, and the remnants of porous pockets and zones, some of them filled with needle-like material; (c) fresh concrete with silica fume, showing the silica fume particles filling the space around the aggregate that was occupied by water in the concrete without silica fume in (a); and (d) less porous transition zone in the mature system of (c). The fine silica fume particles distribute themselves at the interfacial zone, thus increasing the density of the interfacial zone. In the mature system (Fig 3.4(d)), the absence of ettringite and the reduction of CH in favor of an increase in CSH explain the narrower matrix-aggregate interfacial zone. The effects of silica fume on paste-aggregate interface will be discussed more in next section.

3.3.3 Effects of Silica Fume on Interfaces

Over the past decade, many attempts have been made to study the effects of silica fume on interfacial zones. It has been known that silica fume causes enhanced bonding associated

with the formation of a dense microstructure in the interfacial zone. Detwiler and Mehta [1989] have analyzed rigorously the role of silica fume in the improvement of the interfacial bond strength and found that silica fume has both a physical and chemical effect on the interfacial microstructure.

Physical Effect

The physical effect consists of a refinement of the pores. Detwiler and Mehta [1989] suggested that the physical effect of grain refinement, resulting in a more efficient packing of particles at the interface, plays a significant role in improving the strength of concrete, especially at early ages where the chemical effect is unimportant. The silica fume particles distributed themselves very uniformly in the interfacial zone. Thus, the surrounding region becomes more homogeneous and porosity in the interfacial zone is reduced. This physical effect of silica fume is referred to as the "filler effect". The efficient packing and the reduced porosity at the interface provide a good base for the formation of a strong interfacial zone, and later the chemical effect completes the work, by strengthening the interfacial zone.

Chemical Effect

When silica fume is used, it has been found that the amount of CH and ettringite normally present at the interfacial zone is greatly reduced. This reduction results in a more homogeneous interfacial zone and a much better contact between CSH and aggregate surface. Rosenburg and Gaidis [1989] found that the amount of heat liberated during hydration is greater with the silica fume than without and this supports the idea that silica fume accelerates the hydration of cement particles.

In ordinary concrete, cement particles react with water to form CSH and CH, and later no further reactions occur. When silica fume is used, an additional chemical reaction occurs

between silica fume and CH, producing more CSH, and thus provides a more complete hydration of cement particles and a reduction in the amount of CH present at the interfacial zone. Since ettringite is an equilibrium compound formed from sulfate and calcium, it follows that a reduction of CH results in an even greater reduction of ettringite. Therefore, such a chemical or pozzolanic effect of silica fume explains the reduction in the amount of CH and ettringite observed in silica fume concretes. The physical and chemical effects of silica fume are responsible for the better bonding, leading to the improved properties of high strength concrete.

3.4 Interfacial Characteristics

3.4.1 Interaction between Matrix and Aggregate

Interfaces in concrete materials play a major role in the determination of their mechanical properties. Good properties can be realized only if the stresses are effectively transferred between the constituents. Load transfer between the phases of concrete depends on, and is controlled by, the degree of contact and cohesive forces at the interface. In this aspect the interactions between matrix and aggregate of concrete are important. Zhang and Gjorv [1990] suggested three mechanisms as follows (see Fig. 3.5):

- Physical interaction

  For aggregates with well-polished mineral surfaces (e.g. quartz) and no chemical interaction with the matrix, the bond strength may be negligible regardless of the matrix properties. The matrix-aggregate interface becomes the weakest link in the system.

- Physical-chemical interaction

  For aggregatec having a chemical interaction with the cement paste matrix (e.g. carbonate rocks), there is evidence that a strong chemical bond between the cement paste

matrix and the aggregate may develop.

- Mechanical interlocking

  For porous aggregates or aggregates with a rough surface, the cement paste or cement hydration products may penetrate into cavities or large pores on the aggregate surface. These act as multiple "hooks" binding the aggregate and the matrix together.

In general, strong interface can enhance the strength, stiffness, and durability of concrete. However, an important concern about the increase of the bond strength is the possible brittle behavior that limits the use of high strength concrete.

3.4.2 Crack Path in Interfacial Region

Figure 3.6 shows schematically the influence of the tortuosity of the crack path on the stress transferring capacity in the descending branch for larger deformation. In a high strength concrete (HSC) or a lightweight concrete in which cracks run through the aggregates the crack path is smooth as compared to a normal strength concrete, indicating that the interface is strong. Therefore, for normal strength concrete (NSC), the descending branch lies above that one for high strength concrete. Fiber reinforced concrete (FRC) shows a different stress transferring mechanism since there is an effect of the connection of the crack surfaces through the fibers. With the increasing level of the descending branch the fracture energy increases, which means that the material becomes more ductile [Hordjik et al., 1989]. In conclusion, the crack path influenced by the interfacial properties greatly influences the load transfering mechanism and the ductility.

In general, crack propagation can be characterized by the following material properties of each material phase: E = Young's modulus; K_{IC} = critical stress intensity factor; $\sigma - w$ curve = the stress-separation relationship for a cohesive material; and v = the volume fraction of each phase of material, and Γ_i = the interfacial fracture toughness between

component materials. Knowing the volume fractions of the basic constituents and the fracture mode, one can then simulate the fracture behavior of a cement-based materials using two-parameter fracture model [Jenq, 1991]. In the composite fracture model proposed by Jenq [1991], all phases of the composite materials are assumed to follow linear elastic fracture mechanics and have the same Young's modulus. In addition, it is assumed that there is no bond failure at the interfacial region. For a better characterization, however, interfacial properties should be included in the fracture analysis the relative magnitude of the fracture toughness between the interface and the aggregate is an important factor in crack growth in concrete.

3.4.3 Assessment of Interfacial Properties

The major properties of an interface are the bond strength and the fracture toughness. Bond strength has been investigated by many investigators since 1960s. The bond strength is quite related to the formation of microcracks at interfacial zone. Early studies of bond strength revealed that the bond strength was related to the compressive strength of the paste. However, the chemical interaction, which is not yet understood, strongly influences the bond strength. In addition, the bond strength is related to the type of rock, for example, silicious rocks develops the highest strengths. A wide variety of test schemes for the bond strength measurement has been proposed, as shown in Fig. 3.7(a). All of the different test specimens shown are prone to the problems in preparation such as bleeding and shrinkage.

Recently, a number of investigators have tried to determine the fracture mechanics parameters of interfaces. Interfacial fracture toughness plays a key role on the cracking behavior of high strength concrete as well as on improving the stiffness and durability of the concrete. A study on the interface fracture toughness measurement was performed by Hillemeier and Hilsdorf [1977] who proposed a modified compact tension specimen shown in Fig. 3.7(b). They found that the interface exhibits significantly lower toughness than either

the cement pastes or the aggregates. They also concluded that the weakness of the interface is not due to low tensile strength but rather to a low fracture toughness and an extreme notch sensitivity. A beam type specimen shown in Fig. 3.7(b) was used by Wang et al. [1986], who found that densifying the interface with the addition of silica fume increased the interfacial fracture energy considerably. However, the fracture resistance parameters for interfaces obtained by their experimental work were involved in problems such as lack of consideration for mixed mode fracture at interfaces and the shrinkage effect on test specimens. In particular, the fracture at the interfaces often appears in mixed mode by tensile loading and shear loading. Differences between the material properties of matrix and aggregates would also result in the mixed mode fracture failure even when the geometry and loading are symmetric with respect to crack plane. The introduction of the interface fracture mechanics is needed to measure the interfacial fracture toughness over the full range of loading conditions from pure tension to pure shear. In Chapter 4, the basic interface fracture mechanics concepts will be discussed, followed by the description of novel fracture specimens to assess the fracture toughness of mortar-aggregate interfaces in Chapter 5.

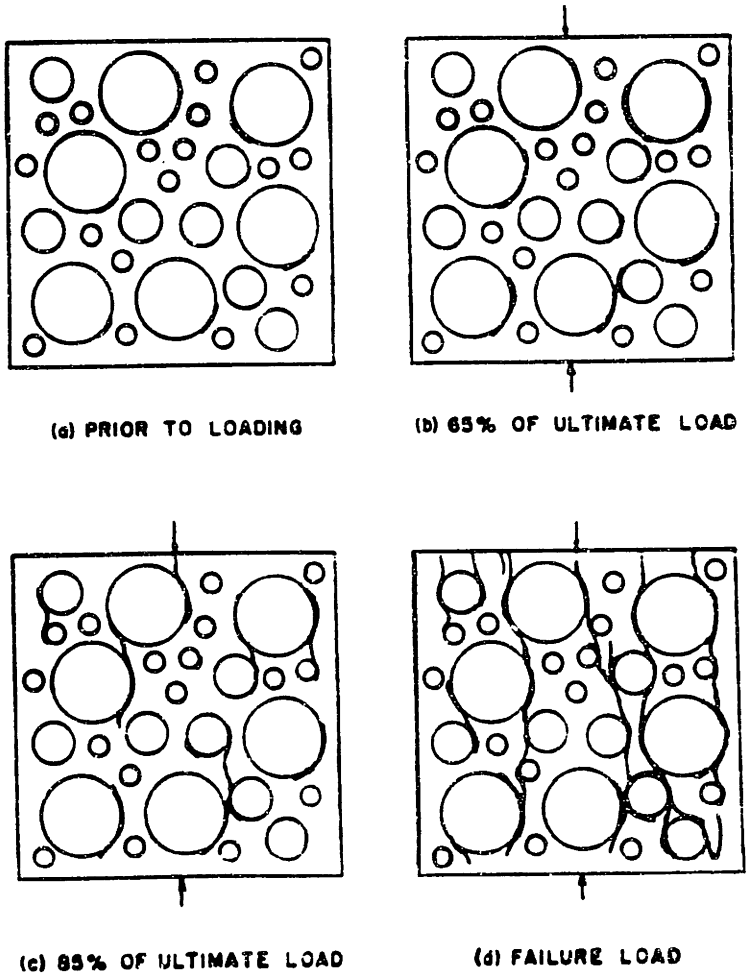

Figure 3.1 Progressive propagation of microcracks (from Liu et al. [1972])

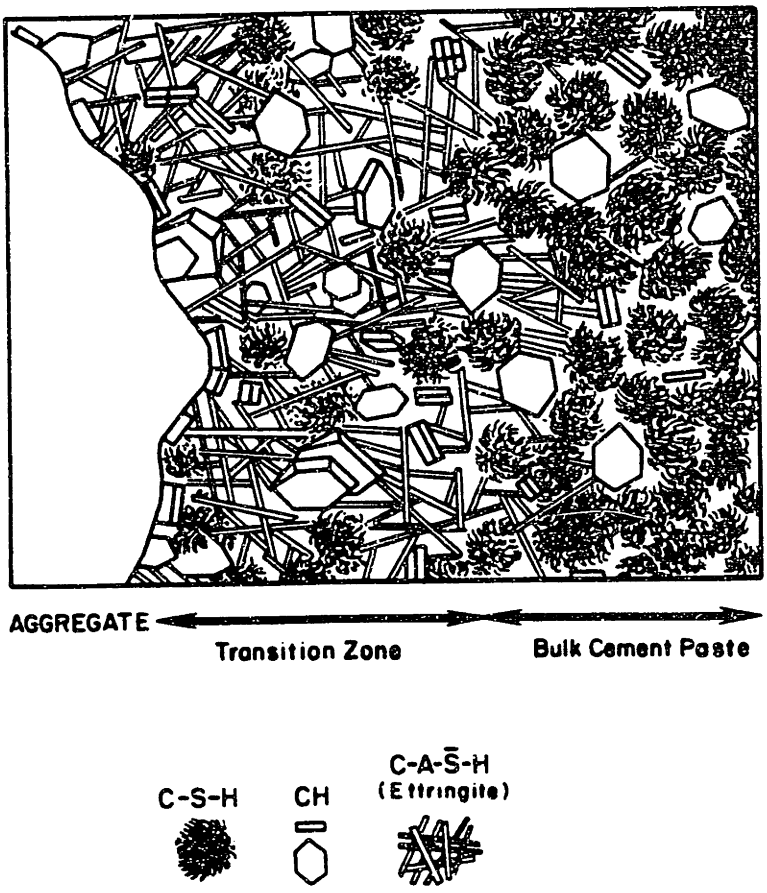

Figure 3.2 Microstructure of interfacial zone (from Mehta [1986])

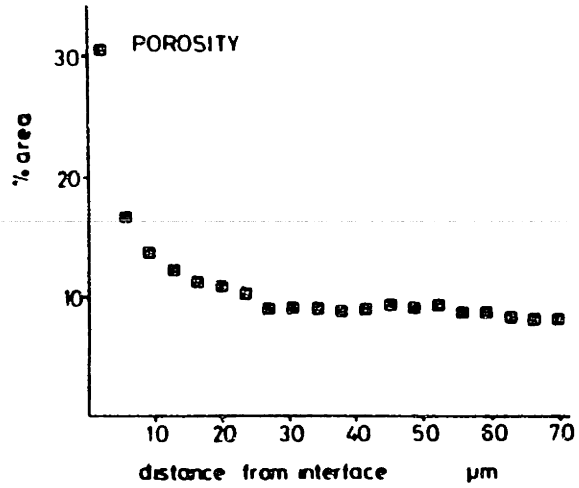

Figure 3.3 Porosity and distance from the interface (from Scrivener and Gartner [1988])

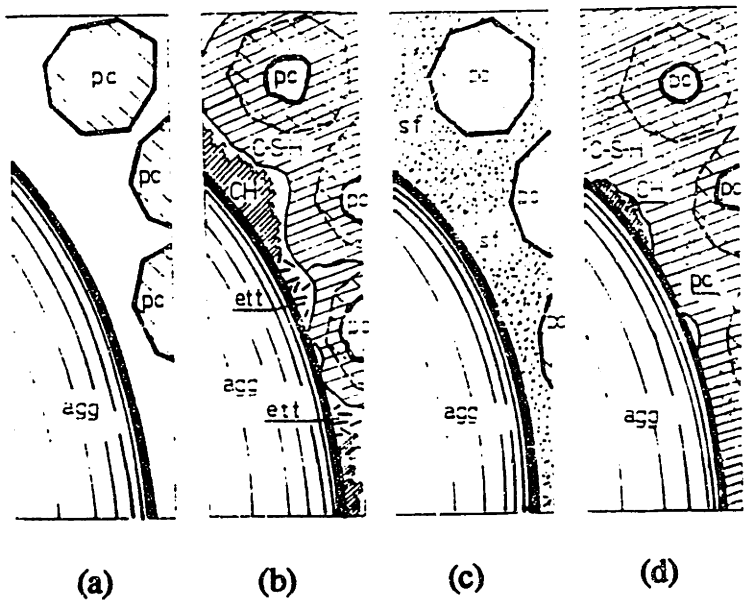

Figure 3.4 A simplified schematic diagram (from Goldman and Bentur [1989])

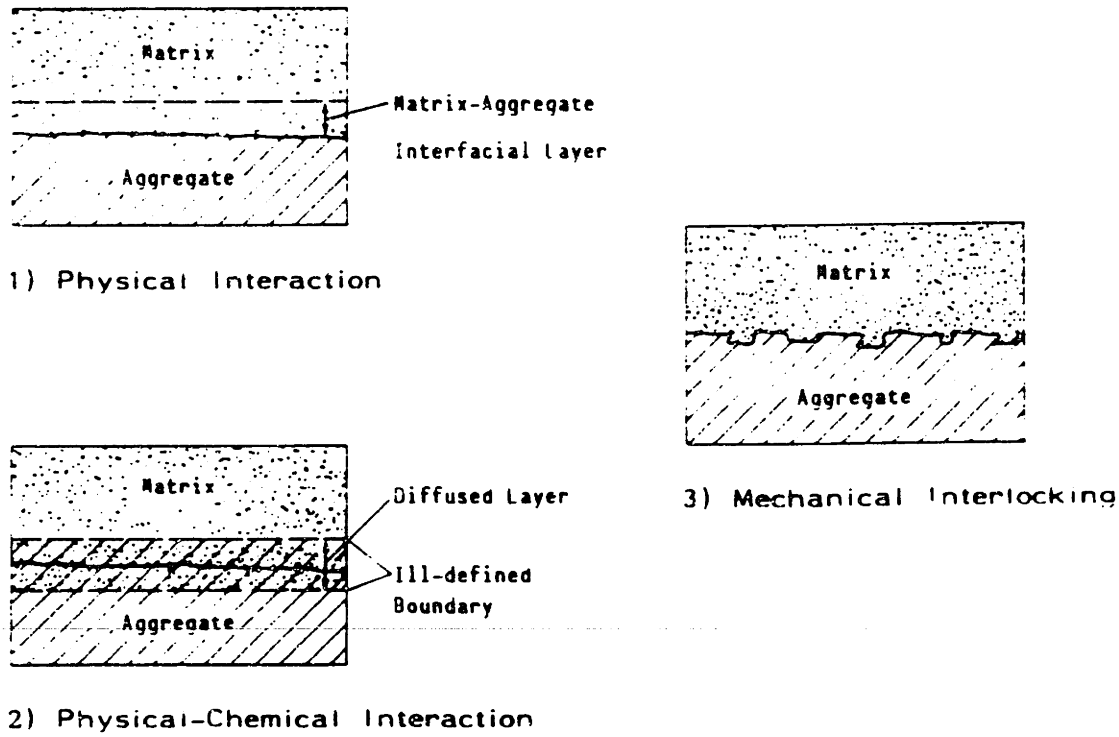

Figure 3.5 Three interactions between matrix and aggregates

(from Zhang and Gjorv [1990])

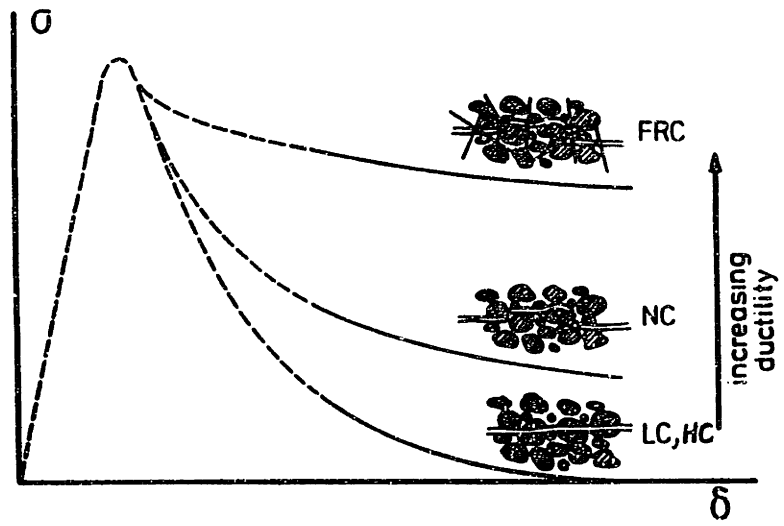

Figure 3.6 Schematic plot showing the influence of crack path on the stress-crack tip opening relation (from Hordjik et al. [1989])

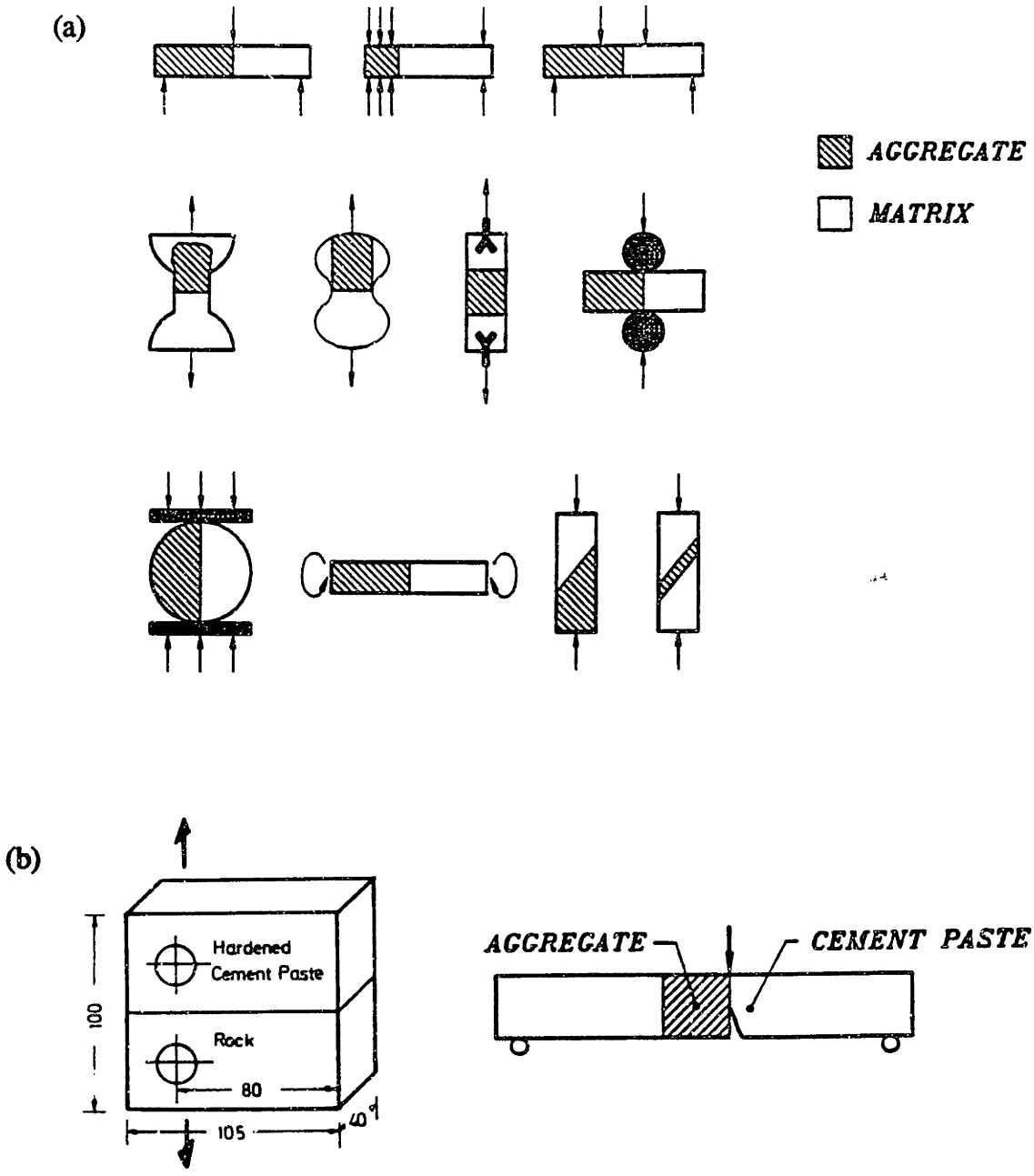

Figure 3.7 Testing schemes for measuring interfacial properties (from Mindess [1992]):

(a) Bond strength; and (b) Interfacial fracture toughness

Chapter 4

Interface Fracture Mechanics

The fundamental objectives of the interface fracture mechanics are to seek a meaningful definition of interfacial toughness, a material property that characterizes the resistance of a bimaterial interface to fracture and to assess the interface fracture toughness of bimaterial systems. This chapter reviews the interface fracture mechanics concepts applicable to mortar-aggregate interfaces in concrete, in particular, the recent work of Hutchinson and his collaborators [Rice, 1988; Hutchinson, 1990; Suo, 1989; Evans and Hutchinson, 1989; Hutchinson and Suo, 1992].

4.1 Bimaterial Elasticity

A bimaterial is a composite of two homogeneous materials with continuity of traction and displacement across interfaces. In this chapter, plane strain deformations in isotropic bimaterial will be discussed. Figure 4.1 shows an interface crack configuration between two dissimilar materials, namely, material 1, and material 2, with the interface on the x_1-axis. Let E_1, μ_1, and ν_1 be the Young's modulus, shear modulus, and Poisson's ratio, respectively, of material 1 lying above the interface. We define similar quantities, E_2, μ_2, and ν_2, for material 2 lying below the interface. Dundurs [1969] has observed that a wide class of plane problems of elasticity for bimaterials depends only on two nondimensional combi-

nations of the elastic moduli. With the convention set in Fig. 4.1, the moduli mismatch parameters of Dundurs, α and β, are

$$\alpha = \frac{\bar{E}_1 - \bar{E}_2}{\bar{E}_1 + \bar{E}_2}, \qquad \beta = \frac{1}{2}\frac{\mu_1(1-2\nu_2) - \mu_2(1-2\nu_1)}{\mu_1(1-\nu_2) + \mu_2(1-\nu_1)} \tag{4.1}$$

where $\bar{E} = E/(1-\nu^2) = 2\mu/(1-\nu)$. The parameter α measures the relative stiffness of the two materials. α approaches +1 when material 1 is extremely stiff compared to material 2 and -1 when material 1 is extremely compliant. In plane strain, the parameter β vanishes when both materials are incompressible ($\nu_1 = \nu_2 = 1/2$). Both α and β vanish when the dissimilarity between the elastic properties of the materials is absent, and α and β change signs when the materials are switched.

In plane strain, the physically admissible values of α and β are restricted to lie within a parrallelogram enclosed by $\alpha = \pm 1$ and $\alpha - 4\beta = \pm 1$ in the (α, β) plane, assuming non-negative Poisson's ratios [Dundurs, 1969]. Representative material combinations are plotted for plane strain in Fig. 4.2 [Hutchinson and Suo, 1992], in every case with the stiffer material 1 so that α is positive. It is noted that most of the (α, β) combinations in Fig. 4.2 fall between $\beta = 0$ and $\beta = \alpha/4$. For later convenience, an average stiffness, E^* is defined as

$$\frac{1}{E^*} = \frac{1}{2}\left(\frac{1}{\bar{E}_1} + \frac{1}{\bar{E}_2}\right) \tag{4.2}$$

4.2 Crack Tip Fields

Consider a semi-infinite traction free crack lying along the interface between two homogeneous isotropic half planes, with material 1 above and material 2 below (see Fig. 4.1). Two

coordinate systems (x, y) and (r, θ) are also depicted in Fig. 4.1. It is important to realize that no specific length or load are presented in the problem. Singular fields are sought to satisfy the continuity of traction and displacement vectors across the bonded portion of the interface, as well as the traction-free condition along the crack faces. This is a homogeneous boundary problem, or an eigenvalue problem [Suo, 1989].

Solutions to bimaterial interface crack problems were presented in the earliest papers on the subject by England [1965], Erdogan [1965], and Rice and Sih [1965]. Williams [1959] discovered the so-called oscillatory near-tip behavior for an interface crack between two isotropic materials. Here, the notations and definitions of Rice [1988] for the crack tip fields will be adopted since these reduce to the conventional notation when the mismatch vanishes. For the plane problems the normal and shear stresses of the singular field acting on the interface a distance r ahead of the tip are given by

$$\sigma_{22} + i\sigma_{12} = \frac{K}{\sqrt{2\pi r}} r^{i\epsilon} \tag{4.3}$$

or

$$\sigma_{22} = Re[Kr^{i\epsilon}](2\pi r)^{-1/2}\,, \quad \sigma_{12} = Im[Kr^{i\epsilon}](2\pi r)^{-1/2} \tag{4.4}$$

where $K = K_1 + iK_2$, the complex interface stress intensity factor, $i \equiv \sqrt{-1}$, and the oscillation index, ϵ, depends on β according to

$$\epsilon = \frac{1}{2\pi} ln(\frac{1-\beta}{1+\beta}) \tag{4.5}$$

The parameter ϵ brings in some complications which are not present in the elastic fracture mechanics of homogeneous solids. It is noted that K_1 and K_2 do not strictly measure the normal and shear singularities on the interface ahead of the crack tip due to the term $r^{i\epsilon}$ in

Eqn. (4.3).

The associated crack face displacements a distance r behind the crack tip, $\delta_i = u_i(r, \theta = \pi) - u_i(r, \theta = -\pi)$, are given by

$$\delta_2 + i\delta_1 = \frac{8K}{E^*(1+2i\epsilon)\cosh(\pi\epsilon)}\left(\sqrt{\frac{r}{2\pi}}\right)r^{i\epsilon} \tag{4.6}$$

The energy release rate per unit length of extension of the crack in the interface is given by [Malyshev and Salganik, 1965]

$$G = \frac{1}{E^*\cosh^2\pi\epsilon}|K|^2 \tag{4.7}$$

where $|K|^2 = {K_1}^2 + {K_2}^2$ and $\cosh^2\pi\epsilon = 1/(1-\beta^2)$.

When $\beta \neq 0$, the notion of mode 1 or mode 2 crack tip field must be defined precisely and the possibility of contact of the crack faces within the region dominated by the near tip K-fields must be considered. As noted by Rice [1988], a generalized interpretation of the mode measure is the most important complication raised by the oscillatory singularity, and the approach recommended here follows his proposals. From Eqn. (4.4), the phase angle $\hat{\psi}$, a measure of the contribution of shear to opening experienced by the interface crack surface, is defined as

$$\hat{\psi} = \tan^{-1}\left[\frac{Im(K\hat{L}^{i\epsilon})}{Re(K\hat{L}^{i\epsilon})}\right] \tag{4.8}$$

where $\hat{L}$ is a reference length. The measure of the proportion of "mode 2" to "mode 1" in the vicinity of the crack tip requires the specification of some length quantity since the ratio of the shear traction to normal traction varies (very slowly) with distance to the tip when

$\beta \neq 0$. Note that $\hat{\psi}$ is often non-zero due to the elastic mismatch across the interface even when the geometry and loading are symmetric with respect to the crack plane.

The choice of reference length $\hat{L}$ is somewhat arbitrary, as will be made clear below. It is useful to distinguish between a choice based on an inplane length of the specimen geometry, such as crack length, and a choice based on a material length scale, such as the size of the fracture process zone or a plastic zone at fracture. The former is useful for discussing the mixed mode character of a bimaterial crack solution, independent of material fracture behavior, while the latter is advantageous in interpreting mixed mode fracture data. Here, the notation $(\hat{\psi}, \hat{L})$ will be used for a choice based on the specimen geometry or a material based choice.

To help motivate the application of the crack tip fields to characterize interface toughness, it is useful to give two examples of stress intensity factors for solved problems. First, we will discuss the problem of the isolated crack of length $2a$ lying on the interface between two semi-infinite blocks subject to remote stresses (Fig. 4.3(a)). For the right hand tip of the crack,

$$K_1 + iK_2 = \frac{(\sigma_{22}^{\infty} + i\sigma_{12}^{\infty})(1 + 2i\epsilon)\sqrt{\pi a}}{(2a)^{i\epsilon}} \tag{4.9}$$

This particular set of intensity factors depends on the elastic mismatch only through ϵ, and is independent of α. Next, the problem of the infinite double cantilever beam (Fig. 4.3(b)) loaded with equal and opposite moments was solved by Suo and Hutchinson [1990]. The solution is

$$K_1 + iK_2 = \frac{2\sqrt{3}Mh^{\frac{1}{2}-i\epsilon}}{\sqrt{1-\beta^2}}\, e^{i\omega^*(\alpha,\beta)} \tag{4.10}$$

where the function, $\omega^*(\alpha, \beta)$ is the shift of the phase angle.

4.3 Interfacial Fracture Toughness

4.3.1 Fracture Toughness Curve

The fracture mode on an interface of dissimilar materials is usually mixed [Hutchinson 1990]. Differences in elastic moduli across an interface disrupt the symmetry even when the geometry and loading are symmetric with respect to the crack plane. Furthermore, an interface is typically brittle compared with the two bulk materials, and an interface crack, even when subjected to substantial shear stresses ahead the tip, tends to stay along the interface. Consequently, one needs a toughness curve to fully characterize the toughness of an interface.

For any interfacial crack problem the complex K will have the form as

$$KL^{i\epsilon} = YT\sqrt{L}e^{i\psi} \tag{4.11}$$

where T is an applied traction loading, L is a relevant length describing the geometry, such as crack length or uncracked ligament length, and Y is a dimensionless real positive number. ψ is the phase angle of the quantity $KL^{i\epsilon}$, but is often called the phase angle of stress intensity factor, or even the loading phase angle. Both Y and ψ generally depend on the ratios of various applied loads and lengths and, for traction prescribed problem, on α and β. The magnitude, $|KL^{i\epsilon}| = |K|$, is given by $YT\sqrt{L}$.

From the value of T at the onset of crack propagation in interface fracture test specimen $|K|_c$ is calculated according to Eqn. (4.11). The value is the toughness of the interface associated with the phase angle $\hat{\psi}$. By changing the relative proportions of loads, i.e., for various phase angle, one obtains the toughness locus of the interface. $|K|$ is related to the energy

release rate G by Eqn. (4.7). The current practice tends to report a G_c - $\hat{\psi}$ curve instead, and they are equivalent. The specific length $\hat{L}$ used should be reported in conjunction with the toughness curve, since it affects the definition of $\hat{\psi}$, as indicated in Eqn. (4.8). The freedom in the choice of $\hat{L}$ in the definition of $\hat{\psi}$ is a consequence of the simple transformation rule from one choice to another. Let ψ_1 be associated with L_1 and ψ_2 be associated with L_2. From the definition in Eqn. (4.8) one can readily show

$$\psi_2 = \psi_1 + \epsilon \, ln(\frac{L_2}{L_1}) \tag{4.12}$$

Thus, as noted by Rice [1988], it is simple to transform from one choice to another. In general, toughness data can be transformed, as will be discussed below.

Let $\hat{L}$ denote a length characterizing the size of the fracture process zone or, perhaps, the typical size of the plastic zone at fracture, and let $\hat{\psi}$ be associated through Eqn. (4.8). Since small scale yielding or a small scale fracture process zone is assumed, $\hat{L}$ necessarily lies within the zone of dominance of the K-field. Given the choice $\hat{L}$, the criterion for interface cracking can again be stated as

$$G = \Gamma_i(\hat{\psi}, \hat{L}) \tag{4.13}$$

where the implicit dependence of the toughness function on $\hat{L}$ has been noted. In other words, $\Gamma_i(\hat{\psi}, \hat{L})$ is the critical value of the energy release rate needed to advance the crack in the interface in the presence of a combination of traction whose relative proportion is measured by $\hat{\psi}$. By Eqn. (4.12), change in one choice of length in the definition of $\hat{\psi}$ to another only involves a shift of the $\hat{\psi}$-origin of Γ_i according to

$$\Gamma_i(\psi_2, L_2) = \Gamma_i(\psi_1 + \epsilon ln(\frac{L_2}{L_1}), L_1) \tag{4.14}$$

When ϵ is small, the shift will generally be negligible even for changes of $\hat{L}$ of several orders of magnitude.

In elastic fracture mechanics, the interface fracture toughness curve is the property of the given interface in the sense that it is independent of specimen geometry and loading system. However, the toughness curve is clearly dependent on the nature of the interface and the testing environment, such as the temperature, the roughness of the free surfaces before bonding, the bonding history, and the chemical composition of the two materials. Systematic study of these effects is still in a primitive stage, and should be the focus of future development of the interface fracture mechanics.

Efforts to measure the interface toughness under mixed mode conditions have been made for several years. Recent works [Cao and Evans, 1989; Evans et al., 1990; Wang and Suo, 1990] have focused on the interface between epoxy and glasses, metals, and plastics. They have attempted the experimental determination of interface toughness on several model systems, including thin films under residual tension, sandwiches, and bending specimens (Fig. 4.4). In all of the testing systems the interface toughness is not a single material parameter, rather it is a function of relative amount of mode 2 to mode 1 acting on the interface. Among several schemes the sandwich specimens seem to be suitable for measuring the mortar-aggregate interface toughness of concrete because they are easy to prepare and test in the laboratory. The analysis of sandwich test specimens will be presented in Chapter 5.

4.3.2 Interface Toughness with $\beta = 0$

Combinations which satisfy $\beta = 0$ give rise to simpler crack tip fields than combinations with $\beta \neq 0$. When $\beta = 0$ (and thus $\epsilon = 0$), Eqn. (4.3) becomes

$$\sigma_{22} + i\sigma_{12} = \frac{(K_1 + iK_2)}{\sqrt{2\pi r}} \tag{4.15}$$

and Eqn. (4.6) reduces to

$$\delta_2 + i\delta_1 = \frac{8(K_1 + iK_2)}{E^*}\left(\sqrt{\frac{r}{2\pi}}\right) \tag{4.16}$$

Then, the interface stress intensity factors, K_1 and K_2, are analogous to their counterparts in elastic fracture mechanics for homogeneous, isotropic solids. The mode 1 component, K_1, is the amplitude of the singularity of the normal stress ahead of the tip and the associated normal separation of the crack flanks, while the mode 2 component, K_2, governs the shear stress on the interface and the relative shearing displacement of the flanks.

When $\beta \neq 0$, the decoupling of the normal and shear components of stress on the interface and associated displacements behind the tip within the zone dominated by the singularity does not occur. When $\beta \neq 0$, the notions of mode 1 and mode 2 require some modification. In addition, the traction-free line crack solution for the displacements implies that the crack faces interpenetrate at some point behind the tip. Both of these features have caused conceptual difficulties in the development of a mechanics of interface fracture. Furthermore, β is small for many practical systems such as mortar/aggregate systems. For this reason, we can choose to introduce the elastic fracture mechanics of interfaces for bimaterial systems with $\beta = 0$, either exactly or as an approximation.

By substituting $\epsilon = 0$ into Eqn. (4.8) the phase angle is given by

$$\psi = tan^{-1}(\frac{K_2}{K_1}) \tag{4.17}$$

With $\epsilon = 0$, ψ is used to represent the phase angle. Here, $\psi = 0°$ corresponds to pure mode 1 and $\psi = 90°$ corresponds to pure mode 2. The finite crack in the infinite plane, Eqn. (4.9) gives

$$\psi = tan^{-1}(\frac{\sigma_{12}^{\infty}}{\sigma_{22}^{\infty}}) \tag{4.18}$$

while the double cantilever beam loaded by equal and opposite moments, Eqn. (4.10), has

$$\psi = \omega^*(\alpha, 0) \tag{4.19}$$

This double cantilever has symmetric geometry and loading. Thus, the asymmetry is due entirely to the elastic mismatch. Note that a substantial mode 2 component is developed when the elastic mismatch becomes significant.

The criterion for initiation of crack advance in the interface when the crack tip is loaded in mixed mode characterized by ψ is

$$G = \Gamma_i(\psi) \tag{4.20}$$

The toughness of the interface, $\Gamma_i(\psi)$, can be thought of as effective surface energy which depends on the mode of loading. Condition of Eqn. (4.20) is also assumed to hold for quasi-static crack advance when crack growth resistance effects can be disregarded.

4.3.3 Characterization of Interface Toughness

A micromechanical modeling of interface toughness is not advanced. An overview of various mechanisms responsible for the strong dependence of interface toughness on the phase angle is given by Evans et al. [1990]. Two primary mechanisms are asperity contact and plasticity. Asperity on the fracture surfaces will tend to make contact for some distance behind the tip when mode 2 is present along with mode 1. A micromechanics model of shielding of the tip due to asperity interaction was presented by Evans and Hutchinson [1989]. That model led to a prediction of $\Gamma_i(\hat{\psi})$ in terms of a nondimensional measure of fracture surface roughness. Crack tip plasticity also depends on $\hat{\psi}$ with the plastic zone in plane strain increasing in size as $|\hat{\psi}|$ increases, with G held fixed [Shih and Asaro, 1988].

A simple, one parameter fracture criterion which captures the trend of interface toughness is

$$\frac{({K_1}^2 + \lambda_2 {K_2}^2)}{E^*} = G_1^c \tag{4.21}$$

The parameter λ_2 adjusts the influence of the mode 2 contribution in the criterion. The limit $\lambda_2 = 1$ is the ideally brittle interface with initiation occurring when $G = G_1^c$ for all mode combinations. This limit coincides with the classical surface energy criterion. When $\lambda_2 = 0$, crack advance only depends on the mode 1 component. For any value of λ_2, G_1^c is the pure mode 1 toughness.

The following criterion can be used for a mixed mode toughness function:

$$\Gamma_i(\hat{\psi}) = G_1^c[1 + (\lambda_2 - 1)sin^2\hat{\psi}]^{-1} \tag{4.22}$$

Other phenomenological criteria have been proposed to characterize mixed mode toughness

data for interlaminate fracture. Two criteria which may realistically represent the data trends for interfacial fracture are given by

$$\Gamma_i(\hat{\psi}) = G_1^c[1 + tan^2((1 - \lambda_2)\hat{\psi})] \tag{4.23}$$

$$\Gamma_i(\hat{\psi}) = G_1^c[1 + (1 - \lambda_2)tan^2\hat{\psi}] \tag{4.24}$$

All three of the interface toughness functions, $\Gamma_i(\hat{\psi})$, are symmetric in $\hat{\psi}$.

4.4 Kinking out of Interfaces

A complexity in interfacial fracture testing is that under a mixed mode load, the crack has a strong tendency to kink into the substrate. Crack kinking has been observed for brittle substrates such as glass, ceramic, and polymer. The question of whether the crack will extend along the interface, or kink into the substrate is addressed in this section. Kinking of interfacial cracks has been analyzed by He and Hutchinson [1989a] and He et al. [1991]. As shown in Fig. 4.5, a semi-crack lies along the interface with its tip at the origin. Prior to kinking ($a = 0$), the parent crack is loaded with a complex interface stress intensity factor $K = K_1 + iK_2$ with mixity $\hat{\psi}$ defined as $\tan^{-1}[Im(K\hat{L}^{i\epsilon})/Re(K\hat{L}^{i\epsilon})]$ relative to some reference length $\hat{L}$ (Eqn. (4.8)). Here, $\hat{\psi}$ will be taken to be positive with kinking down into material 2 as shown in Fig. 4.5. Negative $\hat{\psi}$-loadings with upward kinking can be analyzed by exchanging the material, i.e., switching the signs on α and β.

As in the analysis for the isotropic solid, the energy release rate, G, for straight-ahead advance in the interface is compared with the energy release rate, G^t, for a crack with a segment of length a kinking at an angle Ω to the interface. The ratio of the two release rates, G and G^t, has the form

$$\frac{G}{G^t} = F(\Omega, \tilde{\psi}, \eta, \alpha, \beta) \tag{4.25}$$

where,

$$\eta = T(\frac{a}{E^* G})^{\frac{1}{2}} \tag{4.26}$$

and

$$\tilde{\psi} = \hat{\psi} + \epsilon \ln(\frac{a}{\hat{L}}) \tag{4.27}$$

The complete expression for F is given by He et al. [1991]. The a-dependence of this ratio appears through η and weakly through $\tilde{\psi}$. The effect of β on the ratio in Eqn. (4.25) is relatively weak as discussed by He and Hutchinson [1989a].

The ratio G/G^t_{max} is plotted against ψ in Fig. 4.6 for various values of α, in each case for $\beta = 0$ and $\eta = 0$. Here, G^t_{max} is the maximum of G^t with respect to kink angle Ω for a given ψ. As in the case of the homogeneous isotropic kinking problem there is very little difference between the kink angle which maximizes G^t and that which is associated with $K_{II} = 0$. With $\Gamma_i(\psi)$ denoting the toughness function of the interface and Γ_2 denoting the mode I toughness of material 2, kinking will be favored over continued interface cracking if

$$\frac{G}{G^t_{max}} < \frac{\Gamma_i(\psi)}{\Gamma_2} \tag{4.28}$$

4.5 Deflection vs. Penetration for a Crack Impinging to an Interface

A crack impinging to an interface joining two dissimilar materials may be arrested or may advance by either penetrating into the interface or deflecting along the interface. This is of importance, for example, in the design of concrete composites because the direction of any mortar crack approaching a aggregate strongly influence the concrete behavior. The competition between deflection and penetration is examined in this section when the materials on either side of the interface are assumed to be elastic and isotropic. Some recent studies on deflection vs. penetration of the interfacial cracks in dissimilar materials have been performed by He and Hutchinson [1989b]. In the problem A1 and A2 shown in Fig. 4.7 the semi-infinite reference crack with $a = 0$ is perpendicular to the interface with its tip at the interface. A symmetric loading with respect to the crack plane is applied. The problem B1 and B2 in Fig. 4.7 is a general case.

In Fig. 4.7 a interface crack may advance by either penetrating the interface or deflecting into the interface. The competition between the deflection and the penetration can be determined by the following fracture criterion [He and Hutchinson, 1989b]. The impinging crack is likely to be deflected into the interface if

$$\frac{\Gamma_i(\psi)}{\Gamma_1} < \frac{G_d}{G_p^{max}} \tag{4.29}$$

where, $\Gamma_i(\psi)$ is the toughness of the interface, Γ_1 is the mode 1 toughness of material ahead of the crack tip, G_d is the energy release rate of the deflected crack, and G_p^{max} is the maximum energy release rate of the penetrated crack. Conversely, the crack will tend to penetrate the interface when the inequality is reversed. The ratio G_d/G_p^{max} is plotted as a function of α in Fig. 4.8. The relative amounts of K_1 and K_2 at the right-hand tip of the

deflected cracks are presented in Fig. 4.9 using the phase angle ψ defined in Eqn. (4.17). With $\alpha = 0$ and $\gamma_2 = 90^o$ the critical ratio is approximately 1/4, meaning that the crack will deflect if the interface toughness is less than a quarter of the toughness of the material ahead of the crack.

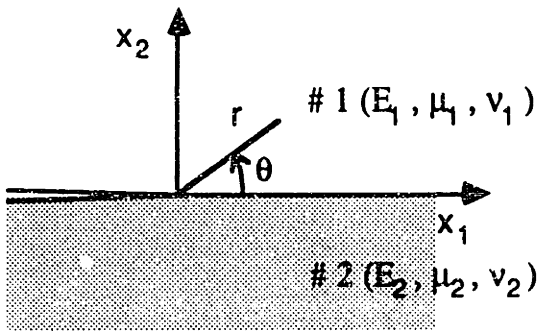

Figure 4.1 Geometry and conventions for an interface crack

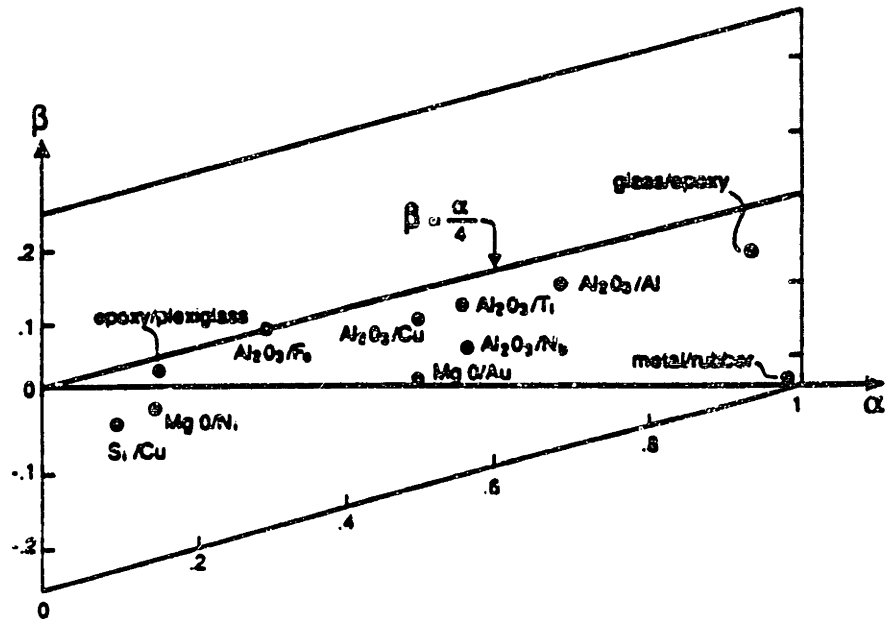

Figure 4.2 Values of Dundurs' parameters for bimaterials

(from Hutchinson and Suo [1992])

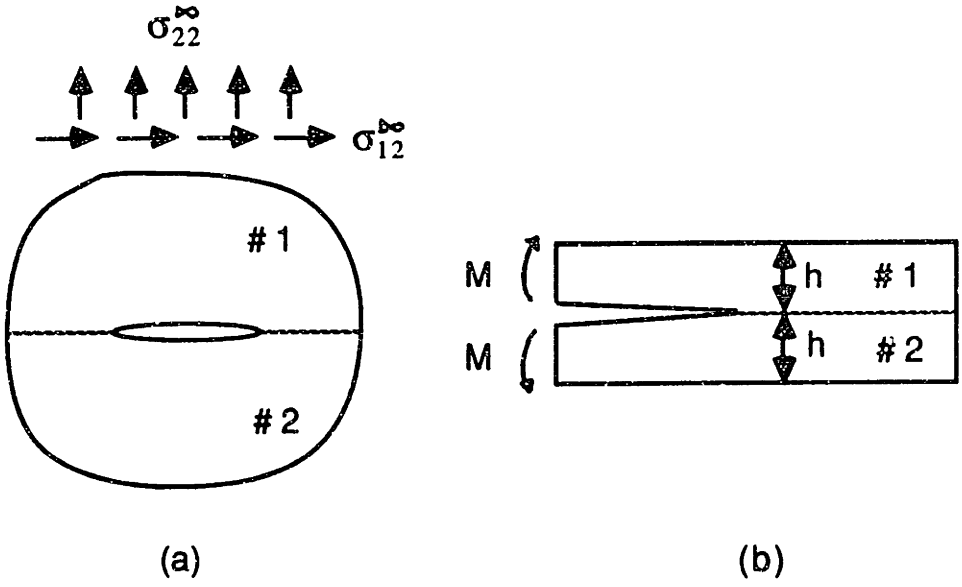

Figure 4.3 Two basic interface crack problems

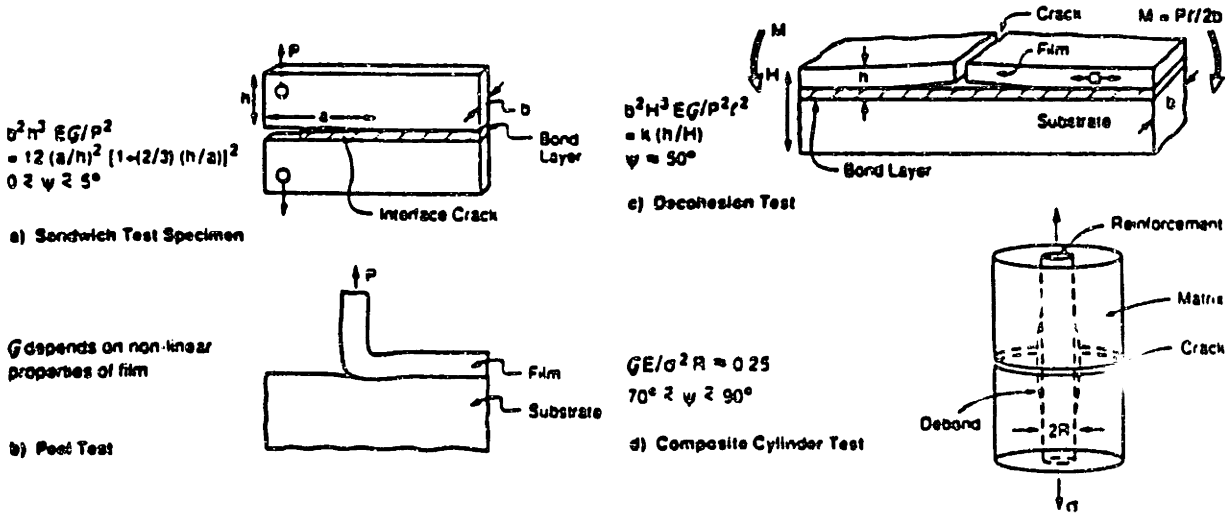

Figure 4.4 Models for experimental determination of interfacial fracture toughness (from Evans et al. [1990])

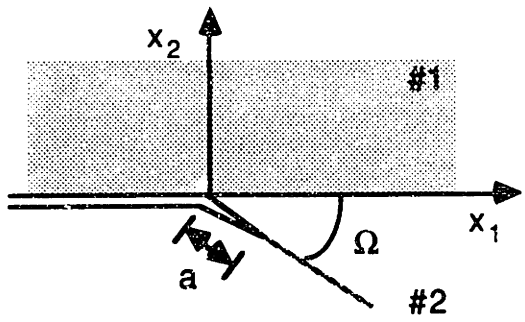

Figure 4.5 Conventions for a crack kinking out of an interface

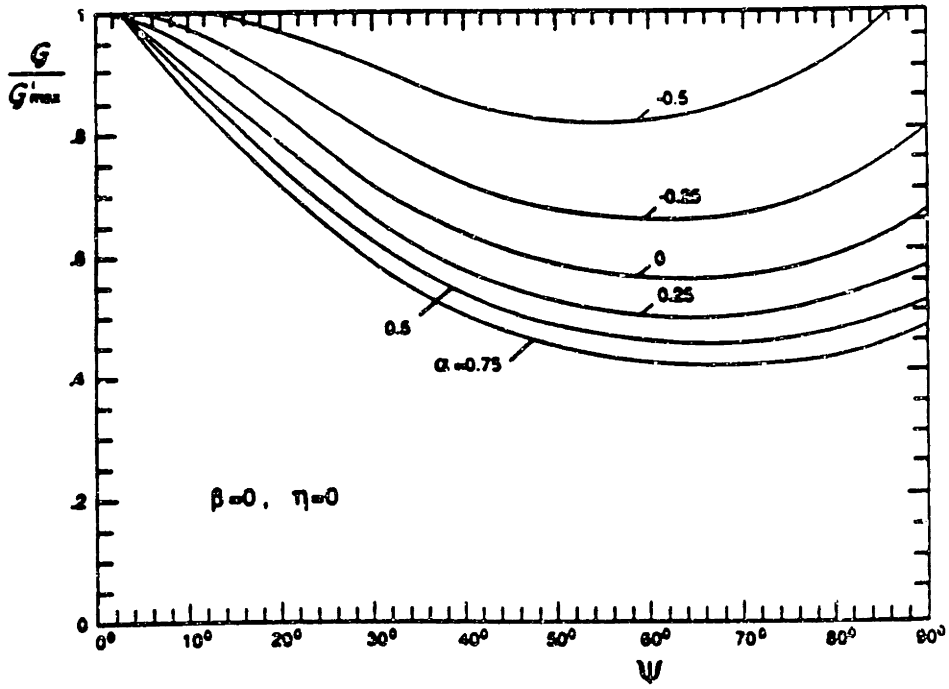

Figure 4.6 Ratio of two energy release rates versus phase angle

(from Hutchinson and Suo [1992])

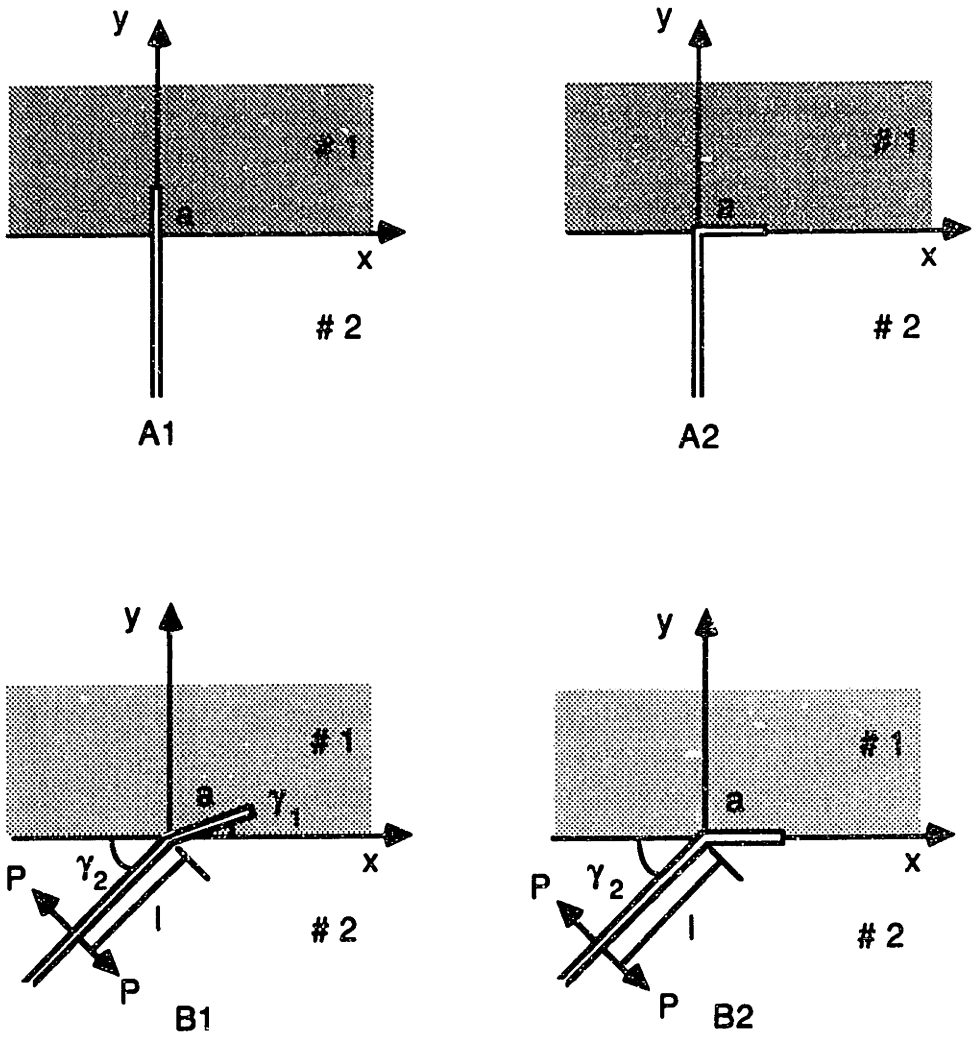

Figure 4.7 Crack geometry

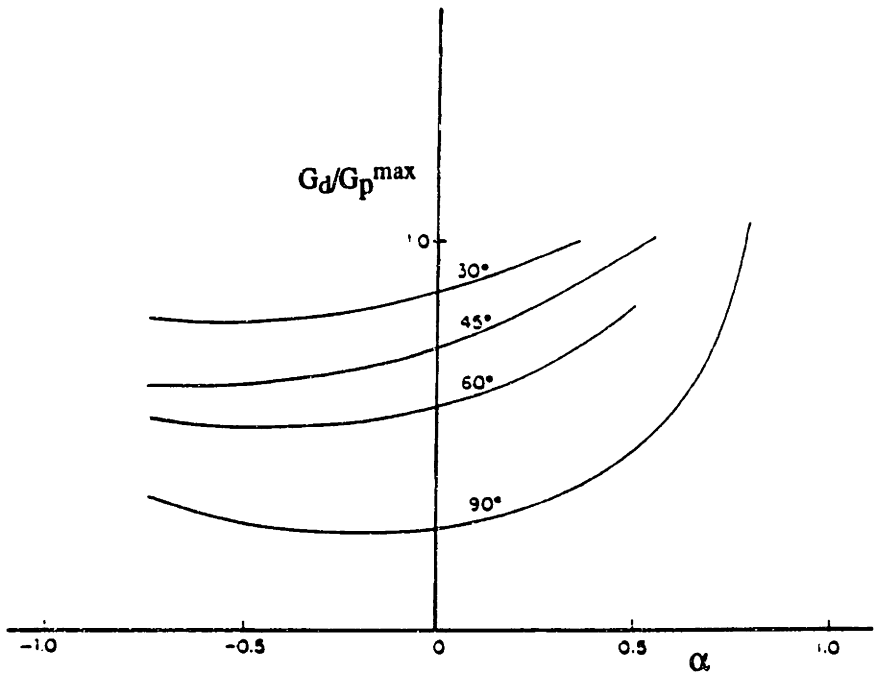

Figure 4.8 Ratio of energy release rate of deflected crack to penetrating crack at same *a* for wedge loaded crack (from He and Hutchinson [1989b])

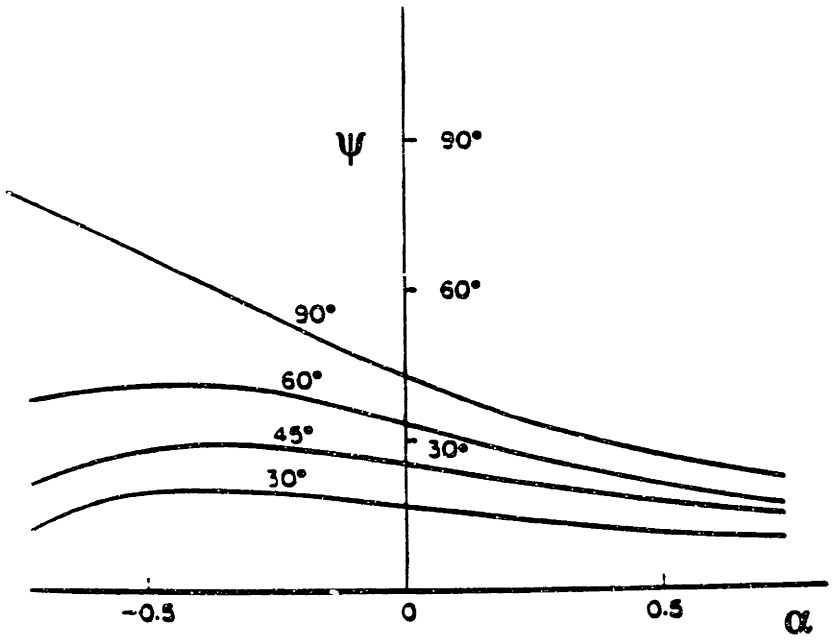

Figure 4.9 Combination of interface stress intensity factors at tip of deflected crack (from He and Hutchinson [1989b])

Chapter 5

Interface Fracture Model: Sandwich Test Specimen

Deformation and failure behavior of concrete is influenced by the characteristics of mortar-aggregate interfaces. The interfaces also play major role in the toughness and durability of concrete. Recently, the interest in the study of the role of interfaces in the material behavior has increased particularly due to the need for the development of high strength concrete. Presently, there is a need for the development of a fracture mechanics based approach for the characterization of interfacial fracture properties. Various methods and standards exist for measuring fracture toughnesses of the constituent materials such as mortar and aggregate. However, no established method exists for characterization of the mortar-aggregate interface. In this chapter, novel fracture model is introduced for characterization of the interfacial fracture properties in concrete. This will be followed by the description of the sandwich test specimens for assessing the fracture toughness properties of mortar-aggregate interfaces; i.e., for the investigation of fracture energy trends of these interfaces.

5.1 Universal Relation for Sandwich Test Specimens

Sandwich test specimens have been proposed by Suo and Hutchinson [1989] as one of interface fracture specimens. The analysis of this specimen will be given here. An interface

crack model including a thin layer of material 2 sandwiched in a homogeneous body of material 1 is shown in Fig. 5.1. Each material is assumed to be isotropic and linearly elastic. The crack lies along one of the interfaces coincident with the x_1-axis with the tip at the origin. If the thickness of the sandwich layer, h, is small compared to the crack length and to all of the other relevant in-plane length quantities, a universal asymptotic relation exists between the interface intensity factors, K_1 and K_2, and the stress intensity factors, K_I and K_{II}, for the homogeneous problem [Suo and Hutchinson, 1989].

The far field for the asymptotic problem in Fig. 5.1 is characterized by mode 1 and mode 2 stress intensity factors, K_I and K_{II}, for the homogeneous specimen. With $K^\infty = K_I + iK_{II}$ as the apparent, or applied, complex stress intensity factor, the traction a distance r far ahead of the crack tip is given by

$$\sigma_{22} + i\sigma_{12} = \frac{K^\infty}{\sqrt{2\pi r}} \tag{5.1}$$

In terms of the far field K_I and K_{II} the energy release rate is

$$G = \frac{1}{\bar{E}_1}({K_I}^2 + {K_{II}}^2) \tag{5.2}$$

where $\bar{E}_1 = E_1/(1-\nu_1^2)$. By elementary energy arguments, or by application of the J-integral, one notes that the energy release rate in Eqn. (4.7) and Eqn. (5.2) must be equal, and hence

$$|Kh^{i\epsilon}| = p\,|K^\infty| \tag{5.3}$$

where,

$$p = \sqrt{\frac{1-\alpha}{1-\beta^2}} \tag{5.4}$$

and $|Kh^{i\epsilon}| = |K|$. Now, the universal relation between the interface stress intensities and the applied stress intensities is obtained as

$$Kh^{i\epsilon} = p\, K^{\infty}\, e^{i\omega(\alpha,\beta)} \tag{5.5}$$

or,

$$K_1 + iK_2 = p\,(K_I + iK_{II})\, h^{-i\epsilon}\, e^{i\omega(\alpha,\beta)} \tag{5.6}$$

where the real function $\omega(\alpha,\beta)$ extracted from the numerical solution to the integral equation is given in Table 5.1 [Suo and Hutchinson, 1989]. The parameter ω represents the shift in phase of the interface intensity factors relative to the applied intensity factors and should be a nondimensional function of the two Dundurs' parameters, α and β.

Here, we also define

$$Kh^{i\epsilon} = |K|\, e^{i\psi^*}\,, \quad K^{\infty} = |K^{\infty}|\, e^{i\phi} \tag{5.7}$$

where the phase angle $\psi^* = \tan^{-1}[Im(Kh^{i\epsilon})/Re(Kh^{i\epsilon})]$ and $\phi = \tan^{-1}(K_{II}/K_I)$. Therefore, Eqn. (5.5) can be expressed as another form,

$$\psi^* = \phi + \omega(\alpha,\beta) \tag{5.8}$$

By assigning $L_1 = h$, $L_2 = \hat{L}$ in Eqn. (4.12) and by substituting Eqn. (5.8) into Eqn. (4.12) the loading phase angle is given by

$$\hat{\psi} = \psi^* + \epsilon\, ln(\frac{\hat{L}}{h}) = \phi + \omega + \epsilon\, ln(\frac{\hat{L}}{h}) \tag{5.9}$$

Thus, by specifying the fixed length $\hat{L}$, one can calculate the loading phase angle $\hat{\psi}$ from Eqn. (5.9), and the actual interface stress intensity factors, K_1 and K_2, can be calculated from the applied stress intensity factors, K_I and K_{II}, through the universal relationship between them, shown in Eqn. (5.6). Now, $\hat{\psi}$ measures the relative proportion of mode 2 to mode 1 on the interfaces. Since β value is relatively small compared to α value and the β-dependence of ω is generally weak, let $\beta = 0$, Eqn. (5.6) is simplified as

$$K_1 + iK_2 = \sqrt{1-\alpha}\,(K_I + iK_{II})\, e^{i\omega(\alpha,0)} \tag{5.10}$$

where ω is a function of α only.

5.2 Sandwich Test Specimens

The actual interfacial stress intensity factors can be determined from the universal relation of the stress intensity factors for the homogeneous specimens without further calibration. The application of the universal relation to a particular sandwich specimen is straightforward. Any specimen which has been successfully used for fracture test of homogeneous materials is acceptable. For the assessment of fracture toughness of mortar-aggregate interfaces in concrete, three types of sandwich test specimens are proposed and described in this section.

5.2.1 Four-point Bending Specimen

First, consider a four point bending specimen with a sandwiched aggregate layer shown in Fig. 5.2. Proper techniques are required to sandwich an aggregate layer into the mortar

matrix and ensure that the crack stays along one of the interface. To apply the universal relation, the thickness of a aggregate layer, h, should be very small compared with the crack length. For this four-point pure bending specimen the apparent intensity factor, K_I, for the homogeneous body, is simply obtained from finite element scheme or the stress analysis of cracks handbook [Tada et al., 1985] as

$$K_I = f_1 \sigma_r \sqrt{\pi a} \tag{5.11}$$

where,

$$\sigma_r = \frac{6M}{bd^2} \tag{5.12}$$

where a is the crack length, M is the applied moment, b is the width, d is the height, and a geometrical correction factor for the four-point pure bending specimen, f_1, is

$$f_1 = 1.122 - 1.40(\frac{a}{d}) + 7.33(\frac{a}{d})^2 - 13.08(\frac{a}{d})^3 + 14.0(\frac{a}{d})^4 \tag{5.13}$$

where a/d is the relative crack length. By substituting Eqn. (5.11) into Eqn. (5.6) the interface stress factors are given by

$$K_1 + iK_2 = ph^{-i\epsilon} \left(f_1 \sigma_r \sqrt{\pi a}\right) e^{i\omega} \tag{5.14}$$

With $\beta = 0$, K_1 and K_2 are

$$K_1 = \sqrt{1-\alpha}\,(f_1 \sigma_r \cos\omega)\sqrt{\pi a} \tag{5.15}$$

$$K_2 = \sqrt{1-\alpha}\,(f_1 \sigma_r \sin\omega)\sqrt{\pi a} \tag{5.16}$$

From Eqn. (5.2) the energy release rate can be calculated as

$$G = \frac{K_I{}^2}{\bar{E}_1} = \frac{f_1^2 \sigma_r^2 \pi a}{\bar{E}_1} \tag{5.17}$$

where $\bar{E}_1$ is defined for material 1 (mortar). By substituting $\phi = 0$ into Eqn. (5.9) the phase angle is calculated as

$$\hat{\psi} = \omega + \epsilon \, ln(\frac{\hat{L}}{h}) \tag{5.18}$$

In fact, this specimen with a sandwich layer is not on mode 1 state at the interface crack tip. Since the shift, ω, is not large according to Table 5.1, this specimen can be considered to be essentially in mode 1.

5.2.2 Four-point Shear Specimen

Next, the four-point shear specimen shown in Fig. 5.3 is considered. This specimen has been rigorously analyzed for mixed mode fracture testing of ceramic materials [He et al., 1988]. For four-point shear specimen the apparent stress intensity factors related to the loads and specimen geometry are given by

$$K_I = Y_1 \kappa Q \sqrt{\frac{\pi \zeta}{d}} \tag{5.19}$$

$$K_{II} = Y_2 Q \sqrt{\frac{\pi \zeta}{d}} \tag{5.20}$$

where,

$$Q = \frac{P(b_2 - b_1)}{(b_2 + b_1)} \tag{5.21}$$

$$\zeta = \frac{a}{d}, \qquad \kappa = \frac{c}{d} \tag{5.22}$$

where P is the applied load, a is the crack length, c is the crack location, and b_1, b_2, and d are geometric quantities. A finite element program developed by Shih and Asaro [1988] was u ed to calculate the calibration factors, Y_1 and Y_2, by He et al. [1988]. Figure 5.4 shows the values of Y_1 and Y_2 as a function of ζ. The calculation reveals that Y_1 and Y_2 are insensitive to both the loading arrangement, $(b_2 - b_1)/(b_2 + b_1)$, and the relative crack location, ζ. Conversely, the phase angle $\phi = tan^{-1}(K_{II}/K_I)$ is strongly dependent on κ, but weakly dependent on crack depth.

By substituting Eqns. (5.19) and (5.20) into Eqn. (5.6) the interface stress intensity factors are given by

$$K_1 + iK_2 = ph^{-i\epsilon}\,(Y_1\kappa + iY_2)\,Q\sqrt{\frac{\pi\zeta}{d}}\,e^{i\omega} \tag{5.23}$$

With $\beta = 0$, K_1 and K_2 are given by

$$K_1 = \sqrt{1-\alpha}\,(Y_1\kappa\cos\omega - Y_2\sin\omega)\,Q\sqrt{\frac{\pi\zeta}{d}} \tag{5.24}$$

$$K_2 = \sqrt{1-\alpha}\,(Y_1\kappa\sin\omega + Y_2\cos\omega)\,Q\sqrt{\frac{\pi\zeta}{d}} \tag{5.25}$$

From Eqn. (5.2) the energy release rate can be calculated as

$$G = \frac{(Y_1{}^2\kappa^2 + Y_2{}^2)Q^2\pi\zeta}{\bar{E}_1 d} \tag{5.26}$$

where $\bar{E}_1$ is defined for material 1 (mortar). By substituting $\phi = tan^{-1}(Y_2/Y_1\kappa)$ into Eqn. (5.9) the phase angle is calculated as

$$\hat{\psi} = tan^{-1}(\frac{Y_2}{Y_1\kappa}) + \omega + \epsilon\, ln(\frac{\hat{L}}{h}) \tag{5.27}$$

Eqn. (5.23) implies that the toughness can be measured over a wide range of phase angles by changing the loading condition and the crack location in this specimen. Consequently, one generates a locus of the critical combinations of the interface intensity factors, K_1 and K_2, or $G_c - \hat{\psi}$ curve.

5.2.3 Brazilian Disk Specimen

Finally, Brazilian disk specimen shown in Fig 5.5 is discussed, consisting of a thin layer of aggregate bonded between substrates of mortars. Brazilian disk specimen has been widely used as an indirect means of measuring the tensile strength of concrete, namely, the splitting tensile strength. Ojdrovic and Petroski [1987] have suggested that this specimen be used to measure the fracture toughness associated with the onset of microcracking ahead of a macrocrack. The Brazilian disk specimen has been rigorously analyzed by Atkinson et al. [1982], and used for mixed mode fracture testing of polycrystalline ceramics [Shetty et al., 1986, 1987; Singh and Shetty, 1989] and the fracture toughness testing of steel/epoxy interface, etc. [Wang and Suo, 1990].

Stress intensity factors for the inclined cracks in the Brazilian disk specimens can be calculated by the finite element scheme and using the solutions given by Atkinson et al. [1982]. Mode 1 and mode 2 stress intensity factors in homogeneous body are calculated from the initial precracked length, a, the fracture load, P, and the crack inclination angle, θ_i,

$$K_I = \frac{P\sqrt{a}}{\sqrt{\pi}Rt} N_1 \tag{5.28}$$

$$K_{II} = \pm\frac{P\sqrt{a}}{\sqrt{\pi}Rt} N_2 \tag{5.29}$$

where the plus sign in Eqn. (5.29) is for tip A, and the minus sign for B. R and t are the disk radius and thickness, respectively. The nondimensional coefficients N_1 and N_2 are functions of the relative crack length (a/R) and the angle of the inclination (θ_i). Fig. 5.6 shows the values of N_1 and N_2 as a function of θ_i with $a/R = 0.25$. Mixed mode stress states ranging from pure mode 1 to pure mode 2 can be achieved in this specimen by selecting the angle of inclination of the central through-crack with respect to the diametral line of compression loading.

By substituting Eqns. (5.28) and (5.29) into Eqn. (5.6) the interface stress intensity factors for tip A are given by

$$K_1 + iK_2 = ph^{-i\epsilon}(N_1 + iN_2)\frac{P\sqrt{a}}{\sqrt{\pi}Rt} e^{i\omega} \tag{5.30}$$

With $\beta = 0$, K_1 and K_2 are

$$K_1 = \sqrt{1-\alpha}(N_1 \cos\omega - N_2 \sin\omega)\,\frac{P\sqrt{a}}{\sqrt{\pi}Rt} \tag{5.31}$$

$$K_2 = \sqrt{1-\alpha}(N_1 \sin\omega + N_2 \cos\omega)\,\frac{P\sqrt{a}}{\sqrt{\pi}Rt} \tag{5.32}$$

From Eqn. (5.2) the energy release rate can be calculated as

$$G = \frac{P^2 a}{\bar{E}_1 \pi R^2 t^2}(N_1{}^2 + N_2{}^2) \tag{5.33}$$

where $\bar{E}_1$ is defined for material 1 (mortar). By substituting $\phi = tan^{-1}(N_2/N_1)$ into Eqn. (5.9) the phase angle for tip A is calculated as

$$\hat{\psi} = tan^{-1}(\frac{N_2}{N_1}) + \omega + \epsilon\, ln(\frac{\hat{L}}{h}) \tag{5.34}$$

By measuring the critical load P and the inclination angle θ_i, and by specifying a length $\hat{L}$, one can calculate G_c and $\hat{\psi}$ according to Eqns. (5.33) and (5.34).

5.3 Theoretical Considerations

5.3.1 ϵ-effects and Small Scale Yielding

In most interfacial fracture problems, ϵ is very small, often less than 0.01 in magnitude. Therefore, the effects of ϵ are negligible for experimental study. Currently, the difficulty in preparing specimens and in measuring the interfacial toughness are much more pertinent than ϵ - effects. Elastic properties of constituent materials and values of α, β for six mortar/aggregate combinations are presented in Table 5.2. Three mortar types (NSM: normal strength mortar, HSM: high strength mortar, VHSM: very high strength mortar) and two type of aggregates (limestone and quartzite) are considered as constituent materials of concrete composites. The Young's modulus and Poisson's ratio listed for each material are typical values [Baalbaki et al., 1991]. It is observed from Table 5.2 that in most of these combinations β values are relatively small, in particular, in HSM/aggregate and VHSM/aggregate systems, indicating that α is more important. Thus, for an simplified approximation, only the parameter α needs to be considered, both to determine fracture

toughness values of mortar-aggregate interfaces and to predict fracture. Although the ϵ-effect is small (i.e., β is small), both α and β values will be considered in the present work for better accuracy.

There are general requirements for a valid toughness measurement of sandwich specimens. First, plane strain condition is usually easy to be satisfied. However, the small scale yielding condition at the crack tip is hard to satisfy. For an isolated interfacial crack tip, the size of the plastic zone around the tip is given by

$$r_p = \Lambda \frac{|K|^2}{\sigma_0^2} \tag{5.35}$$

where K is the complex stress intensity factor, σ_0 is the smaller of the yield strengths of the two solids, and the dimensionless number Λ, ranging from 0.1 to 0.6, is a function of loading phase and also depends weakly on the details of material properties. For the small scale yielding condition to be satisfied for a particular sandwich system, the plastic zone size, r_p, is very small compared with the interlayer thickness: $r_p < 10h$ [Suo, 1989].

5.3.2 Small Scale Contact and Crack Kinking out of an Interface

The requirement of small scale contact sets the range of the loading phase in which toughness can be validly measured for a given interface. With the specimen size L and loading angle ψ, one can readily show that the normal crack face displacement in the near tip region from Eqn. (4.6) is

$$\delta_2 = |\delta_2 + i\delta_1| cos[\psi + \epsilon ln(\frac{r}{L}) - tan^{-1}(2\epsilon)] \tag{5.36}$$

where $|\delta_2 + i\delta_1|$ is the magnitude of the crack face displacement jump and ψ is the phase angle of $KL^{i\epsilon}$. Consider the condition for the crack to be open ($\delta_2 > 0$ for $L/100 < r <$

$L/10$). The factors 1/100 and 1/10 are arbitrary, but the absolute value of this number will not affect the following result significantly. This requirement confines the range of ψ in which valid toughness can be measured

$$-\frac{\pi}{2}+6.6\epsilon<\psi<\frac{\pi}{2}+3\epsilon, \quad for\ \epsilon>0 \tag{5.37}$$

$$-\frac{\pi}{2}+3\epsilon<\psi<\frac{\pi}{2}+6.6\epsilon, \quad for\ \epsilon<0 \tag{5.38}$$

This, is turn, limits the loading phase $\hat{\psi}$ (see Eqn. (5.9)). With sandwich specimens, we choose $\hat{L}=L=h$, and then $\hat{\psi}\approx\psi$. For VHSM-quartzite interface in Table 5.2, for example, ϵ = -0.027, which yields $-100^\circ<\hat{\psi}<85^\circ$. In the interface fracture toughness plot for this interface, all of the data should be in this validity range. In general, this requirement is not significant for mortar-aggregate interfaces because their ϵ values are small and hence, the range covers most of loading cases.

When the crack is trapped at the interface, the fracture toughness of the interface can be measured as a function of $\hat{\psi}$. Otherwise, the crack moves out of the interface, and the measured energy refers either to the mortar or to the aggregate. When the loading phase is large, i.e., shear loading effect becomes large, an interface crack in concrete might tend to kink out of interface. Such a kinking of an interface crack is analyzed in Section 4.4. In general, interfacial cracks in bimaterials with large elastic mismatch tend to kink under predominantly opening mode. This phenomenon is independent of the toughness ratio of the bulk material to the interface, as long as the ratio is not large enough to invalidate the linear fracture mechanics approach or to cause essentially no adhesion of the interface [Wang and Suo, 1990]. This is negligible for the mortar-aggregate interfaces because the elastic mismatch between mortar and aggregate is not large.

Table 5.1 ω values (from Suo and Hutchinson [1989])

α / β	-0.8	-0.6	-0.4	-0.2	0.0	0.2	0.4	0.6	0.8
-0.4	2.2	3.5							
-0.3	3.0	4.0	3.3	1.4					
-0.2	3.6	4.1	3.4	2.0	-0.3	-3.3			
-0.1	4.0	4.1	3.3	2.0	0.1	-2.3	-5.5	-10.8	
0.0	4.4	3.8	2.9	1.6	0.0	-2.1	-4.7	-8.4	-14.3
0.1			2.3	1.1	-0.5	-2.3	-4.5	-7.4	-11.6
0.2					-1.3	-3.0	-4.9	-7.3	-10.5
0.3							-5.8	-7.8	-10.4
0.4									-11.1

Table 5.2. Dundurs' parameters of six mortar/aggregate combinations

Combinations (#1/#2)	E_1 (GPa)	ν_1	E_2 (GPa)	ν_2	α	β	ε
NSM/Limestone	25.4	0.24	49.0	0.16	-0.302	-0.081	0.026
NSM/Quartzite	25.4	0.24	42.0	0.14	-0.227	-0.048	0.015
HSM/Limestone	37.3	0.22	49.0	0.16	-0.124	-0.024	0.008
HSM/Quartzite	37.3	0.22	42.0	0.14	-0.044	0.012	-0.004
VHSM/Limestone	56.5	0.20	49.0	0.16	0.078	0.045	-0.014
VHSM/Quartzite	56.5	0.20	42.0	0.14	0.157	0.084	-0.027

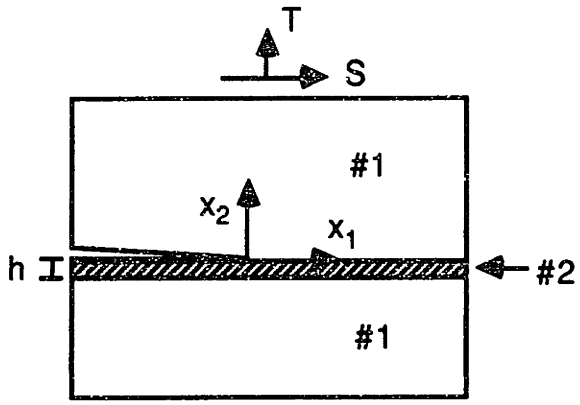

Figure 5.1 Interface crack problem in a sandwiched layer model

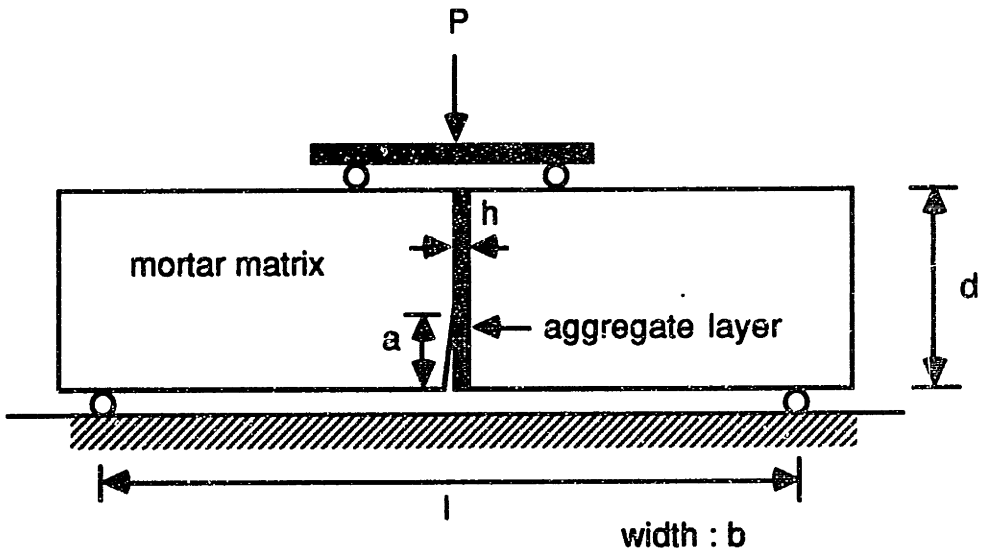

Figure 5.2 Sandwiched four-point bending specimen

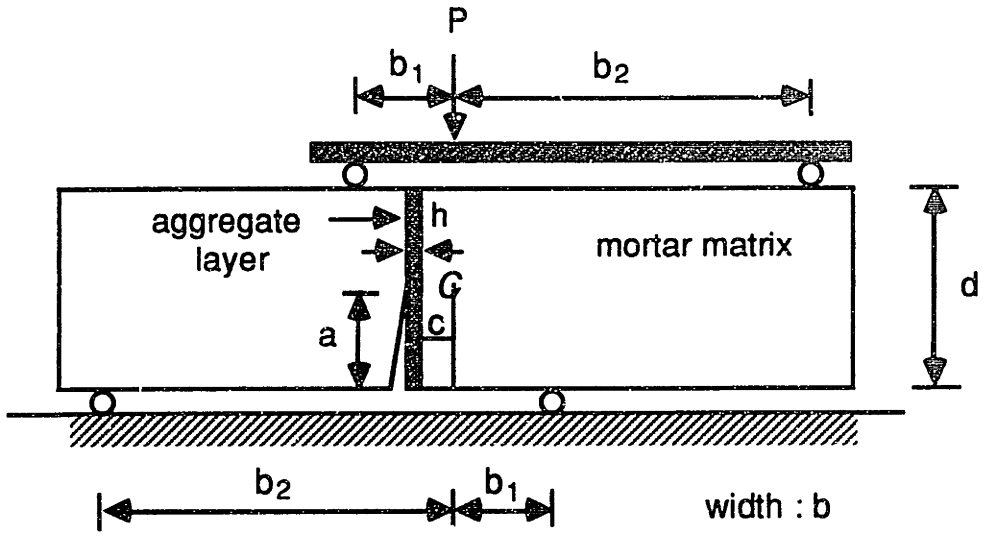

Figure 5.3 Sandwiched four-point shear specimen

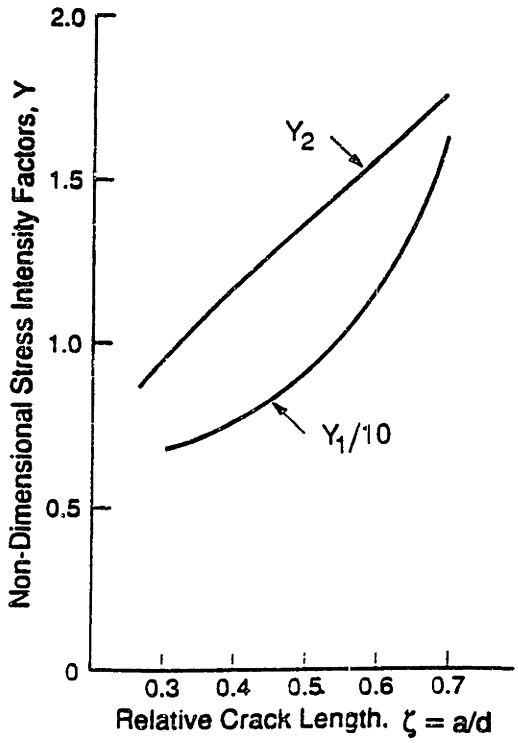

Figure 5.4 Y_1 and Y_2 values versus ζ

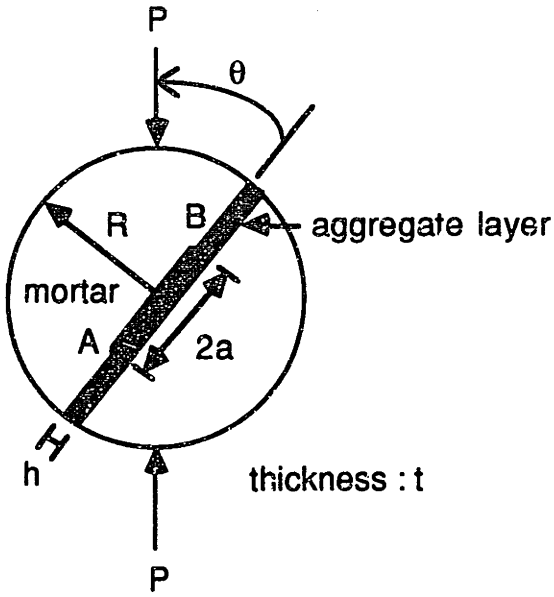

Figure 5.5 Sandwiched Brazilian disk specimen

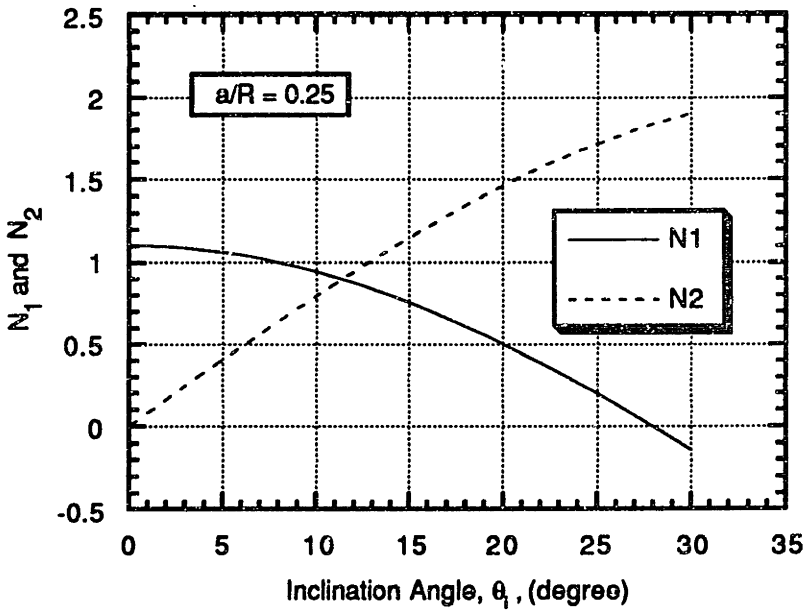

Figure 5.6 N_1 and N_2 values versus θ_i with a/R = 0.25

Chapter 6

Measurement of Fracture Toughness of Mortar-aggregate Interface

Concrete is often viewed as a two-phase mixture of mortar matrix and aggregates. In this two-phase model the bonding between mortar and aggregate plays a major role in determining the concrete properties. In particular, the bond strength and the interfacial fracture toughness are important parameters. Thus, there exist a need for reliable data of the interfacial properties for the better understanding of concrete behavior. In this chapter, experimental work is presented to assess the fracture toughness of mortar-aggregate interfaces using sandwich test specimens. This experimental work is divided into three phases. In Phase I, through preliminary tests three mortars and two types of aggregate materials were selected. The main concern of this phase was to develop a mix design for the mortars with aimed compressive strengths. Phase II of the program was to determine the mechanical properties of selected materials. Compressive strength, elastic modulus, and mode I fracture toughness were measured because these parameters were essential in the main experimental work for the assessment of interfacial fracture toughness. In Phase III of the program the fracture toughness curves for mortar-aggregate interfaces were generated from the sandwiched specimen tests. In this chapter, the data gathered in all three phases was collected and interpreted, and then was discussed.

6.1 Experimental Parameters

Many parameters influence the interfacial fracture toughness in concrete, including loading condition, aggregate surface condition, properties of mortar matrix and aggregate, loading rate, and specimen geometry. In this experimental work three main parameters were selected, namely:

1. Loading condition - pure mode I to pure mode II loading
2. Mortar matrix type - high strength mortar ($f_c' \approx 83$ MPa (12,000 psi)), medium high strength mortar ($f_c' \approx 62$ MPa (9,000 psi)) and normal strength mortar ($f_c' \approx 41$ MPa (6,000 psi))
3. Aggregate type - granite and limestone

Since interface fracture usually involves the mixed mode, loading condition was varied from pure tension (mode I) to pure shear (mode II) to generate the full range of interface fracture toughness values. Two high strength mortars incorporating silica fume were included to investigate the effect of silica fume on the interfacial fracture properties. Two types of aggregates were selected to study the effect of the difference in mechanical properties between the mortar and the aggregate.

6.2 Details of Sandwich Specimens

To measure the interfacial fracture properties, sandwiched specimens composed of an aggregate inclusion embedded in a mortar matrix were used. The analysis of sandwich specimens were given in Chapter 5. In constructing the specimens concrete is assumed to be a two-phase composite consisting of mortar matrix and aggregate inclusions. Two types of sandwich specimens were selected, including the sandwiched beam specimen shown

in Fig. 6.1 for mode I loading test and the sandwiched Brazilian disk specimen shown in Fig. 6.2 for mixed mode and shear loading test. However, the interface crack tip in the beam specimens were not in pure mode I condition due to the elastic mismatch between mortar matrix and aggregate layer. From the testing of the two types of specimens the interface fracture toughness curves can be established in the full range of loading condition.

From the preliminary test the proper specimen sizes were determined. The dimensions of the sandwiched beam specimen were 152.4 mm (6.0 in : length) x 50.8 mm (2.0 in : height) x 38.1 mm or 25.4 mm (1.5 in or 1.0 in : width). The ratio of height to loading span length was 3.0. Radius, R, and thickness, t, of the sandwiched Brazilian disk specimen were 38.1 mm (1.5 in) and 25.4 mm (1.0 in), respectively, and thus, the ratio of the thickness to the diameter was 0.33. The thickness of the aggregate layer, h, was 2.54 mm (0.1 in) for both specimens. The relative crack size (a/R) in the Brazilian disk specimen was fixed to be 0.25 and the relative crack size (a/d) in the beam specimen was 0.375.

6.3 Materials

6.3.1 Batch Design for Mortars

For the production of mortars the following materials were used: Type I Portland cement, quartz sand, silica fume in a slurry form, high range water reducer (HRWR or superplasticizers). The cement and sand were supplied by Waldo Bro. Co., located in Boston, MA. Sand passing sieve #8 were used. The silica fume whose brand name is 'Force 10,000' produced by W. R. Grace & Co., in Cambridge, MA., was used. Force 10,000 is a microsilica based liquid admixture containing 48% silica fume along with 2% foreign particles and 50% water by weight. The brand name of HRWR was 'WRDA-19' (ASTM C-494 Type A & F) produced by W. R. Grace & Co. WRDA-19 is an aqueous solution of a modified naphthalene sulfonate and has low viscosity and contains no added chloride.

Through preliminary tests, the batch design for three mortars (two high strength mortars and one normal strength mortar) was determined. The mix proportions for the three mortars are listed in Table 6.1. As can be seen from Table 6.1, the water to cementitious materials (cement and silica fume) ratios, W/(C+SF), for the three mixes (M1, M2, and M3) were varied 0.50, 0.35, and 0.28 by weight, and the aimed corresponding 28-days compressive strength values were 41 MPa (6,000 psi), 62 MPa (9,000 psi), and 83 MPa (12,000 psi). Sand to cement ratio were fixed to be 2.0 by weight for all mortar mixes. Mortar 2 (M2) mix and mortar 3 (M3) mix were incorporated with 5% and 10% of silica fume to cement ratio and 1% and 2% of HRWR to cement ratio, respectively, while mortar 1 (M1) mix did not contain silica fume and HRWR. All mortar mixes were designed to have the slump values of 203.2 mm (8.0 in) to 228.6 mm (9.0 in).

6.3.2 Selection of Aggregates

Important aspects of rock selection in the production of high strength concrete include particle shape, surface texture, and mineralogy of the rock used. Different types of rock have been used as the aggregate inclusions in high strength concrete: traprock, quartzite, limestone, granite, and gravel. In this experimental work using the sandwich test specimen two types of rock were selected to make aggregate layers: granite (G) and limestone (L). Granite was much stiffer than limestone, which is a light-weighted aggregate material. Both rocks were available in the Materials Laboratory in MIT, and especially, the limestone has been used for the bricks outside of main MIT buildings. Consistent procedures were adopted in slicing rocks and in preparing their surfaces with similar roughness. The consistency of these procedures enabled a valid comparative evaluation of the selected parameters.

The test program involved six different types of mortar/aggregate systems obtained by combining three mortar types and two aggregate types. The following is a list of the mortar/aggregate combinations included in the test program, with the nomenclature used for

each type in parenthesis:

1. Normal strength mortar with granite (M1/G)
2. Normal strength mortar with limestone (M1/L)
3. Medium high strength mortar with granite (M2/G)
4. Medium high strength mortar with limestone (M2/L)
5. High strength mortar with granite (M3/G)
6. High strength mortar with limestone (M3/L)

This nomenclature will be used throughout this thesis.

6.4 Manufacturing of Specimens

From each batch of mortar mix, sandwiched specimens were cast, along with mortar cylinders with the diameter of 76.2 mm (3.0 in) and the length of 152.4 mm (6.0 in) for compressive loading test and beam specimens with a pre-crack for mode I fracture toughness test. To do this, first, the aggregate layers were prepared. The layers were sliced from the blocks of granite or limestone using diamond sawing machine. The dimensions of layers are 76.2 mm (length) x 25.4 mm (height) x 2.54 mm (thickness) for the Brazilian disk specimens, and 50.8 mm (length) x 38.1 mm or 25.4 mm (height) x 2.54 mm (thickness) for the beam specimens. Although the layer should be very thin by the assumption of sandwich specimen analysis, the aggregate layer thickness of 2.54 mm was an experimental limit. The surfaces of aggregate layers were consistently prepared as to have the same roughness, and then the layers were cleaned using water and dried in air.

Next, molds for making beams and Brazilian disk specimens were prepared. The beam mold made of plexiglass has been used in many other concrete experimental works performed in MIT. The molds for Brazilian disk specimens shown in Fig. 6.3 were newly designed using paper cylinders. To avoid the water absorption of paper oil coating was applied to the inner surface of the paper molds twice or three times. To make a sharp crack, a notch plate made of thin plastic with the thickness of 0.1 mm was attached to one side of the aggregate layer using paraffin or glue. Then, the aggregate layers were placed at the center of the beam mold and the cylinder molds for manufacturing Brazilian disk specimen. In addition to the sandwich specimen molds, cylinder molds for compressive test specimens and beam molds for fracture test specimens were prepared. After all of the molds were ready, the mortar mixture was prepared. For mixing, an Omni mixer, Model OM-30AV, manufactured by Chiyoda & Gar-Bro Co., as shown in Fig. 6.4, was used. This mixing machine improves the quality of the mixture by uniformly pressurizing the mixtures inside of chamber and rotating the direction of a flexible rubber drum attached to a vertical bar. The mixing speed can be easily changed.

The mixing procedure for mortar was summarized as follows:

1. prepare the right amount of ingredients: water, sand, cement, and admixtures
2. mix cement and dry sand first at an atmospheric pressure for 2 - 3 minutes
3. add water to the cement-sand mix and only for making high strength mortars (M2 and M3) add silica fume and HRWR to the water before pouring the water into the mixer
4. close the mixing chamber and pressurize to approximately 50 cmHg
5. operate the mixer for 5 minutes to make the fresh mortar

The fresh mortar was then poured into the molds prepared. After pouring, the molds were externally vibrated for 3 minutes to ensure proper placing of the mortar. All specimens were

covered with plastic for 24 hours after the fresh mortar were poured in the molds. After the notch plates were removed from the sandwiched specimens, all specimens were placed in water until the day of testing. Just before mode I fracture testing of mortar beam specimens a very sharp crack was introduced at the center of the beams using the diamond sawing machine. All specimens were tested after 28 days of curing age.

6.5 Test Set-up and Procedure

6.5.1 Testing Equipment

For the experimental work the following equipment was used:

Test Loading Machines

The loading machine used for the bending test of beams and the compression test of Brazilian disk specimens was the INSTRON model 1331 (see Fig. 6.5). This INSTRON machine is hydraulically powered with a maximum capacity of 133.5 kN (30 kips) and by changing the load cell the load limit can be lowered to 8.9 kN (2 kips) or 22.25 kN (5 kips). The feedback control on the machine allows three different test types: load control, stroke control (displacement of the actuator), or strain control. The machine is operated by an attached computer. The axial force exerted by the test machine is measured by using a calibrated INSTRON load cell and the stroke is measured using an internal LVDT (Linear Variable Differential Transformer).

The axial loading machine used for the compression test of cylinders was the Baldwin model (see Fig. 6.6). This Baldwin machine is hydraulically driven with a maximum capacity of 890 kN (200 kips), and is controlled through a feedback-loop by a software program 'MTEST' installed in IBM PC. Feedback to the controller is provided by LVDT on the crosshead and a pressure sensor on the hydraulic loading system.

LVDT

Deformations of the specimens were measured using Linear Variable Differential Transformer (LVDT). The alternating current LVDT is a small (9.525 mm (3/8 in) diameter x 25.4 mm (1.0 in) long), light weight (5 oz.) device. The full range of traverse is +/-10 volts. The LVDT consists of a coil assembly and a core. The core, when displaced linearly along the axis and within the core of the coil assembly, produces a change in the output voltage. Output voltage level is proportional to the magnitude of the core displacement, while its polarity is related to the direction of the core displacement [Bakhoum et al., 1989].

Data Acquisition System

Data measured during the test included the applied force by loading machine, the displacement of the cross-head in loading machine, and the displacement measured by LVDT fixed at chosen positions on the test specimens. In using INSTRON machine a Fluke 2285B data acquisition system interface controlled by a software 'PROLOG' installed in an IBM personal computer was used to collect data during testing. The Fluke and IBM PC system are shown in Fig. 6.5. Twenty channels were available in the Fluke system to get data from measuring devices. The time interval was found to be dependent on the number of channels used in the Fluke system. In general, the time interval for one channel was about 1 second. In using Baldwin machine, an automatic data acquisition system installed in IBM PC was used to record signals from the machine. A software program 'MTEST' is capable of controlling the data acquisition system as well as the Baldwin machine. MTEST was developed by Advanced Machine Technology, Inc., Cambridge, MA.

Scanning Electron Microscope (SEM)

The scanning electron microscope (SEM) is a powerful tool for the microstructural and chemical characterization of cement and concrete. Imaging techniques such as secondary electron, backscattered electron, and X-ray imaging provide information about surface texture, microstructure, aggregates, and the air void system. Fig. 6.7 shows the SEM system used in the microstructural study. This SEM is Model STEREOSCAN 240 manufactured by Cambridge Instruments, Ltd., Cambridge, England.

6.5.2 Mechanical Testing of Mortars and Rocks

For the compression test of mortar cylinders, the Baldwin machine was used. Prior to testing, the cylinders were capped with hydrostone to ensure an even and smooth contact surface between the top or bottom of the cylinders and the platens in loading frame. The machine was stroke controlled at a loading rate of 0.254 mm/min (0.01 in/min). During testing, the applied load and the corresponding deformation were recorded using the data acquisition system installed in IBM PC. In order to measure the relative displacement between two fixed positions in the middle of cylinders, two LVDTs were mounted diametrically from each other on a metallic frame such that the gauge length was 57.15 mm (2.25 in). From measured loads and displacements the stress-strain curves for mortars in compression were obtained and then the compressive strength and the elastic modulus of mortars were determined.

To measure the compressive strength and the elastic modulus of granite and limestone, three cylinders (38.1 mm diameter x 76.2 mm height) for each type of aggregate were tested in compression. To ensure the results two cubics (25.4 mm x 25.4 mm x 25.4 mm) for each type of rock were also tested. During testing the loads and the displacements at increasing loading steps were recorded. From the results the compressive strengths and the elastic moduli of rocks were determined.

Standard methods are available for determining plane strain fracture toughnesses of metallic materials [ASTM, 1983]. However, many geomaterials are quasi-brittle and the nature of fracture process zones in concrete and rocks may be different from that of plastic zone in metals. Thus, the direct applications of such standards to these materials may not be appropriate. However, since standard has not yet been set for fracture toughness determination of geomaterials, the three-point bending test on pre-notched beam specimen was adopted to measure the plane strain fracture toughness, K_{IC}, of mortars and rocks. This method is based on linear elastic fracture mechanics (LEFM). Three pre-notched beam specimens for either each mortar or each rock were tested using the INSTRON machine. From the peak load mode I fracture toughness values K_{IC} were determined and then, critical energy release rates G_{IC} were calculated through an equation, $G_{IC} = K_{IC}^2(1-\nu^2)/E$.

6.5.3 Testing of Sandwiched Specimens

Bending Test of Sandwiched Beam Specimens

The specimen was placed in loading frame of the INSTRON machine. Four-point bending test was then performed on sandwiched beam specimens. This method has been widely used for measuring the fracture energy or the modulus of rupture of concrete. The Fluke data acquisition system was connected to the INSTRON to collect the applied load and the displacement of the cross head. The specimens were tested under a stroke controlled configuration with a loading rate of 0.0762 mm/min (0.003 in/min). The fracture toughness of mortar-aggregate interface was calculated from the peak load of the tested specimen.

Diametral Compression Test of Sandwiched Brazilian Disk Specimens

The sandwiched Brazilian disk specimen was placed between the top and bottom platens in the INSTRON machine, and then diametral compression test on the specimen was performed. This testing was similar to the tensile splitting test method for concrete except that

the specimen thickness is relatively thin. To achieve the mixed mode loading condition the inclination angle of the Brazilian disk specimen was adjusted ranging from 7^o ($\phi = 29^o$) to 25^o ($\phi = 83^o$) with the deviation of $\pm 0.5^o$. Although the specimen was designed to be subjected to the full range of loading, i.e, from pure tension to pure shear loading, the inclination angle was not in reality lowered below 7^o because the aggregate layer would be buckled in the low inclination angle. This limitation is schematically described in Fig. 6.8. The specimens were tested under a stroke controlled configuration with a loading rate of 0.0762 mm/min (0.003 in/min). During testing, the applied load and the load-line displacement signals from the INSTRON machine were recorded by the Fluke system. From the measured failure load and the inclination angle of the tested specimen, the interface fracture toughness and the corresponding phase angle were calculated.

6.6 Results and Discussion

6.6.1 Mechanical Properties of Tested Materials

Mechanical properties of the tested materials are listed in Table 6.2. The average 28-day compressive strengths of the selected mortars (M1, M2, and M3), were 42.5 MPa (6,100 psi), 58.5 MPa (8,700 psi), and 80.5 MPa (11,300 psi), respectively. Design strengths were achieved within 5.0% compared with measured values. The measured elastic moduli of the three mortars were 27.9 GPa, 33.8 GPa, and 39.2 GPa, respectively. The compressive strengths of granite and limestone were 140.1 MPa and 57.5 MPa, respectively. For all six mortar/aggregate combinations the mismatch parameters, α, β, and the oscillation index, ϵ, are given in Table 6.3. These parameters were defined in Eqns (4.1) and (4.5). It is seen from Table 6.3 that the values of β are relatively small compared with α for the mortar-aggregate combinations tested.

6.6.2 Fracture Toughness Curves of Mortar-aggregate Interfaces

The peak load at the onset of failure was converted to interfacial fracture toughness (or interface fracture energy) from Eqns. (5.17) and (5.33) and the corresponding phase angle was calculated from Eqns. (5.18) and (5.34). The fixed length $\hat{L}$, was selected to be 2.54 mm (0.1 in), which is the thickness of the aggregate layer, and thus, the term $\epsilon ln(\hat{L}/h)$ in Eqns. (5.18) and (5.34) did not affect the phase angle because $ln(\hat{L}/h) = ln1 = 0$. The phase shift angles ω, for six mortar/aggregate combinations, are given in Table 6.3. For M1/G system, the total phase shift is about 2.8°. Almost no phase shift is required for M2/L system. It is observed from Table 6.3 that as the absolute value of α decreases the phase angle shift becomes smaller.

Fracture toughness values for the six mortar-aggregate interfaces are listed in Tables 6.4 - 6.9 and plotted in Figs. 6.9, 6.10, and 6.11. From the figures showing interface fracture toughness versus loading phase angle curves it was observed that the interface fracture toughness markedly increases as the loading phase increases, i.e., the shear effect increases. For the M1/G interface the fracture energy for $\hat{\psi} = 0°$ is 1.3 J/m^2, while it is 7.0 J/m^2 for $\hat{\psi} = 45°$ and 18.0 J/m^2 for $\hat{\psi} = 70°$. This is attributed to the shielding effects at the interfaces with increased shear loading, implying that the full range of interfacial fracture toughness values from mode I to mode II should be involved in the cracking analysis at the interfacial regions. It was also observed that the fracture characteristics of M2/G or M3/G interfaces are very different from those of the interfaces in M1/G systems due to the effects of silica fume with the use of superplasticizer at low w/c ratio used for making high strength mortars (M2 and M3). A well known effect of silica fume with high specific surface area is to densify the paste matrix microstructure in the vicinity of the aggregate surface, thus improving bonding. Water reduction also changes the interfacial microstructure and improves the bonding.

The fracture toughness of the M3/G interface is much higher than that of the M1/G interface when the phase angle is small (less than 30°). As seen from Fig. 6.9 and Fig. 6.11, for the cases that nearly represent mode I condition, the M3/G interface fracture toughness is about twice that for the M1/G interface. However, for higher phase angles the difference between the interface fracture toughnesses of the two material systems is relatively small. This may be attributed to different specimen geometries and different failure modes observed in the tested specimens. Sandwiched beam specimens were used in mode I loading condition only ($\phi = 0°$) and sandwiched Brazilian disk specimens were used in mix mode loading condition ($30° < \phi < 80°$). Furthermore, M1/G systems failed by interface cracking but M2/G and M3/G systems exhibited a complicated failure mode combined with interface cracking, mortar cracking, and/or aggregate cracking. The fracture toughness curves of mortar-limestone interfaces (M1/L, M2/L, and M3/L) show similar trends as those for mortar-granite interfaces. However, when the shear loading effect increases ($\hat{\psi} > 40°$), the fracture energy values of both M2/L and M3/L are much smaller than those of M2/G and M3/G because of the different failure modes. The failure modes of the tested specimens will be discussed in the next section.

The fracture toughness of M1/G interface in mode I condition, K_{IC}^{i}, was about 35% of M1 and the fracture toughness of M3/G interface is 45% of M3. K_{IC}^{i} is the apparent fracture toughness given in Eqn. (5.11). Although these values are somewhat smaller than the values predicted from the equation $K_{IC}^{i} = 0.6K_{IC}^{m}$ proposed by Zaitsev [1983], they are similar to the test results seen by other investigators, as illustrated in Fig. 6.12. However, it should be noted that among different fracture test methods there is a large degree of variability, and it is not clear yet which one is preferable for carrying out the interface fracture toughness measurements. Figure 6.13 shows two interface fracture toughness curves drawn by using an equation given in Eqn. (4.23). These curves can be fit to the data trends for interfacial fracture toughness with the phase angle ranging from 30° to 45°. When cracks in

the matrix encounter aggregate inclusions the phase angle of the deflected crack is predicted to be within 30° to 45°, and hence, this loading range is selected for modeling. The values of two parameters, G_1^c and λ_2, used for the curve fitting, are given in Fig. 6.13. However, it is premature at this stage to rely on micromechanical models to predict phenomenological functional forms of toughness curves. For better modeling of the interface fracture toughness, extensive and comprehensive research is required.

6.6.3 Failure Modes of Tested Specimens

The observed failure mode of tested sandwich specimens was very brittle as illustrated in load versus load-line displacement curves for the three sandwiched Brazilian disk specimens (Fig. 6.14). The tested specimens exhibited the linear behavior in the ascending branch and little or no post peak behavior. This indicates that the crack propagated dynamically. Consequently, it is expected that the small scale yielding (or small size of the process zone) condition is satisfied. For the sandwich specimen with a mortar-aggregate interface the applicability of linear elastic fracture mechanics (LEFM) has not been theoretically established. However, considering the load-deformation curves, it can be assumed that the applicability of the LEFM to the fracture analysis of mortar-aggregate interfaces is not unrealistic.

Figure 6.15 schematically shows the two different types of failure modes observed in the sandwich specimens, namely, interface cracking (Failure Mode 1) and combined mode cracking (Failure Mode 2). All sandwiched beam specimens failed by the interface cracking as shown in Fig. 6.16. However, the failure types of the sandwiched Brazilian disk specimens were not simple, as shown in Fig. 6.17 and Fig. 6.18. For lower phase angle, interface cracking was a major failure mode for all mortar/granite systems (M1/G, M2/G, and M3/G). In this loading range most specimens failed in FT1-b, although some specimens showed FT1-c or FT1-d. In FT1-c, after interface cracking started at tip A, the crack

ran along the interfaces for a short distance, and then kinked into the other interface at tip B. When the loading phase is small, the failure mode of mortar/limestone systems (M1/L, M2/L, and M3/L) was similar to that of mortar/granite systems.

However, for high phase angle values (i.e., shear loading effect increases), M2/G and M3/G systems exhibited a mixed failure mode with initial mortar cracking, while M1/G system fails by interface cracking only when $\hat{\psi}$ is less than 70°. In some of the M2/G or M3/G systems aggregate layer cracking in the bonding direction occurred, implying the interfaces were very strong. This is attributed to the silica fume effects with low w/c ratio, resulting in strong bonding between mortar matrices (M2 and M3) and granite inclusions. In this loading range the failure mode of mortar/limestone systems is somewhat different from that of mortar/granite systems. As shear loading effect increases, M2/L and M3/L systems exhibited limestone cracking initially and subsquently mortar cracking and interface cracking occurred. Thus, the difference of initial cracking between high strength mortar/granite (M2/G and M3/G) and high strength mortar/limestone systems (M2/L and M3/L) results in a lower values of the measured fracture toughness of mortar-limestone interfaces because limestone is weaker than M2 or M3.

When crack propagation is confined to the interface, the fracture toughness of the interface can be obtained as a function of the loading phase angle. If the crack moves out of the interface, the measured energy refers to the weaker material, i.e. either to the mortar or to the aggregate. This observation of crack kinking out of interface can be explained using a criterion given in Eqn. (4.28). When $\hat{\psi}$ = 70°, M3/G system exhibited the crack kinking. This case will be discussed as an example. The fracture energy of M3 is 16.7 J/m^2 and from Fig. 4.6 the G/G^t_{max} ratio is 0.5. Thus, to satisfy the crack kinking condition given in Eqn. (4.28) the interface fracture toughness $\Gamma_i(70^o)$ should be larger than 16.7 J/m^2 x 0.5 = 8.35 J/m^2. This is reasonable because toughness value obtained from sandwiched Brazilian disk specimen testing was approximately 18.0 J/m^2. It should also be noted that this measured

interface fracture toughness value for high phase angle is actually an underestimation.

6.6.4 Microstructure of Failed Specimens

After the testing of sandwich specimens, the microstructure of failure surface was investigated using scanning electron microscope (SEM). Secondary electron (SE) imaging and backscattered electron (BE) imaging were included in the SEM technique. Secondary electrons are low-energy electrons produced as a result of an inelastic collision of a primary beam electron with an electron of an atom within the specimen. SE imaging is useful for examining surface texture and crystal morpology. In BE imaging, image contrast is generated by compositions of different phases relative to their average atomic number. Anhydrous cement appears brightest followed by calcium hydroxide, calcium silicate hydrate, and aggregate; voids appear dark. The best use of BE imaging is examination of flat, polished surfaces. Figure 6.19 shows the SEM pictures using SE and BE imaging. Clearly, BE imaging technique provided a better resolution. This imaging technique can be used for the measurement of the roughness of the aggregate layers as well as the interfacial microstructures.

6.7 Problems in the Measurement of Interfacial Fracture Toughness

In general, measured interfacial fracture toughness values may depend on factors such as specimen size, specimen geometry, test method, loading rate, the moisture content of the specimen, the test temperature, and so on. These problems are common to all concrete testing and hence, need to be studied further for interface fracture toughness measurements. Figure 6.20 shows the interface fracture toughness values versus specimen thickness. It is observed from Fig. 6.20 that when the thickness ratio, t/R, is 0.33, the interface fracture toughness values are much higher than those with $t/R = 0.67$ or 1.0. This may show the

specimen size dependence of interface fracture toughness or the plane strain condition was not satisfied in $t/R = 0.33$. Therefore, unless standard test methods for measuring interfacial fracture toughness can be developed, it will not be possible to compare the values measured in different laboratories by different methods. Sandwiched specimens developed would be candidates for standard interface fracture toughness specimens. For this, more experimental work should be performed to investigate the effects of the specimen size, the loading rate effects, and so on. Ziegeldorf [1983] and Mindess [1992] discussed the problems in specimen preparation for the measurement of interfacial properties. These problems were observed in the present experimental work. In what follows, some difficulties occurred in specimen preparation and testing will be described.

1. Roughness of the aggregate surface

   The bond between mortar matrix and rock must depend on some combination of chemical bonding, physical bonding due to van der Waals' forces, and mechanical interlock, with the relative importance of these three mechanisms varying with different rock types and cement compositions, as illustrated in Fig. 3.5. Clearly, the amount of mechanical interlock will depend on the roughness of the aggregate surface. In the present experimental work, the aggregate surface was consistently prepared as to have the same roughness. To study the effects of the roughness of rock surface limited tests were performed using M1/L Brazilian disk specimens. As shown in Fig. 6.21, the interface fracture toughness values with polished rock surface is much lower than those with regular surface. Thus, it is observed that the roughness of rock surface is an important factor. Several investigators have treated rock surface in different ways: polishing the rock surface [Odler and Zurz, 1988], grinding the surfaces with particular size of grit [Struble and Mindess, 1983], and preparing the rather rough surface of rock [Alexander et al., 1992]. There is no "right" or "wrong" method of

surface preparation, but obviously these different surface finishing will provide quite different mechanical interfacial properties. Therefore, one should report the degree of the roughness of rock surface and the surface preparation procedure with the test results of interfacial fracture properties.

2. Bleeding

Another problem in preparing specimens for interfacial fracture toughness testing is that of bleeding. Bleeding arises because, under the force of gravity, the solid aggregate particles is suspended in fresh concrete tend to settle. For specimens prepared for interfacial studies, it is very difficult to avoid the development of a water-rich layer right at the rock face, though this problem can at least be minimized if the specimens are rotated in a vertical plane slowly but continuously until setting has taken place. In preparing the specimens, excessive use of vibrator for placing mortar mixtures might result in more bleeding.

3. Shrinkage

It is well known that hydrating cement paste specimens expand when stored in water but shrink when stored in a sealed condition. The shrinkage is even more pronounced when the specimen is not sealed so that loss of humidity occurs. In any case there will be relative volume change of the cement paste part relative to the aggregate part of an interface specimen leading to residual stresses and eventually to cracks. In sandwich test specimens the aggregate layer embedded in mortar matrix is thin and thus the shrinkage may be reduced. It was observed in the present experiment that the shrinkage effect is more significant in beam specimens subjected to mode I loading than Brazilian disk specimen because the interfacial fracture toughness in tension is very small.

4. Interfaces in test specimens versus interfaces in real concrete

There appears to be some difference between the interfaces occurring in real concrete and those which result from the casting of cement paste or mortar against a rock layer. Consequently, it is extremely difficult to simulate in the laboratory the interface in commercially produced concrete. Therefore, when we prepare test specimens for interfacial studies, we will always have to consider the fact that the results are essentially dependent on the details of specimen preparation and handling.

Table 6.1 Mix proportions for the mortar mixes (by weight)

	W/(C+SF)	Sand/C	SF/C (%)	HRWR/C (%)	Slump (mm)
Mortar 1	0.50	2.0	0.0	0.0	>230.0
Mortar 2	0.35	2.0	5.0	1.0	>200.0
Mortar 3	0.28	2.0	10.0	2.0	>200.0

W : water, C : cement, SF : silica fume, and HRWR : high range water reducer

Table 6.2 Mechanical properties for the mortars and the aggregates

	σ_c (MPa)	E (GPa)	G_{IC} (J/m^2)	ν^*
Mortar 1 (M1)	42.5	27.8	10.3	0.22
Mortar 2 (M2)	58.5	33.8	14.8	0.22
Mortar 3 (M3)	80.5	39.2	16.7	0.20
Granite (G)	140.1	55.3	17.5	0.16
Limestone (L)	57.5	34.5	11.8	0.18

* assumed values

Table 6.3 Dundurs' parameters, α and β, oscillation index, ε, and phase shift, ω, for six mortar/aggregate combinations

Combination (#1/#2)	α	β	ε	ω (°)*
Mortar1/Granite	-0.320	-0.099	0.032	2.8
Mortar2/Granite	-0.230	-0.065	0.021	2.0
Mortar3/Granite	-0.163	-0.049	0.015	1.5
Mortar1/Limestone	-0.099	-0.022	0.007	0.5
Mortar2/Limestone	-0.002	0.015	-0.005	-0.1
Mortar3/Limestone	0.068	0.033	-0.011	-1.0

* from Table 5.1

Table 6.4 Fracture toughness values for mortar1-granite (M1/G) interface

Beam Specimen	Apparent Fracture Toughness K_{IC} (MPa*m$^{1/2}$)	$\hat{\psi}$ (degree)	Γ_i (J/m^2)	Failure Mode[1]
M1/G-B1	0.18	2.8	1.11	I
2	0.20	2.8	1.37	I
3	0.21	2.8	1.51	I

[1] I : interface cracking and C : combined mode cracking

Brazilian Disk	θ (degree)	P (kN)	$\hat{\psi}$ (degree)	Γ_i (J/m^2)	Failure Mode
M1/G-D1	7.0	4.70	31.5	3.41	I
2	7.0	5.18	31.5	4.14	I
3	8.0	5.80	35.4	5.38	I
4	9.0	5.60	39.1	5.20	I
5	10.0	4.93	42.8	4.18	I
6	10.0	5.62	42.8	5.44	I
7	10.0	6.03	42.8	6.27	I
8	10.0	6.24	42.8	6.71	I
9	14.0	6.55	56.8	8.76	I
10	15.0	6.82	59.4	9.94	I
11	15.0	7.49	59.4	12.0	I
12	16.0	7.21	62.4	11.64	I
13	20.0	8.94	73.7	21.48	C
14	20.0	9.22	73.7	22.87	C
15	20.0	9.81	73.7	25.90	C
16	20.0	9.85	73.7	26.09	C
17	23.0	8.99	81.0	24.86	C
18	25.0	9.44	85.8	29.87	C
19	25.0	10.43	85.8	36.47	C

Table 6.5 Fracture toughness values for mortar1-limestone (M1/L) interface

Beam Specimen	Apparent Fracture Toughness K_{IC} (MPa*m$^{1/2}$)	$\hat{\Psi}$ (degree)	Γ_i (J/m^2)	Failure Mode
M1/L-B1	0.16	0.5	0.88	I
2	0.18	0.5	1.11	I

Brazilian Disk	θ (degree)	P (kN)	$\hat{\Psi}$ (degree)	Γ_i (J/m^2)	Failure Mode
M1/L-D1	7.0	4.52	29.3	3.16	I
2	10.0	4.98	40.6	4.28	I
3	10.0	5.78	40.6	5.75	I
4	10.0	6.01	40.6	6.22	I
5	15.0	6.42	57.2	8.82	I
6	15.0	7.20	57.2	11.10	I
7	15.0	7.46	57.2	11.90	I
8	20.0	8.44	71.5	19.15	C
9	20.0	8.80	71.5	20.85	C
10	20.0	8.94	71.5	21.51	C
11	25.0	9.25	83.8	28.70	C
12	25.0	9.67	83.8	31.30	C

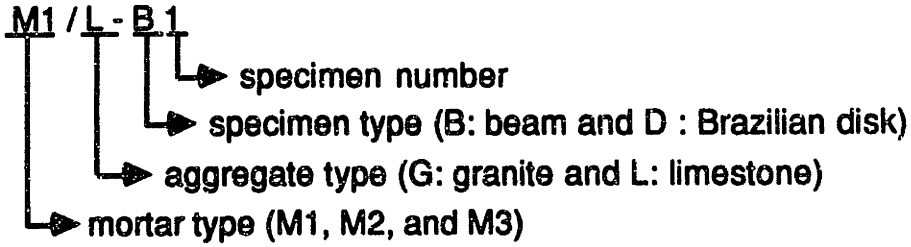

Table 6.6 Fracture toughness values for mortar2-granite (M2/G) interface

Beam Specimen	Apparent Fracture Toughness K_{IC} ($MPa*m^{1/2}$)	$\hat{\psi}$ (degree)	Γ_i (J/m^2)	Failure Mode
M2/G-B1	0.26	2.0	1.89	I
2	0.29	2.0	2.35	I

Specimen	θ (degree)	P (kN)	$\hat{\psi}$ (degree)	Γ_i (J/m^2)	Failure Mode
M2/G-D1	7.0	5.85	30.9	4.44	I
2	10.0	6.65	42.1	6.39	C
3	10.0	7.77	42.1	8.71	C
4	10.0	8.25	42.1	9.83	C
5	15.0	7.81	58.8	10.94	C
6	15.0	8.14	58.8	11.88	C
7	20.0	8.56	73.0	16.54	C
8	20.0	10.00	73.0	22.58	C
9	25.0	9.59	85.3	25.86	C
10	25.0	10.35	85.3	30.10	C

Table 6.7 Fracture toughness values for mortar2-limestone (M2/L) interface

Beam Specimen	Apparent Fracture Toughness K_{IC} (MPa*m$^{1/2}$)	$\hat{\psi}$ (degree)	Γ_i (J/m^2)	Failure Mode
M2/L-B1	0.25	-0.1	1.75	I
2	0.27	-0.1	2.04	I

Brazilian Disk	θ (degree)	P (kN)	$\hat{\psi}$ (degree)	Γ_i (J/m^2)	Failure Mode
M2/L-D1	7.0	5.88	28.8	4.48	I
2	10.0	6.41	40.0	5.93	C
3	10.0	7.07	40.0	7.22	C
4	15.0	7.13	56.7	9.12	C
5	20.0	8.17	70.9	15.07	C
6	20.0	8.76	70.9	17.31	C
7	25.0	8.92	83.2	22.35	C

Table 6.8 Fracture toughness values for mortar3-granite (M3/G) interface

Beam Specimen	Apparent Fracture Toughness K_{IC} (MPa*$m^{1/2}$)	$\hat{\psi}$ (degree)	Γ_i (J/m^2)	Failure Mode
M3/G-B1	0.36	1.5	3.17	I
2	0.37	1.5	3.35	I

Brazilian Disk	θ (degree)	P (kN)	$\hat{\psi}$ (degree)	Γ_i (J/m^2)	Failure Mode
M3/G-D1	7.0	6.42	30.4	4.49	I
2	7.0	6.30	30.4	4.32	C
3	10.0	7.53	41.6	6.88	C
4	10.0	8.22	41.6	8.21	C
5	10.0	8.66	41.6	9.11	C
6	15.0	8.64	58.3	11.26	C
7	15.0	9.24	58.3	12.87	C
8	20.0	9.73	72.5	17.96	C
9	20.0	10.30	72.5	20.11	C
10	20.0	11.13	72.5	23.50	C
11	25.0	11.76	84.8	32.65	C

Table 6.9 Fracture toughness values for mortar3-limestone (M3/L) interface

Beam Specimen	Apparent Fracture Toughness K_{IC} (MPa*m$^{1/2}$)	$\hat{\Psi}$ (degree)	Γ_i (J/m^2)	Failure Mode
M3/L-B1	0.32	-1.0	2.50	I
2	0.34	-1.0	2.83	I

Brazilian Disk	θ (degree)	P (kN)	$\hat{\Psi}$ (degree)	Γ_i (J/m^2)	Failure Mode
M3/L-D1	7.0	6.19	27.9	4.17	I
2	10.0	6.84	39.1	5.68	C
3	10.0	7.23	39.1	6.34	C
4	15.0	7.30	55.8	8.03	C
5	15.0	7.91	55.8	9.43	C
6	20.0	8.41	70.0	13.42	C
7	20.0	8.54	70.0	13.83	C
8	25.0	9.31	82.3	20.46	C

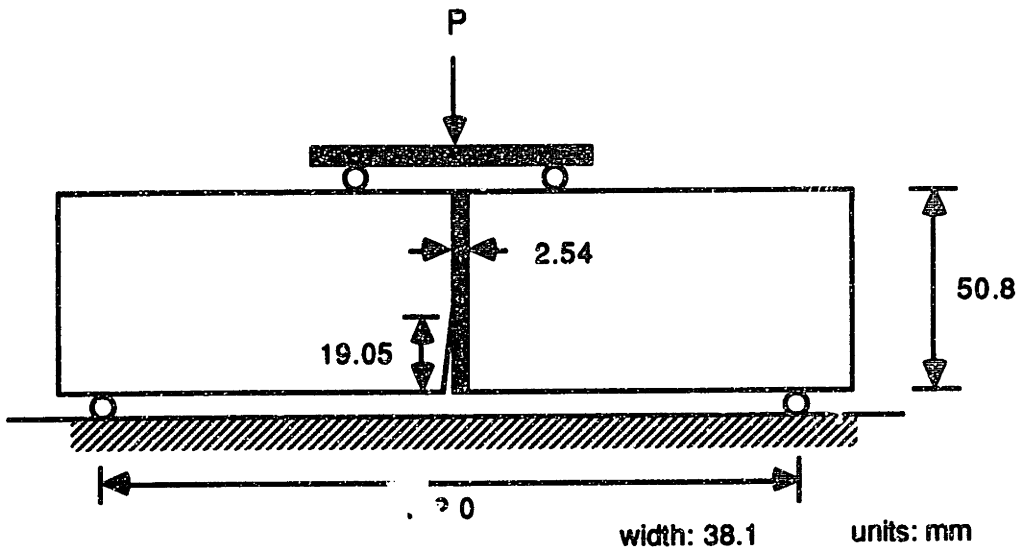

Figure 6.1 Geometry of sandwiched beam specimen

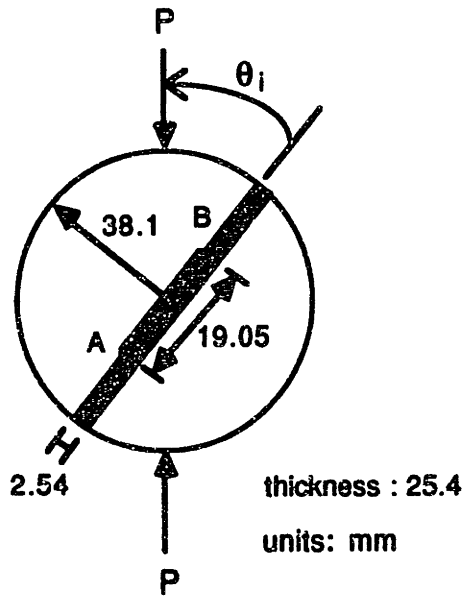

Figure 6.2 Geometry of sandwiched Brazilian disk specimen

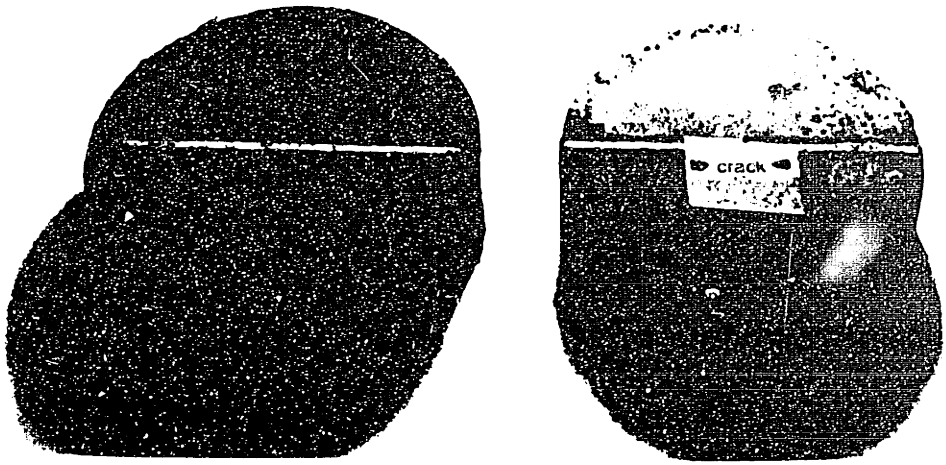

Figure 6.3 Mold used for manufacturing Brazilian disk specimens

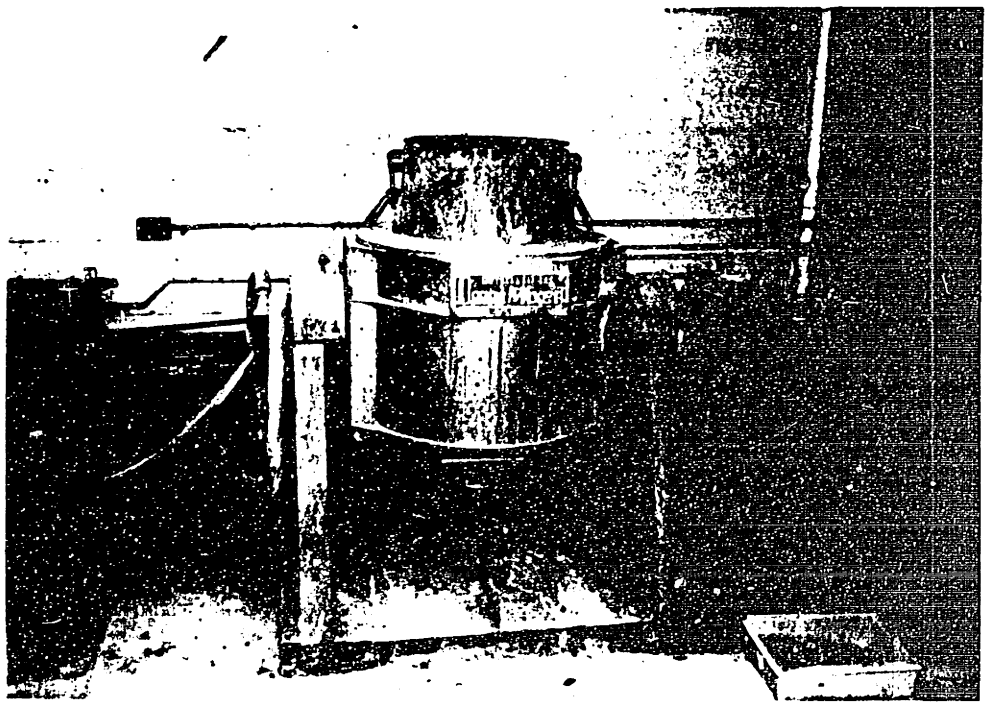

Figure 6.4 Omni mixer

(a)

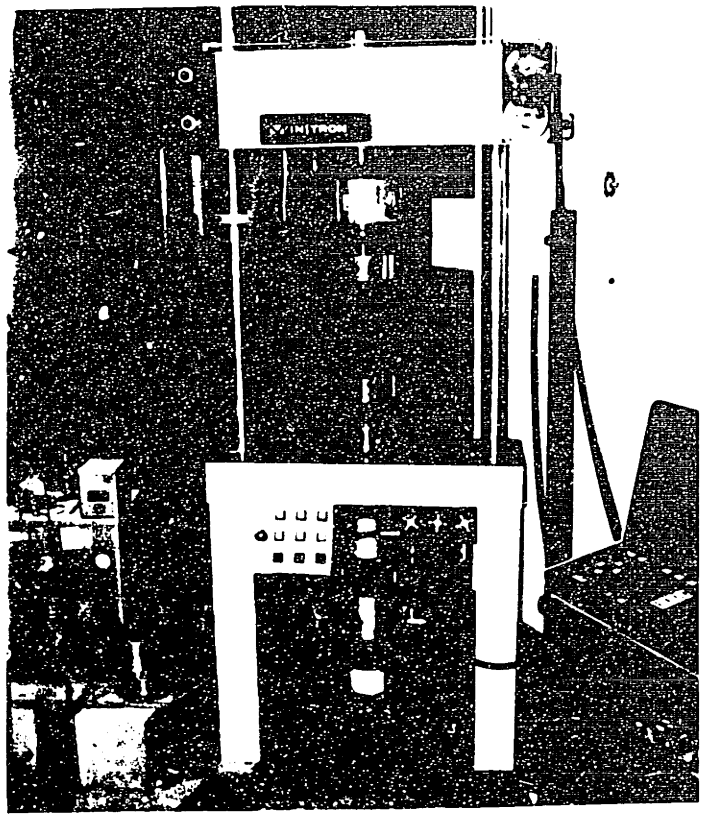

(b)

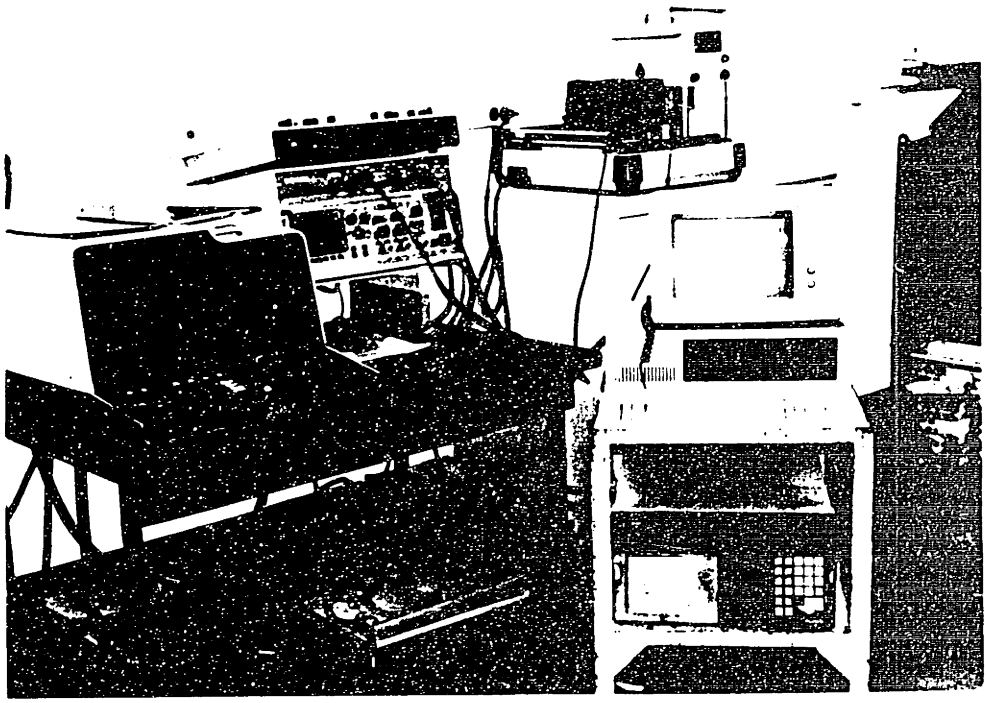

Figure 6.5 INSTRON machine system: (a) INSTRON Loading frame; and (b) Control panel, IBM PC, and Fluke data acquisition system

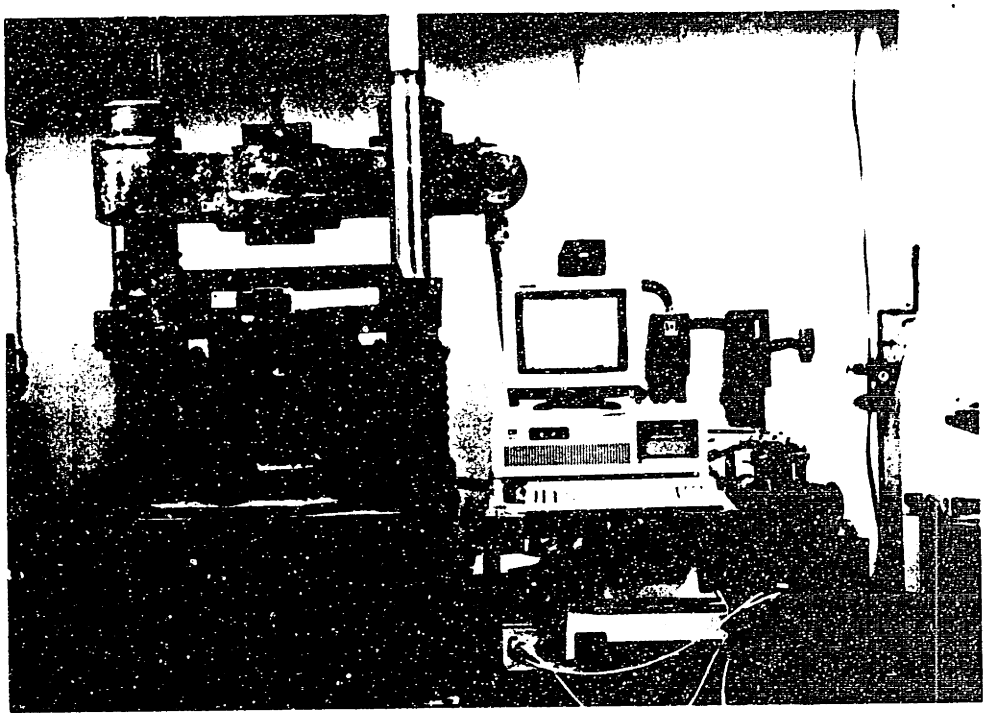

Figure 6.6 Baldwin machine and IBM PC

(a)

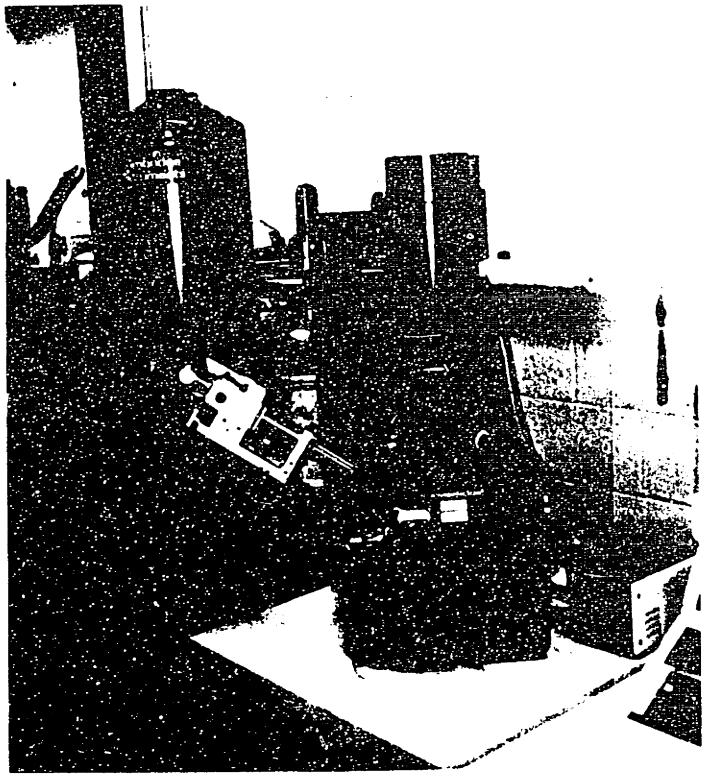

(b)

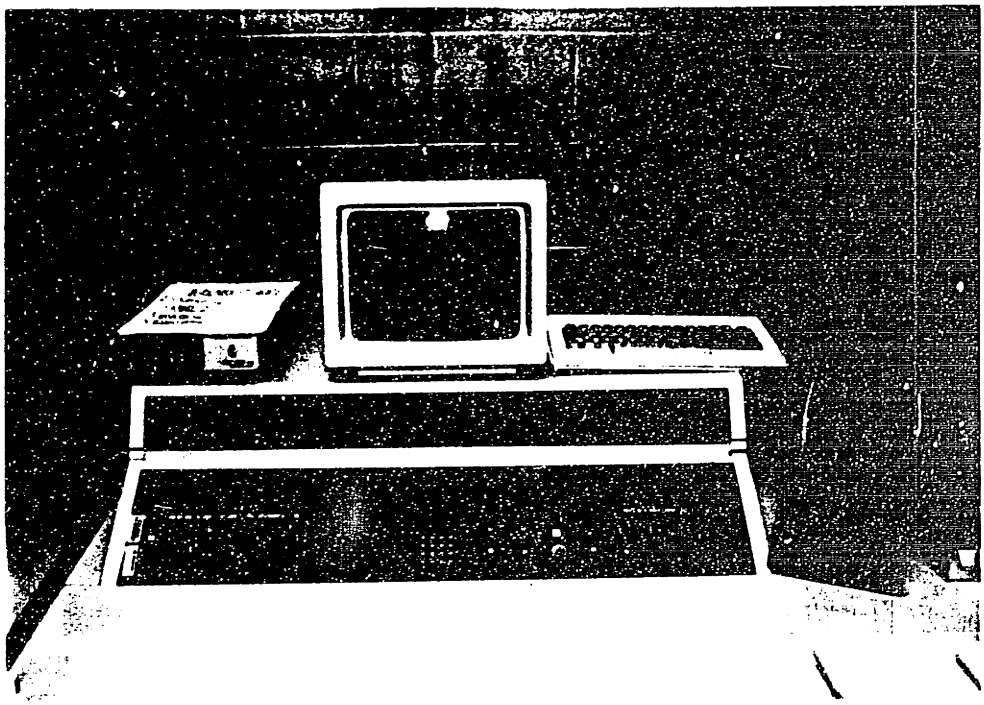

Figure 6.7 Scanning electron microscope (SEM): (a) Chamber; and (b) Control panel

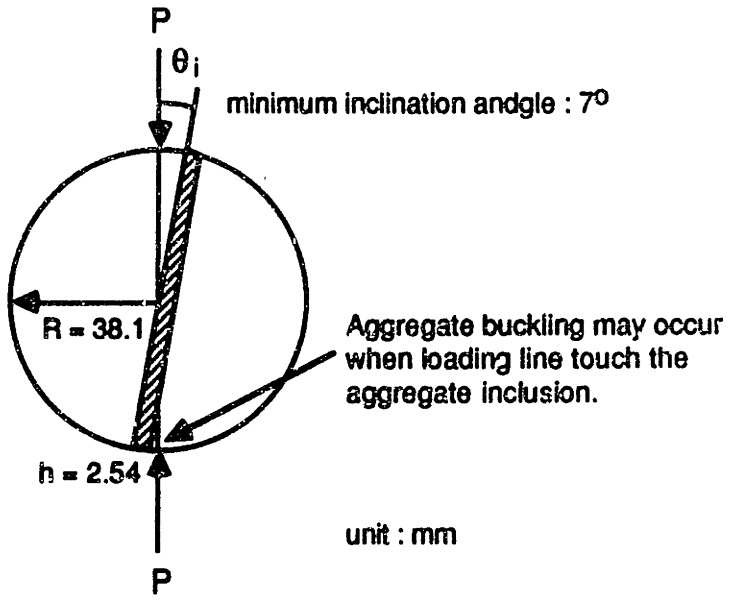

Figure 6.8 Limitation of inclination angle in Brazilian disk specimen

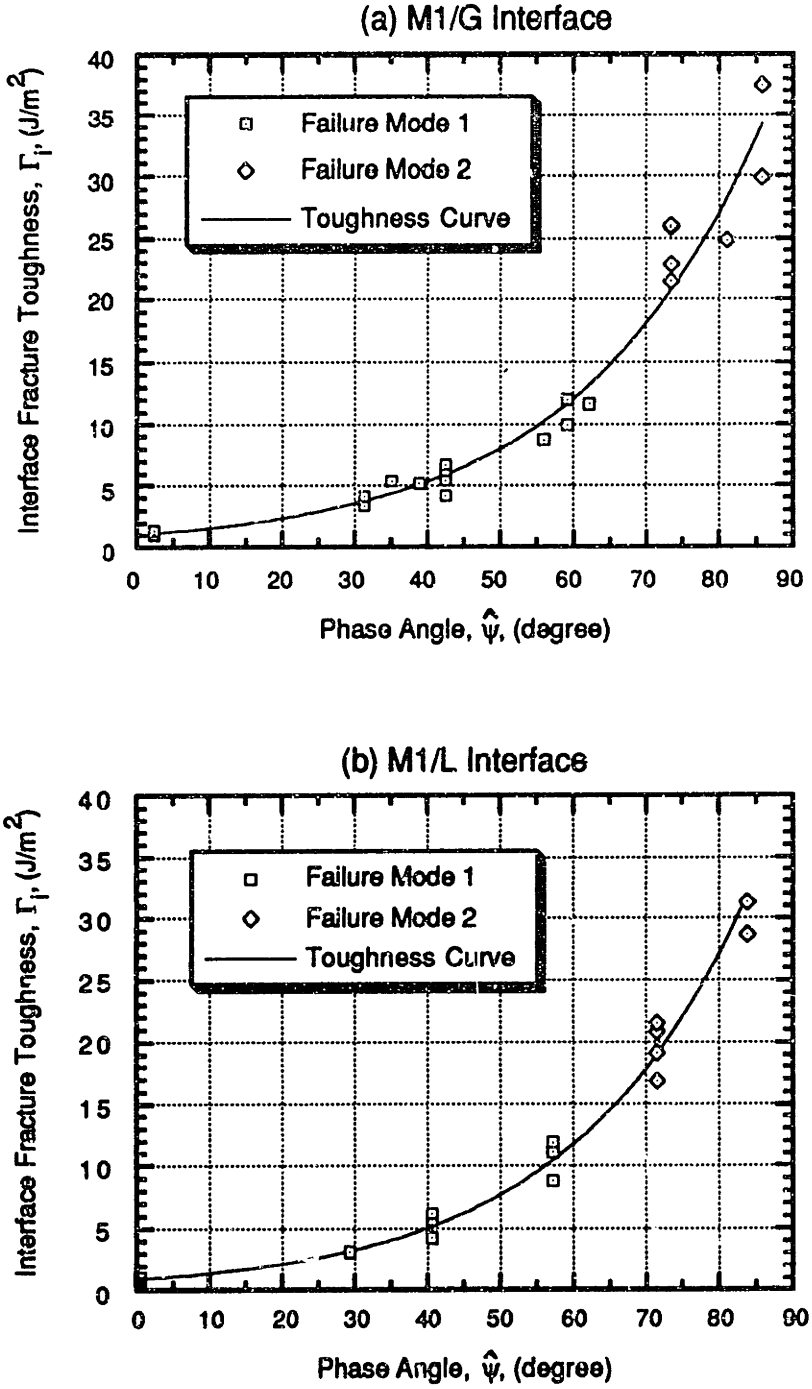

Figure 6.9 Interface toughness curves: (a) M1/G interface; and (b) M1/L interface

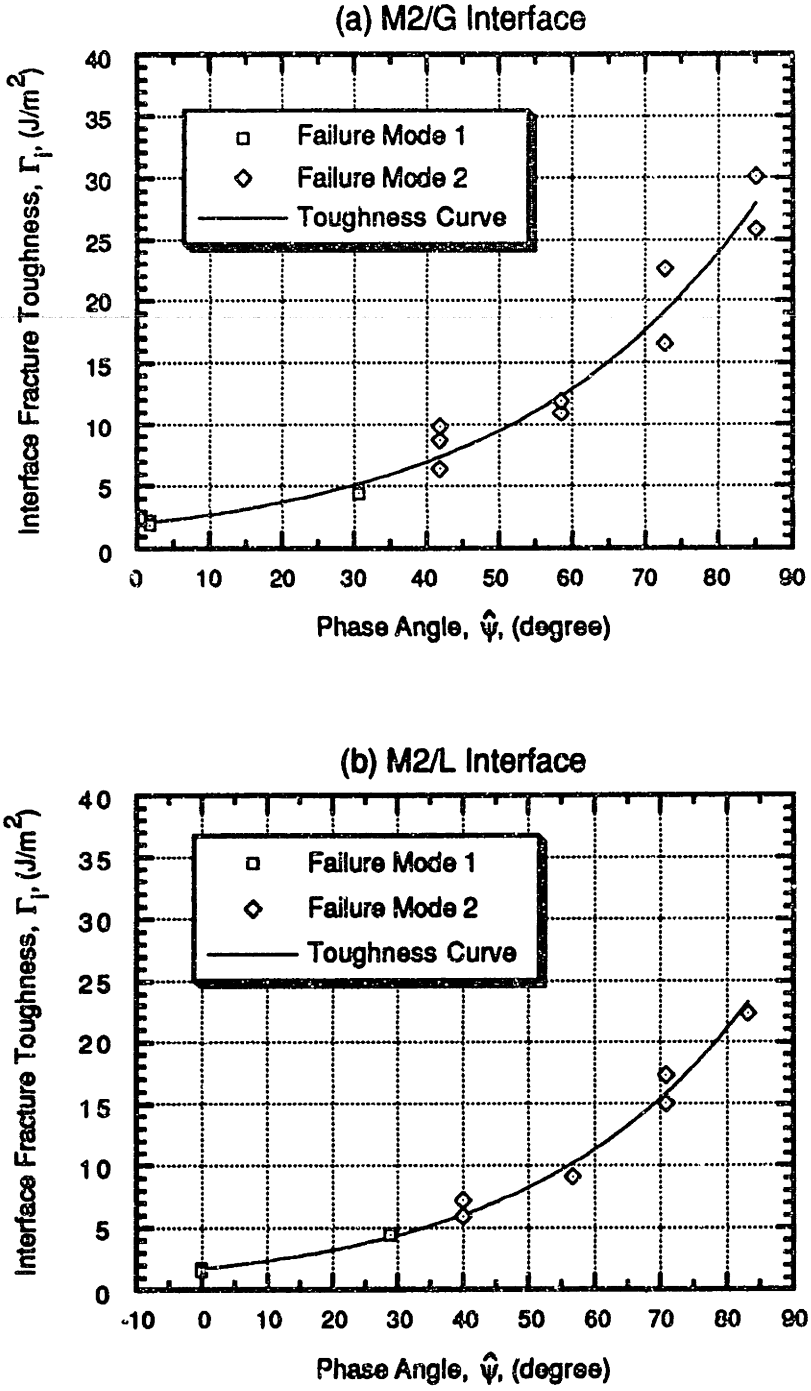

Figure 6.10 Interface toughness curves: (a) M2/G interface; and (b) M2/L interface

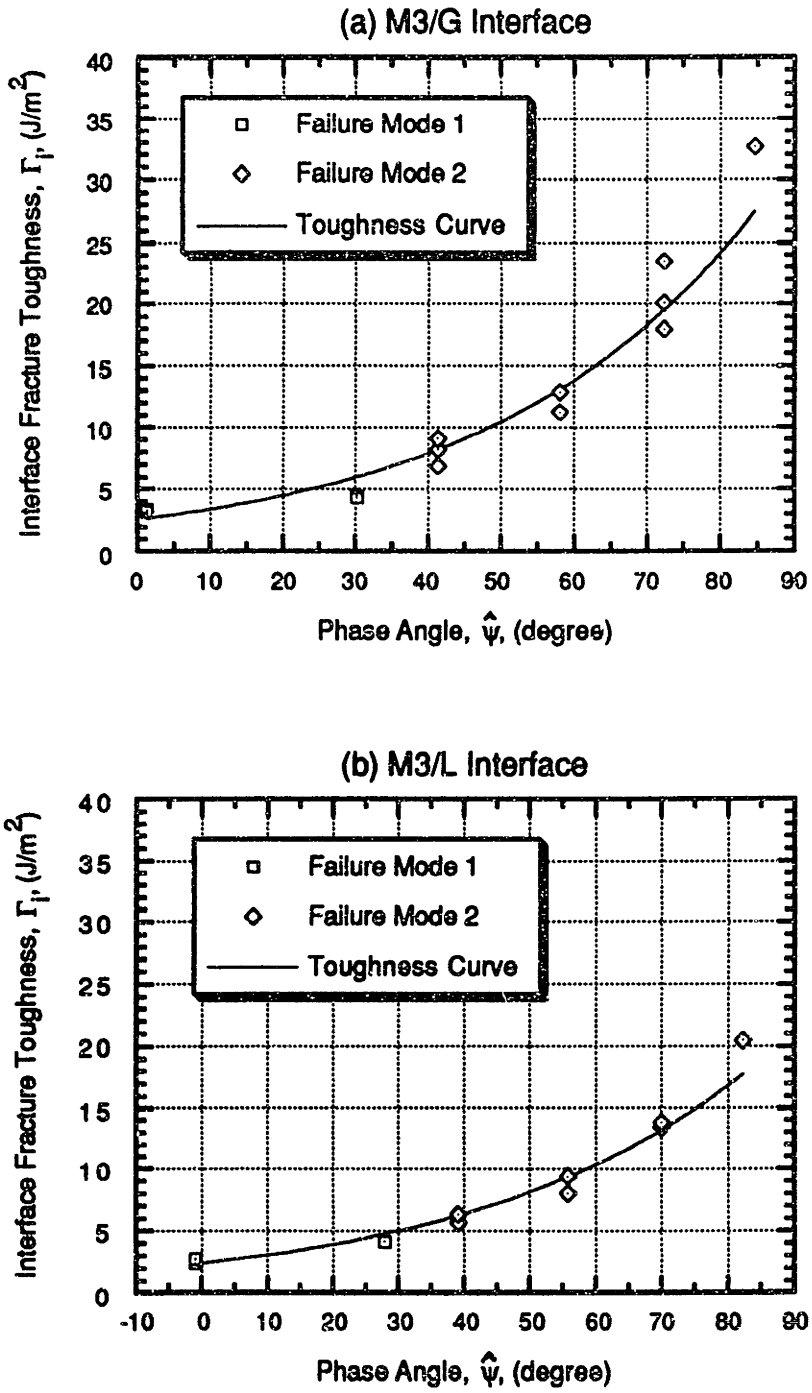

Figure 6.11 Interface toughness curves: (a) M3/G interface; and (b) M3/L interface

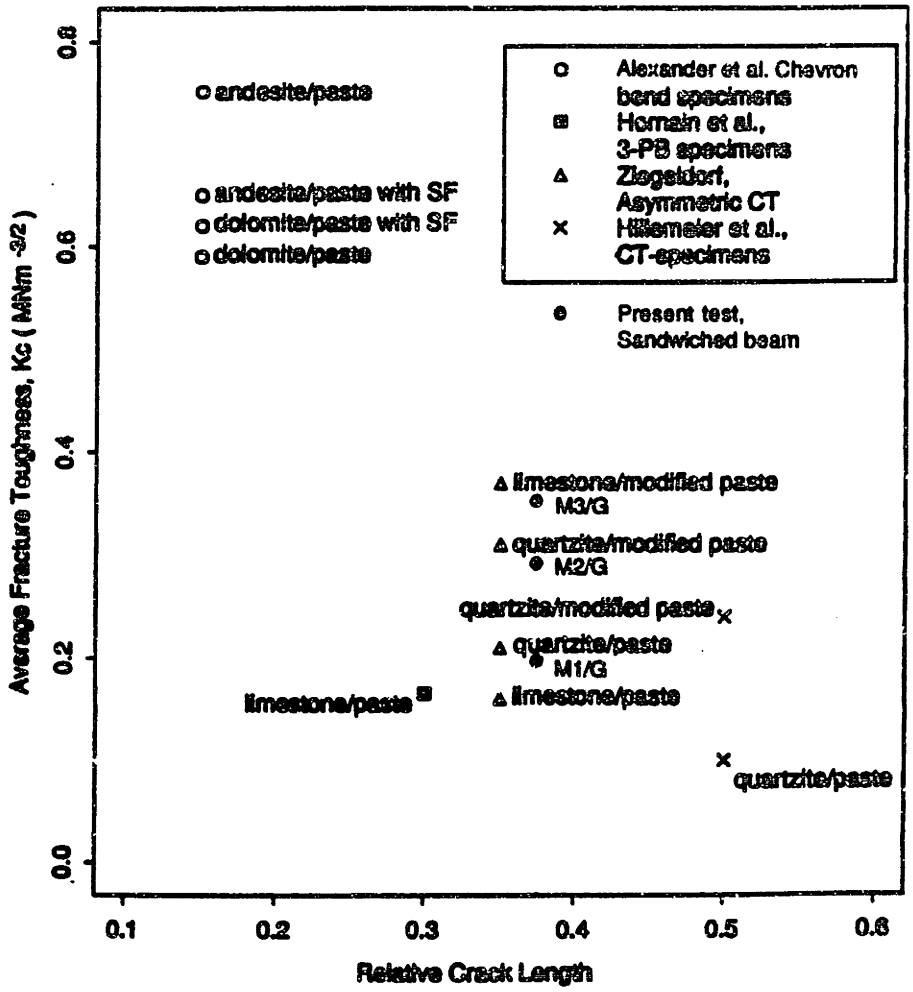

Figure 6.12 Comparison with interface fracture toughness values in mode I loading by different investigators (from Alexander et al. [1992])

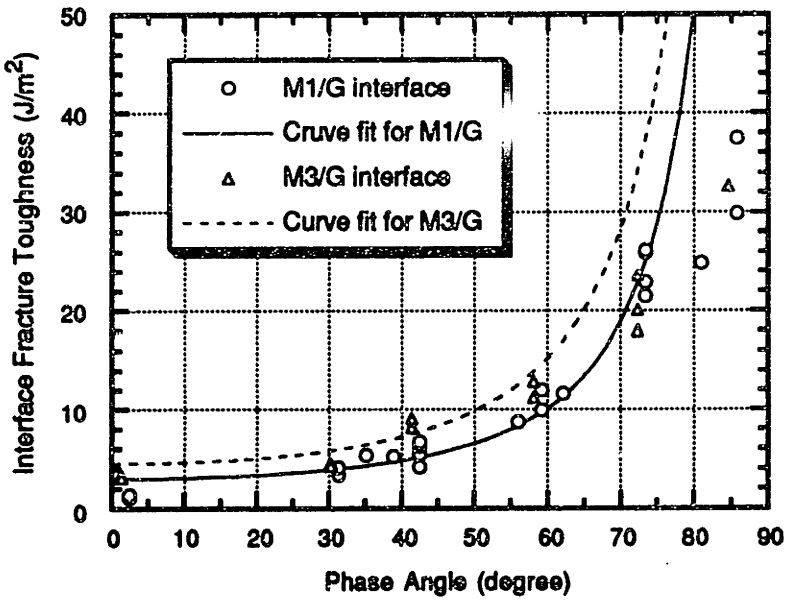

$G_1^c = 3.0$ J/m^2 and $\lambda_2 = 0.05$ for M1/G interface

$G_1^c = 4.5$ J/m^2 and $\lambda_2 = 0.05$ for M3/G interface

Figure 6.13 Comparison of interface fracture toughness curves

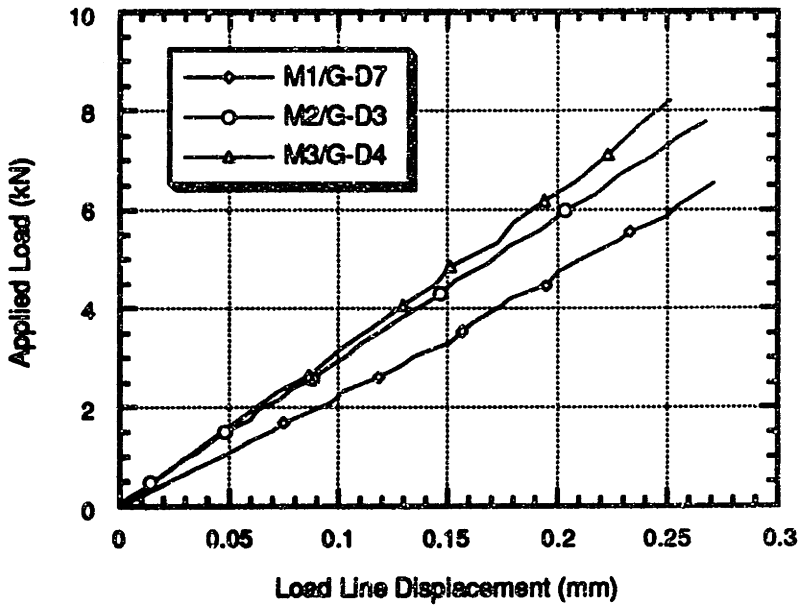

Figure 6.14 Typical load versus load-line displacement curves for sandwiched Brazilian disk specimens

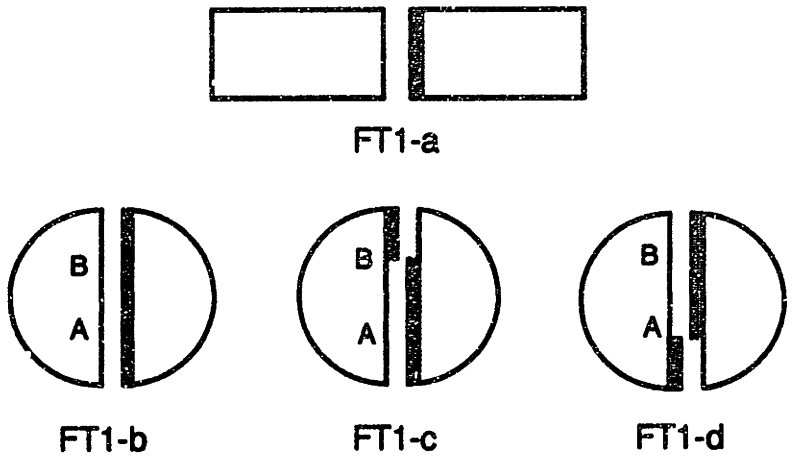

(a) Failure type 1 - interface cracking

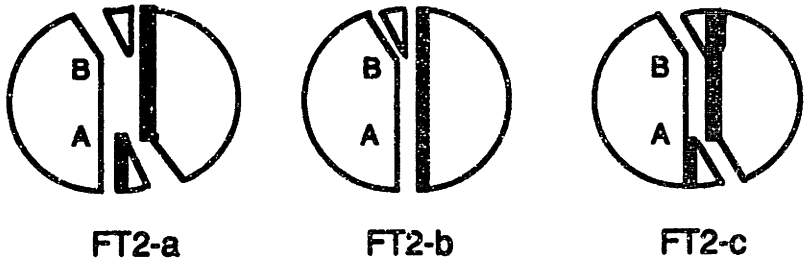

(b) Failure type 2 - combined mode cracking

Figure 6.15 Failure modes of tested sandwich specimens

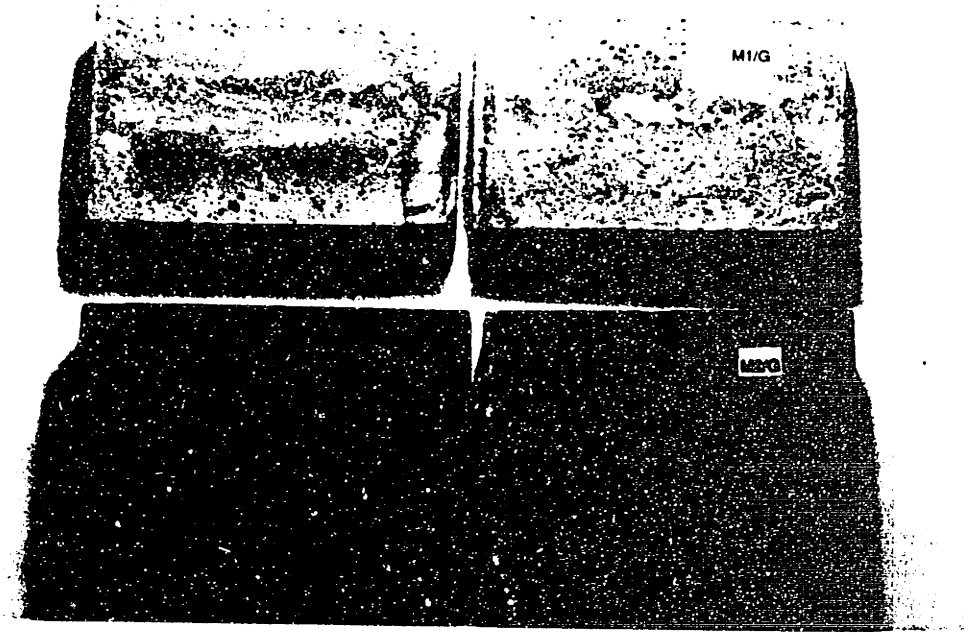

Figure 6.16 Failed beam specimens with M1/G and M2/G interfaces

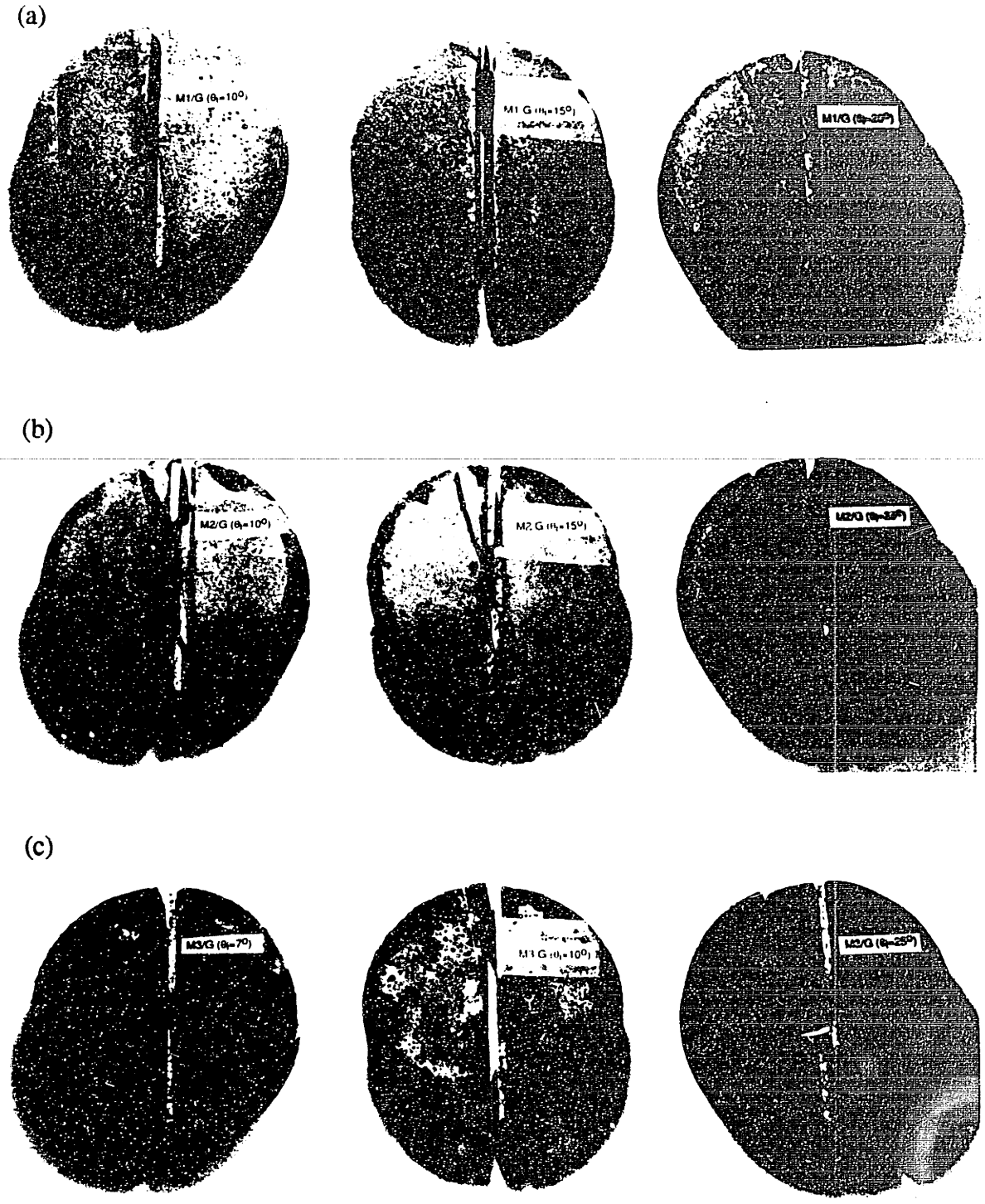

Figure 6.17 Failed Brazilian disk specimens with mortar-granite interfaces: (a) M1/G; (b) M2/G; and (c) M3/G

(a)

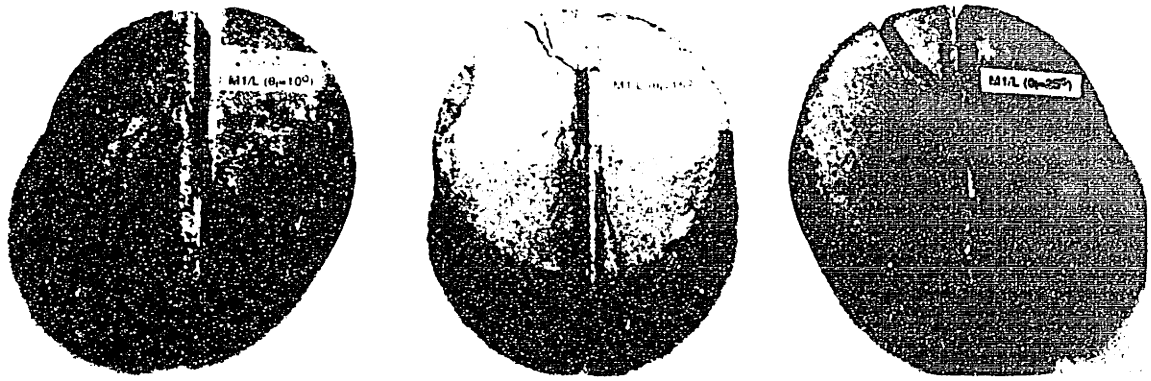

(b)

(c)

Figure 6.18 Failed Brazilian disk specimens with mortar-limestone interfaces: (a) M1/L; (b) M2/L; and (c) M3/L

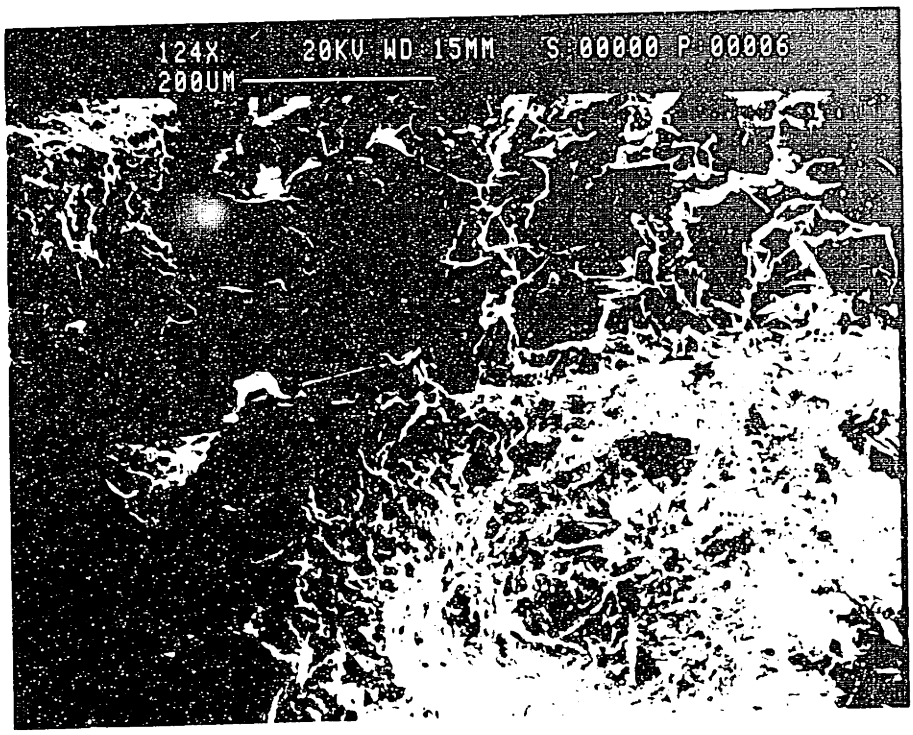

(a) SE imaging

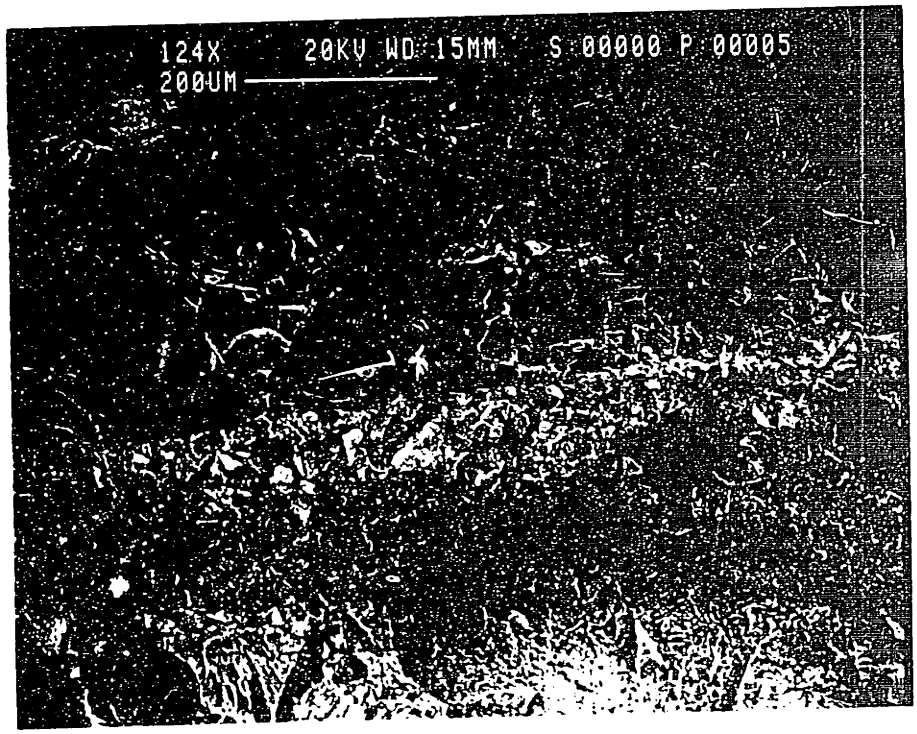

(b) BE imaging

Figure 6.19 Comparison of SEM pictures

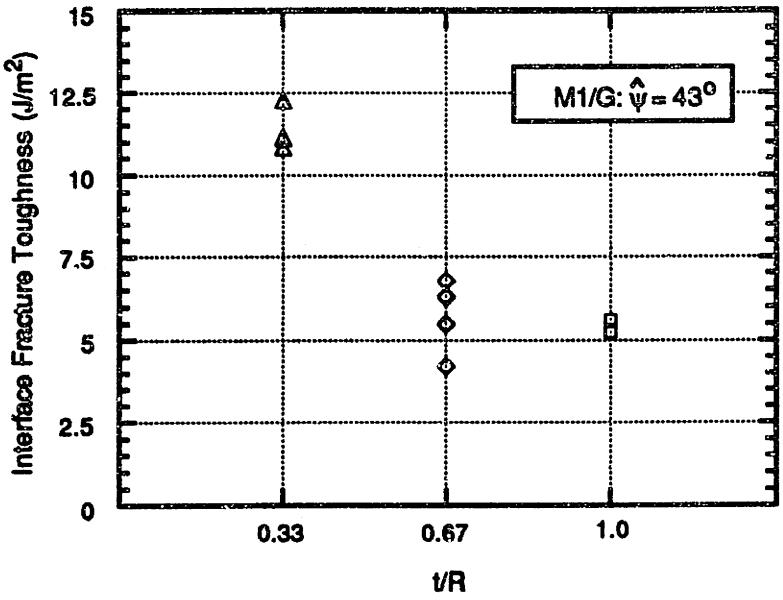

Figure 6.20 Interface fracture toughness values versus specimen thickness

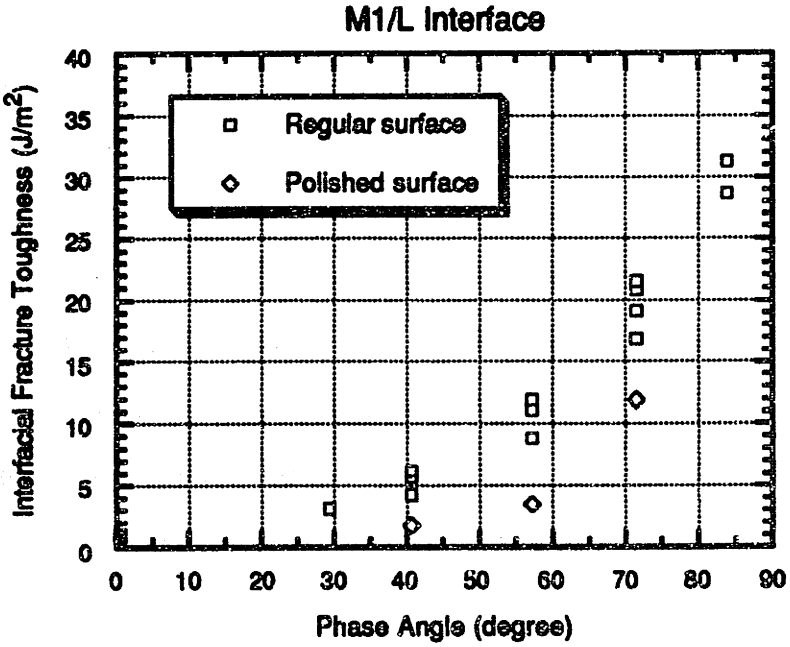

Figure 6.21 Interface fracture toughness with different roughnesses

Chapter 7

Numerical Evaluation of Interface Fracture Parameters: G and ψ

Analysis of crack growth at the interface is pertinent not only to composite materials but also to structures with adhesive joints, thin films and coatings. Criteria are needed for the crack growth at the interfaces. Interface fracture occurs when the interfacial energy release rate G reaches the interfacial fracture energy Γ_i. The fracture energy, Γ_i, is a property that characterizes the fracture resistance of interfaces and the loading phase angle, ψ, which is a measure of the contribution of shear to opening experienced by the interface crack surface. Therefore, for the analysis of interface fracture both the energy release rate and the loading phase angle must be evaluated. Analytical solutions for interface cracking problems in semi-infinite body or simplified geometries exist but for complex geometries numerical methods must be employed. In this chapter, a fracture mechanics based numerical method will be discussed for obtaining the two parameters at the interfaces of the bimaterial systems. Numerical calculations are performed on two application problems using the ADINA finite element program. The numerical results are then compared with the analytical solutions.

7.1 Numerical Evaluation of Energy Release Rate along the Interface

7.1.1 Virtual Crack Extension Method

For the linear elastic material behavior the energy release rate G can be determined through the *J-Integral* which is defined as the potential energy, Π, change per unit crack advance.

$$G = J_{el} = -\frac{\partial \Pi}{\partial a} \tag{7.1}$$

In finite element analysis J is usually calculated by the virtual crack extension method [Parks, 1977]. This method considers the variation of the total potential energy due to a virtual infinitesimal change in the crack length, in order to evaluate the energy release rate of a cracked body. The method is applicable to linear and nonlinear elastic materials, including elastic-plastic materials characterized by the deformation theory of plasticity with no unloading. The virtual crack extension method can be also applied to bimaterial crack problems to compute J as long as the crack surfaces remain traction free.

According to the virtual crack extension method, the energy release rate G can be evaluated as

$$G = -\frac{1}{2} \sum_{n=1}^{No.\ of\ elements} \{u_n\}^T \left(\frac{\partial [S]}{\partial a}\right) \{u_n\} \tag{7.2}$$

where $\{u_n\}$ denotes the nodal displacement vector, $[S]$ is the stiffness matrix for the mesh of elements, and $\partial/\partial a$ is differentiation with respect to crack length. The symbol Σ implies summation over all the distorted elements during the virtual crack extension. In the virtual crack extension method the vector $\{u_n\}$ is first calculated by solving the boundary value problem using the finite element method. Next, a small virtual crack extension is

introduced in the plane of the crack and a new stiffness matrix is computed. Usually, the crack is extended by rigidly moving a core of elements around the tip and distorting only one ring such as the shaded one shown in Fig. 7.1. That is, all elements outside the distorted ring are also held rigid. Consequently, in the core of rigid elements and in the outer rigid area, $\partial[S]/\partial a = 0$. As a result, the computation of changed stiffness is limited and the multiplication involved in Eqn. (7.2) involves small vectors and matrices.

7.1.2 Method Based on External Work

From the definition of the energy release rate given in Eqn. (7.1) the difference of the work done by the applied load when the crack is advanced by Δa, divided by the area of crack extension, represents the energy release rate for an interface crack as illustrated in Fig. 7.2. That is, the value of G can be calculated by

$$G = \frac{\Delta W_p}{\Delta A} \tag{7.3}$$

where ΔW_p is the shaded area and ΔA is the fracture area when the crack is extended by Δa. This method was applied to cracking problems in two-phase concrete composite model [Lee et al., 1992]. It should be noted that this method may have a higher mesh sensitivity than the virtual crack extension method.

7.2 Numerical Evaluation of Phase Angle

7.2.1 Virtual Displacement Method

Consider an interface crack problem involving the computation of the interface stress intensity factors, K_1 and K_2. First, solve the problem by the finite element method to find $\{u_n\}$. From this, compute G by the virtual crack extension method described in Section

7.1.1. Then add to $\{u_n\}$ the displacements $\{\Delta u_n\}_1$ for a problem in the same geometry for which $K_1 = \Delta K_1$ and $K_2 = 0$. It should be noted that the displacement field is actually needed only for the nodes associated with the distorted ring of element. In view of this, the asymptotic crack tip displacements can be used everywhere as a suitable field. That is,

$$\Delta \mathbf{u}_1{}^j = \frac{\Delta K_1}{2\mu_j}\sqrt{\frac{r}{2\pi}}\frac{e^{\pi\epsilon}}{(1+e^{2\pi\epsilon})}\mathbf{f}_1(r,\theta,\epsilon,\nu_j) \tag{7.4}$$

where j denotes material 1 or 2 and $\mathbf{f}_1$ is given by Matos et al. [1989]. The vector $\{\Delta u_n\}_1$ is obtained from Eqn. (7.4) at the required nodes. With the value of $\partial[S]/\partial a$ already computed for the computation of G, the calculation in Eqn. (7.2) is repeated with the vector $\{u_n\} + \{\Delta u_n\}_1$ instead of $\{u_n\}$. The result of this calculation, $G + \Delta_1 G$, can be shown from Eqn. (4.7) to be

$$\Delta_1 G = \frac{1}{E^* cosh^2 \pi\epsilon}(\Delta K_1{}^2 + 2K_1\Delta K_1) \tag{7.5}$$

Solving for K_1 gives

$$K_1 = \frac{E^* cosh^2 \pi\epsilon}{2}\frac{\Delta_1 G}{\Delta K_1} - \frac{1}{2}\Delta K_1 \tag{7.6}$$

The second term can be neglected if ΔK_1 is selected to be small.

The procedure can then be repeated for an added vector $\{\Delta u_n\}_2$ such that $K_1 = 0$ and $K_2 = \Delta K_2$, in which case an expression for K_2 can also be derived. These displacements are such that

$$\Delta \mathbf{u}_2{}^j = \frac{\Delta K_2}{2\mu_j}\sqrt{\frac{r}{\pi}}\frac{e^{\pi\epsilon}}{(1+e^{2\pi\epsilon})}\mathbf{f}_2(r,\theta,\epsilon,\nu_j) \tag{7.7}$$

where f_2 is given by Matos et al. [1989]. Then, from Eqn. (4.7) $\Delta_2 G$ is given by

$$\Delta_2 G = \frac{1}{E^* cosh^2 \pi\epsilon}(\Delta {K_2}^2 + 2K_2 \Delta K_2) \tag{7.8}$$

Thus, by rearranging Eqn. (7.8) K_2 is obtained as

$$K_2 = \frac{E^* cosh^2 \pi\epsilon}{2} \frac{\Delta_2 G}{\Delta K_2} - \frac{1}{2}\Delta K_2 \tag{7.9}$$

There is another way of calculating K_1, i.e., from Eqn. (4.7) K_2 can be computed with a prior calculations of G and K_1 as follows

$$K_2 = \sqrt{G E^* cosh^2 \pi\epsilon - {K_1}^2} \tag{7.10}$$

Consequently, from Eqn. (7.6) and Eqn. (7.9) or Eqn. (7.10) the loading phase angle is calculated as

$$\hat{\psi} = \tan^{-1}[\frac{Im(K\hat{L}^{i\epsilon})}{Re(K\hat{L}^{i\epsilon})}] \tag{7.11}$$

where $K = K_1 + iK_2$ and $\hat{L}$ is the fixed length for defining the phase angle.

7.2.2 Crack Surface Displacement Method

The phase angle may be evaluated using the crack surface displacement (CSD) method in which the crack surface displacements associated with the opening and the shear modes are considered. As given in Eqn. (4.6), the relative displacements of the two points at the

top and the bottom crack surfaces, δ_1 and δ_2 are obtained in terms of the interface stress intensity factor, $K = K_1 + iK_2$. For the evaluation of the phase angle Eqn. (4.6) can be written as

$$|\delta|e^{i\phi_\delta} = C\hat{L}^{\frac{1}{2}}K\hat{L}^{i\epsilon}(\frac{r}{\hat{L}})^{\frac{1}{2}+i\epsilon}e^{-i\phi_\epsilon} \tag{7.12}$$

where

$$C = \frac{4(1/\bar{E}_1 + 1/\bar{E}_2)}{\sqrt{2\pi(1+4\epsilon^2)}cosh(\pi\epsilon)} \tag{7.13}$$

and δ and ϕ_δ are the modulus and argument of the complex quantity $(\delta_2 + i\delta_1)$, respectively, and ϕ_ϵ is the principal argument of the complex term $(1 + 2i\epsilon)$. The rules for the calculation of the argument ϕ_δ is depicted in Fig. 7.3. The term $K\hat{L}^{i\epsilon}$ in Eqn. (7.12) can be defined as

$$K\hat{L}^{i\epsilon} = |K|e^{i\hat{\psi}} \tag{7.14}$$

where $\hat{\psi}$ is the real phase angle of the complex term $K\hat{L}^{i\epsilon}$. Note that $|\hat{L}^{i\epsilon}| = 1$ and $|K\hat{L}^{i\epsilon}| = |K|$. $\hat{L}$ can be selected as any length quantity. By substituting Eqn. (7.14) into Eqn. (7.12), one can rewrite Eqn. (7.12) with all complex quantities expressed in polar form

$$|\delta|e^{i\phi_\delta} = C\hat{L}^{\frac{1}{2}}(\frac{r}{\hat{L}})^{\frac{1}{2}}|K|e^{i(\hat{\psi}-\epsilon ln\frac{\hat{L}}{r}-\phi_\epsilon)} \tag{7.15}$$

Then, the expressions for the phase angle $\hat{\psi}$ and the modulus $|K|$ are given by

$$\hat{\psi} = \phi_\delta + \epsilon ln(\frac{\hat{L}}{r}) + \phi_\epsilon \tag{7.16}$$

and

$$|K| = \frac{|\delta|}{C\sqrt{r}} \tag{7.17}$$

The displacements (δ_1 and δ_2) obtained from the finite element calculations can be used to evaluate the phase angle $\hat{\psi}$ and the modulus $|K|$ from Eqns. (7.16) and (7.17). The accuracy of $|K|$ computed using the displacement magnitudes is dependent on the numerical errors introduced to the nodal displacements in the crack tip region. Two estimates for $|K|$, one from the virtual crack extension method, i.e., by substituting G into Eqn. (4.7), and the other from the crack surface displacement method described herein should be compared. From Eqn. (4.7), $|K|$ is given by

$$|K| = \sqrt{GE^* cosh^2(\pi\epsilon)} \tag{7.18}$$

On that basis the distance r_c from the crack tip at which nodal displacements give a good estimate of $|K|$ can be chosen. The crack surface displacements at this location are used to compute the phase angle. The loading phase angle can then be evaluated by Eqn. (7.16).

7.3 Applications

7.3.1 Center-notched Plate

A center-notched plate shown in Fig. 7.4 is selected as the first application problem. This is the case of a crack lying along the interface of a plate subjected to tensile stresses at the boundaries. Due to the symmetry of the model, the analysis was performed on the right half of the plate in plane strain condition. Figure 7.5 shows the finite element model consisting of 384 elements including a focused mesh of 64 elements surrounding the crack tip. 16 singular elements with quarter mid-points were generated around the crack tip. Finite element

calculations were performed to obtain energy release rates along the interface direction. Table 7.1 presents the elastic moduli ratios, the Poisson's ratios, and the Dundurs' parameters α and β for the five cases considered in the numerical analysis. A comparison between the numerical calculations and the analytical solution provided by Rice and Sih [1965] is given in Table 7.2. It is observed that in the numerical calculation of the energy release rate, accurate results which compare favorably to the analytical solutions are obtained. It should be noted that the present model for numerical calculations is a finite plate, and thus, actual energy release rate values should be slightly higher than the analytical solutions obtained from the infinite bimaterial body. It is found that as the elastic modulus mismatch increases, the error in the energy release rate calculations increases. This is expected as the higher the elastic mismatch, the less accurate is the representation of singularity by the quarter mid-point node element.

The effect of the type of focused mesh on the accuracy of the computed energy release rate was investigated. The energy release rates divided by $\sigma_y^2 a(1-\nu_1^2)/E_1$ are shown in Fig. 7.6. It is observed that the G-calculations are almost constant for all finite element models with different total number of elements. Even the relatively coarse mesh provides good results for the energy release rate. On the other hand, finite element calculations using rectangular meshes around the crack tip represents about 10 % error compared to the exact solutions. Thus, it is concluded that the focused meshes with singular triangle elements around the tip is more effective than the rectangular meshes.

7.3.2 Bimaterial Beam

The second example is a bimaterial beam subjected to four-point bending (Fig. 7.7). The analytical solution of the energy release rate can be obtained for cracks located between the inner loading points where the cracked ligament is subjected to constant moment conditions. For the purpose of analysis, the subscript 1 indicates quantities relevant to the top layer,

whereas the subscript 2 denotes the corresponding quantities for the bottom layer. The steady state value G_{ss}, can be deduced analytically by recognizing that it is simply the difference in the strain energy in the uncracked and cracked beam. Since there is negligible strain energy in the beam above the crack, G_{ss} can be deduced by considering the energies in the uncracked section, and in a section of the lower beam beneath the crack [Charalambides et al., 1989]. From Euler-Bernoulli beam theory and plane strain conditions, these energies can be expressed in terms of the applied moment M as

$$U = \frac{(1-\nu^2)M^2}{2EI} \tag{7.19}$$

where U is the strain energy per unit cross-section and I is the second moment of area per unit width. Consequently,

$$G_{ss} = \frac{M^2(1-\nu_2^2)}{2E_2}\left(\frac{1}{I_2} - \frac{\lambda}{I_c}\right) \tag{7.20}$$

where

$$\lambda = \frac{E_2(1-\nu_1^2)}{E_1(1-\nu_2^2)} \tag{7.21}$$

and the subscript c refers to the composite beam. Note that the moment per unit width $M = Pl/2b$, with P being the total load and l the spacing between inner and outer load lines,

$$I_c = \frac{h_1^3}{12} + \frac{\lambda h_2^3}{12} \frac{\lambda h_1 h_2 (h_1 + h_2)^2}{4(h_1 + \lambda h_2)} \tag{7.22}$$

and

$$I_2 = \frac{h_2^3}{12} \tag{7.23}$$

The dimensions are shown in Fig. 7.7. The strain energy release rate is

$$\frac{G_{ss}E_2b^2h^3}{(1-\nu_2^2)P^2l^2} = \frac{3}{2}[\frac{1}{\eta_2^3} - \frac{\lambda}{\eta_1^3 + \lambda\eta_2^3 + 3\lambda\frac{\eta_1\eta_2}{\eta_1+\lambda\eta_2}}] \tag{7.24}$$

where $\eta_i = h_i/h$ $(i = 1, 2)$. Evidently, the nondimensional G_{ss} increases monotonically with increase in relative upper beam thickness, h_1/h_2 and decreases as the relative modulus of the lower layer E_2/E_1, increases.

The finite element analysis was carried out half the beam because of symmetry about the mid-section. Figure 7.8 shows the mesh and the boundary condition for the beam with $h_1/h_2 = 1.0$. The elements used in the mesh generation were two-dimensional (2D) eight node plane strain isoparametric elements. The number of elements varied with the relative thickness, h_1/h_2, and the relative crack location, a/l. In the crack tip region the mesh was refined using 5 element rings. 16 triangular elements with quarter mid-point nodes were used around the crack tip. To calculate the phase angle, the fixed length $\hat{L}$ is selected to be the thickness of upper beam, h_1. The node which offers a good agreement in energy release rates from the crack extension method and the crack surface displacement method (i.e., less than 2 % difference) was chosen to calculate the phase angle $\hat{\psi}$.

Figure 7.9 shows the graphs of energy release rate and phase angle versus the thickness ratio, h_1/h_2, for five material combinations listed in Table 7.1. Within the steady-state region, the energy release rates obtained from finite element method (normalized by

$P^2l^2(1-\nu_2^2)/E_2h^3b^2$) are in good agreement with the analytical solutions in Eqn. (7.24). It is also noted that as the elastic modulus mismatch increases, the error in the energy release rate calculations increases and the corresponding phase angle varies slightly with elastic modulus ratio. In particular, when $E_2/E_1 > 5.0$ the difference in $\hat{\psi}$ is very small. Figure 7.10 shows the trends in energy release rate and phase angle versus relative crack length, a/l. As predicted by the analytical solution, the energy release rate and the phase angle are essentially constant within the inner loading lines.

7.4 Summary

A fracture mechanics based numerical method was applied to two interface crack problems. In the numerical calculation of the energy release rate and the phase angle, accurate results are obtained, when compared to the analytical solutions. Thus, it can be concluded that the numerical method is a good tool to evaluate the interfacial fracture parameters of an interface crack in a bimaterial system. In Chapter 8, crack propagation in interfacial region of concrete composites will be investigated using the numerical method described in this chapter.

Table 7.1 Dundurs' parameters α and β for five material combinations considered in the finite element calculations

E_2/E_1	ν_1	ν_2	α	β	ε
1.0	0.3	0.3	0.0	0.0	0.0
2.5	0.3	0.3	-0.483	-0.122	0.039
5.0	0.3	0.3	-0.667	-0.190	0.061
10.0	0.3	0.3	-0.818	-0.234	0.076
25.0	0.3	0.3	-0.923	-0.264	0.086

Table 7.2 Comparison of the energy release rates in center-notched plate from the finite element calculation and the analytical solution with the ratio E_2/E_1

E_2/E_1	G from finite element calculation[1] (I)	G from analytical solution[1] (II)	Error (%) (I-II)/II
1.0	3.231	3.143	2.8
2.5	2.280	2.145	1.6
5.0	1.758	1.776	1.0
10.0	1.516	1.578	-3.9
25.0	1.349	1.455	-7.2

[1] divided by $\sigma_y^2 a(1-\nu_1^2)/E_1$

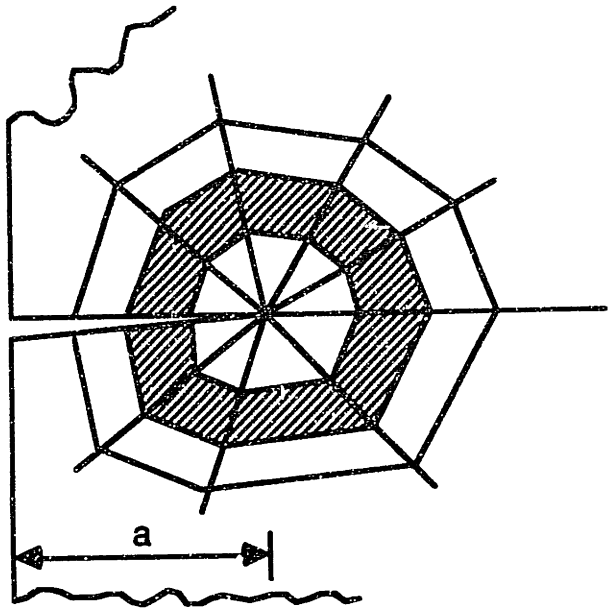

Figure 7.1 A typical ring of elements to be distorted in the J-calculations

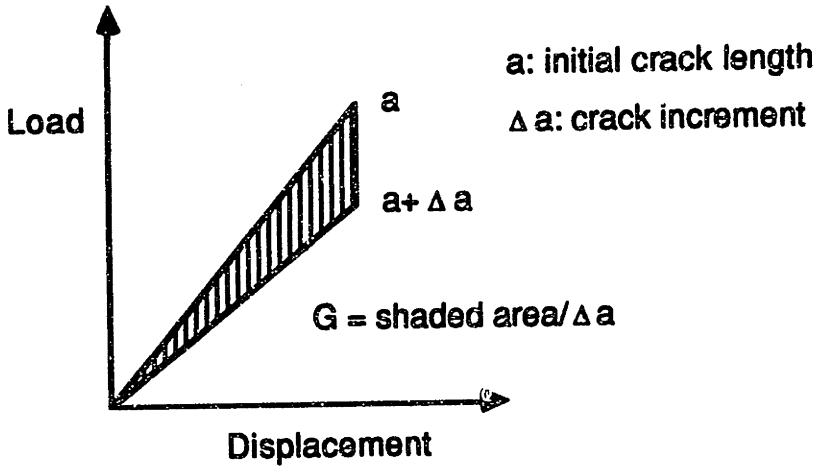

Figure 7.2 Calculation of energy release rate (G)

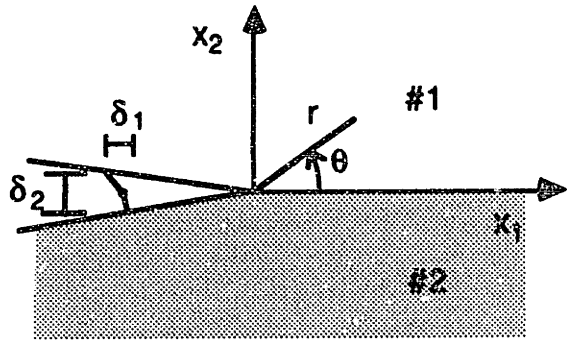

(a)

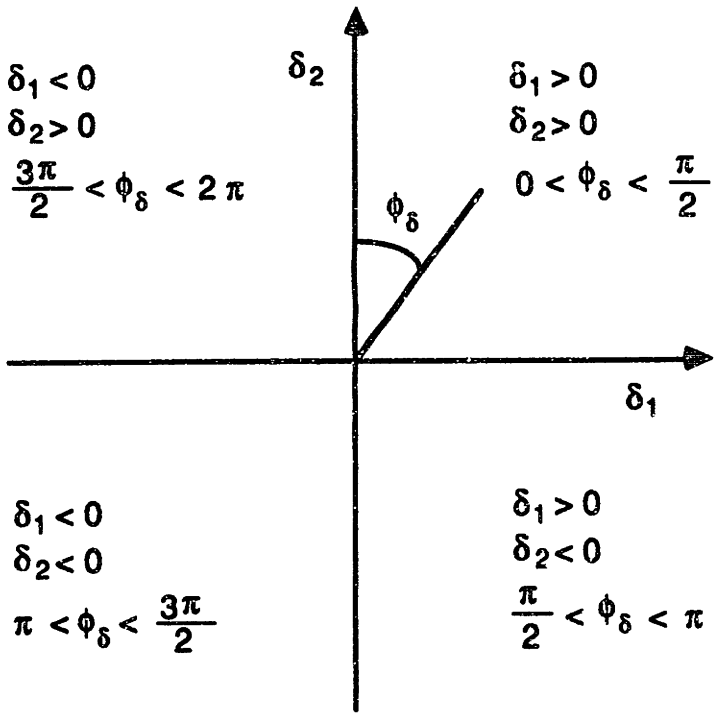

(b)

Figure 7.3 Calculation of ϕ_δ : (a) The crack tip region for an interfacial crack; and (b) The rules for the calculation of ϕ_δ

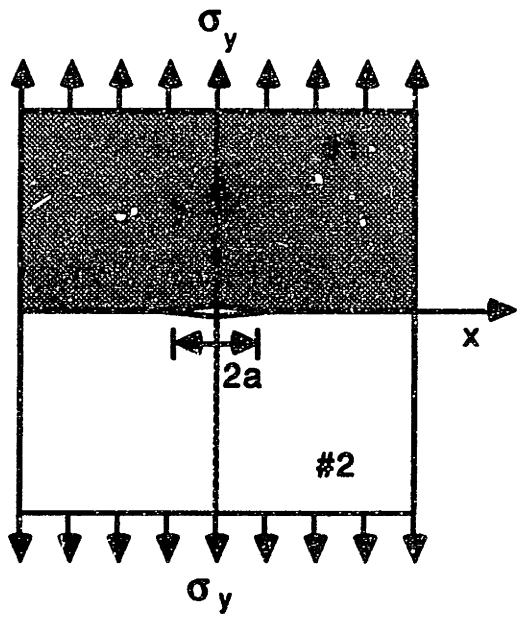

Figure 7.4 A center-notched plate model

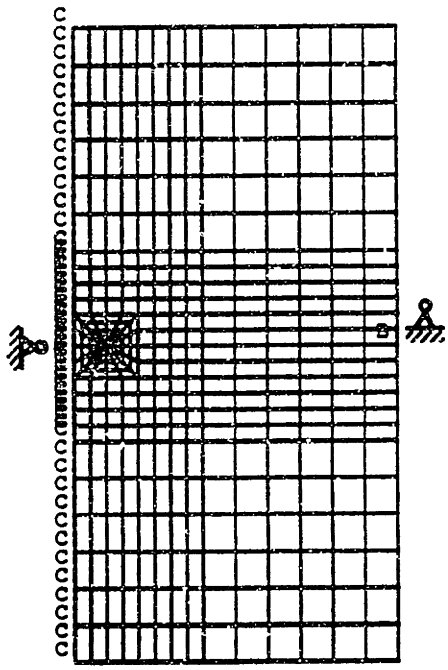

(a) Mesh and boundary conditions

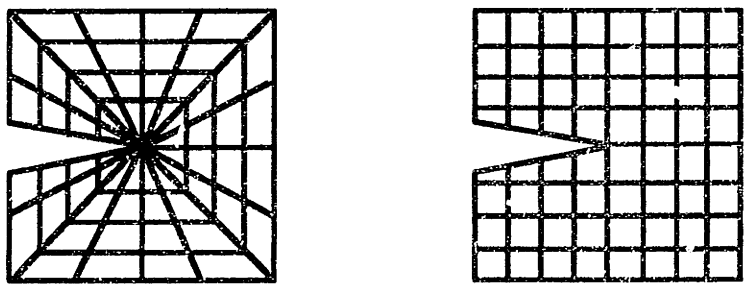

(b) Focused mesh around the crack tip

Figure 7.5 Mesh used in the center-notched plate model

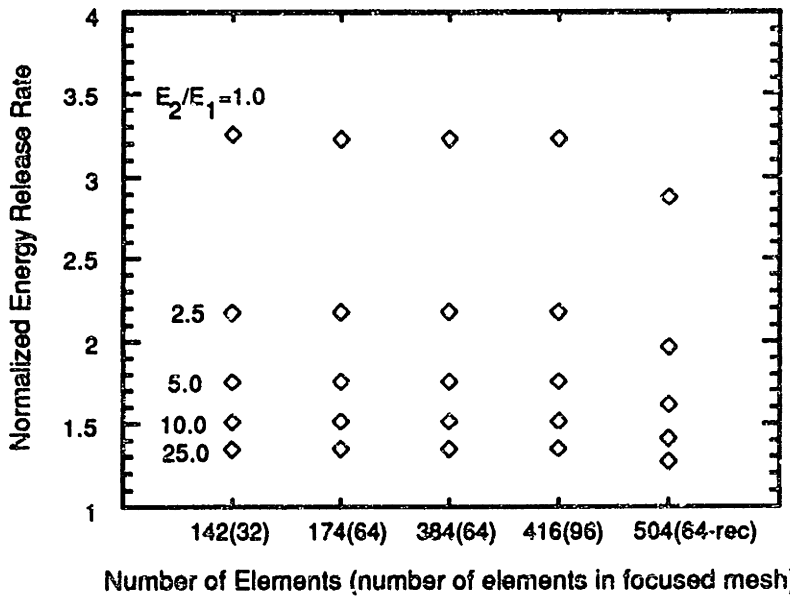

Figure 7.6 Effect of number of elements on G-calculations

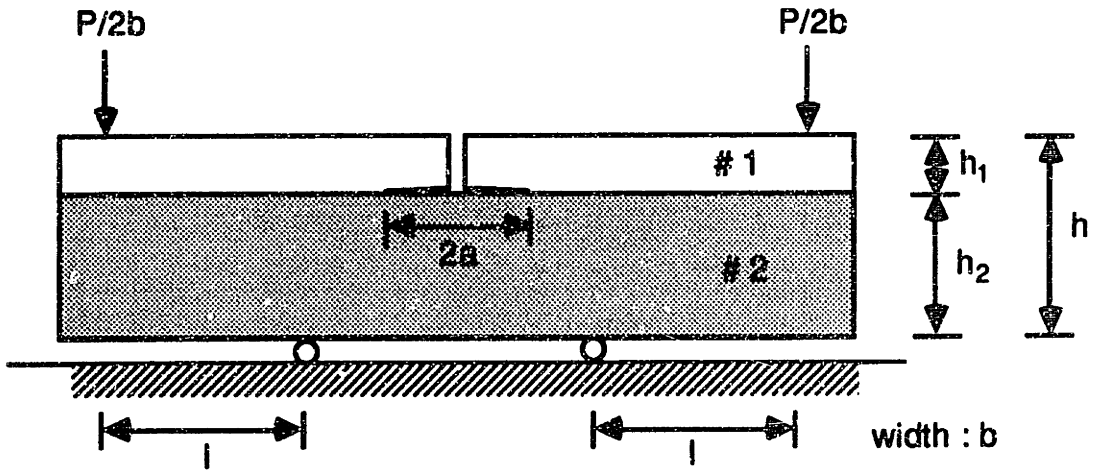

Figure 7.7 Bimaterial beam model subjected to four-point bending

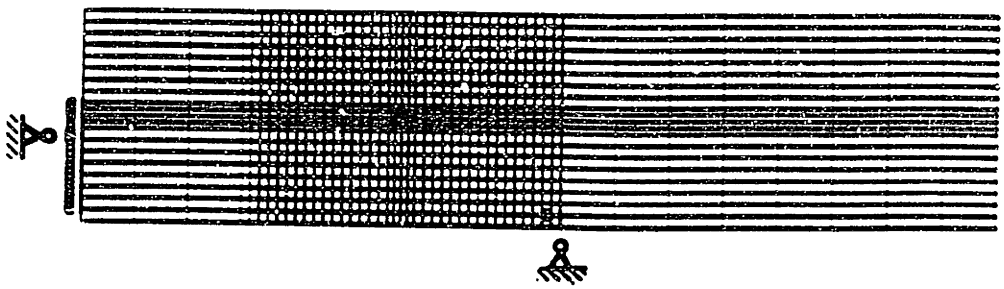

(a) Mesh

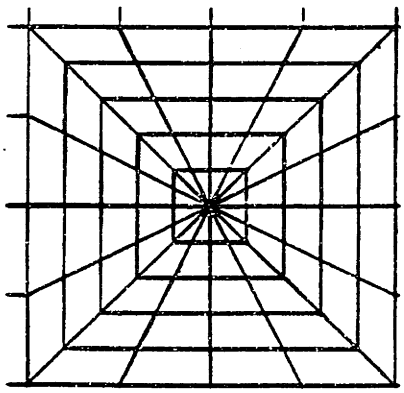

(b) Focused mesh around the crack tip

Figure 7.8 Mesh and boundary conditions of the beam model

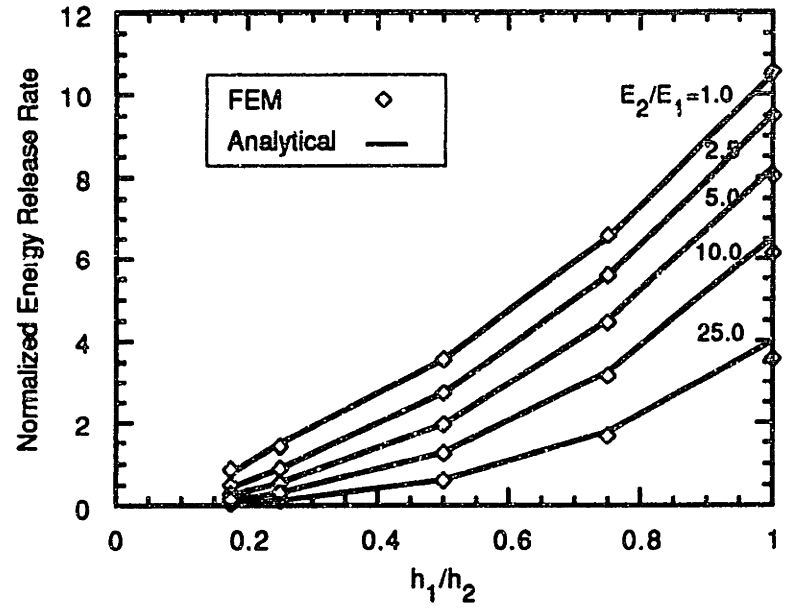

(a) Trends in energy release rate

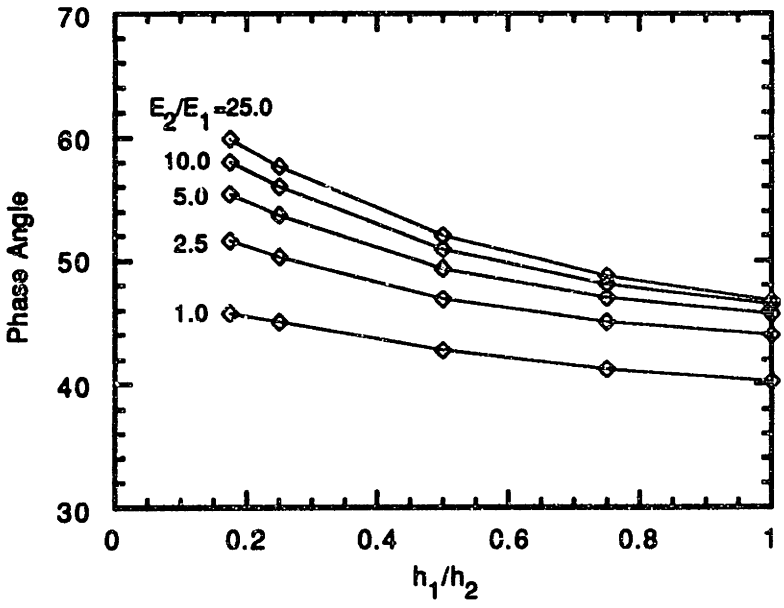

(b) Trends in phase angle

Figure 7.9 Steady-state energy release rate and phase angle with the thickness ratio, h_1/h_2

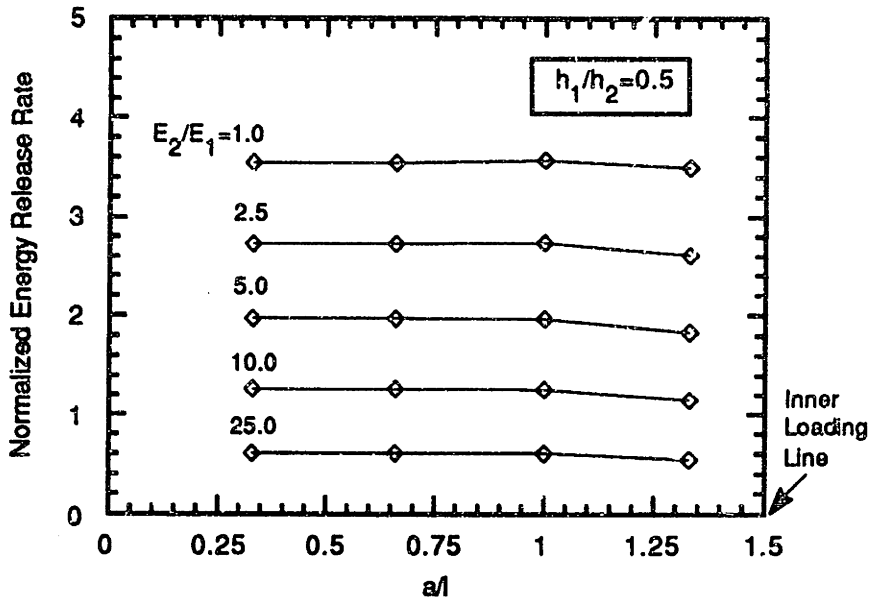

(a) Trends in energy release rate

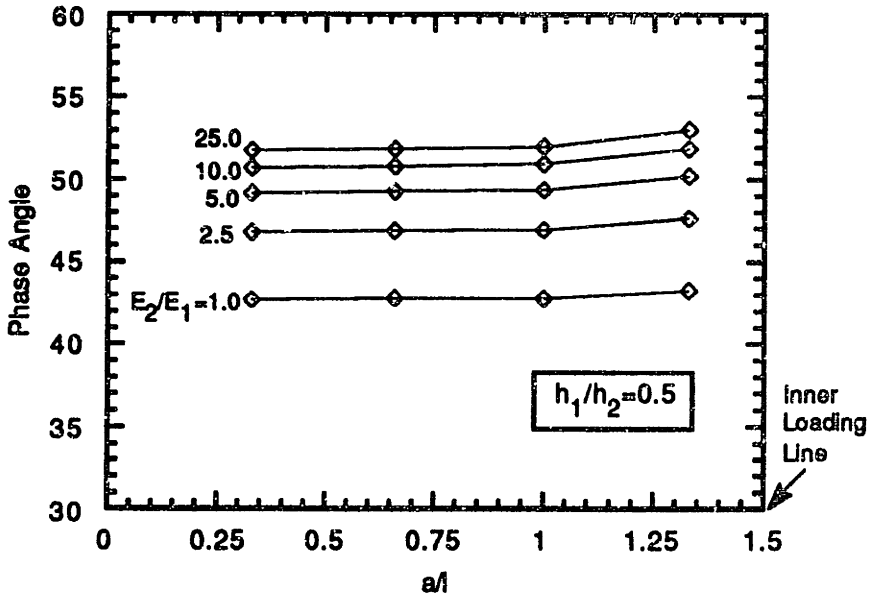

(b) Trends in phase angle

Figure 7.10 Steady-state energy release rate and phase angle with the relative crack length, a/l

Chapter 8

Analysis of Crack Propagation in Interfacial Region

Concrete can be modeled as a two-phase composite material, consisting of mortar matrix and aggregate inclusions, and hence the relative properties of the mortar and the aggregate materials, and the characteristics of the interface greatly influence the cracking and deformation of the concrete composite. Various scenarios of crack initiation and crack propagation in the matrix versus at the interface, or crack penetration into the aggregate need to be studied in order to engineer the material for an optimal behavior. Solutions for studying such cracking scenarios are rare. Hence, there is a need to develop rigorous methodologies and novel models employing fracture mechanics concepts for studying cracking in the interfacial regions of the concrete composite. Such a methodology would involve both testing of physical laboratory models and numerical analysis. In this chapter, crack propagation in the interfacial regions of a two-phase beam composite model consisting of mortar matrix and an aggregate inclusion is investigated. The results from the experimental/numerical work on the beam model are compared with those obtained from testing of sandwiched specimens.

8.1 Scope

A composite model shown in Fig. 8.1 was developed as an application to study the crack penetration versus crack deflection in interfacial regions. This model consists of a beam of material 2 and a slab inclusion of material 1. Here, material 1 and 2 refer to aggregate and mortar matrix, respectively. One can achieve different crack hitting angles in the beam model by appropriately inclining the embedded inclusion. By changing the loading configuration, different loading conditions ranging from mode I to mode II can be achieved. One of the purposes of this composite model study is to verify the application of a criterion given in Eqn. (4.29) to cracking problems that may occur in concrete composites. Besides this, in the case that a crack deflection occurs in tested specimens, one can induce interface fracture toughness values with specific loading phase angles through a numerical study.

In experimental/numerical analysis of the two-phase composite beam model, the following parameters were chosen:

1. Mode I loading - four-point and three-point bending
2. Three types of inclination of aggregate slab - 90°, 60° and 30° with respect to an impinging crack
3. Three mortar matrix types - same types as those selected for sandwich specimen testing (M1, M2, and M3)
4. Two aggregate types - same types as those selected for sandwiched specimen testing (granite and limestone)

For consistent approach throughout the research work the same types of mortar matrices and aggregates used for making sandwiched specimens were selected.

The experimental/numerical work described in this chapter consists of three phases. In Phase I, two-dimensional two-phase composite beam model was tested to study crack

propagation scenarios in interfacial regions, namely, crack deflection and crack penetration. Phase II of the work was the numerical analysis of the model using finite element method (FEM) based on an interface fracture mechanics concept. This method was described in Chapter 7. In Phase III the predictions from numerical simulation were compared with the results from sandwiched specimen tests.

8.2 Experimental Work

8.2.1 Test Specimens and Materials

A composite beam model shown in Fig. 8.2 was tested to study the crack propagation in interfacial regions. The dimensions of the beam for three-point bending test were 228.6 mm (9.0 in : length) x 76.2 mm (3.0 in : height) x 38.1 mm (1.5 in : width) and the dimensions of the inclusion were 50.8 mm (2.0 in) x 12.7 mm (0.5 in) x 38.4 mm (1.5 in). Four-point bending test specimens had a different width of 25.4 mm (1.0 in). The inclination angle of aggregate slab, γ, was adjusted to three different angles, 90°, 60° and 30°, with respect to the impinging crack. The crack length, a, was 25.4 mm (1.0 in), and thus, the ratio of the crack length to the beam height was 0.33.

For manufacturing of beam specimens three mortar mixes (M1, M2, and M3) for matrices and two types of aggregates (granite and limestone) for inclusions were used. M1 (42.5 MPa, 28-day compressive strength) is normal strength mortar with no silica fume, and M2 (58.5 MPa) and M3 (80.5 MPa) are high strength mortars with silica fume. The mix proportions of the mortar mixes were same as those used for the sandwiched specimens, as listed in Table 6.1. Mechanical properties and bimaterial parameters such as Dundurs' mismatch parameters are listed Tables 6.2 and 6.3. From Table 6.2 mode I critical energy release rates of granite and limestone were found to be 17.5 J/m^2 and 11.8 J/m^2, respectively.

After aggregate inclusions were placed in the beam molds made of plexiglass, fresh

mortar mixture was poured. The mixing procedure for mortar was same as that for making sandwich specimens described in Section 6.4. The specimens were removed from the molds 24 hours later, and cured in water for 28 days. Before testing of beams, a pre-crack was introduced in the middle of beams using a diamond saw. This pre-crack was very close to an aggregate inclusion such that a distance between the crack tip and the bottom surface of the aggregate inclusion was less than 1.0 mm.

8.2.2 Test set-up and Procedure

The beam specimen was placed in a loading fixture for bending test and then, three- and four-point bending test was performed using an INSTRON machine with a stroke control at a loading rate of 0.0762 mm/min. The shear span length l_1, was 57.15 mm (2.25 in) in four-point bending test. The Fluke data acquisition system was used to collect the applied load and the deflection at the middle of the beam. The crack path was also monitored.

8.2.3 Test Results

The cracking loads and cracking modes of tested specimens subjected to three-point bending are listed in Table 8.1. Figure 8.3 shows the trends of the cracking loads. For M1/G system the cracking loads of three specimens with $\gamma = 90°$, $60°$ and $30°$ were 1.75kN, 1.02kN, 0.40kN, respectively; the cracking mode was crack deflection, i.e., interface cracking occurred. The cracking loads for M3/G systems were somewhat higher than those for M1/G systems. However, their cracking modes were still crack deflection along the interface. This implies that M3/G interface is stronger than M1/G interface and thus, the results agree well with the results obtained from sandwiched specimen tests. M1/L or M3/L systems tested exhibited lower cracking loads than M1/G or M3/G systems, respectively, but the cracking modes were almost the same. Only M3/L system with $\gamma = 90°$ showed the crack penetration, i.e., transgranular cracking occurred.

The cracking loads and cracking modes of tested specimens subjected to four-point bending are listed in Table 8.2. Figure 8.4 shows the trends of the cracking loads. When the hitting angle was 90° the failure loads of three M1/G specimens ranged from 2.22 kN to 2.63 kN; the failure mode being crack deflection. On the other hand, for both M2/G and M3/G system with $\gamma = 90°$ the failure mode was crack penetration. This is attributed by the silica fume effects combined with water reduction, resulting in the strong interface. An interesting observation is that crack penetration occurred in one of M2/G system with $\gamma = 60°$ and its cracking load was almost the same as those for M2/G or M3/G system with $\gamma = 90°$. The other M2/G system with $\gamma = 60°$ failed by crack deflection and showed much lower cracking load. Cracking loads of mortar/limestone systems were lower values and their cracking mode were somewhat different compared with mortar/granite systems. An example is that M2/L system with $\gamma = 90°$ failed by crack deflection. Since M2/G system with $\gamma = 90°$ exhibited crack penetration, the M2/L system was also expected to have failed by crack penetration because limestone is weaker than granite. It is observed from Table 8.1 and Table 8.2 that as the hitting angle decreases, the cracking load decreases and the cracking mode tends to be the crack deflection. This is caused by the fact that the energy release rate of the interface direction increases but the corresponding interfacial fracture toughness decreases. Failed specimens subjected to four-point bending are shown in Fig. 8.5.

8.3 Numerical Analysis of Composite Model

8.3.1 FEM Modeling

For the composite beam model tested, the energy release rate and the loading phase angle for the deflected crack were calculated by the finite element analysis scheme described in Chapter 7. This numerical method is based on the virtual crack extension method for the evaluation of the energy release rate and the crack surface displacement method for the

evaluation of the phase angle. Finite element analysis was performed on the models with $\gamma = 90°$. Materials constituting the beam model were assumed to be linear and elastic. The finite element mesh shown in Fig. 8.6 consists of 2D isoparametric eight-node plane strain elements. In the crack tip region the mesh was refined using 9 element rings, and 24 triangular elements with quarter mid-point nodes at the crack tip. The total number of elements was 1488. For the analysis of the deflected crack, a small crack Δa of 2.286 mm was introduced along the interface. Six different material conditions were considered in the finite element calculations. Table 8.3 presents the Poisson's ratios and the mismatch parameters α and β for the material combinations. Figure 8.7 shows the deformed mesh and the original mesh of the beam model.

8.3.2 Numerical Results from Finite Element Analysis

Numerical calculations were carried out using the finite element program ADINA which allows the computation of the energy release rate. The input data file and the plot file are given in Appendix A. For each material combination, the energy release rate of the deflected crack, G_d, and the corresponding phase angle, $\hat{\psi}$, were calculated. For the calculation of the phase angle the fixed length was selected to be 2.54 mm because this value was used in calculating the phase angle for the interpretation of sandwiched specimen test results.. The distance r_c behind the crack tip, at which the two estimates of $|K|$ using the crack extension method and the crack surface displacement method agree well, was found to be approximately $\frac{1}{100}a$. Since numerical errors may be substantial in the first node (quarter mid-point), the second node (r/a = 0.01) was chosen to calculate $\hat{\psi}$. Table 8.4 shows the values of G_d and $\hat{\psi}$. Note that G_d values are normalized by $P^2 l_1^2 (1 - \nu_1^2) a / E_1 d^4 b^2$. It is observed from Table 8.4 that as the parameter α decreases the phase angle $\hat{\psi}$ increases. This trend agrees well with the results by He and Hutchinson [1989b] (see Fig. 4.9).

8.3.3 Numerical Simulation

Comparison of cracking modes from the composite model tests and those from the numerical results is given in Table 8.5. This numerical simulation was confined to models with $\gamma = 90^o$ only. As an example, the test results of M1/Granite system subjected to four-point bending will be discussed. In M1/G system the phase angle of a deflected crack is 37^0 (Table 8.4). The mode I fracture energy of granite, Γ_g, was 17.5 J/m^2 and the interface fracture energy of M1/G interface, $\Gamma_i(37^o)$, was approximately 5.0 J/m^2 from Fig. 6.9. The ratio G_d/G_p^{max} is 0.37 from Fig. 4.8. Therefore, the ratio $\Gamma_i(37^o)/\Gamma_g = 5.0/17.5 = 0.28$ is found to be less than $G_d/G_p^{max} = 0.37$. Thus, Eqn. (4.29) predicts the deflection of the impinging crack. This agrees with the test result showing the interface cracking. For this case, the interfacial fracture toughness can be obtained because the test specimen exhibited the crack deflection. Using the cracking loads ranging from 2.22 kN to 2.63 kN, the interface fracture energy, $\Gamma_i(37^o)$ is predicted to be from 4.9 J/m^2 to 6.8 J/m^2 from numerical calculations, as given in Table 8.6. The interface fracture energy values predicted in this way are somewhat higher than the average value, 5.0 J/m^2, directly measured from the sandwiched specimen testing. This difference may be attributed to either the linear elastic material assumption in the numerical analysis or the difference of specimen geometries. However, the agreement is reasonable.

For the M3/G system subjected to four-point bending, the ratio $\Gamma_i(41^o)/\Gamma_g = 8.0/17.5 = 0.46$ is found to be larger than the ratio $G_d/G_p^{max} = 0.30$. Thus, according to Eqn. (4.29), crack penetration is predicted. This agrees with the test result showing transgranular cracking. For this case, the fracture toughness of aggregate can be obtained. From the cracking loads, the average fracture toughness of granite is predicted to be 25.0 J/m^2. The predicted fracture toughness value of granite are 34 % higher than the average measured value of 17.5 J/m^2, as obtained from fracture toughness testing of granite. As shown in

Table 8.5, of the 14 specimens the four cases exhibited a discrepancy between the cracking mode from composite model testing and from the criteria. Of these four, three cases occurred in mortar/limestone systems. This might be the result of the dependence of specimen size and specimen geometry on aggregate fracture toughness, and for the case of the mortar/limestone, the application of linear elastic fracture mechanics may be unrealistic.

8.4 Summary

A finite element simulation is presented to investigate a crack penetration versus crack deflection scenarios in a two-phase composite beam consisting of an aggregate inclusion embedded in a mortar matrix. The numerical predictions were compared with the results from composite model test, and generally, good correlation was obtained. In conclusion, this fracture mechanics based numerical analysis scheme can be appropriately applied to the study of cracking in the interfacial regions of concrete composites. This study represents an initial step for the use of such methods in providing a fundamental understanding of the cracking behavior, and further studies are required to develop a general predictive capability. The present approach is based on linear elastic interface fracture mechanics. This aspect needs to be further investigated.

Table 8.1 Cracking load and cracking mode of tested specimens subjected to three-point bending

Material Combination	Hitting Angle, γ (degree)	Cracking Load (kN)	Cracking Mode[1]
M1/G3-1	90	1.75	D
M1/G3-2	60	1.05	D
M1/G3-3	30	0.40	D
M3/G3-1	90	2.43	D
M3/G3-2	60	1.38	D
M3/G3-3	30	0.79	D
M1/L3-1	90	1.02	D
M1/L3-2	60	0.39	D
M1/L3-3	30	0.23	D
M3/L3-1	90	1.36	P
M3/L3-2	60	0.73	D
M3/L3-3	30	0.44	D

[1] D : crack deflection and P : crack penetration

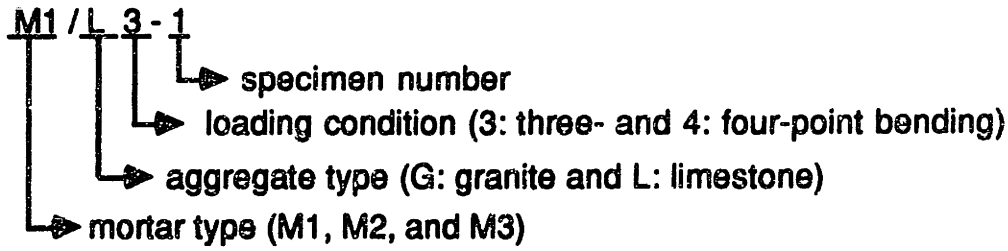

Table 8.2 Cracking load and cracking mode of tested specimens subjected to four-point bending

Material Combination	Hitting Angle, γ (degree)	Cracking Load (kN)	Cracking Mode
M1/G4-1	90	2.22	D
M1/G4-2	90	2.47	D
M1/G4-3	90	2.63	D
M1/G4-4	60	1.48	D
M2/G4-1	90	2.76	P
M2/G4-2	90	3.00	P
M2/G4-3	60	2.01	D
M2/G4-4	60	3.03	P
M3/G4-1	90	2.92	P
M3/G4-2	90	3.17	P
M3/G4-3	60	1.84	D
M1/L4-1	90	1.45	D
M1/L4-2	60	1.05	D
M2/L4-1	90	1.61	D
M2/L4-2	60	1.26	D
M3/L4-1	90	1.90	P
M3/L4-2	60	1.43	D

Table 8.3 Dundurs' parameters for six mortar-aggregate combinations

Combinations (#2/#1)	E_1 (GPa)	ν_1	E_2 (GPa)	ν_2	α	β
M1/G	55.3	0.16	27.8	0.22	0.320	0.099
M2/G	55.3	0.16	34.0	0.22	0.227	0.064
M3/G	55.3	0.16	39.2	0.20	0.163	0.049
M1/L	34.5	0.18	27.8	0.22	0.099	0.022
M2/L	34.5	0.18	34.0	0.22	-0.001	-0.016
M3/L	34.5	0.18	39.2	0.20	-0.068	-0.033

Table 8.4 Numerical results of the energy release rate and the corresponding phase angle

	Three-point bending		Four-point bending	
Combination	G_d[1]	$\hat{\psi}$[2]	G_d	$\hat{\psi}$
M1/G	0.3125	39.9	0.4460	37.4
M2/G	-	-	0.3970	39.2
M3/G	0.2609	43.2	0.3672	40.6
M1/L	0.3890	44.6	0.5454	42.0
M2/L	-	-	0.4920	44.2
M3/L	0.3316	48.5	0.4599	45.8

[1] nondimensionalized by $P^2 l_1^2 (1-\nu_1^2) a / E_1 d^4 b^2$

[2] with the fixed length = 2.54 mm

Table 8.5 Comparison of cracking mode from the tested results and the predictions by criteria

Material Combination	Cracking Mode from Testing	Γ_i/Γ_a	G_d/G_p[1]	Cracking Mode by Criteria	Remarks
M1/G3-1	D	0.31	0.37	D	O.K.
M3/G3-1	D	0.48	0.30	P	N.G.
M1/L3-1	D	0.50	0.28	P	N.G.
M3/L3-1	P	0.59	0.26	P	O.K.
M1/G4-1	D	0.28	0.37	D	O.K.
M1/G4-2	D	0.28	0.37	D	O.K.
M1/G4-3	D	0.28	0.37	D	O.K.
M2/G4-1	P	0.40	0.33	P	O.K.
M2/G4-2	P	0.40	0.33	P	O.K.
M3/G4-1	P	0.46	0.30	P	O.K.
M3/G4-2	P	0.46	0.30	P	O.K.
M1/L4-1	D	0.46	0.28	P	N.G.
M2/L4-1	D	0.55	0.26	P	N.G.
M3/L4-1	P	0.63	0.26	P	O.K.

[1] from Fig. 4.8 (He and Hutchinson [1989b])

Table 8.6 Fracture toughness values obtained from numerical simulation

	Fracture Toughness from Composite Model (I)		Fracture toughness from Fracture Test (II)		(I-II)/II
Combination	Interface[1]	Aggregate	Interface	Aggregate	Error (%)
M1/G3-1	3.8		5.5		-30.9
M3/G3-1	6.1		8.5		-28.2
M1/G4-1	4.9		5.0		-2.0
M1/G4-2	6.0		5.0		20.0
M1/G4-3	6.8		5.0		36.0
M2/G4-1		20.2		17.5	15.4
M2/G4-2		23.9		17.5	36.6
M3/G4-1		23.1		17.5	32.0
M3/G4-2		27.2		17.5	35.4

[1] phase angle is given in Table 8.4

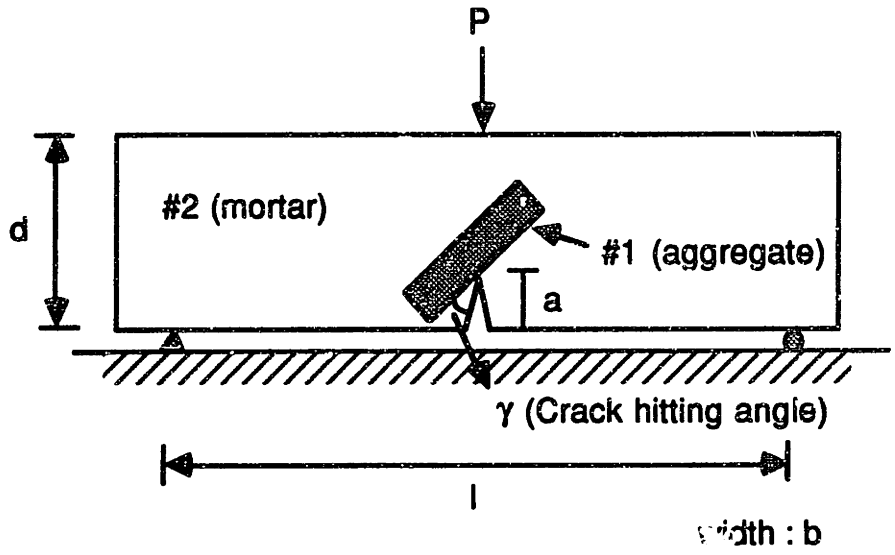

Figure 8.1 Two-phase beam composite model

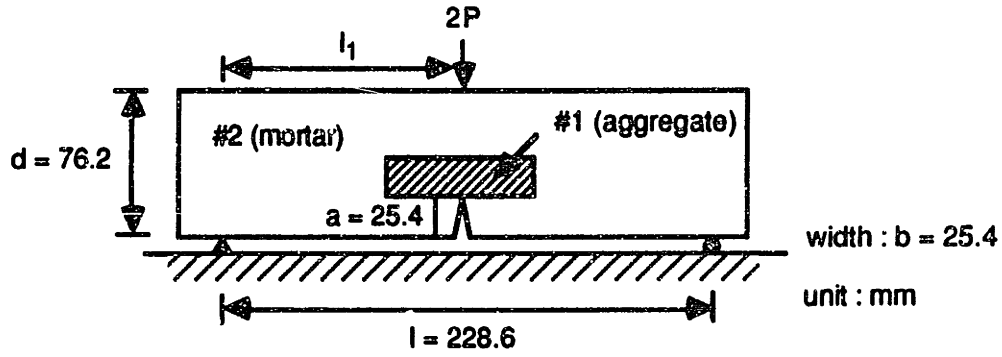

(a) Three-point bending condition

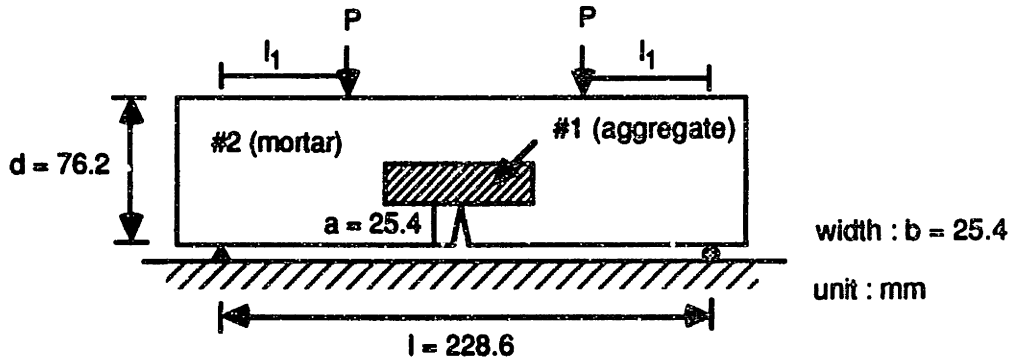

(b) Four-point bending condition

Figure 8.2 Geometries and loading configuration of beam composite models with $\gamma = 90^o$

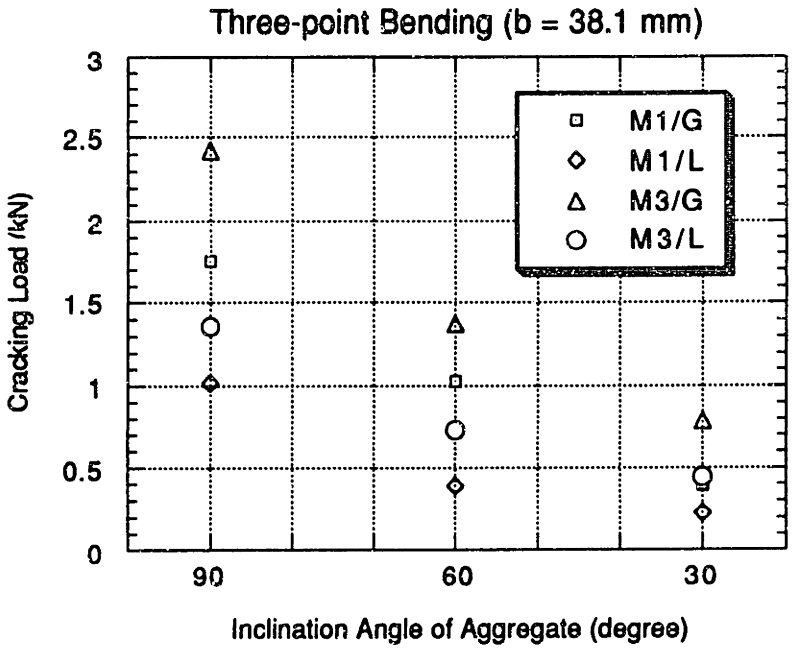

Figure 8.3 Cracking load of three-point bending specimens tested

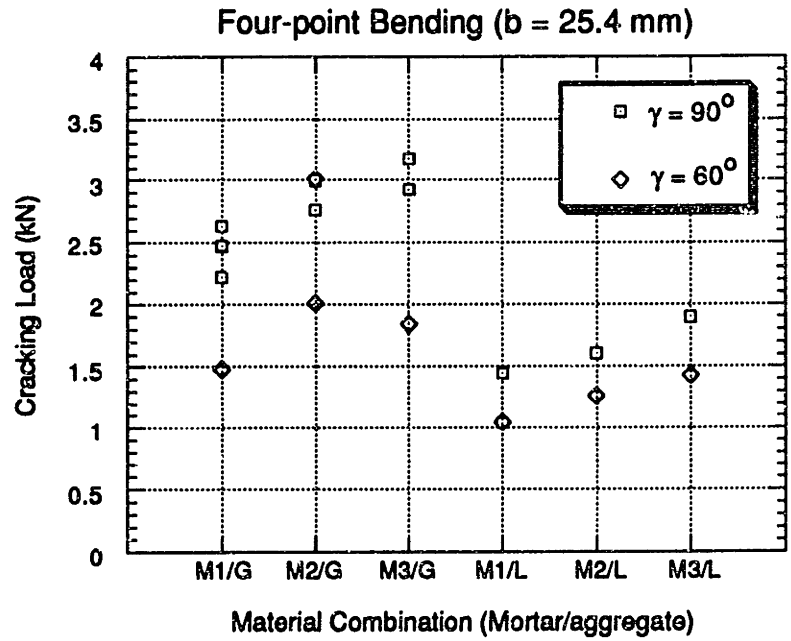

Figure 8.4 Cracking load of four-point bending specimens tested

(a)

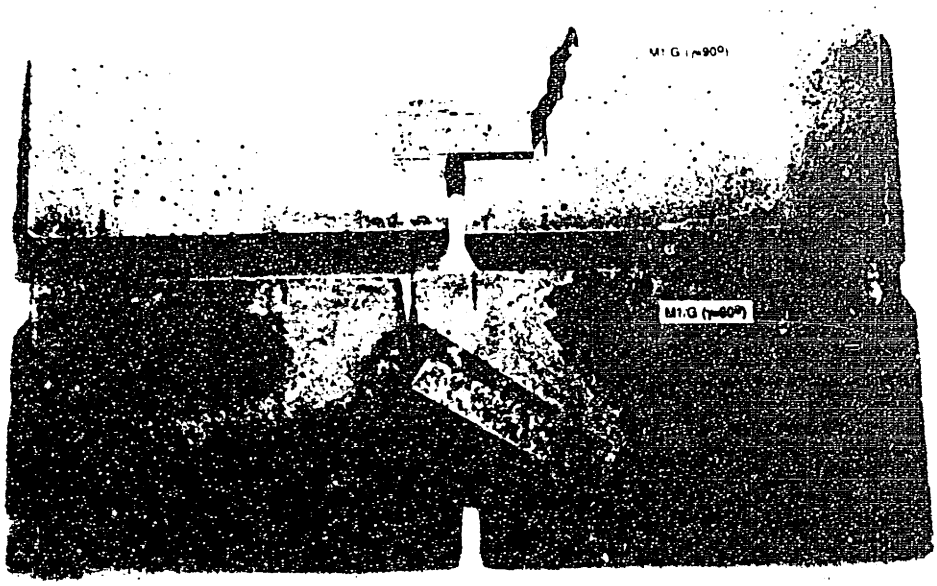

(b)

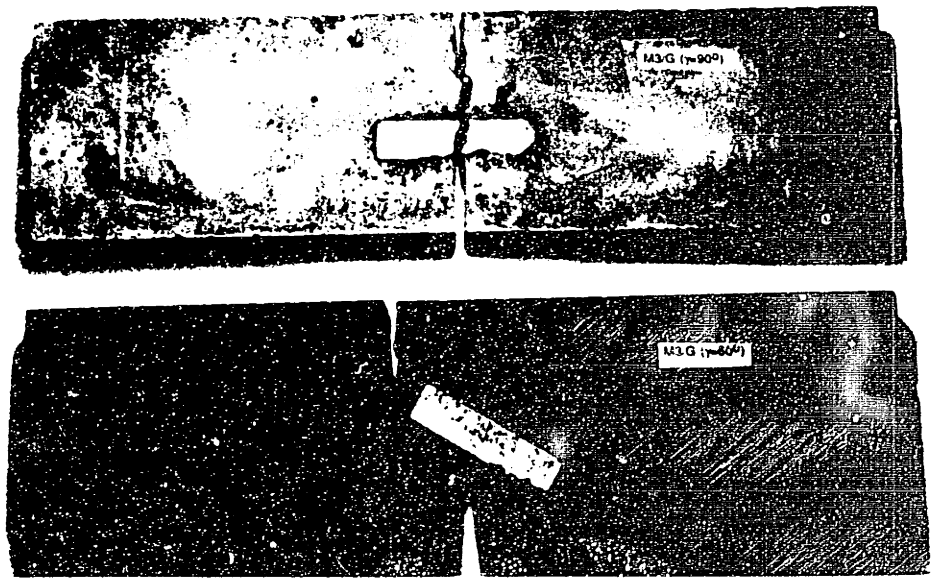

Figure 8.5 Failed specimens subjected to four-point bending:

(a) M1/G system; and (b) M3/G system

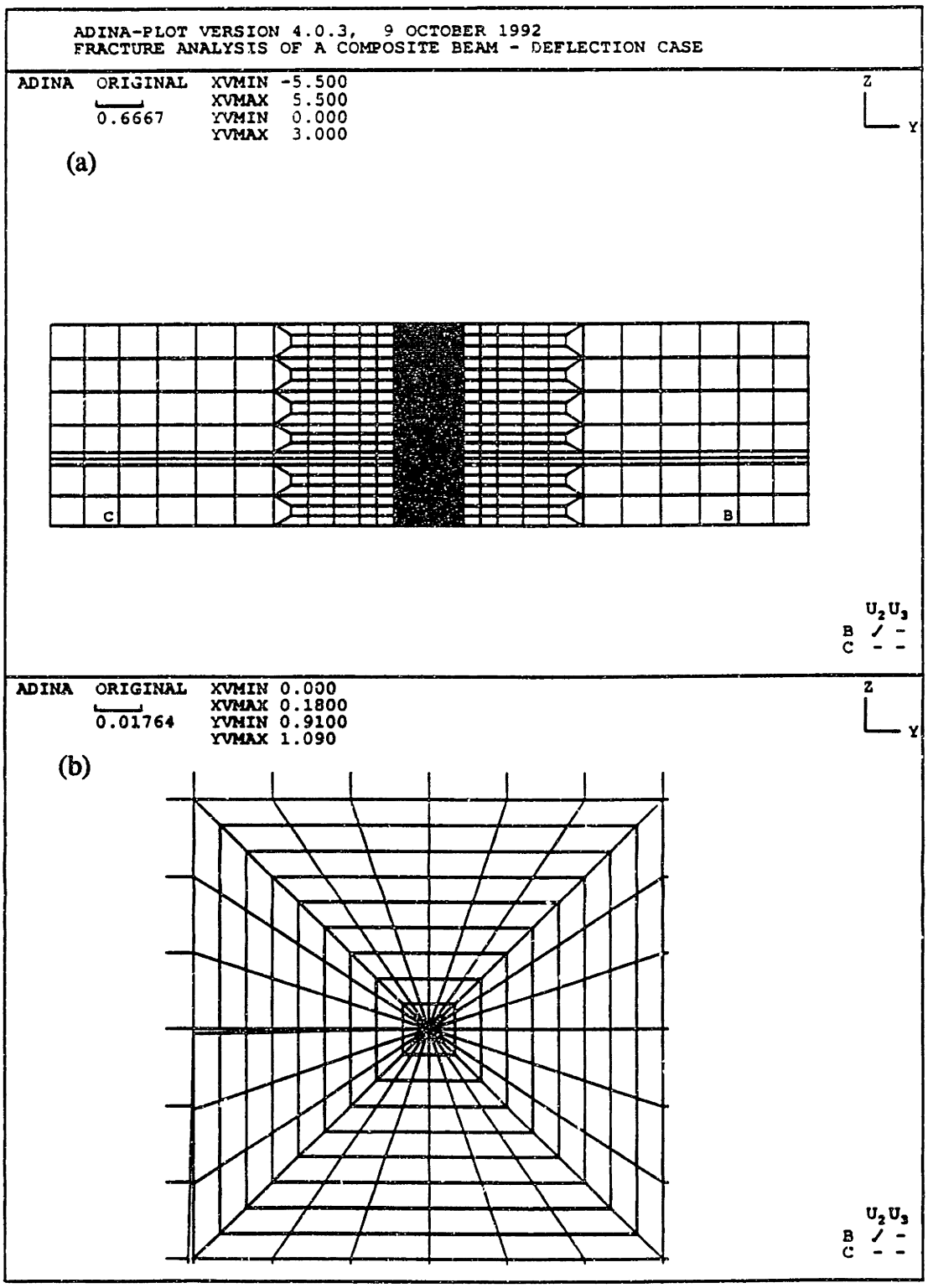

Figure 8.6 Finite element modeling of a beam composite model subjected to four-point bending: (a) Finite element mesh; and (b) Focused mesh around the crack tip

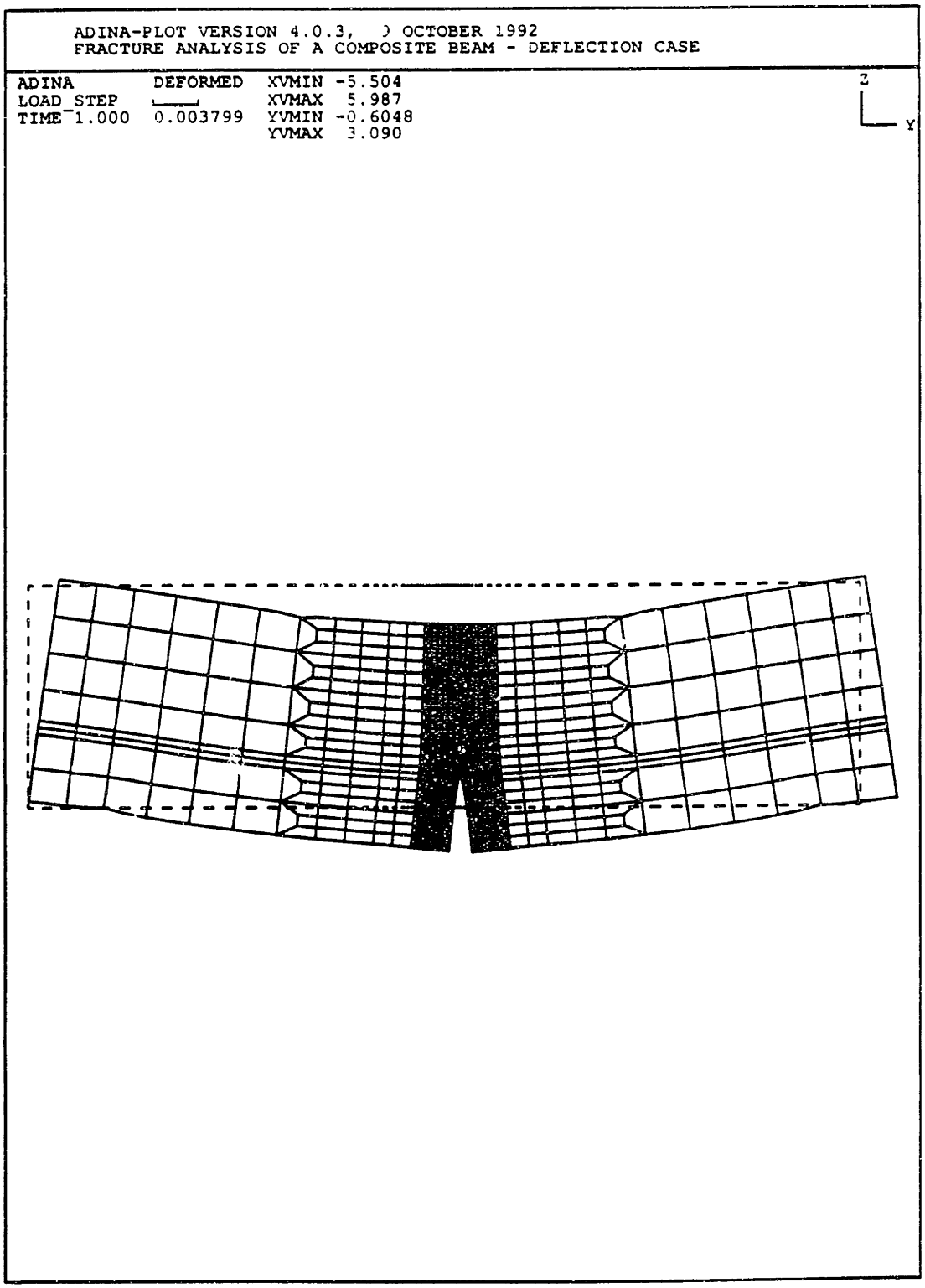

Figure 8.7 Deformed and original meshes for a beam composite model subjected to four-point bending

Chapter 9

Material Design of High Strength Concrete

High strength concrete should have good ductility as well as high strength and high stiffness for an effective and innovative applications in structures. High strength concrete should also be more durable due to lower permeability and possess good abrasion resistance. Properties of high strength concrete can be altered by changing its compositions, or by using different manufacturing procedures, etc. Furthermore, a better understanding of the effects of microstructures and cracking mechanism on the overall concrete performance can provide a better control in the production of high strength concrete. In this Chapter, factors controlling high strength concrete properties will be addressed with emphasis on the role of interfaces and aggregates. Afterward, results from two-phase composite model tests and real concrete tests will be presented to examine factors governing the basic mechanical properties of concrete: strength, stiffness, and toughness. Finally, based on fracture mechanics parameters, guidelines for the development of high strength concrete will be discussed.

9.1 Factors Controlling High Strength Concrete Properties

There are several ways to produce concrete with higher strength, e.g., reducing water/cement ratio and/or adding admixtures such as silica fume and superplasticizers. Although high strength usually refers to high compressive strength, most factors influencing compressive strength may have the same effects on tensile strength or elastic modulus. For example, using small-size aggregate reduces the size of the bond cracks and the initial dominant crack size, resulting in both high compressive and high tensile strengths. The addition of silica fume in combination with superplasticizers can lead to reduced water demand, densified cement paste, and stronger bonding. The resulting higher strength concrete is characterized by the distribution of fine pores and the densification of the microstructure in the cement paste-aggregate interfacial zone. In this section, the factors controlling strength, stiffness, and toughness of concrete will be discussed in the light of the available theoretical models and experimental results.

9.1.1 Strength

The compressive strength of brittle solids such as ceramics and concrete is much greater than the tensile strength because in tension the material can fail by rapid propagation of a single flaw or microcrack. Since a number of cracks must coalesce together to cause a compressive failure, in compression much more energy is needed for the formation and extension of the microcrack system. In general, compressive strength decreases with increasing pore size or total porosity and increases with reduced aggregate size. Even with good mixing, bleeding may produce large inhomogeneities near the aggregate and in particular, the site of the largest aggregate particle is often associated with the largest flaw. They may reduce the concrete strength. As long as large pores and microcracks continue to be present in the

interfacial zone, the strength of aggregate particle simply plays no part in determining the strength of the concrete composite since there is no effective stress transfer between the bulk cement paste and aggregate.

It has been reported that an improvement in interfacial bond strength would increase the tensile strength, and to a lesser extent the compressive strength, of concrete. However, there are many contradictory results, and information on the role of interfaces in concrete strengths is rare. Hence, this aspect needs to be studied further. On the effects of interface bonding on concrete strength Mindess [1988] indicated that "most studies of strength, be it tensile, compressive or flexural, have shown that improving the cement-aggregate bond strength does increase the concrete strength, but the effect tends to be moderate. In going from little or no bond to the best bond that can be achieved, strength have been observed to increase by about 20-40%".

The aggregate properties are also important factors determining the compressive strength of high strength concrete. Many attempts have been made to study the effects of aggregates on the strength and elastic modulus of high strength concrete [Aitcin and Mehta, 1990; Baalbaki et al., 1991]. The results of uniaxial compressive test on concrete cylinders incorporating with four different aggregate types are shown in Fig. 9.1. The average 28-day compressive strength values for concretes made with granite, gravel, limestone, and diabase were 85 MPa, 92 MPa, 97 MPa, and 101 MPa, respectively. It was found that the concrete mixtures containing either granite or gravel aggregate gave lower strength than the corresponding concretes containing either diabase or limestone. A probable cause for this behavior was identified on examination of the failure surface of test specimens. The occurrence of an exclusively transgranular type of fracture in the granite concrete proved that the granite aggregate used was indeed a weak aggregate. The gravel aggregate concrete exhibited the numerous cases of aggregate-cement paste debonding, indicating the weak interfaces. Both limestone and diabase concretes showed little evidence of aggregate-cement

paste debonding, but frequent occurrences of transgranular fracture due to the strong interfaces.

Unfortunately, although the factors influencing concrete strength is generally known, it has not as yet been possible to develop equations for strength. Strength depends not only on the properties and proportions of the components of concrete, but also on the cement paste-aggregate interfacial bond and the failure mechanism. In addition, realistic strength models must take into account the way in which cracks initiate and then propagate. Mindess [1989] indicated some problems in the strength model development: "we do not know what the strength-determining flaws in concrete are. Is strength governed by the stress concentrations around the gel pores? Around the capillary pores? At the cement paste-aggregate interface? Or simply by the total porosity? Only when we can provide unequivocal answers to such questions will we be able to produce meaningful strength models, based not on elaborate curve-fitting procedures, but on the scientific principles".

In what follows, the existing micromechanical models for concrete strength prediction will be reviewed. The Griffith tensile fracture theory and concepts of continuum mechanics can be used to predict that the compressive strength of a homogeneous brittle material is eight times the tensile strength. In general, experimental data on compressive strength can be fitted to the equation [Mehta and Aitcin, 1990a]

$$C = C_0(1 - P)^m \tag{9.1}$$

where C is the compressive strength of the material containing the volume fraction porosity P, C_o is the intrinsic compressive strength at zero porosity, and m is a factor depending on intercrystalline bonding in the solid, shape and size of pores or flaws, grain size, and presence of impurities. It is observed from Eqn. (9.1) that as the total porosity increases, the compressive strength of the concrete decreases.

By the application of linear elastic fracture mechanics, it may be possible to predict the tensile strength of concrete composite. For high strength concrete in which bond cracking does not occur, the cracking stress subject to tension is given by

$$\sigma_o = \sqrt{\frac{\Gamma E}{\pi a}} \tag{9.2}$$

where 2a is the diameter of the largest matrix flaw (or other pores), Γ and E are the fracture energy and the elastic modulus of the concrete composite, respectively. According to Eqn. (9.2), tensile strength controlling parameter is not the total porosity, but the size of the largest flaw in the highly stressed regions of the concrete system.

It was reported that the tensile strength of a quasi-brittle Griffith material (e.g., concrete) can be expressed in terms of its fracture toughness (K_{IC}) and its critical crack tip opening displacement ($CTOD_C$) [Jenq and Shah, 1985; John and Shah, 1989]. The crack tip opening displacement is a general representation for the material's critical flaw sizes. The theoretical uniaxial tensile strength can be expressed as:

$$f_t' = C_t \frac{(K_{IC})^2}{E * CTOD_C} \tag{9.3}$$

where C_t is a coefficient and E is the elastic modulus of the concrete composite It should be noted that above two material properties, K_{IC} and $CTOD_C$, were measured from the overall composite response. It is observed from Eqn. (9.3) that in order to enhance the tensile strength of concrete, one has to increase its critical stress intensity factor and, in the mean time, reduce its critical crack tip opening displacement.

9.1.2 Elastic Modulus

The elastic modulus of high strength concrete is strongly influenced by the elastic properties of coarse aggregate, comparing to the bonding between the cement paste and aggregates. However, it has been reported that in high strength concrete there is a higher contribution of the bond strength to the modulus rather than in normal strength concrete. This aspect needs to be studied further. With a simplified assumption that concrete is composed of mortar matrix and aggregate inclusions, a number of studies have been done to predict the effects of the mechanical properties of the constituent on the elastic properties of concrete composites using simple composite theories such as the mechanics of materials and the elasticity theory [Mindess, 1988, 1989; Baalbaki et al., 1992]. The mechanics of materials approach to stiffness usually use the models sketched in Fig. 9.2. The models are composed of cement paste and aggregate inclusions that are assumed to be homogeneous and isotropic, and their Young's moduli and volume fractions are denoted to E_p and v_p for the mortar matrix, and E_a and v_a for the aggregates. Two models represents the upper bound and the lower bound of elastic modulus. The two more realistic models lie between these extremes.

An experimental study by Aitcin and Mehta [1990] showed that concrete mixtures containing either a granite or a gravel aggregate gave significantly lower elastic modulus than those containing either a diabase or a limestone aggregate (see Fig. 9.1(b)). The elastic modulus values for concretes made with granite, gravel, limestone, and diabase were 32 GPa, 34 GPa, 38 GPa, and 37 GPa, respectively. To understand the reasons underlying these differences in behavior, the stress-strain curves and the loading-unloading hysteresis loops for concrete mixtures were examined (see Fig. 9.1). Loading and unloading of specimens in the elastic range produced much wider hysteresis loops in the case of concrete containing the granite and gravel aggregates. A large residual strain on unloading is indicative of either a weak interface or sources of weakness present within the aggregate particle. In the

case of limestone or diabase aggregates, a narrow hysteresis loop, which tended to close completely (no plastic strain within the elastic range), was indicative of a strong aggregate and a strong interface between the aggregate and cement paste in concretes.

9.1.3 Fracture Toughness

There is general agreement that, qualitatively, plain concrete becomes more brittle as its strength increases. There are contradictory results, however, as to the quantitative aspects of the stress-strain behavior of high strength concrete. Nevertheless, it has been accepted that as the strength of concrete increases, the ascending branch of the compressive stress-strain curve becomes more nearly linear, even as the peak load is approached. Of more significance, the descending branch of the curve becomes much steeper. This brittle deformation and failure behavior is caused by a strong bond at the interface between the matrix and the aggregate.

The ductility of high strength concrete can be expressed using fracture energy values. Fracture energy indicates the material's capability in dissipating energy during crack propagation. Higher fracture energy means that the material will behave in a ductile manner. Therefore, one important aspect in developing high strength concrete is to increase the fracture energy values. It was shown that if a concrete composite is made of materials with similar properties, the increase in fracture energy is very limited because this increase is bounded by the highest fracture energy value of the basic constituents and the composite exhibits a homogeneous behavior. Low ductility of high strength concrete is attributed to this fact because high strength mortar matrix is as tough as aggregate. Therefore, in order to achieve the better ductility of high strength concrete, in selecting materials the fracture property difference between mortar and aggregate should be considered, and furthermore, better understanding of the toughening mechanisms of concrete is essential. In what follows, the major toughening mechanisms for concrete are discussed.

As the dominant crack expands into the matrix in normal strength concrete, the toughness of the concrete is expected to be higher than that of the matrix because the dominant crack will deflect around the cement paste-aggregate interface (or mortar-aggregate interface) as it intercepts an aggregate and the distributed interfacial cracks in front of the dominant crack will provide a shielding effect. The former toughening mechanism, the crack deflection toughening, will be discussed first. The fracture path is generally tortuous in normal strength concrete, in contrast to plain cement paste in which the fracture path is rather planar. The tortuosity of the fracture path may be related to the crack deflection effect. When the dominant crack intercepts another aggregate, it would most likely deflect around the aggregate because the cement paste-aggregate interface is weak. Deflection reduces the stress intensity factor at the new crack tip because the deflected crack tip orientation is no longer perpendicular to the applied load, and then, the material toughness increases. In addition to the deflection toughening, the presence of cracks at the interfaces may influence the toughness. The interfacial cracks reduce the elastic modulus of the material ahead of the dominant crack. The stress intensity factor at the dominant crack tip is lowered by the reduced local modulus, providing a shielding effect on the dominant crack and resulting in a toughening effect.

In high strength concrete with good interfacial bonding and small-size aggregates, cracks do not necessarily nucleate at the cement paste-aggregate interface (or mortar-aggregate interface), and crack path usually go through course aggregate particles, implying a different failure mechanism compared with that in normal strength concrete. Therefore, toughening due to the crack deflection or distributed interfacial cracks will no longer exist. In this case, different toughening mechanisms are applicable, namely, crack front trapping mechanism and crack bridging mechanism. The idea of the crack front trapping mechanism is that a straight crack front approaching a well bonded particle would be hindered in its propagation at the particle site (Fig. 9.3). As the rest of the crack front bows around this trap site, the

stress intensity factor at this bow-out portion of the crack front is reduced, resulting in a retardation of its propagation process. The stress intensity factor of the crack front at the trap site, however, would rise with increasing amount of the adjacent crack front. Further propagation would require additional loading, thus providing an apparent toughening effect to the composite. In crack front trapping mechanism the concrete toughness increases as the volume fraction of aggregates in concrete increases [Huang, 1990].

If the crack front passes the trap site without rupturing the particle or breaking the interfacial bond, a complete bridge is left behind. This particle bridge acts as a spring exerting a closing pressure on the crack flanks. The resulting reduction of the crack driving force leads to an additional toughening effect. As the crack front moves forward, a series of bridges will be left behind forming a process zone (Fig. 9.4). The extent of the process zone and the amount of energy absorbed depends on the constitutive behavior of the bridge springs. Various spring actions result in different bridging mechanisms. It was reported by Huang [1990] that if the aggregate particles exhibit elastic and brittle behavior, the energy absorption in the process zone would not be significant. This is likely to be the case of high strength concrete in which the aggregates would be elastically stretched and eventually ruptured in the small size of process zone.

9.2 Testing of Composite Models and Real Concrete Specimens

9.2.1 Description of Composite Models

In the previous section, general principles governing high strength concrete properties were reviewed and however, for the high strength concrete development the following questions still exist:

1. What is a major factor to control compressive strength and elastic modulus of high strength concrete? Is it true that the uniaxial compressive strength is controlled by the weakest component of the concrete?

2. Is the fracture toughness of high strength concrete affected by the cracking scenarios in interfacial regions? What are additional factors to influence the ductility of high strength concrete?

In order to answer these questions, two-phase composite models are proposed and tested. They include block specimens subjected to uni-axial compression shown in Fig. 9.5(a) and beam type specimens shown in Fig. 9.5(b). Each specimen is composed of one or more aggregate inclusions embedded in a mortar matrix. To simplify the models the circular types of aggregate inclusions are selected, although regular aggregates have various shapes such as cubic and elliptical. The shapes of all models are prismatic and rectangular.

The block specimens have been widely used in past research [Buyukozturk et al., 1971, 1972; Liu et al., 1972; Mitsuru and Mitsunori, 1986; Maji and Shah, 1988; Oumera, 1991] for studying the microcracking and deformation of concrete under compressive loading. Friction problems in compression test of the block specimens can be significantly reduced by using aluminum blocks at top and bottom of the specimens [Oumera, 1991]. By testing the block specimens uni-axial compressive strength and elastic modulus of concrete composite can be determined.

The pre-notched beam specimens subjected to three-point bending have been used to measure either the mode I fracture toughness (K_{IC}) or the fracture energy (G_F) of concrete. The beam specimens have a pre-crack at the middle of the long span and embed one or more aggregate inclusions ahead of the pre-crack. By testing these specimens the fracture energy values, G_F, and two linear elastic fracture mechanics (LEFM) parameters, the model I fracture toughness, K_{IC}, and the critical crack tip opening displacement, $CTOD_C$, can be

determined. During the testing of the specimens, a crack that initiates in the mortar matrix is predicted to reach an aggregate inclusion and then to hit the aggregate. Now, one can expect three crack paths: (1) crack stops due to the crack arrest by the aggregate; (2) crack goes through aggregate provided that the aggregate is weak and the interface is strong; and (3) crack goes around the aggregate, i.e., aggregate debonding occurs. These expected different crack patterns may strongly influence the toughening mechanism of high strength concrete. In order to observe the crack front trapping mechanism, type 1 cross section is proposed (Fig. 9.5(b)) and then, the beam specimen can be considered as a three-dimensional model.

9.2.2 Details of Composite Models and Materials

To examine factors controlling the compressive strength and the elastic modulus of high strength concrete, block specimens whose dimensions were 76.2 mm (3.0 in : width) x 101.2 mm (4.0 in : height) x 25.4 mm (1.0 in : thickness) were tested. The size of the inclusions were 38.1 mm (1.5 in : diameter) x 25.4 mm (1.0 in : height) for specimens with one inclusion (Block 1) and 22.225 mm (0.875 in) x 25.4 mm (1.0 in) for specimens with two inclusions (Block 2). Volume fractions for Block 1 and Block 2 were 0.15 and 0.10, respectively.

In order to make block specimens two mortar mixes (M1 and M3) were used and two aggregates, granite and limestone, were selected to make aggregate inclusions. The mix proportions of the mortar mixtures were listed in Table 6.1. Mechanical properties and other parameters such as Dundurs' mismatch parameters are given in Tables 6.2 and 6.3. The average 28-day compressive strengths of M1 and M3 were 42.5 MPa and 80.5 MPa, respectively. The elastic modulus of M1 and M3 were 27.8 GPa and 39.2 GPa, respectively.

9.2.3 Preparation of Composite Specimens and Testing Procedure

The block specimens which were made of different combination of mortar matrix and aggregate were manufactured and tested. In manufacturing the test specimens, aggregate inclusions were prepared first and then, the mold in which six block specimens could be manufactured at the same time was prepared. Aggregate inclusions were cored from rock blocks using a diamond core. After placing the aggregate inclusions in the mold, mortar mixtures were made. The procedure for mortar preparation was given in Section 6.4. After the fresh mortar was poured into the mold, the specimens were covered with plastic for 24 hours. After that, they were placed in water. All specimens were tested after 28 days of curing.

Fig. 9.6 shows the loading configuration of the uni-axial compression test of block specimens. A block specimen was placed between top and bottom platens of Baldwin machine and then, uni-axial compressive loading was applied with a stroke control at a loading rate of 0.0508 mm/min. Two LVDTs were placed to measure the relative displacement of two positions, as shown in Fig. 9.6. From the test results, the compressive strength and the elastic modulus were determined.

9.2.4 Results from Composite Model Tests

The results from block specimen tests are listed in Table 9.1, including failure loads, compressive strengths, and elastic moduli. Figures 9.7 and 9.8 show the relative mechanical properties for all tested systems. They include the fracture energy values obtained from pre-notched beam tests performed by Kitsutaka et. al [1992]. Measured compressive strengths of mortars were about 20% higher than those from the cylinder tests. This is attributed to the differences of specimen geometries and/or failure patterns. The block specimens usually exhibited splitting failure. The compressive strength of M1/G and M1/L are almost the same as that of M1, indicating that the strength control factor is M1 for both systems.

However, M3/L system shows 15% lower strength than M3, whereas the strength of M3/G system is somewhat higher than that of M3. Therefore, in M3/L system the limestone controls the compressive strength and in M3/G system M3 controls the compressive strength, implying that the uniaxial compressive strength of concrete composites is controlled by the weakest component.

Elastic moduli of M1/G and M3/G systems are higher than those of M1 and M3, respectively, but those of M1/L and M3/L systems are almost equivalent to those of mortar systems. This may mean that granite, with higher elastic modulus than M3, considerably influences the elastic modulus of the M3/G composite but limestone, with lower elastic modulus than M3, weakly affects the elastic modulus of the M3/L composite. However, since the test results are obtained from a small number of specimens with only one or two inclusions, further experiments are needed to confirm these results. Failed specimens are shown in Fig. 9.9 and Fig. 9.10. The failure mode of M1/L and M3/L systems is more complicated than that of M1/G and M3/G systems. An interesting observation is that during testing of M3/L system, the limestone inclusion failed first, leading to its low strength. Load versus load-line displacement curves and crack patterns for tested block specimens are given in Fig. B.1 - Fig. B.8 of Appendix B.

Both M1/G and M1/L systems with one inclusion (type 2 cross-section in Fig. 9.5(b)) have smaller fracture energy than M1 but M1/G system with two inclusions (type 1 cross-section) has higher fracture energy than M1 or M1/L system [Kitsutaka et al., 1992]. Both M3/G and M3/L systems with one inclusion (type 2 cross-section) have smaller fracture energy than M3. These mean that composite beam models embedding discontinuous inclusions (type 2 cross-section) may simulate well the real concrete behavior because the granite concrete is expected to have higher fracture energy than the mortar. It is observed that crack path of M1/G and M3/G systems is crack deflection, while crack path of M1/L and M3/L systems is crack penetration. This implies that the crack patterns influenced by

the relative fracture properties between aggregates and interfaces considerably affect the toughening mechanism in concrete.

9.2.5 Results from Real Concrete Specimen Tests

To avoid the limitations of composite models such as two-dimensional condition and low volume fraction of aggregates, real concrete specimens were manufactured and tested. They included cylinders (76.2 mm x 152.4 mm) for uni-axial compression test and pre-notched beams (228.6 mm x 76.2 mm x 50.8 mm) for fracture energy test. One mortar mix (M3) and two types of crushed aggregate (granite and limestone) were used. Maximum size of aggregates was 18.0 mm and volume fraction of the aggregates was 0.35 for both M3/G and M3/L concretes. In manufacturing the specimens, aggregate materials were prepared first by crushing granite and limestone blocks and then, mortar mixture was made and mixed with crushed rocks. After the concrete mixture was poured into the mold, the specimens were covered with plastic for 24 hours. All specimens were tested after 28 days of curing in water.

Table 9.2 lists the results from the real concrete tests and Fig. 9.11 shows the relative properties of M3, M3/G concrete and M3/L concrete. From the tests of cylinders, 28-day uniaxial compressive strength and elastic modulus of concrete were determined. The compressive strength and elastic modulus of M3/G concrete were almost same as those of M3 but the compressive strength and elastic modulus of M3/L concrete were 35% and 15% lower than those of M3, respectively. This implies that in high strength concrete, weaker component material controls the compressive strength and elastic modulus. This agrees with the results obtained from block specimens tests.

From the tests of pre-notched beam specimens, the fracture energy of concrete was determined. Load versus load-line displacement curves for tested beam specimens are given in Fig. B.9 - Fig. B.11 of Appendix B. The fracture energy of M3/G concrete was 50% higher

than that of M3, whereas the fracture energy of M3/L concrete was 10% lower than that of M3. This indicates that granite with high strength and toughness considerably enhances the fracture energy of high strength concrete but limestone with low strength and toughness weakly affects the fracture energy value. It was observed that both granite concrete and limestone concrete exhibited same cracking mode of transgranular cracking although their fracture energy were quite different. This implies that the fracture energy of concrete is affected by the aggregate type as well as the crack pattern. Therefore, to increase fracture energy of high strength concrete aggregates with good qualities are needed and then, proper interfacial properties influencing the cracking behavior are required to engineer optimum material behavior of the concrete.

9.3 Guidelines for Mix Design of High Strength Concrete

9.3.1 Material Design Parameters

For producing high strength concrete, the relative properties of mortar, aggregates, and interface between them should be considered. Assuming that mortar matrix is fixed, material design parameters based on fracture mechanics approach are proposed in the following:

- α - Dundurs' parameter describing the elastic modulus mismatch between two mortar and aggregate in plane strain condition (Eqn. (4.1))

At high levels of stress, there is a stress concentration at the mortar-aggregate interface due to the large difference in the elastic modulus between the mortar and the aggregate. The parameter α may affect the bond cracking development and the stress transfer in concrete.

- $D = \Gamma_i(\psi)/\Gamma_a$ - the ratio of interface fracture energy to mode I fracture energy of aggregate

The parameter D can be used to explain the competition between deflection and penetration of a crack impinging to an interface. The interface cracking occurs provided that D is

less than a critical value D_C for given geometry and loading conditions. The presence and effectiveness of the toughening mechanism would depend on D. In particular, the deflection toughening and the crack front trapping mechanism are strongly influenced by D. If the aggregate particle is weak, the crack may penetrate into the particle, and the trap site would then be eliminated by particle failure. If the matrix-aggregate interface is not strong enough, the crack front at the trap site may rapidly turn onto an interfacial crack, and only partial trapping can be obtained, but the crack deflection toughening may occur. If the matrix-aggregate interface is extremely weak, the trap size may vanish. Eventually, by altering the ratio D, one can control the toughness of concrete.

The parameter D is applied to investigate the cracking behavior of M3/G composite system. For this combination the value of α is 0.099. When the aggregate shape is assumed to be circular, an average hitting angle is predicted to be 60^o for cracks impinging to interface between mortar and aggregate. Then, from Figs. 4.8 and 4.9 the critical value D_c and the corresponding phase angle are found to be 0.55 and 40^o, respectively. The values of $\Gamma_i(40)$ and Γ_g, mode I fracture energy of granite, are 7.0 J/m^2 and 17.5 J/m^2, respectively. Finally, the ratio D is calculated to be 0.40 which is less than 0.55, the critical value and thus, it is predicted that at least half of impinging cracks is deflected along the interface, i.e., interface cracking occurs. If transgranular cracking is preferable, higher interfacial toughness should be used. However, for the practical use of D in material design of high strength concrete, the study of the role of D in the toughening mechanism is needed.

- $F = \Gamma_i/\Gamma_m$ - the ratio of interface fracture energy to mode I fracture energy of mortar

The parameter F can be used to explain the competition between crack kinking into the mortar matrix or crack propagation along the interface. The crack kinking occurs provided that F is larger than a critical value F_C for given geometry and loading condition. This ratio governs the crack path and the interaction between bond cracks and mortar cracks,

influencing the toughening mechanism of concrete.

Besides these fracture mechanics parameters, the following parameters associated with aggregates are important:

- v - the aggregate volume fraction

Concrete is a composite material consisting of cement paste and aggregate. The cement paste is the binder for the aggregate. In general, the strength, permeability, and other properties of concrete depend on the binder/aggregate ratio and the quality of each of the two materials. In concrete production, the volume fraction of aggregate is usually limited to 65 % for the adequate dimensional stability of concrete.

- MSA - the maximum size of coarse aggregate

To maintain both strength and toughness, it may be necessary to optimize the mix with respect to aggregate size. There is some controversy regarding the choice of maximum size of aggregate (MSA). With high-strength concrete mixtures, there is a large amount of data showing that the use of larger than 25 mm MSA generally impairs the strength and impermeability of concrete. Since the interfacial zone is strong in high strength concrete, the aggregate can indeed be strength limiting, which is seldom a matter for concern with conventional concretes. With most rocks, reducing the MSA to 10 to 15 mm often eliminates any internal defects present within the aggregate particle (such as microcracks, large pores, and inclusions of soft minerals). Hence, 10 to 15 mm MSA may be considered optimum for high strength concrete.

9.3.2 Procedure for Mix Design of High Strength Concrete

In conventional mix design method all materials are mixed at the same time and hence, it is difficult to identify the fracture mechanics parameters given in previous section. To avoid

this difficulty a mix design method is proposed, based on the material design parameters and general considerations for material selection and proportioning. This step by step mix design procedure for high strength concrete is summarized as follows:

Step 1: Choice of Compressive Strength

One choose a 28-day compressive strength ranging from 41 MPa (6,000 psi) to 123 MPa (18,000 psi) and elastic modulus of concrete. Other properties for special purposes are specified.

Step 2: Mix Design of Mortar Mixture

One mortar mixture having about 5 - 10 % higher compressive strength than the aimed concrete is prepared in this step because the laboratory mixtures usually show somewhat higher strength. Cementitious material types are determined first. For this, four options are available as following: Option 1 - Portland cement (PC) alone, Option 2 - PC and silica fume (SF), Option 3 - PC and SF and either fly ash (FA) or blast-furnace slag (BAS), and Option 4 - PC and either FA or BAS. By a cost-benefit analysis based on local situation, one option is selected. After the volume fraction of cement-paste components is fixed, amounts of water and cementitious materials are determined. Water/cementitious material ratio is dependent on the aimed strength. Next, the amounts of fine aggregates are determined, based on the total volume fraction of aggregate materials. As fine aggregate (< 0.5 mm), natural sands with a medium-to-high fineness modulus (viz. 2.5 to 3) are generally adequate. The dosage of superplasticizer is then estimated to satisfy the workability (or slump values) of mortar mixture. The mix proportions for the first trial mortar mixture are calculated and then, laboratory test using actual mortars is performed. From the test, following mechanical properties of the mortar are measured: 28-day compressive strength, elastic modulus, Poisson's ratio, tensile strength, and mode I fracture energy. The slump value is

also measured.

Step 3: Selection of Rock

The choice of rock type for making coarse aggregates is very important in high strength concrete production. For use as coarse aggregate, equidimensional particles, obtained by crushing a dense limestone rock or a plutonic-type igneous rock (such as granite and diabase), are usually satisfactory. Certain types of rocks may impair the concrete properties. The tensile strength of aggregates would be important in controlling concrete toughness, and this is also consistent with experience in controlling compressive strength. Of rocks locally available two or three types are selected first and their mechanical properties are measured. Next, the fracture mechanics parameters are calculated. After examining the effects of the parameters on the concrete properties, one type of rock is chosen.

Step 4: Trial Batch Adjustment

First trial batch using the actual constituent materials selected in previous steps is prepared and tested. If the measured properties are satisfactory, this mixture can be used as an initial concrete batch. If not, after adjusting the mix proportions of mortar mixture and/or selecting the other rock type, one repeats actual concrete testing.

The mix design procedure described above is shown schematically in Fig. 9.12.

9.4 Control of Interface

Many attempts have been made to modify the cement paste-aggregate interface or the mortar-aggregate interface in order to improve the concrete properties. These attempts have been mostly in the form of aggregate coating and aggregate surface treatment. In concrete production, the latter has been popular for enhancing the strength of the concrete by crush-

ing aggregates, resulting in the rough surface of aggregates. The importance of controlling the interface properties is obvious in light of their significance in concrete performance. The theoretical studies concerning the interface effects on the concrete properties are expected to make these attempts more systematic and efficient by providing a guide towards achieving the optimum concrete properties.

Table 9.1 Results from block model tests

Specimen No.	Failure Load (kN)	Compressive Strength (MPa)	Elastic Modulus (GPa)
M1-0-1	94.7	49.0	22.4
M1-0-2	106.3	54.9	23.5
M1-G1-1	100.1	51.7	29.7
M1-G1-2	95.7	49.4	28.9
M1-L1-1	101.0	52.2	23.1
M1-L1-2	102.8	53.2	25.2
M3-0-1	183.3	94.7	-
M3-0-2	186.0	96.1	27.9
M3-G1-1	187.8	97.0	32.1
M3-G1-2	186.4	96.4	30.4
M3-G2-1	196.7	101.7	-
M3-G2-2	187.3	96.7	-
M3-L1-1	146.8	76.0	28.3
M3-L1-2	160.2	82.8	29.0
M3-L2-1	165.1	85.4	-
M3-L2-2	166.0	85.7	-

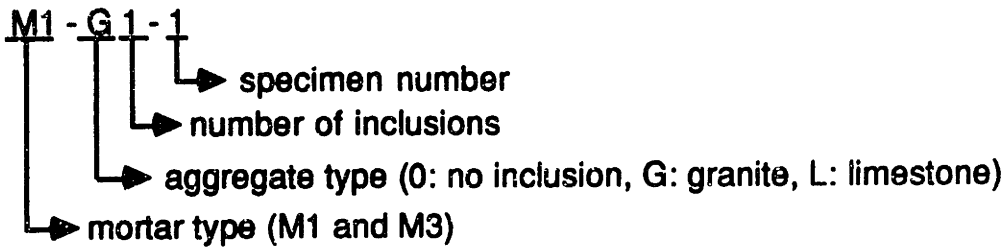

Table 9.2 Results from real concrete tests

Specimen No.	Compressive Strength (MPa)	Elastic Modu. (GPa)	Fracture Energy (J/m^2)
M3-0-1	75.4	41.1	75.5
M3-G-1	75.5	40.0	132.5
M3-G-2	72.5	38.0	103.9
M3-L-1	51.2	36.0	70.2
M3-L-2	48.0	34.6	67.3

Note : Compressive strength and elastic modulus were measured from the cylinder tests and fracture energy was measured from the pre-notched beam tests.

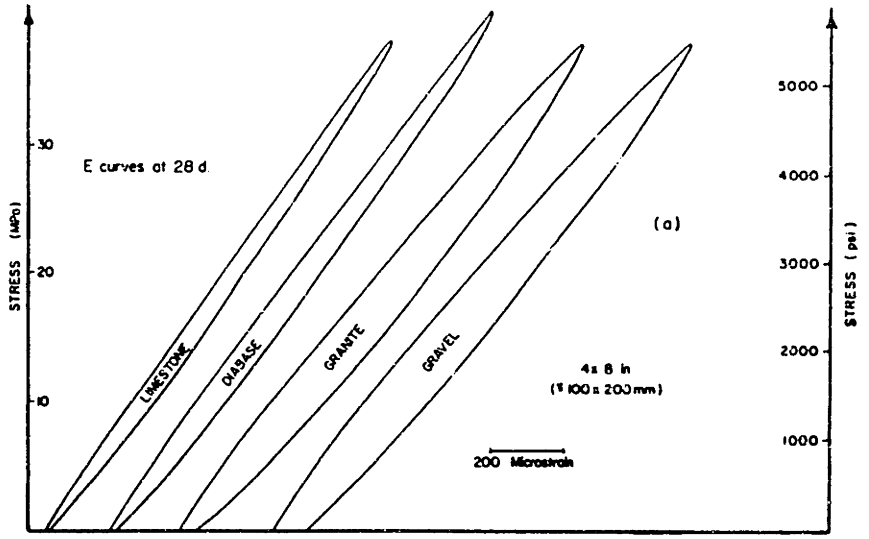

(a) Loading-unloading hysteresis loops

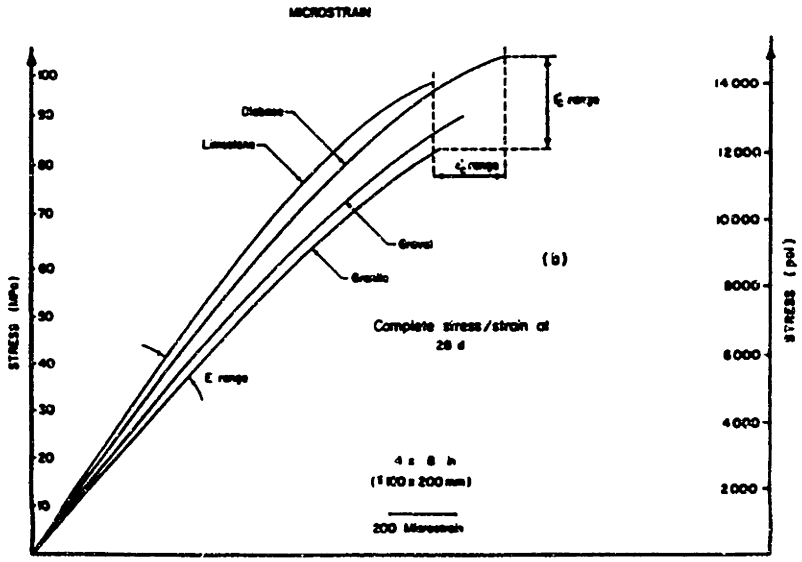

(b) Stress-strain behavior

Figure 9.1 Influence of aggregate type on strength and elastic modulus of high strength concrete (from Aitcin and Mehta [1990])

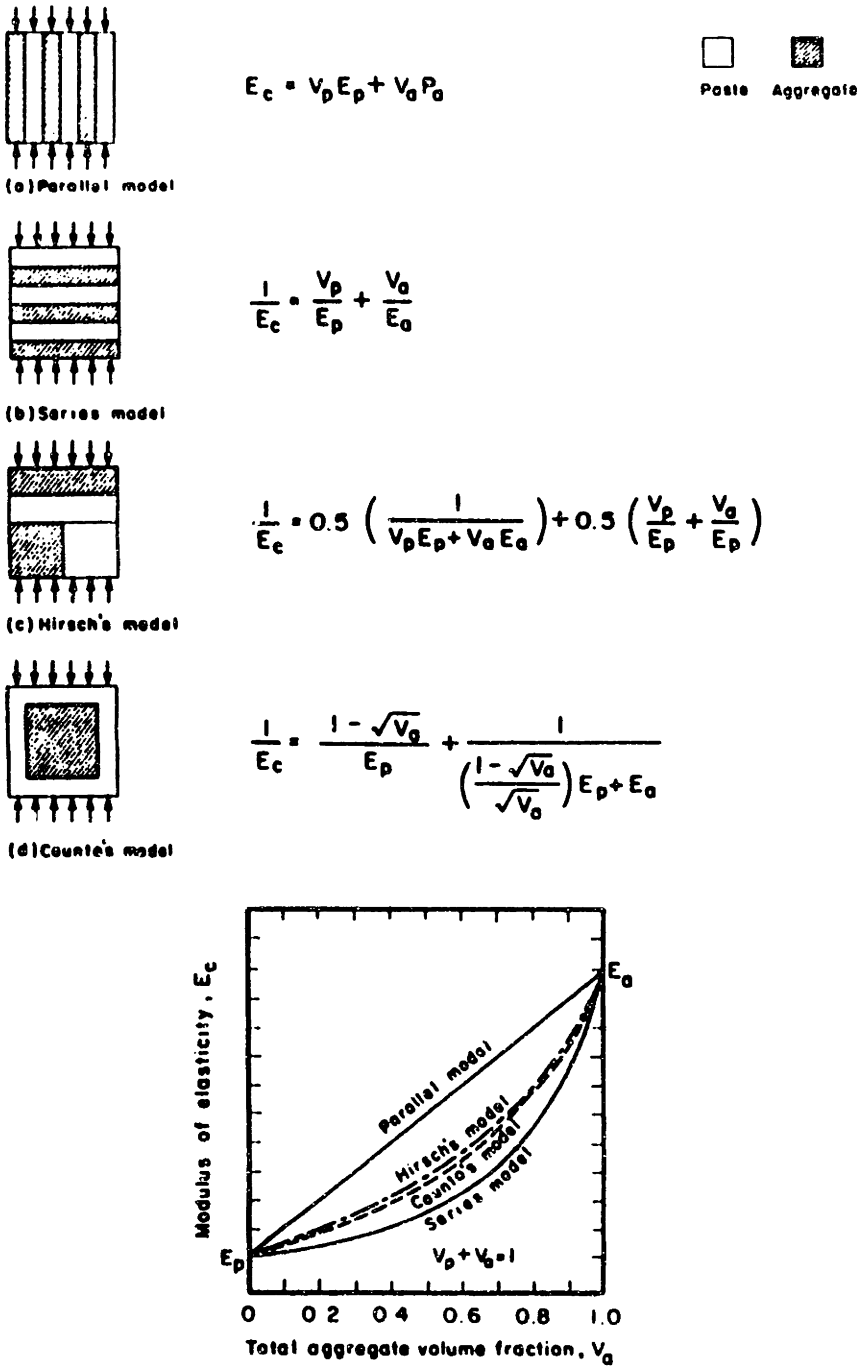

Figure 9.2 Models for the prediction of elastic moduli of concrete (from Mindess [1988])

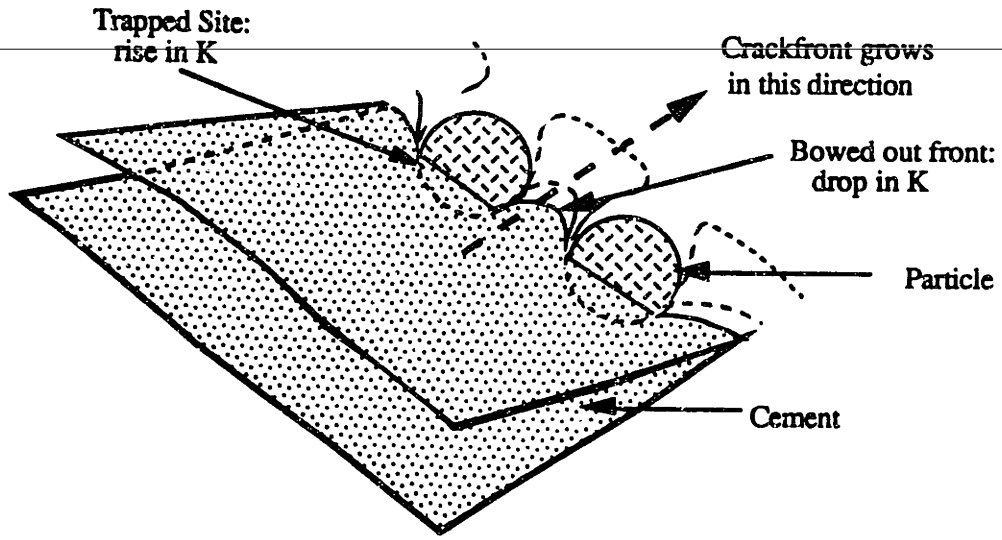

Figure 9.3 Crack front trapping mechanism (from Huang [1990])

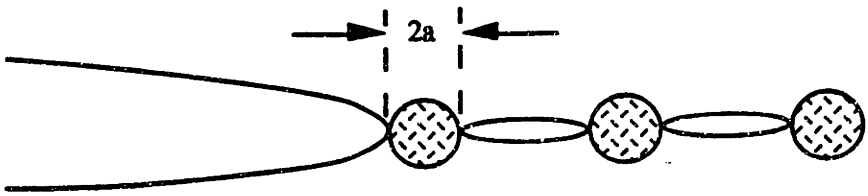

Figure 9.4 Bridge toughening mechanism (from Huang [1990])

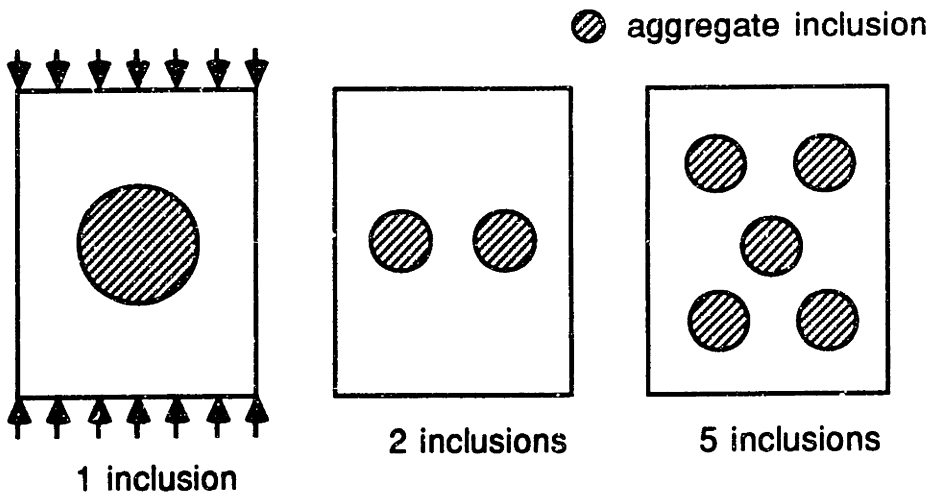

(a) Block composite models

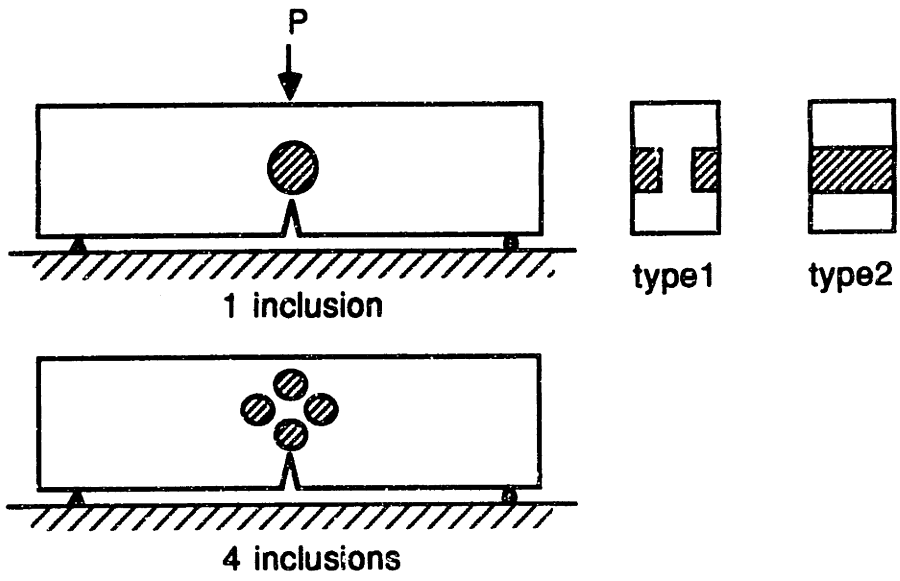

(b) Pre-notched beam composite models

Figure 9.5 Two-phase composite models

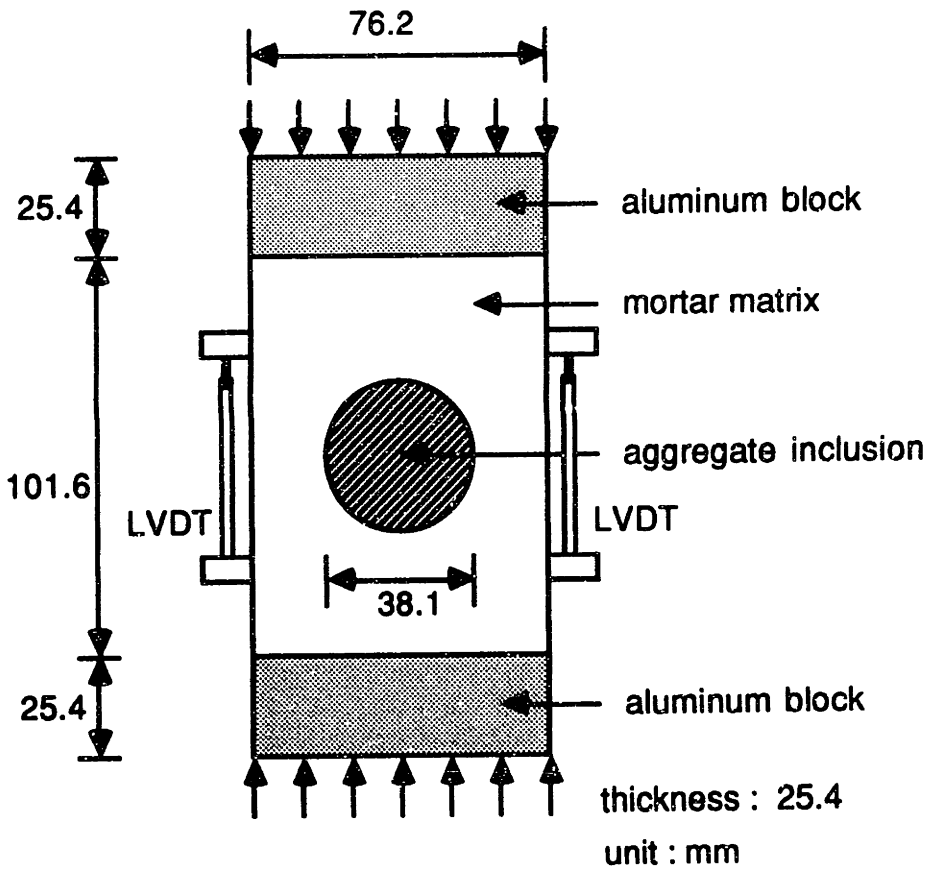

Figure 9.6 Loading configuration of block model subjected to uni-axial compression

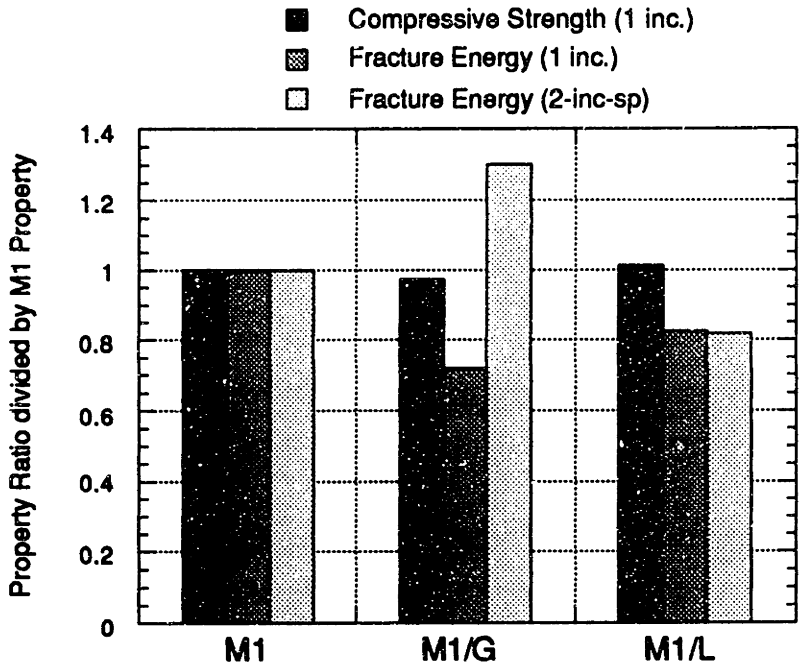

Figure 9.7 Relative properties of M1, M1/G, and M1/L composite specimens

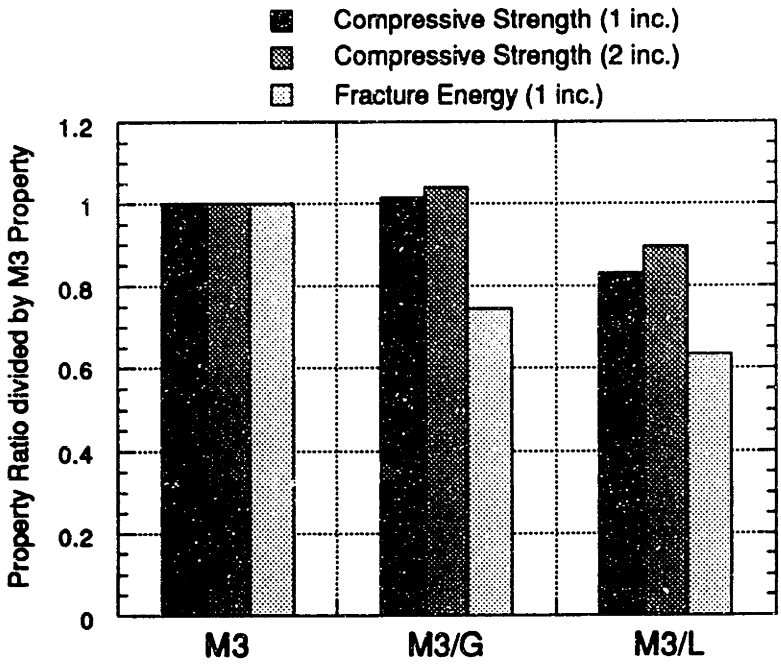

Figure 9.8 Relative properties of M3, M3/G, and M3/L composite specimens

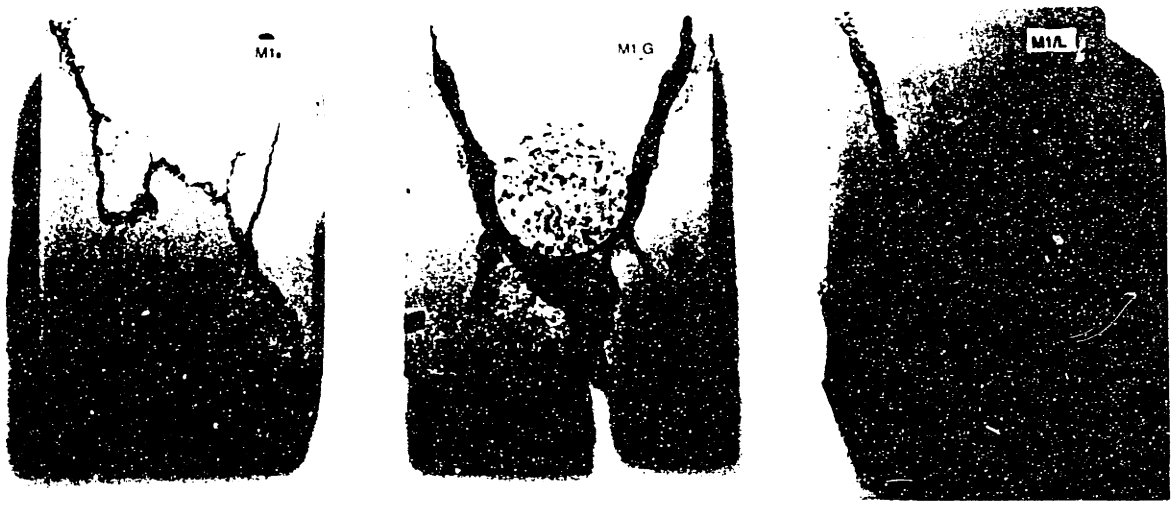

Figure 9.9 Failure mode of M1-0, M1-G1, and M1-L1 block specimens

Figure 9.10 Failure mode of M3-0, M3-G1, and M3-L1 block specimens

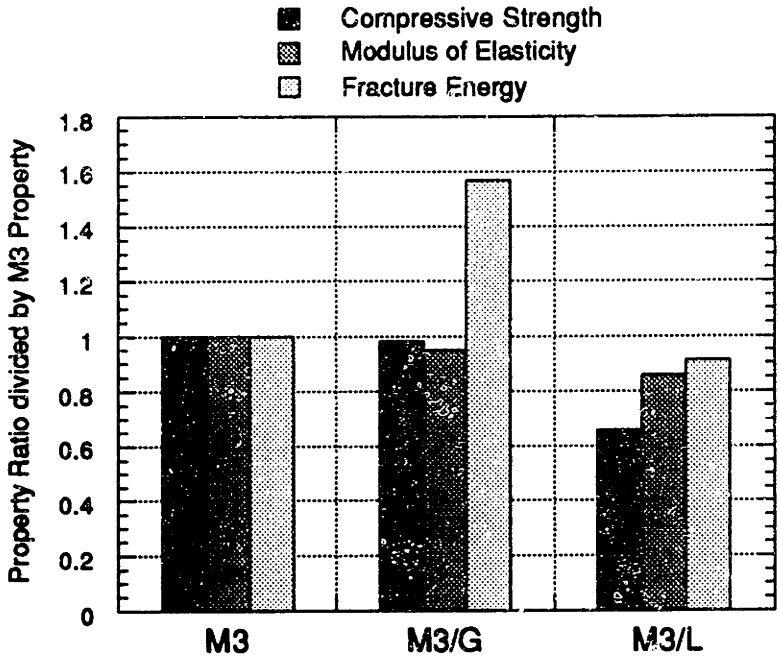

Figure 9.11 Relative properties of M3, M3/G concrete, and M3/L concrete

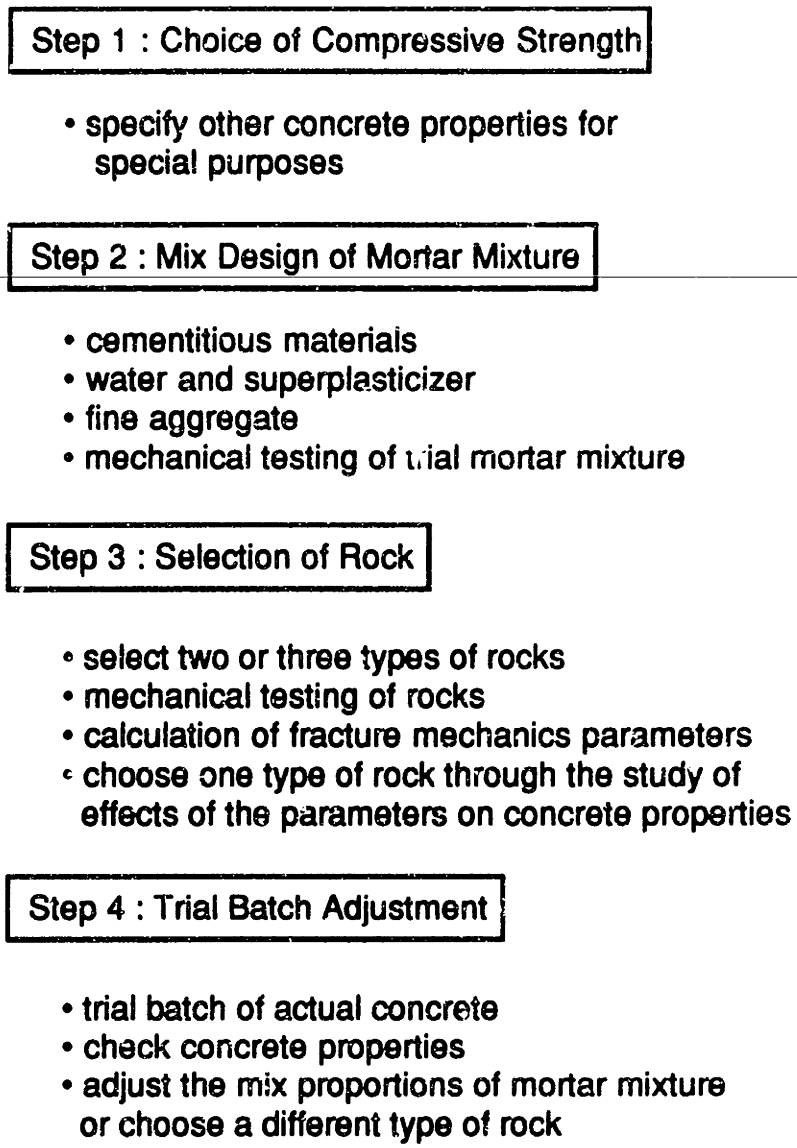

Figure 9.12 Mix design procedure for high strength concrete

Chapter 10

Summary, Conclusions and Future Work

10.1 Summary

In this research, novel experimental/numerical methodology based on fracture mechanics are developed to study the interfacial fracture in high strength concrete. In the study of the concrete fracture, the characterization of the mortar-aggregate interfaces is essential. However, at present no established method exists for the assessment of the fracture toughness of the mortar-aggregate interface. In this research, novel fracture models, called sandwich test specimens, are proposed and used to measure the interfacial fracture toughness under mixed-mode loading conditions involving tensile and shear loadings. They include the sandwiched beam specimen for mode I loading test and the sandwiched Brazilian disk specimen for mixed mode loading test.

The crack path criterion for elastically homogeneous materials is not valid when the crack advances at an interface because, in this case, the consideration of the relative magnitudes of the fracture toughness between the interface and the aggregate or the mortar are involved. For the prediction of crack path at interfaces, fracture criterion based on energy release rate concepts is considered and composite beam models are developed to investigate crack penetration versus crack deflection scenarios in interfacial regions. Analytical

solutions for interface cracking problems in semi-infinite body or simplified geometries exist but for complex geometries numerical methods must be employed. For the composite model study, fracture mechanics based numerical method is proposed for obtaining the two interface fracture parameters such as the energy release rate and the loading phase angle.

Finally, on the basis of fracture mechanics parameters and principles governing concrete behavior, a mix design procedure for high strength concrete is proposed. Composite models, including block specimens for uni-axial compression test and pre-notched beam specimens for fracture energy test, are proposed and tested to investigate factors influencing mechanical properties of high strength concrete. Also, to avoid some limitations which may be observed in composite models real concrete specimens are tested. This is an initial attempt in the field of interface fracture in concrete and fracture mechanics based material design for high strength concrete.

10.2 Conclusions

The main conclusions obtained from the research are given as follows:

Measurement of fracture toughness of mortar-aggregate interfaces

1. The fracture toughness of mortar-aggregate interface markedly increases as the loading phase increases due to the shielding effects. The fracture characteristics of high-strength mortar-aggregate interfaces are much different from those of normal-strength mortar-aggregate interfaces due to the silica fume effects with the use of superplasticizers and the reduced water amount on the interfaces. It is found that silica fume in combination with superplasticizers improves the bonding with the formation of a dense microstructure in the interfacial region due to the high pozzolanic reaction and the significant water reduction.

2. In high phase loading angles, Brazilian disk specimens composed of high-strength mortar and aggregate layer exhibit the crack kinking into mortar or aggregate. Only when crack propagation is confined to the interface, the fracture toughness of the interface can be obtained as a function of the loading phase angle. Therefore, the measured interface fracture toughness values for high phase angle is actually an underestimation.

3. Quantitative studies of interfacial fracture toughness can offer great potential for the understanding of the global behavior of concrete, leading to develop high performance materials.

Analyses of crack propagation in interfacial regions

1. A fracture criterion based on energy release rate concepts is applied to the crack penetration versus crack deflection problem in interfacial regions of concrete.

2. The results from the composite model study are well correlated with those obtained from fracture testing of sandwich test specimens. Fracture mechanics based numerical analysis can be appropriately applied to the study of cracking in the interfacial regions of concrete composites.

3. Experimental and numerical analyses of crack propagation can provide a scientific basis for the underlying mechanisms of cracking and failure of high strength concrete.

A guideline for the development of high strength concrete

1. For the efficient material development, material design parameters based on fracture mechanics approach are proposed. On the basis of these parameters and general considerations of material selection and mix proportioning of concrete, guidelines are proposed for manufacturing high strength concrete.

2. From the composite model tests basic principles are verified: the weakest material controls the compressive strength of high strength concrete. To improve fracture toughness of concrete, aggregates with good qualities should be used and then, proper interfacial fracture properties are required to engineer optimal behavior of concrete.

10.3 Recommendations for Future Work

1. The present approach is based on linear elastic interface fracture mechanics concepts and is considered to be appropriate due to the observed linear elastic behavior and brittle failure of the interfaces. This aspect needs to be studied further.

2. Experimental work should be extended to study the effects of roughness variations of aggregate surfaces, the size effects of the test specimens, the effects of the specimen geometries and the loading rate effects.

3. Experimental/numerical analysis on the composite models is an initial step for the crack propagation study and further studies are required to develop a general predictive capability. Furthermore, more comprehensive composite models for better representation of the cracking behavior of concrete should be developed.

4. For the quantitative study on the role of fracture mechanics parameters in global behavior of concrete experimental and analytical works should be performed.

Bibliography

[1] ACI Committee 226 (1987), "Silica Fume in Concrete," *ACI Materials Journal*, Vol. 84, March-April, pp. 158-166.

[2] ACI Committee 363 (1984), "State-of-the Art Report on High Strength Concrete," *ACI Journal*, Vol. 81, July-Aug., pp. 363-411.

[3] ACI Committee 363 (1987), "Research Need for High Strength Concrete," *ACI Materials Journal*, Vol. 84, Nov.-Dec., pp. 559-561.

[4] Ahmad, S. H., and Shah, S. P. (1985), "Properties of High Strength Concrete for Structural Design," *Very High Strength Cement Based Materials*, MRS Symposia, Vol. 42, pp. 169-181.

[5] Aitcin, P.-C., and Mehta, P. K. (1990), "Effect of Coarse-Aggregate Characteristics on Mechanical Properties of High Strength Concrete," *ACI Materials Journal*, Vol. 87, Mar.-April, pp. 103-107.

[6] Alexander, M. G., Mindess, S., and Qu, L. (1992), "The Influence of Rock and Cement Types on the Fracture Properties of the Interfacial zone," *Interfaces in Cementitious Composites*, RILEM Proceedings 18, pp. 129-137.

[7] ASTM (1983), "Standard Test Method for Plane-Strain Fracture Toughness of Metallic Materials," *Standard E399-83*, Annual Book of ASTM Standards, Vol. 03.01, pp. 519-554.

[8] Atkinson, C., Smelser, R. E., and Sanchez, J. (1982), "Combined Mode Fracture via the Cracked Brazilian Disk Test," *International Journal of Fracture*, Vol. 18, No. 4, April, pp. 279-291.

[9] Baalbaki, W., Aitcin, P.-C., and Ballivy, G. (1992), "On Predicting Modulus of Elasticity in High Strength Concrete," *ACI Materials Journal*, Vol. 89, No. 5, pp. 517-520.

[10] Baalbaki, W., Benmokrane, B., Chaallal, O., and Aitcin, P.-C. (1991), "Influence of Coarse Aggregate on Elastic Properties of High-performance Concrete," *ACI Materials Journal*, Vol. 88, Sept.-Oct., pp. 499-503.

[11] Bakhoum, M. M., Buyukozturk, O., and Beattie, S. M. (1989), "Structural Performance of Joints in Precast Concrete Segmental Bridges," *MIT Research Report No. R89-26*, Dept. of Civil Engineering, MIT, Cambridge, MA.

[12] Bentur, A., Goldman, A., and Cohen, M. D. (1988), "The Contribution of the Transition Zone to the Strength of High Quality Silica Fume Concrete," *Bonding in Cementitious Composites*, MRS Symposia, Vol. 114, pp. 97-103.

[13] Bentur, A., and Mindess, S. (1986), "The Effect of Concrete Strength on Crack Patterns," *Cement and Concrete Research*, Vol. 16, pp. 59-66.

[14] Buyukozturk, O., Nilson, A. H., and Slate, F. O. (1971), "Stress-strain Response and Fracture of a Concrete Model in Biaxial Loading," *ACI Journal*, Vol. 68, No. 8, pp. 590-599.

[15] Buyukozturk, O., Nilson, A. H., and Slate, F. O. (1972), "Deformation and Fracture of Particulate Composite," *Journal of Engineering Mechanics*, ASCE, Vol. 98, No. 6, pp. 581-593.

[16] Cao, H. C., and Evans, A. G. (1989), "Experimental Study of the Fracture Resistance of Bimaterial Interfaces," *Mechs. Mater.*, Vol. 7, pp. 295-304.

[17] Carlsson, M., Hope, R., and Pedersen, J. (1986), "Use of Condensed Silica Fume (CSF) in Concrete," *Fly Ash, Silica Fume, Slag and Natural Pozzolans in Concrete*, ACI SP-91, V. M. Malhotra, Ed., pp. 1013-1030.

[18] Carrasquillo, R. L., Nilson, A. H., and Slate, F. O. (1981a), "Microcracking and Behavior of High Strength Concrete Subject to Short-Term Loading," *ACI Journal*, Vol. 78, May-June, pp. 179-186.

[19] Carrasquillo, R. L., Nilson, A. H., and Slate, F. O. (1981b), "Properties of High Strength Concrete Subject to Short-Term Loads," *ACI Journal*, Vol. 78, May-June, pp. 171-178.

[20] Chatalambides, P. G., Lund, J., and Evans, A. G. (1989), "A Test Specimen for Determining the Fracture Resistance of Bimaterial Interfaces," *Journal of Applied Mechanics*, Vol. 56, March, pp. 77-82.

[21] Chen, R. C., Carrasquillo, R. L., and Fowler, D. W. (1985), "Behavior of High Strength Concrete under Uniaxial and Biaxial Compression," *High Strength Concrete*, ACI SP-87, pp. 251-273.

[22] Colaco, J. P. (1985), "75-Story Texas Commerce Plaza, Houston - The Use of High-Strength Concrete," *High Strength Concrete*, ACI SP-87, pp. 1-8.

[23] Detwiler, R. J., and Mehta, P. K. (1989), "Chemical and Physical Effects of Silica Fume on the Mechanical Behavior of Concrete," *ACI Materials Journal*, Vol. 86, No. 6, Nov.-Dec., pp. 609-614.

[24] Dundurs, J. (1969), "Edge-bonded Dissimilar Orthogonal Elastic Wedges," *Journal of Applied Mechanics*, ASME, Vol. 36, pp. 650-652.

[25] England, A. H. (1965), "A Crack between Dissmilar Media," *Journal of Applied Mechanics*, Vol. 32, pp. 400-402.

[26] Erdogan, F. (1965), "Stress Distribution in Bonded Dissimilar Materials with Cracks," *Journal of Applied Mechanics*, Vol. 32, pp. 403-410.

[27] Evans, A. G., Ruhle, M., Dalgleish, B. J., and Charalambides, P. G. (1990), "The Fracture Energy of Bimaterial System," *In Metal-Ceramic Interfaces*, M. Ruhle, A. G. Evans, M. F. Ashby, and J. P. Hirth, Eds., Pergamon Press, New York, pp. 345-364.

[28] Evans, A. G., and Hutchinson, J. W. (1989), "Effects of Non-planarity on the Mixed Mode Fracture Resistance of Bimaterial Interfaces," *Acta metall.*, Vol. 37, No. 3, pp. 909-916.

[29] Gerstle, K. (1979), "Material Behavior under Various Types of Loading," *Proc. of Workshop on High Strength Concrete*, National Science Foundation, pp. 43-78.

[30] Gjorv, O. E. (1983), "Durability of Concrete Containing Condensed Silica Fume," *Fly Ash, Silica Fume, Slag and Other Mineral By-Products in Concrete*, ACI SP-79, pp. 695-708.

[31] Goldman, A., and Bentur, A. (1989), "Bond Effects in High-Strength Silica-Fume Concretes," *ACI Materials Journal*, Vol. 86, No. 5, Sept.-Oct., pp. 440-447.

[32] He, M.-Y., Cao, H. C., and Evans, A. G. (1988), "Mixed-Mode Fracture: The Four-Point Shear Specimen," *Research Report M88-44*, Materials Dept., University of California at Santa Barbara.

[33] He, M.-Y., and Hutchinson, J. W. (1989a), "Kinking of a Crack out of an Interface," *Journal of Applied Mechanics*, Vol. 56, June, pp. 270-278.

[34] He, M.-Y., and Hutchinson, J. W. (1989b), "Crack Deflection at an Interface between Dissimilar Elastic Materials," *Int. J. Solids Struct.*, Vol. 25, No. 9, pp. 1053-1067.

[35] He, M.-Y., Bartlett, A., Evans, A. G., and Hutchinson, J. W. (1991), "Kinking of a Crack out of an Interface: Role of In-plane Stress," *J. Am. Ceram. Soc.*, Vol. 74, No. 4, pp. 767-771.

[36] Hillemeier, B., and Hilsdorf, H. K. (1977), "Fracture Mechanics Studies on Concrete Compounds," *Cement and Concrete Research*, Vol. 7, pp. 523-535.

[37] Hordjik, D. A., Van Mier, J. G. M., and Reinhart, H. W. (1989), "Material Properties," *Fracture Mechanics of Concrete Structures: From Theory to Application*, RILEM Report, pp. 67-127.

[38] Hsu, T. T. C., Slate, F. O., Sturman, G. M., and Winter, G. (1963), "Microcracking of Plain Concrete and the Shape of the Stress-strain Curve," *ACI Journal*, Vol. 60, No. 2, pp. 209-223.

[39] Huang, Q. J. (1990), *Micromechanical Modeling of the Fracture Behavior of Second-phase Reinforced Cementitious Materials*, Ph.D. Thesis, Dept. of Civil Engineering, MIT, Cambridge, MA.

[40] Hutchinson, J. W. (1990), "Mixed Mode Fracture Mechancis of Interfaces," *In Metal-Ceramic Interfaces*, M. Ruhle, A. G. Evans, M. F. Ashby, and J. P. Hirth, Eds., Pergamon Press, New York, pp. 295-306.

[41] Hutchinson, J. W., and Suo, Z. (1992), "Mixed Mode Cracking in Layered Materials," *Advances in Applied Mechanics*, Vol. 29, eds., J. W. Hutchinson and T. Y. Wu, Academic Press, pp. 63-191.

[42] Jahren, P. A. (1983), "Use of Silica Fume in Concrete," *Fly Ash, Silica Fume, Slag and Other Mineral By-Products in Concrete*, ACI SP-79, pp. 625-642.

[43] Jahren, P. A. (1986), "Performance of Concrete Incorporating Condensed Silica Fume and Superplasticizers," *Fly Ash, Silica Fume, Slag and Natural Pozzolans in Concrete*, ACI SP-91, pp. 865-892.

[44] Jenq, Y. S. (1991), "Non-linear Fracture Behavior of Multi-phase Materials," *Cement and Concrete Composites*, Vol. 13, pp. 79-86.

[45] Jenq, Y. S., and Shah, S. P. (1985), "Two Parameter Fracture Model for Concrete," *Journal of Engineering Mechanics*, ASCE, Vol. 111, No. 10, pp. 1227-1241.

[46] John, R., and Shah, S. P. (1989), "Fracture Mechanics Analysis of High Strength Concrete," *Journal of Materials*, ASCE, Vol. 1, pp. 185-198.

[47] Kitsutaka, Y., Buyukozturk, O., and Lee, K. M. (1992), "Fracture Energy of High Strength Concrete," *In preparation*,

[48] Lacroix, R., and Jaugey, P. (1985), "High-Strength Concrete: How to use it everyday," *High Strength Concrete*, ACI SP-87, pp. 35-50.

[49] Lee, K. M., Buyukozturk, O., and Oumera, A. (1992), "Fracture Analysis of Mortar-Aggregate Interfaces in Concrete," *Journal of Engineering Mechanics*, ASCE, Vol. 118, No. 10, pp. 2031-2047.

[50] Liu, T. C., Nilson, A. H., and Slate, F. O. (1972), "Stress-strain Response and Fracture of Concrete in Uniaxial and Biaxial Compression," *ACI Journal*, Vol. 69, No. 5, pp. 291-295.

[51] Maji, A., and Shah, S. P. (1988), "Initiation and Propagation of Bond Cracks as Detected by Laser Holography and Acoustic Emission," *Bonding in Cementitious Composites*, MRS Symposia, Vol. 114, pp. 55-64.

[52] Malhotra, V. M. (1984), "Use of Mineral Admixtures for Specialized Concrete," *Concrete International*, April, pp. 19-24.

[53] Malyshev, B. M., and Salganik, R. C. (1965), "The Strength of Adhesive Joints using the Theory of Cracks," *Int. J. Fracture Mech.*, Vol. 5, pp.114-128.

[54] Matos, P. P. L., McMeeking, P. G., Charalambides, P. G., and Drory, M. D. (1989), "A Method for Calculating Stress Intensities in Bimaterial Fracture," *International Journal of Fracture*, Vol. 40, pp. 235-254.

[55] Mehta, P. K. (1983), "Pozzolanic and Cementitious By-Products as Mineral Admixtures for Concrete - A Critical Review," *Fly Ash, Silica Fume, Slag and Other Mineral By-Products in Concrete*, ACI SP-79, pp. 1-46.

[56] Mehta, P. K. (1986), *Concrete: Structure, Properties and Materials*, Prentice Hall, Englewood Cliffs, NJ.

[57] Mehta, P. K. (1989), "Pozzolanic and Cementitious By-Products in Concrete - Another Look," *Fly Ash, Silica Fume, Slag, and Natural Pozzolans in Concrete*, ACI SP-114, pp. 1-43.

[58] Mehta, P. K., and Aitcin, P. C. (1990a), "Microstructural Basis of Selection of Materials and Mix Proportions for High-Strength Concrete," *High Strength Concrete*, ACI SP-121, pp. 265-286.

[59] Mehta, P. K., and Aitcin, P. C. (1990b), "Principles Underlying Production of High-Performance Concrete," *Cement, Concrete, and Aggregates*, Vol. 12, No. 2, Winter, pp. 70-78.

[60] Mehta, P. K., and Monteiro, P. J. M. (1988), "Effect of Aggregate, Cement, and Mineral-Admixtures on the Microstructure of the Transition Zone," *Bonding in Cementitious Composies*, MRS Symposia, Vol. 114, pp. 65-75.

[61] Mindess, S. (1988), "Bonding in Cementitious Composites: How important is it," *Bonding in Cementitious Composites*, MRS Symposia, Vol. 114, pp. 3-10.

[62] Mindess, S. (1989), "Interfaces in Concrete," *In Materials Science of Concrete I*, J. P. Skalny, ed., Am. Cer. Soc., Westerville, OH., pp. 165-180.

[63] Mindess, S. (1992), "State of the Art Report: Tests to Determine the Mechanical Properties of the Interfacial Zone," *Interfaces in Cementitous Composites*, RILEM.

[64] Mitsuru, S., and Mitsunori, K. (1986), "Resistance of the Cement-aggregate Interfacial Zone to the Propagation of Cracks," *Cement and Concrete Research*, Vol. 16, pp. 653-661.

[65] Ngab, A. S., Slate, F. O., and Nilson, A. H. (1981), "Shrinkage and Creep of High Strength Concrete," *ACI Journal*, Vol 78, No. 4, pp. 255-261.

[66] Nilson, A. H. (1985), "Design Implications of High-Strength Concrete," *High Strength Concrete*, ACI SP-87, pp. 25-50.

[67] Odler, I., and Zurz, A. (1988), "Structure and Bond Strength of Cement-Aggregate Interfaces," *Bonding in Cementitious Composites*, MRS Symposia, Vol. 114, pp. 21-27.

[68] Ojdrovic, R. P., and Petroski, H. J. (1987), "Fracture Behavior of Notched Concrete Cylinder," *Journal of Engineering Mechanics*, ASCE, Vol. 113, No. 10, pp. 1551-1564.

[69] Oumera, A. A. (1991), *Crack Propagation in the Aggregate-mortar Interface Regions of Concrete*, MS Thesis, Dept. of Civil Engineering, MIT, Cambridge, MA.

[70] Parks, D. M. (1977), "The Virtual Crack Extension Method for Nonlinear Material Behavior," *Comp. Meth. Appl. Mech. Engng.*, Vol. 12, pp. 353-364.

[71] Peterman, M. B., and Carrasquillo, R. L. (1986), *Production of High Strength Concrete*, Noyes Publication, Park Ridge, New Jersey.

[72] Radjy, F. F., Bogen, T., Sellevold, E. J., and Loeland, K. E. (1986), "A Review of Experiences with Condensed Silica Fume Concretes and Products," *Fly Ash, Silica Fume, Slag and Natural Pozzolans in Concrete*, ACI SP-91, pp. 1135-1152.

[73] Randall, V., and Foot, K. (1989), "High Strength Concrete for Pacific First Center," *Concrete International*, Vol. 11, No.4, pp.

[74] Raphael, M. J. (1984), "Tensile Strength of Concrete," *ACI Journal*, Vol. 81, No. 2, pp. 158-165.

[75] Rice, J. R. (1988), "Elastic Fracture Concepts for Interfacial Cracks," *Journal of Applied Mechanics*, Vol. 55, pp. 98-103.

[76] Rice, J. R., and Sih, G. C. (1965), "Plane Problems of Cracks in Dissimilar Media," *Journal of Applied Mechanics*, Vol. 32, pp. 418-423.

[77] Rosenburg, A. M., and Gaidis, J. M. (1989), "A New Mineral Admixture for High-Strength Concrete," *Concrete International*, Vol. 11, April, pp. 31-36.

[78] Sarkar, S. L., Diatta, Y., and Aitcin, P. C. (1988), "Microstructural Study of Aggregate/Hydrated Paste Interface in Very High Strength River Gravel Concretes," *Bonding in Cementitous Composites*, MRS Symposia, Vol. 114, pp. 111-116.

[79] Scrivener, K. L., and Gartner, E. M. (1988), "Microstructural Gradients in Cement Paste around Aggregates Particles," *Bonding in Cementitous Composites*, MRS Symposia, Vol. 114, pp. 77-85.

[80] Sellevold, E. J., and Nilsen, T. (1987), "Condensed Silica Fume in Concrete: A World Review," *Supplementary Cementing Materials for Concrete*, ed., V. M. Malhotra, CANMET, pp. 167-243.

[81] Shah, S. P. (1979), "A Summary," *Proc. of a Workshop on High Strength Concrete*, NSF, pp. 1-7.

[82] Shah, S. P. (1988), "Fracture Toughenss of Cement-Based Materials," *Materials and Structures*, Vol. 21, pp. 145-150.

[83] Shah, S. P. and Winter, G. (1966), "Inelastic Behavior and Fracture of Concrete," *Causes, Mechanism, and Control of Cracking in Concrete*, ACI SP-20, pp. 5-28.

[84] Shetty, D. K., Rosenfield, A. R., and Duckworth, W. H. (1986), "Mixed-Mode Fracture of Ceramics in Diametral Compression," *Journal of American Ceramic Society*, Vol. 69, No. 6, pp. 437-443.

[85] Shetty, D. K., Rosenfield, A. R., and Duckworth, W. H. (1987), "Mixed-Mode Fracture Biaxial Stress State: Application of the Diametral-Compression (Brazilian Disk) Test," *Engineering Fracture Mechanics*, Vol. 26, No. 6, pp. 825-840.

[86] Shih, C. F., and Asaro, R. J. (1988), "Elastic-Plastic Analysis of Cracks on Bimaterial Interfaces: Part I - Small Scale Yielding," *Journal of Applied Mechanics*, Vol. 55, June, pp. 299-316.

[87] Shih, T. S., Lee, G. C., and Chang, K. C. (1989), "On Static Modulus of Elasticity of Normal-Weight Concrete," *Journal of Structural Engineering*, ASCE, Vol. 115, No. 10, pp. 2579-2587.

[88] Singh, D., and Shetty, D. K. (1989), "Fracture Toughness of Polycrystalline Ceramics in Combined Mode I and Mode II Loading," *Journal of American Ceramic Society*, Vol. 72, No. 1, pp. 78-84.

[89] Struble, L. (1988), "Microstructure and Fracture at the Cement Paste-Aggregate Interface," *Bonding in Cementitious Composites*, MRS Symposia, Vol. 114, pp. 11-20.

[90] Struble, L. and Mindess, S. (1983), "Morphology of the Cement-Aggregate Bond," *Int. J. of Cement Composites and Lightweight Aggregate*, Vol. 5, pp. 79-86.

[91] Struble, L., Skalny, J., and Mindess, S. (1980), "A Review of the Cement-Aggregate Bond," *Cement and Concrete Research*, Vol. 10, pp. 277-286.

[92] Suo, Z (1989), *Mechanics of Interface Fracture*, Ph.D Thesis, Division of Applied Sciences, Harvard University, Cambridge, MA.

[93] Suo, Z, and Hutchinson, J. W. (1989), "Sandwich Test Specimens for Measuring Interface Crack Toughness," *Materials Science and Engineering*, A107, pp. 135-143.

[94] Suo, Z., and Hutchinson, J. W. (1990), "Interface Crack between Two Elastic Layers," *International Journal of Fracture*, Vol. 43, pp. 1-18.

[95] Swamy, R. N. (1986), "Properties of High Strength Concrete," *Cement, Concrete, and Aggregates*, ASTM, Vol. 8, No. 1, pp. 33-41.

[96] Swamy, R. N., Al-Taan, S., and Ali, S. A. R. (1978), "Steel Fibers for Controlling Cracking and Deformation," *Concrete International*, Vol. 1, No. 8, pp. 318-329.

[97] Tada, H., Paris, P. C., and Irwin, G. R. (1985), *The Stress Analysis of Cracks Handbook*, 2nd ed., Paris Productions Inc., St. Louis, Missouri.

[98] Yamaguchi, E., and Chen, W.-F. (1991), "Microcrack Propagation Study of Concrete under Compression," *Journal of Engineering Mechanics*, ASCE, Vol. 117, No. 3, pp. 653-673.

[99] Yamato, T., Emoto, Y., and Soeda, M. (1987), "Strength and Freezing and Thawing Resistance of Concrete Incorporating Condensed Silica Fume," *Fly Ash, Silica Fume, Slag and Natural Pozzolans in Concrete*, ACI SP-91, V. M. Malhotra, Ed., pp. 1095-1117.

[100] Wang, J., Lin, B., Xie, S., and Wu, Z. (1986), "Improvement of Paste-aggregate Interface by Adding Silica Fume," *8th Int. Congress on the Chemistry of Cement*, Vol. III, Finep, Rio de Janeiro, Brazil, pp. 460-465.

[101] Wang, J.-S., and Suo, Z. (1990), "Experimental Determination of Interfacial Toughness Curves Using Brazil-Nut-Sandwiches," *Acta metall. mater.*, Vol. 38, No. 7, pp. 1279-1290.

[102] Williams, M. L. (1959), "The Stress around a Fault or Crack in Dissimilar Media," *Bull. Seismol. Soc. Am.*, Vol. 49, pp. 199-204.

[103] Wittmann, F. H. (1979), "Micromechanics of Achieving High Strength and Other Superior Properties," *Proc. of Workshop on High Strength Concrete*, NSF, pp. 8-30.

[104] Wolsiefer, J. (1984), "Ultra High-strength Field Placeable Concrete with Silica Fume Admixtire," *Concrete International*, Vol. 6, No. 6, pp. 25-34.

[105] Zaitsev, Y. (1983), "Crack Propagation in a Composites Material," *Fracture Mechanics of Concrete*, F. H. Wittmann, Ed., Elsevier Science Pub., Netherlands, pp. 251-299.

[106] Zhang, M. H., and Gjorv, O. E. (1990), "Microstructure of the Interfacial Zone between Lightweigth Aggregate and Cement Paste," *Cement and Concrete Research*, Vol. 20, pp. 610-618.

[107] Zia, P. (1979), "Structural Design Considerations for High Strength Concrete," *Proc. of a Workshop on High Strength Concrete*, NSF, pp. 179-193.

[108] Ziegeldorf, S. (1983), "Fracture Mechanics Parameters of Hardened Cement Paste, Aggregates, and Interfaces," *Fracture Mechanics of Concrete*, F. H. Wittmann, Ed., Elsevier Science Pub., Netherlands, pp. 371-409.

Appendix A

Input Files for Numerical Analysis of Beam Composite Model

```
*ADINA-IN 3.0 INPUT FILE
*
FILEUNITS LIST=8 LOG=7 ECHO=7
*
DATABASE CREATE
*
HEAD 'FRACTURE ANALYSIS OF A COMPOSITE BEAM - DEFLECTION CASE'
*
MASTER IDOF=100111 NSTEP=1 REACTION=YES
*
PRINTOUT CARDIMAGE=NO IPDATA=4,
IOUTPT=1 IPRIC=0 IPRIT=0 IDC=1,
IVC=0 IAC=0 PRINTDEFAULT=NO
PORTHOLE FORMATTED=YES FILE =60
TIMEFUNCTION 1
0 0.
1 1.
ESAVESTEPS FIRST1=1 1 1
NSAVESTEPS FIRST1=1 1 1
PRINTSTEPS FIRST1=1 1 1
PRINTNODES FIRST1=13 LAST1=13 INCR1=1 FIRST2=87 87 1
*
COORDINATES / ENTRIES NODE Y Z
1 5.5 3.0
2 5.5 1.5
3 5.5 1.09
4 5.5 1.0
5 5.5 0.91
6 5.5 0.0
7 4.5 3.0
8 4.5 1.5
9 4.5 1.09
10 4.5 1.0
11 4.5 0.91
12 4.5 0.0
13 2.25 3.0
14 2.25 1.5
15 2.25 1.09
16 2.25 1.0
17 2.25 0.91
18 2.25 0.0
19 1.75 3.0
20 1.75 1.5
21 1.75 1.09
22 1.75 1.0
23 1.75 0.91
24 1.75 0.0
25 1.0 3.0
26 1.0 1.5
27 1.0 1.09
28 1.0 1.0
29 1.0 0.91
```

30 1.0 0.0
31 0.5 3.0
32 0.5 1.5
33 0.5 1.09
34 0.5 1.0
35 0.5 0.91
36 0.5 0.0
37 0.4 3.0
38 0.4 1.5
39 0.4 1.09
40 0.4 1.0
41 0.4 0.91
42 0.4 0.0
43 0.18 3.0
44 0.18 1.5
45 0.18 1.09
46 0.18 1.0
47 0.18 0.91
48 0.18 0.0
49 0.09 3.0
50 0.09 1.5
51 0.09 1.09
52 0.09 1.0
53 0.09 0.91
54 0.09 0.0
55 0.0 3.0
56 0.0 1.5
57 0.0 1.09
58 0.0 1.0
59 0.0 0.91
60 0.0 0.0
61 -0.002 0.91
62 -0.002 0.0
63 -0.4 3.0
64 -0.4 1.5
65 -0.4 1.09
66 -0.4 1.0
67 -0.4 0.91
68 -0.4 0.0
99 -5.5 3.0
100 -5.5 1.5
101 -5.5 1.09
102 -5.5 1.0
103 -5.5 0.91
104 -5.5 0.0
93 -4.5 3.0
94 -4.5 1.5
95 -4.5 1.09
96 -4.5 1.0
97 -4.5 0.91
98 -4.5 0.0
87 -2.25 3.0

```
88 -2.25 1.5
89 -2.25 1.09
90 -2.25 1.0
91 -2.25 0.91
92 -2.25 0.0
81 -1.75 3.0
82 -1.75 1.5
83 -1.75 1.09
84 -1.75 1.0
85 -1.75 0.91
86 -1.75 0.0
75 -1.0 3.0
76 -1.0 1.5
77 -1.0 1.09
78 -1.0 1.0
79 -1.0 0.91
80 -1.0 0.0
69 -0.5 3.0
70 -0.5 1.5
71 -0.5 1.09
72 -0.5 1.0
73 -0.5 0.91
74 -0.5 0.0
105 0.0 0.998
*
MATERIAL 1 ELASTIC E=4.0E06 NU=0.3
*
EGROUP 1 TWODSOLID STRAIN
GSURFACE 7 8 2 1 EL1=3 EL2=2
GSURFACE 8 9 3 2 EL1=1 EL2=2
GSURFACE 9 10 4 3 EL1=1 EL2=2
GSURFACE 10 11 5 4 EL1=1 EL2=2
GSURFACE 11 12 6 5 EL1=2 EL2=2
GSURFACE 13 14 8 7 EL1=3 EL2=4
GSURFACE 14 15 9 8 EL1=1 EL2=4
GSURFACE 15 16 10 9 EL1=1 EL2=4
GSURFACE 16 17 11 10 EL1=1 EL2=4
GSURFACE 17 18 12 11 EL1=2 EL2=4
GSURFACE-E B 13 14 20 19 EL1=3 EL2=1 EL3=9
GSURFACE-E B 14 15 21 20 EL1=1 EL2=1 EL3=3
GSURFACE 21 22 16 15 EL1=1 EL2=1
GSURFACE 22 23 17 16 EL1=1 EL2=1
GSURFACE-E B 17 18 24 23 EL1=2 EL2=1 EL3=6
GSURFACE 25 26 20 19 EL1=9 EL2=2
GSURFACE 26 27 21 20 EL1=3 EL2=2
GSURFACE 27 28 22 21 EL1=1 EL2=2
GSURFACE 28 29 23 22 EL1=1 EL2=2
GSURFACE 29 30 24 23 EL1=6 EL2=2
GSURFACE 31 32 26 25 EL1=9 EL2=2
GSURFACE 34 35 29 28 EL1=1 EL2=2
GSURFACE 35 36 30 29 EL1=6 EL2=2
GSURFACE-E B 31 32 38 37 EL1=9 EL2=1 EL3=27
```

GSURFACE-E B 34 35 41 40 EL1=1 EL2=1 EL3=3
GSURFACE-E B 35 36 42 41 EL1=6 EL2=1 EL3=18
GSURFACE 43 44 38 37 EL1=27 EL2=3
GSURFACE 46 47 41 40 EL1=3 EL2=3
GSURFACE 47 48 42 41 EL1=18 EL2=3
GSURFACE 49 50 44 43 EL1=27 EL2=3
GSURFACE 52 47 46 52 EL1=9 EL2=3
GSURFACE 52 53 47 52 EL1=9 EL2=3
GSURFACE 53 54 48 47 EL1=18 EL2=3
GSURFACE 55 56 50 49 EL1=27 EL2=3
GSURFACE 52 59 53 52 EL1=9 EL2=3
GSURFACE 52 105 59 52 EL1=9 EL2=3
GSURFACE 59 60 54 53 EL1=18 EL2=3
GSURFACE 63 64 56 55 EL1=27 EL2=5
GSURFACE 66 67 61 58 EL1=3 EL2=5
GSURFACE 67 68 62 61 EL1=18 EL2=5
GSURFACE-E B 69 70 64 63 EL1=9 EL2=1 EL3=27
GSURFACE-E B 72 73 67 66 EL1=1 EL2=1 EL3=3
GSURFACE-E B 73 74 68 67 EL1=6 EL2=1 EL3=18
GSURFACE 75 76 70 69 EL1=9 EL2=2
GSURFACE 78 79 73 72 EL1=1 EL2=2
GSURFACE 79 80 74 73 EL1=6 EL2=2
GSURFACE 81 82 76 75 EL1=9 EL2=2
GSURFACE 82 83 77 76 EL1=3 EL2=2
GSURFACE 83 84 78 77 EL1=1 EL2=2
GSURFACE 84 85 79 78 EL1=1 EL2=2
GSURFACE 85 86 80 79 EL1=6 EL2=2
GSURFACE-E B 87 88 82 81 EL1=3 EL2=1 EL3=9
GSURFACE-E B 88 89 83 82 EL1=1 EL2=1 EL3=3
GSURFACE 89 90 84 83 EL1=1 EL2=1
GSURFACE 90 91 85 84 EL1=1 EL2=1
GSURFACE-E B 91 92 86 85 EL1=2 EL2=1 EL3=6
GSURFACE 93 94 88 87 EL1=3 EL2=4
GSURFACE 94 95 89 88 EL1=1 EL2=4
GSURFACE 95 96 90 89 EL1=1 EL2=4
GSURFACE 96 97 91 90 EL1=1 EL2=4
GSURFACE 97 98 92 91 EL1=2 EL2=4
GSURFACE 99 100 94 93 EL1=3 EL2=2
GSURFACE 100 101 95 94 EL1=1 EL2=2
GSURFACE 101 102 96 95 EL1=1 EL2=2
GSURFACE 102 103 97 96 EL1=1 EL2=2
GSURFACE 103 104 98 97 EL1=2 EL2=2
*
COORDINATES / ENTRIES NODE Y Z
2133 0.0875 0.99994444
2159 0.0875 0.999129629
2186 0.0875 0.998314814
2053 0.0875 0.9975
2079 0.088333333 0.9975
2106 0.089166667 0.9975
1565 0.09 0.9975
1591 0.090833333 0.9975

```
1618 0.091666667 0.9975
1473 0.0925 0.9975
1498 0.0925 0.998333333
1523 0.0925 0.999166667
1548 0.0925 1.0
*
POTENTIALENERGY 52
*
MATERIAL 2 ELASTIC E=4.0E6 NU=0.3
*
EGROUP 2 TWODSOLID STRAIN
GSURFACE 32 33 27 26 EL1=3 EL2=2
GSURFACE 33 34 28 27 EL1=1 EL2=2
GSURFACE-E B 32 33 39 38 EL1=3 EL2=1 EL3=9
GSURFACE-E B 33 34 40 39 EL1=1 EL2=1 EL3=3
GSURFACE 44 45 39 38 EL1=9 EL2=3
GSURFACE 45 46 40 39 EL1=3 EL2=3
GSURFACE 50 51 45 44 EL1=9 EL2=3
GSURFACE 52 46 45 52 EL1=9 EL2=3
GSURFACE 52 45 51 52 EL1=9 EL2=3
GSURFACE 56 57 51 50 EL1=9 EL2=3
GSURFACE 52 51 57 52 EL1=9 EL2=3
GSURFACE 52 57 58 52 52 EL1=9 EL2=3
GSURFACE 64 65 57 56 EL1=9 EL2=5
GSURFACE 65 66 58 57 EL1=3 EL2=5
GSURFACE-E B 70 71 65 64 EL1=3 EL2=1 EL3=9
GSURFACE-E B 71 72 66 65 EL1=1 EL2=1 EL3=3
GSURFACE 76 77 71 70 EL1=3 EL2=2
GSURFACE 77 78 72 71 EL1=1 EL2=2
*
COORDINATES / ENTRIES NODE Y Z
3998 0.0925 1.00083333
4023 0.0925 1.00166667
4048 0.0925 1.0025
4073 0.09166667 1.0025
4098 0.09083333 1.0025
4123 0.09 1.0025
4228 0.08916667 1.0025
4253 0.08833333 1.0025
4278 0.0875 1.0025
4304 0.0875 1.00166667
4331 0.0875 1.00083333
4358 0.0875 1.0
*
POTENTIALENERGY 52
*
LOADS CONCENTRATED / 13 3 -1000 / 87 3 -1000
*
BOUNDARIES 101111 / 12
BOUNDARIES 111111 / 98
*
END
```

```
*ADINA-PLOT 4.0 INPUT FILE
*
FILEUNITS LIST=8 LOG=7 ECHO=7
*
DATABASE CREATE FORMATTED=YES
*
CONTROL PLOTUNIT=PERCENT HEIGHT=1.25
FCONTROL SIZE=ISO ISO=-4.5 XSF=5 YSF=5
*
WORKSTATION SYS=12 COLORS=RGB BACKGROUND=WHITE
COLORS ORI=INVERSE EL=INVERSE BC=INVERSE XYA=INVERSE XYL=INVERSE
COLORS DEF=INVERSE VE=INVERSE ST=INVERSE
*
* ORIGINAL MESH
*
WINDOW 1 0.0 0.18 0.91 1.09
LIST WINDOW
*
FRAME
MESH ORIGINAL=1 DEFORMED=0 BCODE=ALL SUBFRAME=1122
MESH ORIGINAL=1 DEFORMED=0 BCODE=ALL WINDOW=1,
SUBFRAME=1121
*
FRAME
MESH DMAX=5
MESH ORIGINAL=2 DEFORMED=0 LINES=1 WINDOW=-1,
PLOTAREA=-1 TEXT=NO AXES=NO
*
EINFO VAR=YES
CONSTANT E 4.0E6
CONSTANT NU 0.3
CONSTANT SYMMETRYFACTOR -1.0
ZLIST VAR=Z-ENERGY_RELEASE_RATE
ALIAS YD VAR=Y-DISPLACEMENT
ALIAS ZD VAR=Z-DISPLACEMENT
*
* CHECK LISTING
*
CONTROL EJECT=NO LINPAG=10000
FILEUNITS LIST=9
NPOINT NOD2133 NOD=2133
NPOINT NOD4358 NOD=4358
NPOINT NOD2134 NOD=2134
NPOINT NOD4359 NOD=4359
NPOINT NOD2135 NOD=2135
NPOINT NOD4360 NOD=4360
NPOINT NOD2136 NOD=2136
NPOINT NOD4361 NOD=4361
NPOINT NOD2137 NOD=2137
NPOINT NOD4362 NOD=4362
NPOINT NOD2138 NOD=2138
NPOINT NOD4363 NOD=4363
```

```
NPOINT CRACK_TIP NOD=52
PLIST CRACK_TIP VAR=Y-ENERGY_RELEASE_RATE YD ZD
NLINE TEST
2133
4358
2134
4359
2135
4360
2136
4361
2137
4362
2138
4363
LLIST TEST TSTART=1 TEND=1 TSKIP=1 YD ZD
*
END
```

Appendix B

Results from Model Tests and Real Concrete Tests

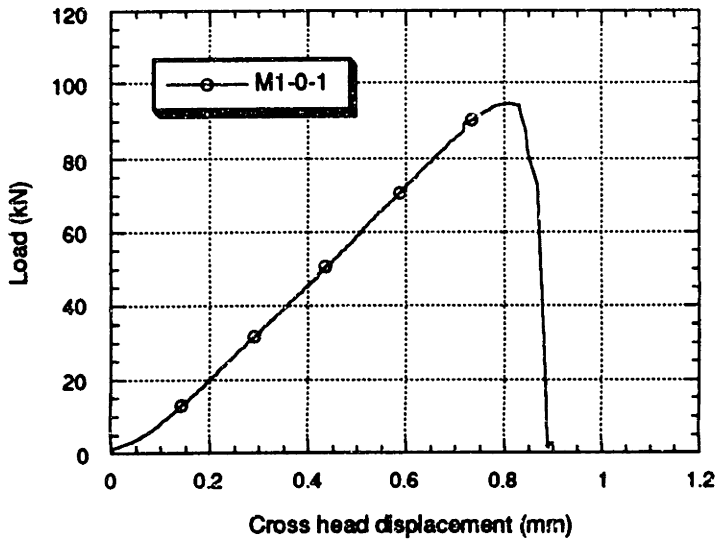

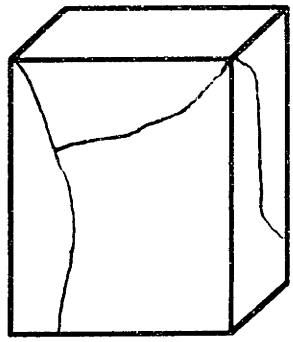

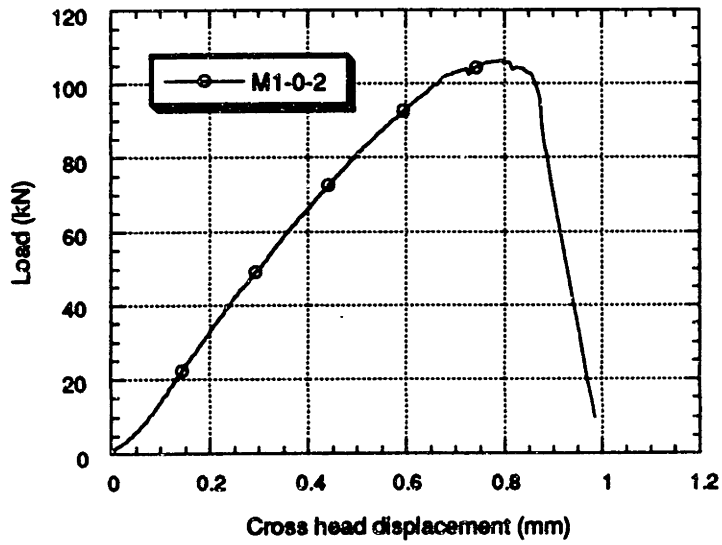

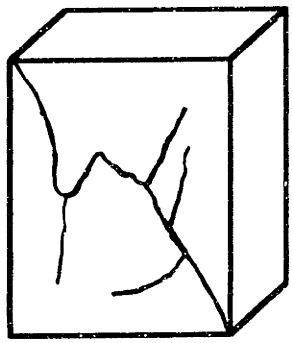

Figure B.1 Load versus cross head displacement curves of M1 block specimens

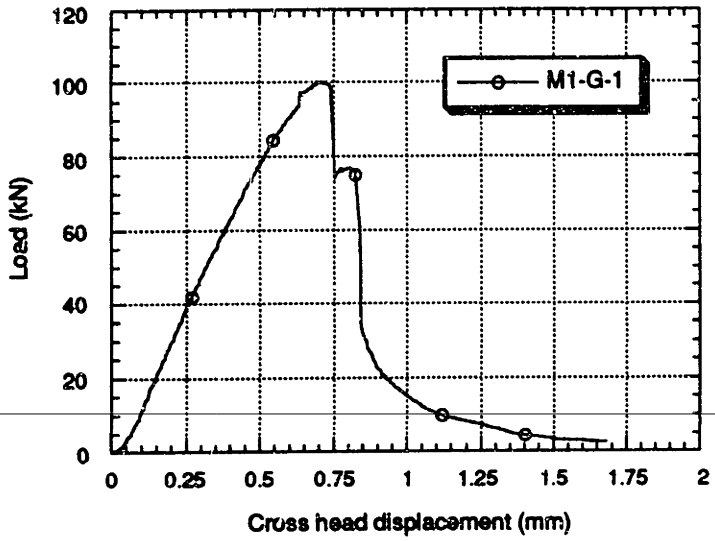

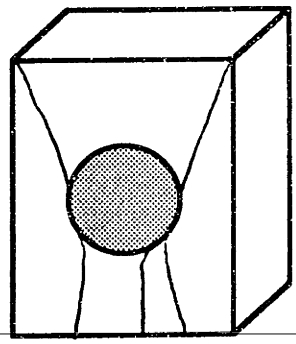

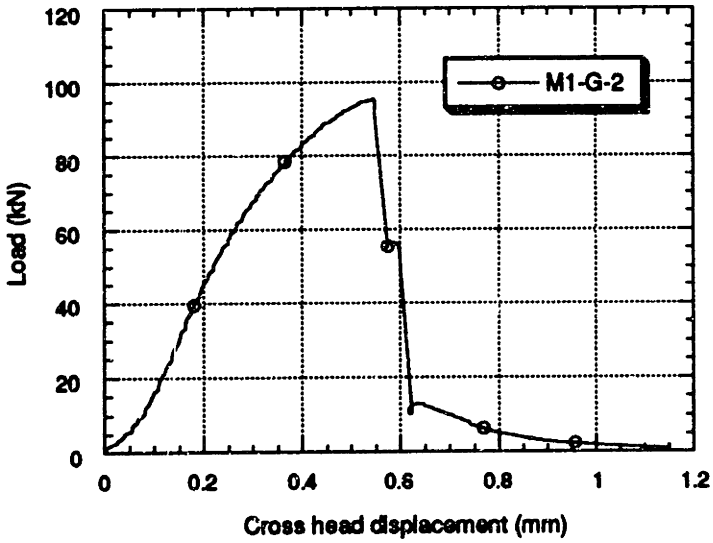

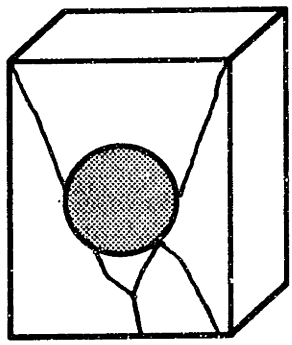

Figure B.2 Load versus cross head displacement curves of M1/G block specimens

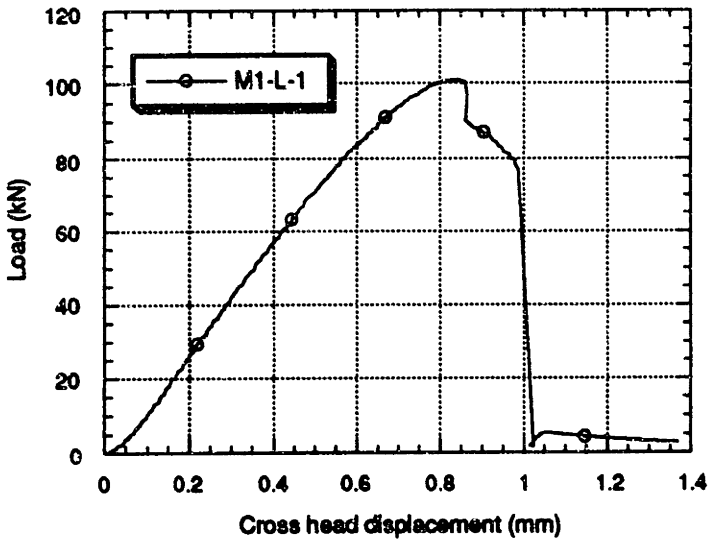

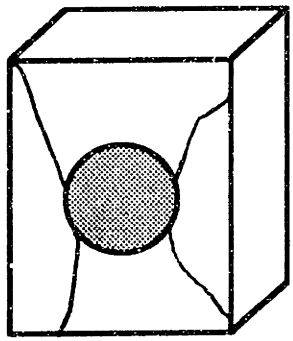

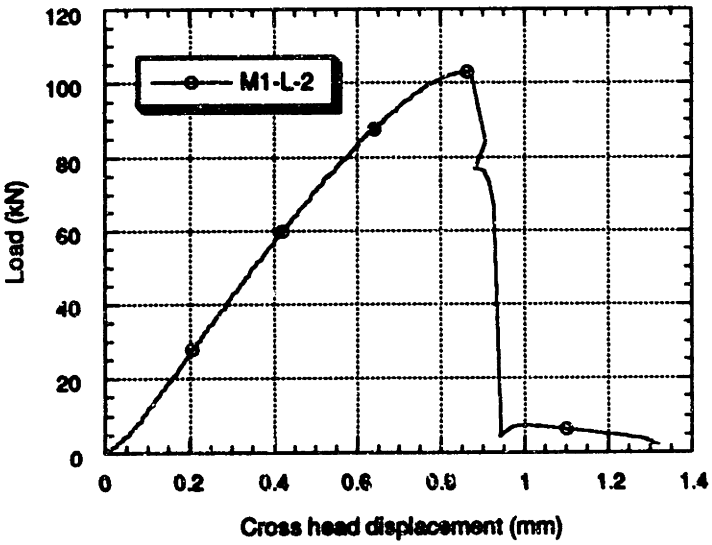

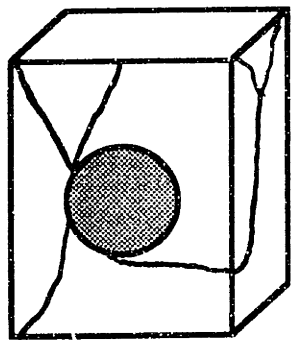

Figure B.3 Load versus cross head displacement curves of M1/L block specimens

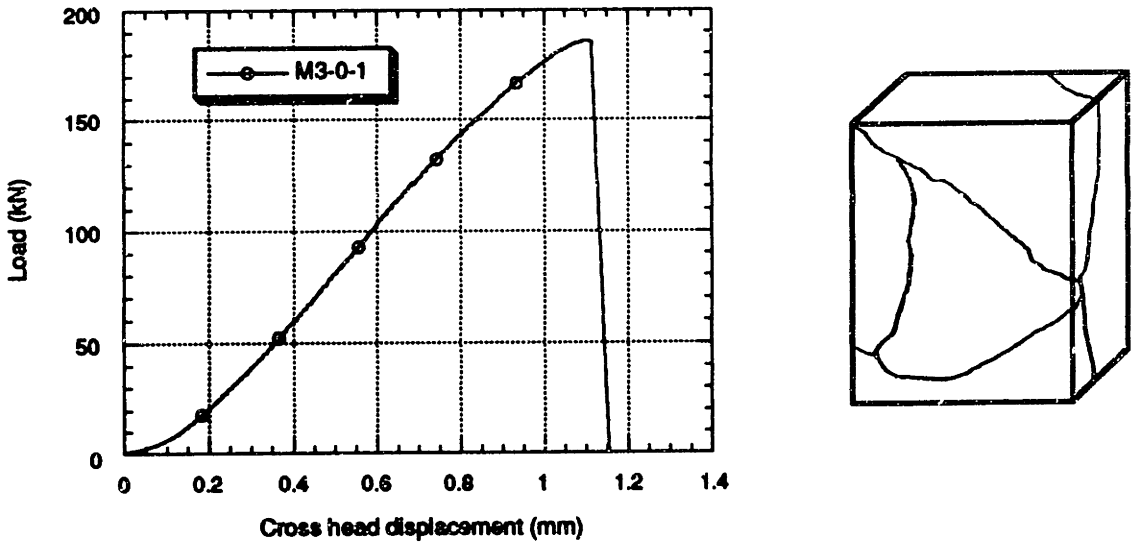

Figure B.4 Load versus cross head displacement curves of M3 block specimens

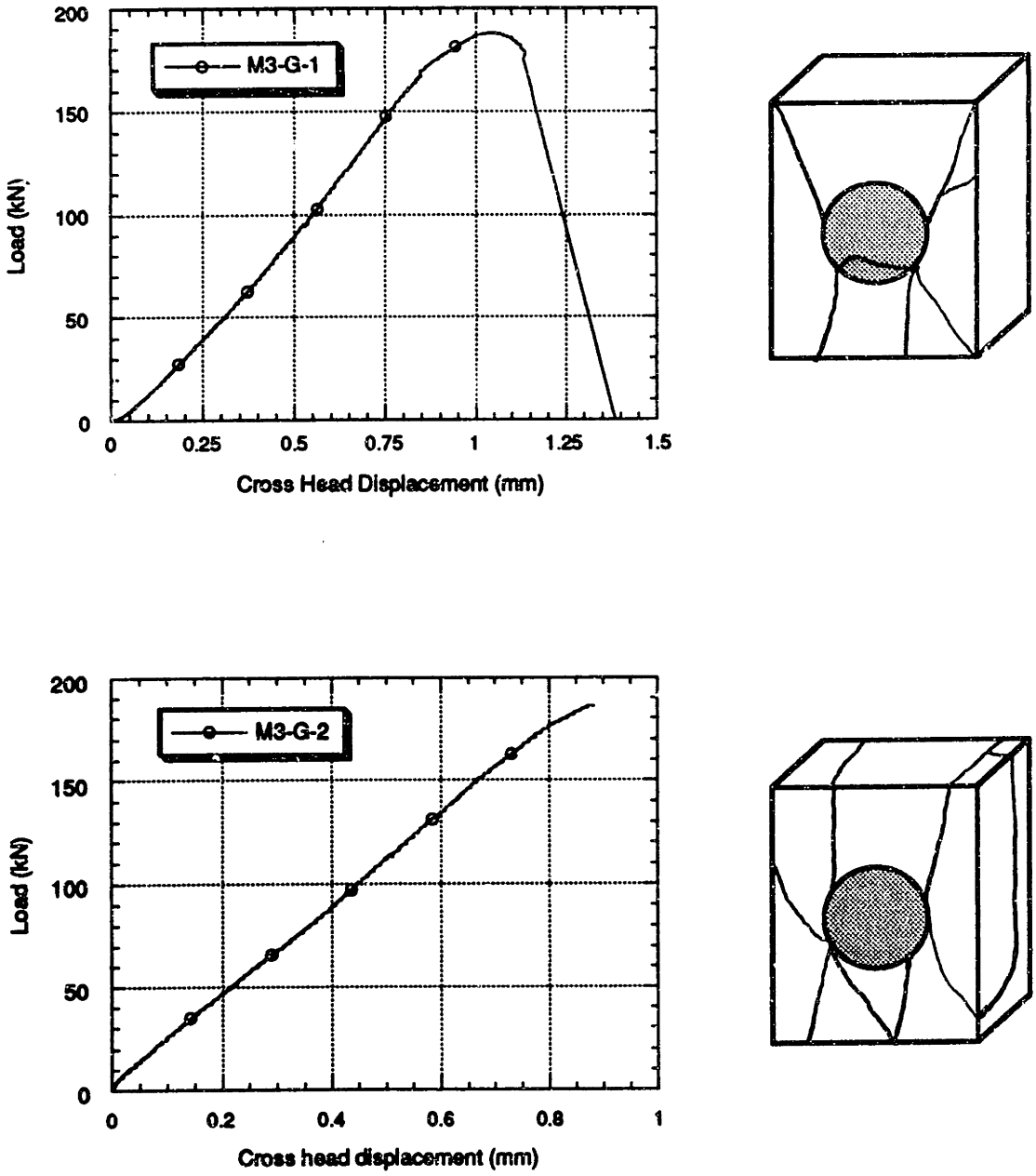

Figure B.5 Load versus cross head displacement curves of M3/G block specimens with one inclusion

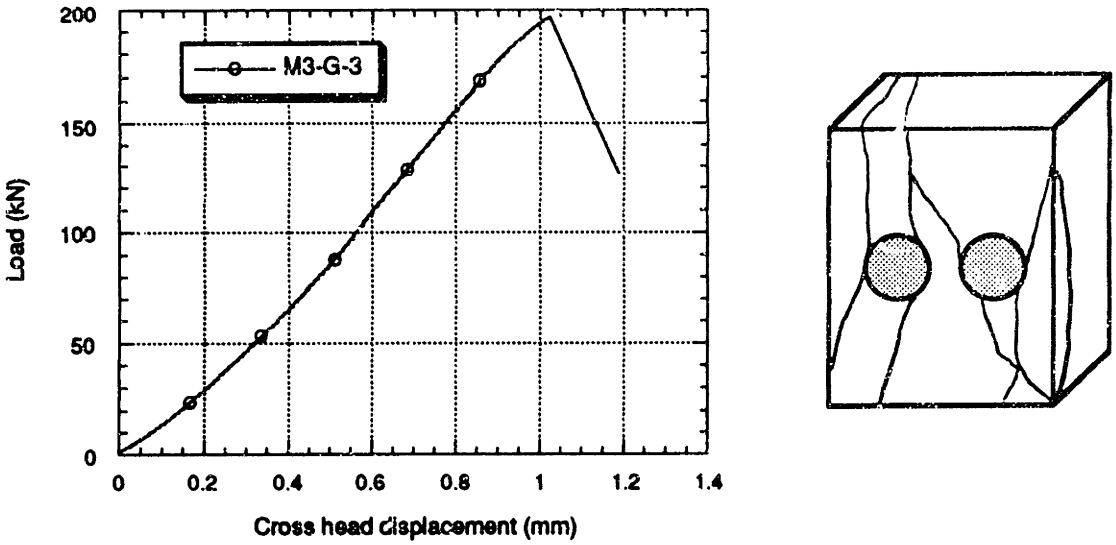

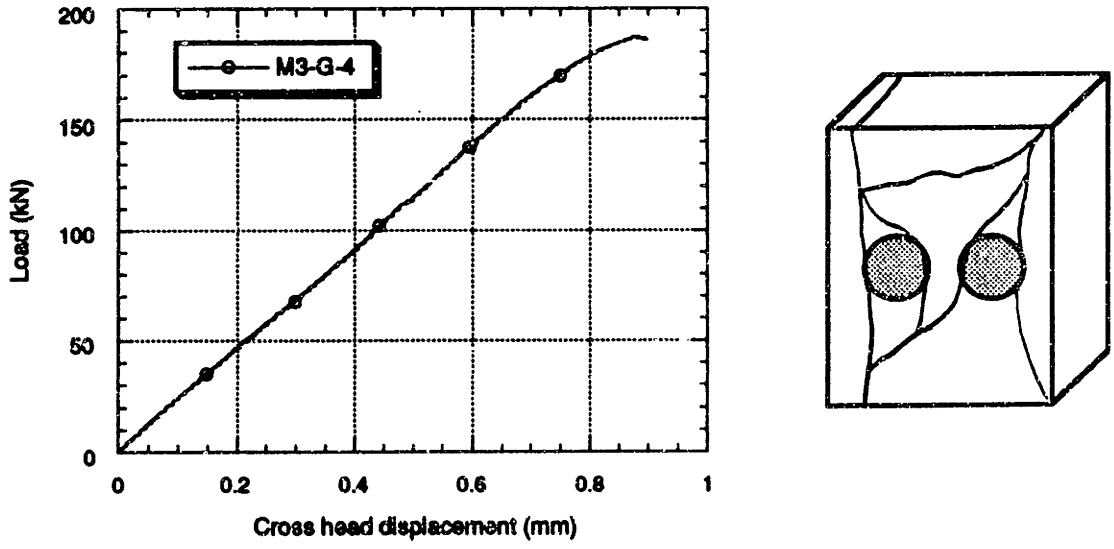

Figure B.6 Load versus cross head displacement curves of M3/G block specimens with two inclusions

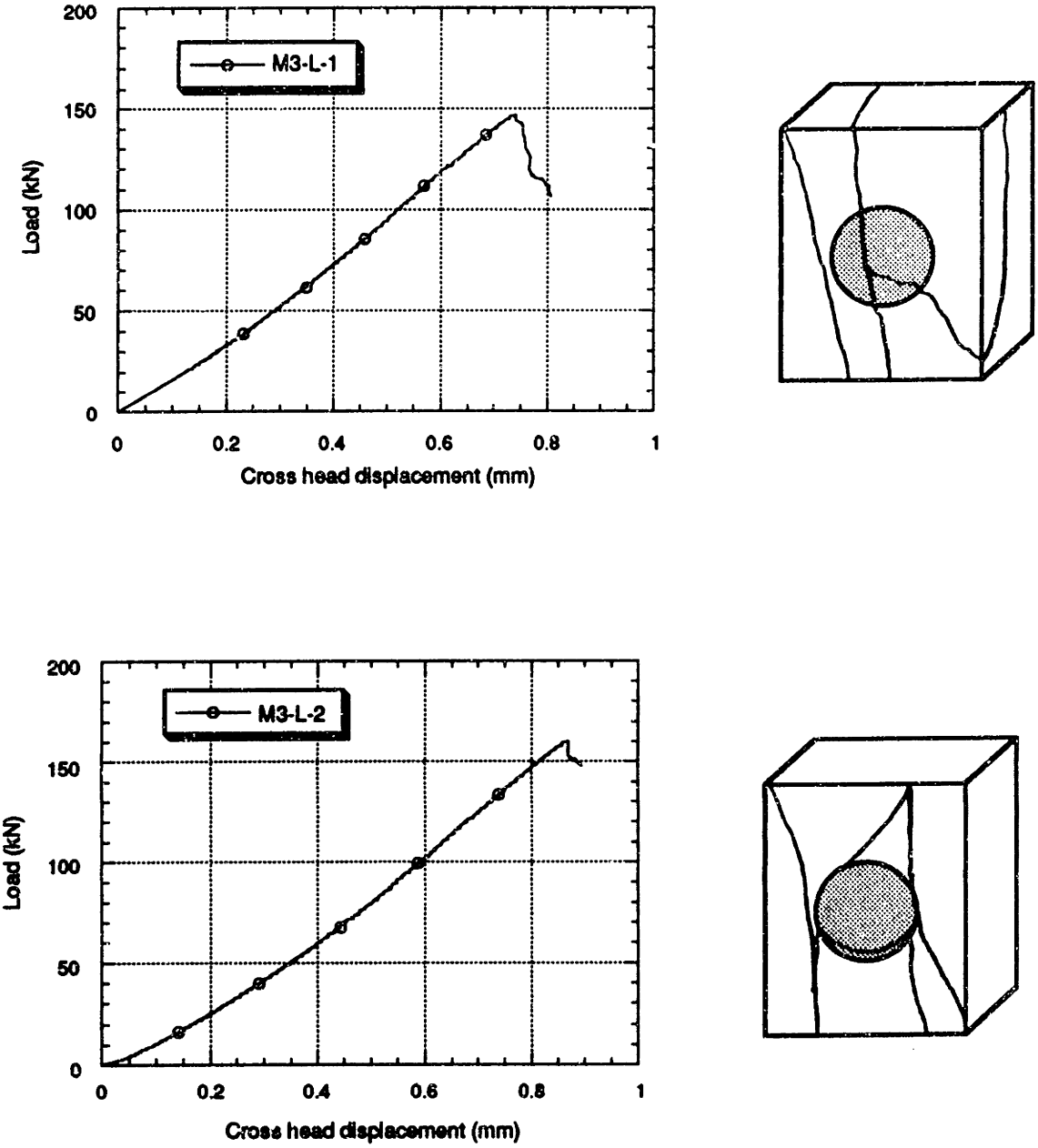

Figure B.7 Load versus cross head displacement curves of M3/L block specimens with one inclusion

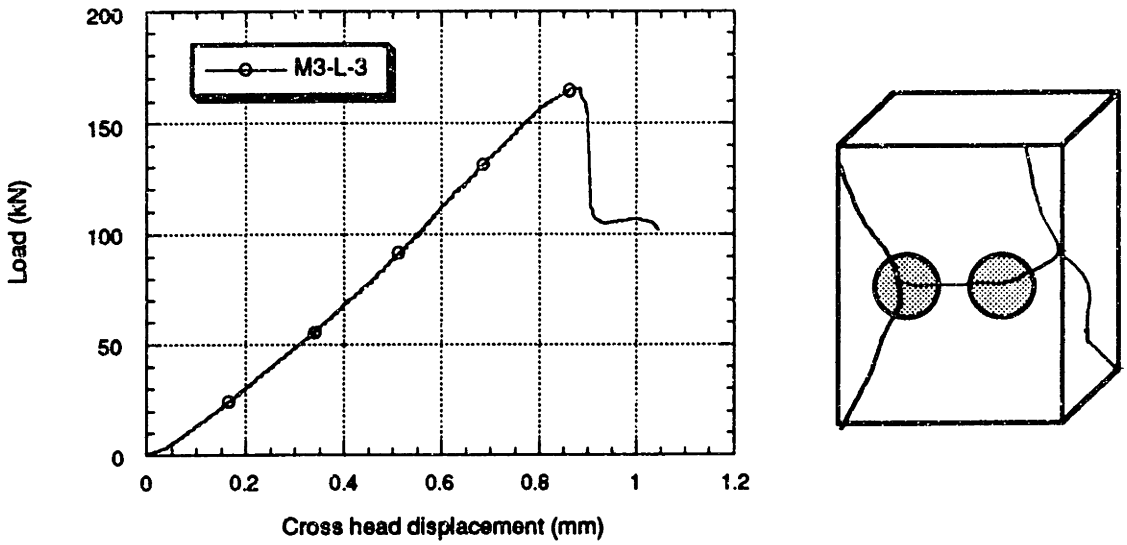

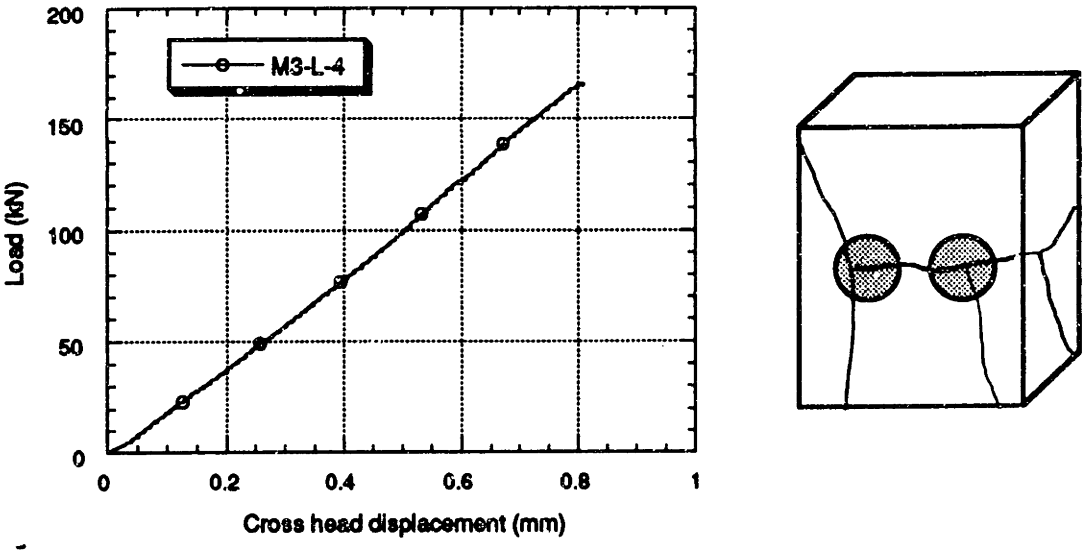

Figure B.8 Load versus cross head displacement curves of M3/L block specimens with two inclusions

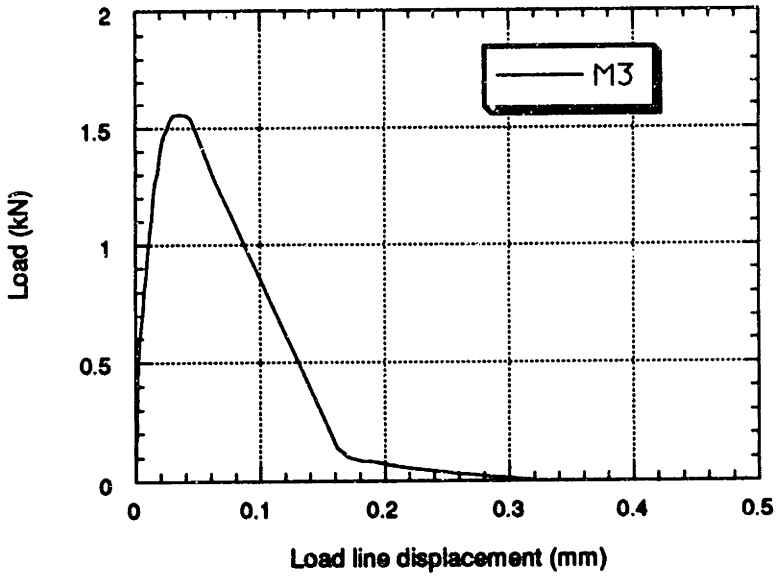

Figure B.9 Load versus load line displacement curve of pre-notched beam specimen composed of M3

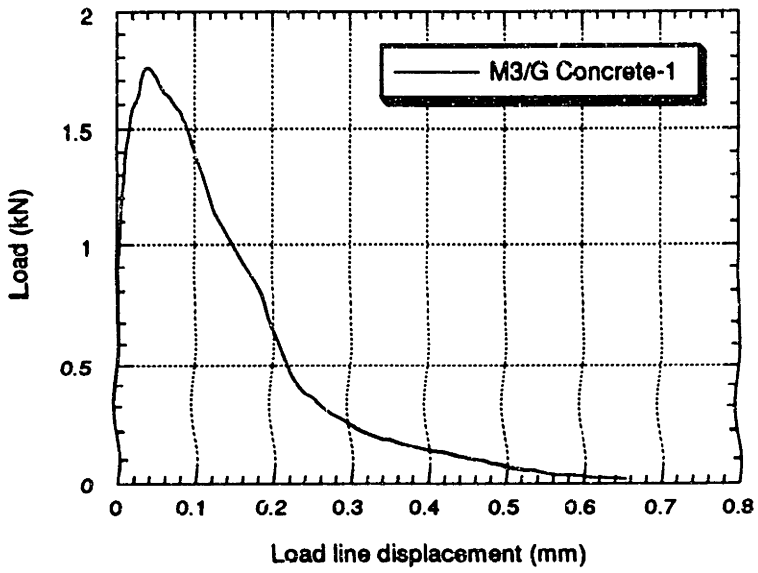

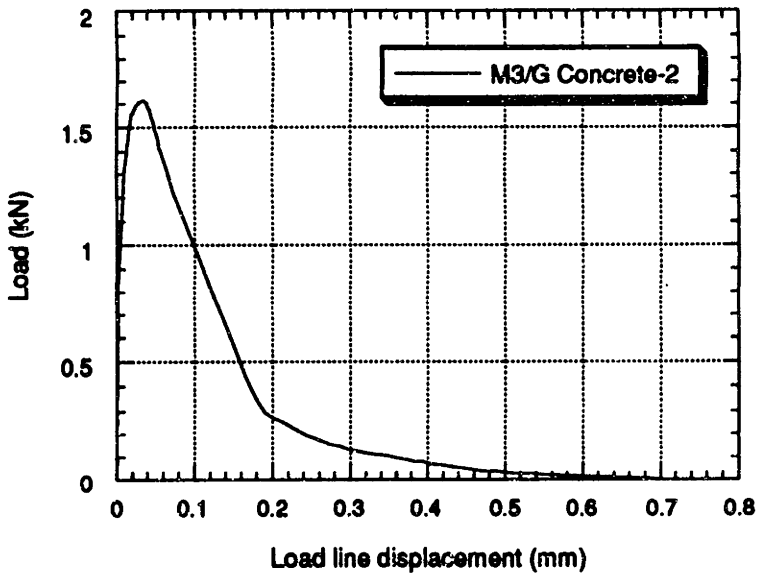

Figure B.10 Load versus load line displacement curves of pre-notched beam specimen composed of M3 and granite

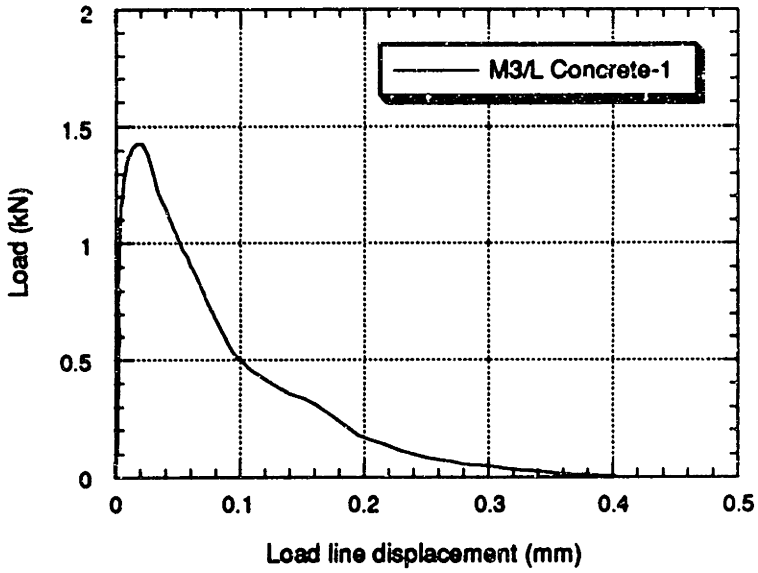

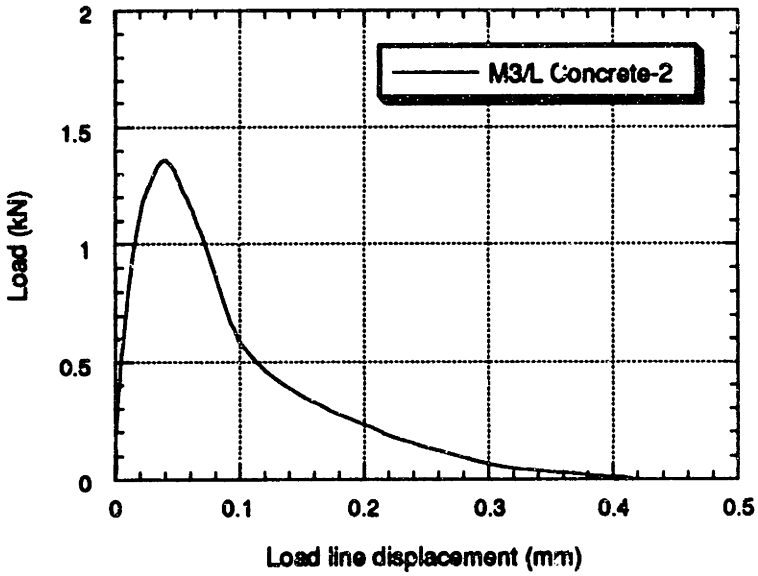

Figure B.11 Load versus load line displacement curves of pre-notched beam specimen composed of M3 and limestone